FLUID BEARING SPINDLES
FOR DATA STORAGE DEVICES

ZHANG QIDE

NATIONAL UNIVERSITY OF SINGAPORE

2003

FLUID BEARING SPINDLES
FOR DATA STORAGE DEVICES

ZHANG QIDE
(B. Eng., M. Eng.)

A THESIS SUBMITTED

FOR THE DEGREE OF DOCTOR OF PHILOSOPHY

DEPARTMENT OF MECHANICAL ENGINEERING

NATIONAL UNIVERSITY OF SINGAPORE

2003

ACKNOWLEDGEMENTS

I wish to express my gratitude to many people who have helped me during this project. The completion and success of the project would not have been possible without their invaluable guidance, support and advice.

Firstly, I would like to express my utmost gratitude to my supervisor, Assoc. Prof. S. H. Winoto for his precious encouragement, guidance and fervent assistance whenever I approach him.

Next, I would like to thank the late Dr. Chen Shixin of Data Storage Institute (DSI) for his precious advice and fruitful discussions during the process of the project.

I would also like to sincerely thank some of the staff of Data Storage Institute, Singapore for their support and assistance in the project, especially to Dr. Liu Zhejie for his advice in electrical motor design. The understanding and support from the management of DSI is greatly appreciated and acknowledged.

Finally, the invaluable understanding and support from my wife, my daughter and my family members are forever remembered and cherished.

TABLE OF CONTENTS

SUMMARY

Four different types of fluid bearing, namely, hydrodynamic bearing, aerodynamic bearing, hybrid fluid bearing and bi-directional rotating fluid bearing are studied in the work.

First, hydrodynamic bearings were investigated. The dynamic characteristics of five type journal bearings are studied and compared, and the herringbone grooved journal bearing is selected and recommended as the journal bearing to be used in spindle motors for data storage devices. The optimal design parameters for herringbone grooved journal bearing, herringbone grooved thrust bearing and spiral grooved thrust bearing are identified by parametric studies and can be used in future designs of hydrodynamic bearings. Using Taguchi's robust design method, effect of parts machining tolerance to the performance of fluid bearings is examined. The relative importance of the individual parameter and its sensitivity to parts machining tolerance are identified.

Secondly, aerodynamic bearings were investigated. Their merits and drawbacks are discussed and compared with hydrodynamic bearings. Effect of changing groove pattern parameters on the performance of aerodynamic bearings is investigated. A set of optimal design parameters is proposed for a short journal bearing that has the ratio of $L/D = 0.2$ only.

Then, a hybrid configuration of fluid bearing system consisting of oil lubricated journal bearings and air lubricated thrust bearings is proposed and investigated. The numerical prediction show that the spindle motors with the hybrid bearing system has 20% lower power consumption than those spindle motors with fully oil lubricated bearing system. The measurement results to the prototypes confirmed above conclusion.

To break the limitation of unidirectional rotation of current fluid bearings and extend their application areas, a bi-directional rotating fluid bearing system is introduced and its characteristics are investigated and compared with unidirectional rotating fluid bearings. With the bi-directional rotational capability, the application of fluid bearings becomes possible in devices that request reversible rotation during operation.

Two types of prototype, namely, the ferro-fluid bearing and the hydro-aerodynamic hybrid bearing spindles were fabricated and tested. The experimental results are presented and compared with those of ball bearing spindles. The good performance of fluid bearing spindles is confirmed. The major steps and difficulties of designing a hydrodynamic bearing spindle motor are also addressed and the solutions are discussed.

The comparisons between ball bearing and fluid bearing spindle motors were carried out to study: 1) the response of two types of spindles to unbalanced magnetic force; 2) the vibration characteristics of disks mounted on ball bearing and fluid bearing spindle motors.

It is found that the unbalanced magnetic force causes vibration and acoustic noise for ball bearing spindle motors and horizontally positioned fluid bearing spindle motors. However, it can enhance the performance for vertical positioned fluid bearing spindle motors with some given conditions.

The experimental results showed that when the disks were mounted on fluid bearing spindle motors, the rocking mode of disks could not be observed and the vibration modes caused by the waviness and flaws on the ball bearing surface were successfully suppressed. Hence, the risk of the track misregistration caused by disk vibration is much reduced.

NOMENCLATURE

a_{c}	stator tooth arc (mm)
a_{g}	ratio of groove width to total width of a pair of groove and ridge region.
b_{tb}	width of tooth body (mm)
B_c	flux density at tooth tip surface (T)
B_g	air gap flux density (T)
B_{ry}	flux density in rotor yoke (T)
B_{sy}	flux density in stator yoke (T)
B_{tb}	flux density in tooth body (T)
B_{tt}	flux density in tooth tip (T)
C	clearance of bearing, R_{c} for journal bearing, and A_{c} for thrust bearing (mm)
D	diameter of shaft (mm)
D_{ij}	damping coefficients of bearing, (N•s/m)
d_0	diameter of hole along axis of shaft (mm)
d_{co}'	estimated outer diameter of conductor (mm)
d_{co}	outer diameter of conductor including insulation (mm)
d_{or}	outer diameter of rotor (mm)
d_{os}	outer diameter of stator (mm)
E_a	average back e.m.f. (V)
E_m	peak value of back e.m.f. (V)
g	air gap length
G_{d}	groove depth (μm) or ratio of groove depth
h	fluid film height (μm)
h_m	magnet thickness (mm)

h_r	film thickness above ridge region (mm)
h_{ry}	rotor yoke height (mm)
h_{sy}	height of stator yoke (mm)
H	non-dimensional fluid film height
H_g	air gap field intensity (A/m)
H_m	field intensity at working point of magnet (A/m)
K_{ij}	stiffness of bearing (N/m)
I_{st}	starting current (A)
l_s	effective axial length of stator lamination (mm)
L	length of journal (mm)
M_f	frictional torque (mN•m)
N	total number of turns per coil
N_g	number of grooves
N_p	number of turns per phase winding
N_s	operating speed of spindle motor (rpm)
p	number of pole pairs
p	pressure (Pa)
p_{il}	total iron loss in stator (W)
p_{st}	iron loss in stator yoke (W)
p_{tb}	iron loss in tooth bodies (W)
p_{tt}	iron loss in tooth tips (W)
P	power consumption of bearing system or power transmitted by shaft (W)
P_a	ambient pressure (N/m^2)
q	number of coils connected in series per phase
r_e, r_i	outer, inner radius of thrust plate (mm)

R	radius of the journal bearing/thrust bearing (mm)
R_a	phase resistance (Ω)
R_m	motor resistance (Ω)
S_s'	slot space available for one coil (mm^2)
S_s	slot space occupied by conductor bundles (mm^2)
T	temperature (°C)
T_s	Starting torque (mili-N•m)
U	linear velocity of rotating surface (m/s)
V	relative velocity (m/s)
V_{cc}	supply voltage (V)
W	load capacity of bearing (Newton).
$\mathrm{W_r}$	radial load capacity of herringbone journal bearing (N)
W_{st}	weight of stator yoke (kg)
W_{tb}	weight of tooth bodies (kg)
W_{tt}	weight of tooth tips (kg)
z	coordinate in axial direction (mm)
Z	total number of conductors

α	groove inclined angle (degree)
α_w	waveform coefficient for air gap field
γ_g	ratio of groove region to the length of journal bearing
ε	eccentricity ratio of journal bearing
θ	coordinate in circumferential direction (degree).
Λ	bearing number

μ	dynamic viscosity of lubricant (Pa•s).
ρ	density of lubricant (kg/m^3)
τ	pole pitch (mm)
Ψ	relative clearance
ω	angular speed of journal bearing / thrust bearing

LIST OF FIGURES

LIST OF TABLES

Chapter 1

INTRODUCTION

1.1 Background and Motivation

Hard disk drive is a data storage device using magnetic medium and one of the most important computer components (Bhushan, 1996). With the rapid progress of computer technology and its applications, the hard disk drive industry has also developed rapidly. The industry produced about 220 million hard disk drives in 2002, and the forecast for 2006 is 390 million units as the shipment of hard disk drives follow the upward path of various types of computer and consumer markets (Donovan, 2003).

A disk drive typically includes a single or multiple magnetic disks concentrically mounted on the hub of a precision spindle motor assembly in which the ball bearing system is commonly used. Digital information can be stored in the concentric data tracks on the disk surface (Ashar, 1997; Kozierok, 1999). The combined movement of the spindle and the actuator allows the magnetic read/write head to access any portion of the disk tracks, hence, read data from or write data onto disks. For a hard disk drive, the basic requirements are to safely and reliably keep as much as possible data into disks, and to read or write data as fast as possible (Grochowski and Hoyt, 1996).

In recent years, the demands for high performance computer products have stimulated and accelerated the advancement of magnetic recording technology towards miniaturization, high storage capacity, and fast data transfer rate (MacLeod, 1995; Schirle and Lieu, 1995). The data storage capacity was increased with an amazing speed. From a few megabytes (5MB) of early hard disk drives to 70-80 gigabytes (GB) of present hard disk drives (Disk/Trend, 1999, IBM, 2000)[*]. The storage capacity was increased by several thousands times. The increase of data storage capacity of a disk drive is directly related to the increase of areal density of disks (Guo and Bozorgi, 2000). Recently, the areal density of hard disks was increased rapidly by almost 100% per year. The old estimated limitation of areal density of 40 Gbites/in^2 has been broken. The long time goal of 100 Gbites/in^2 has been achieved. The new target is 200 Gbites/in^2 and people even discuss the possibility of 1 Tbites/in^2 now. (Speliotis, 1999; Frey and Zipperian, 2000; Wood *et al*., 2002).

The areal density of a disk consists of linear density (bits/inch) and track density (tracks/inch) (Grochowski and Thompson, 1996). The areal density of a disk can either be increased by increasing its linear density or by increasing its track density (Speliotis, 1999). The increase of linear density mainly depends on the development of media material. The track density, which is another factor to determine the areal density of disks, is however limited by the accuracy and consistency of the rotational motion of the spindle assembly. Therefore, to increase the track density, the spindle motor has to be improved. It is required that the disk drive spindles must have a low magnitude of random vibration in both of axial and radial directions, that is, lower axial and radial non-repeatable run out is required (Yoshida *et al*., 1996). In addition to the requirement of low non-repeatable run out, the spindle motor bearing should also possess the following characteristics: higher stiffness, higher load capacity, especially in the radial direction, higher shock resistance capability, low power consumption and low acoustic noise (Quantum, 2000a and 2000b).

Since the areal density will soon reach the level of 200 Gb/in^2, the shortcomings of the conventional ball bearing supported spindle assembly become

---

[*] Up to April 2003, the 250 GB hard disk drives are available in market.

more acute with such high areal density. Major problems with the use of a ball bearing spindle assembly are its high level of non-repeatable-runout (NRRO), and wear rate (Noguchi, 1999). Because of the non-uniformity and geometric imperfectness of bearing balls, inner and outer races, unpredictable runout can occur during operation, and it represents the main constrains for the data storage track width which has to accommodate the magnitude of the irregular vibration in the radial and the axial directions. As a result, the maximum achievable track density is limited by the level of NRRO. In practice, pre-loading measures for the ball bearing spindles are commonly used in order to reduce the NRRO. However, excessive pre-loading force will cause further increase in the wear rate and frictional losses, whilst any further miniaturization of the disk drives demands lower power losses since heat dissipation becomes more difficult to manage. Due to direct surface contacts between bearing members, ball bearings have relatively high wear rate. This shortcoming makes it an undesirable choice for high speed applications. In order to prevent any wear debris, dust, foreign bodies and evaporating substances from exhaling out of the bearings and contaminating the magnetic data storage media, a seal mechanism has to be provided to the ball bearing spindle motors. The performance of this seal mechanism tends to degrade with increasing wear, which represents another disadvantage of ball bearing spindles for high speed applications. Furthermore, with further reduction in size of hard disk drives, the size reduction of ball bearing faces some limitations, therefore, they cannot always fit in the progressively miniaturized disk drive formats.

Fluid film bearings (FFB) appear to be a promising choice for high precision spinning motion (Swan *et al.*, 1996). In a self-acting FFB system, the bearing surfaces are kept separate by a lubricant film, so that there is no metal-to-metal contact during operation, and therefore minimizing wear rate. Moreover, fluid bearing spindles provide extremely low NRRO spinning (Bouchard *et al*., 1987; Ku *et al*., 1998), as compared with ball bearing spindles, without having the previously mentioned drawbacks. Recently, attempts have been made to incorporate FFB technology in hard disk drives (Blount, 2001; Matsuoka *et al*., 2001).

Depending on the lubricant used, fluid bearings can be classified as hydrodynamic bearings, aerodynamic bearings and hybrid bearings. Hydrodynamic bearings use liquid lubricants such as various mineral oils and synthetic oils. Aerodynamic bearings use gas as their lubricant for which air is the most frequently used for obvious reasons. Hybrid bearing systems use both gas and liquid as lubricants. According to the design requirement, there can be a combination of oil lubricated journal bearings and air lubricated thrust bearing or vice versa (Zhang *et al*., 1999).

The most difficult problem in using hydrodynamic bearings for hard disk drives is the lubricant sealing. The bearing lubricant must be securely confined by a seal mechanism since lubricant leaking into the space of the data storage disks causes contamination of the recording media and may result in malfunction of the disk drives. Lubricant leakage can also cause degradation of the bearing performance, resulting in failure of the disk read and write processes (Khan and Rudd, 1999; Zhang and Koka, 1999). Hence, a good design of sealing mechanism is an important as well as difficult task, since such sealing may cause excessive frictional loss, in case a contact seal is used. On the other hand, the use of non-contact sealing may be insufficient since the spindle must be able to withstand a high level shock. Other alternatives using sophisticated sealing mechanism may only be realized at a higher manufacturing cost (Brink *et al*., 1993; Brown, 1995).

Air lubricated bearing spindles are attractive since they do not require sealing. However, in practice, most of gas lubricated bearing spindles are static (external pressurized) bearings, that is, an air compressor is needed to supply and maintain the air pressure in the bearings. Aerodynamic (self-acting) bearings suffer from one major weakness, that is, the difficulty to achieve sufficient load capacity and stiffness. Compared to hydrodynamic bearings, the load capacity and stiffness of aerodynamic bearings are relatively lower than those of hydrodynamic bearings (Fuller, 1984). Measures to enhance the rigidity of the air bearing system, for example, to reduce the bearing clearance, will inevitably increase the manufacturing cost. Furthermore, disk drives should be able to withstand a high level shock. When the rotating mass is large, for instance in high capacity disk drives that have large number of disks, the stiffness constraint becomes more stringent. As a result, the utilization of the self-acting FFB system lubricated fully by air is limited to cases where the passive load is relatively light such as the spindle of the polygon mirror scanners. A particular problem with the use of an aerodynamic journal bearing system is the occurrence of instability during operation, especially when its radial load is small (Szeri, 1998).

The present work thus attempts to carry out some parametric studies to investigate and compare the performance of different types of fluid bearing systems, find their advantages and disadvantages, and to develop a spindle motor suitable for hard disk drives and other data storage devices.

1.2 Literature Review

A brief historical account on the development of hard disk drives as well as its spindle motor, and the development of fluid bearings is presented in this section. Such an overview of spindle motors used in hard disk drives and the development of fluid bearing system may be useful in determining the direction of the present work.

1.2.1 Development of hard disk drives and spindle motors

The first disk drive (Model 350) called RAMAC (Random Access Method of Accounting and Control) was introduced by IBM in 1957 (Stevens, 1981). This drive was invented at the IBM research laboratory in San Jose, California. It consisted of 50 rotating disks mounted on a vertical shaft, each 24 inches in diameter and each having a magnetic medium coating to store data. Accessing the data was done by a pair of air-bearing supported heads mounted on an access arm that could be moved under servo control to one of the 50 disks. The heads were also able to move in and out across the radius of a disk. The areal density of IBM 350 was 2,000 bits/in^2 with linear density of 100 bits/in and track density of 20 tracks/in. The storage capacity of the system was 5 MB. The rotating speed of the disk was 1,200 rpm (revolutions per minute), and the data rate of the information was 12.5 kB/s (Harker, 1981; IBM, 2000).

In 1962, using self-acting air slider-bearing support of the magnetic read/write head in hard disk drive, the IBM Model 1301 was produced. The 1301 drive had two 28 MB storage modules, each with a stack of 25 disks, equipped with a comb of 50 head sliders positioned on the disk surfaces by a hydraulic actuator. The disks were rotated at 1,800 rpm and the average seeking time of the actuator was 165 ms. With a track density of 50 tracks/in and a bit density of 520 bits/in, the storage density achieved was about 13 times of the model 350 disk drive (Stevens, 1981).

In 1969, a project to develop the "Winchester" disk drive was started to provide a new data storage device for small systems. The resulting disk drive IBM Model 3330 had a removable data module that contained either two or four disks as well as the disk spindle and bearings, the carriage, and the head-arm assembly with two low-mass sliders per disk surface. The diameter of the disks was reduced to 14 inch. The area density was increased to 1.69 Mb/in^2, an increase of 845 times of that of the 350 RAMAC (Daniel *et al.*, 1999).

With the development of database applications that required disk data to be available at all time, the disk drive returned to fixed disk technology. In 1976, the IBM Model 3350 was introduced using Winchester technology, with eight 14-inch disks per spindle, and achieved a capacity of 317.5 MB. The track density was increased to 478 t/in and the bit density to 6,425 b/in with the areal density of 3.07 Mb/in^2.

In 1979, the thin-film head was introduced into disk drive and was used in IBM Model 3370. It represented a major advance over the magnetic heads of earlier disk drives. The model 3370 had a capacity of 571 MB and contained seven 14-inch-diameter disks with a rotating speed of 2,964 rpm and a media data rate of about 1.9 MB/s. The new and smaller sliders of thin film head reduced the head flying height from 50 μin (1.2 μm) to 13 μin (320 nm). The areal density was 7.7 Mb/in^2 with the bit density of 12,134 b/in and the track density of 635 t/in. Then Model 3380 was introduced in 1981. It had a capacity of 1,260 MB and rotated at 3,620 rpm. In 1989 IBM Model 3390 with a capacity of 3,784 MB and contained nine 10.8-inch particulate disks was introduced. The smaller disks reduced the power consumption by more than a factor of 3 of that of the earlier Model 3380. The IBM 3390 had a bit density of 27,940 b/in and a track density of 2,242 t/in for an areal density of 62.6 Mb/in^2, which was a 31,320-fold improvement over the 350 RAMAC.

To reduce the power consumption of disk drives, the format factor of the disk drives was continuously reduced (Grochowski *et al.*, 1993). The first move to smaller disks was in 1979, from 14 inch to 8 inch with the IBM Model 3310. Next came the first 5.25-inch diameter disk drive of the Seagate ST 506 in 1980 (Seagate, 2000). In 1983, the first 3.5-inch drive, the Rodime RO 352, was produced and the first 2.5-inch drive, the Prairie Tek 220, was introduced in 1988 (Danial *et al.*, 1999). In 1998, IBM announced their new product of 1-inch hard disk drive (IBM, 1998). The principal motivation for the trend is the limited space and the power available in desktop personal computers that began to appear in the late 1970s. With the reduction of disk format factor, the rotating speed of the disk drives also gradually increased to 3,600 rpm, 4,500 rpm, 5,400 rpm, 7,200 rpm, 10,000 rpm, 14,000 rpm and 15,000 rpm in 2000 (IBM, 2001).

In the late 1980s and early 1990s, the development of magnetoresistive head (MR head); the high-coercivity, thin-film disk; and the Partial Response, Maximum Likelihood (PRML) channel further accelerated the increase of areal density of disk drive. The areal density growth rate was almost 60% per year in the middle of 1990s and increased to 100% per year in the late 1990s and early 2000s. Nowadays, the next target of the areal density is 200Gb/in^2. With such high areal density, the requirement to the spindle motors used in hard disk drives also becomes higher and higher (Chen *et al.*, 1999; Matsuoka *et al.*, 2001).

Currently, most hard disk drives use ball bearing spindle motors. However, because of the inherent drawbacks mentioned previously, ball bearing spindle motors are no longer suitable for the next generation, high-performance disk drives. Spindle motors with better bearings are urgently needed. Fluid bearing spindle motor is a promising alternative to the conventional ball bearing spindle motor. According to the experiment and measurement carried out by Bouchard *et al.* (1987), the non-repeatable runout (NRRO) of the fluid bearing spindle motors is at least one order of magnitude smaller than that of conventional ball bearing spindle motors. Besides having lower non-repeatable run out, fluid bearing spindle motors also possess lower acoustic noise and higher shock resistant capability, which are essential for applications in audio and video devices (Haystead, 2001; Porter, 2001).

1.2.2 Development of fluid bearings

The fluid bearing has been widely used in various engineering applications. The history of fluid film bearings goes back to the late part of 19th century. Petrov (1836-1920), Tower (1845-1904) and Reynolds (1842–1912), independently discovered and formulated the concept of hydrodynamic lubrication during a short period, from 1883 to 1886. It was Petrov who first recognized the importance of fluid viscosity in friction and that the nature of friction in a bearing was not the result of the rubbing of two solid surfaces but stemmed from the viscous shearing of an intervening fluid film. He proposed the nature of friction in a bearing and formulated the expression of friction force in a bearing, known as Petrov's equation $F_\tau = \mu UA/h$. But the load carrying capacity of bearings was discovered by Beauchamp Tower, who in 1883-1884 conducted a series of experiments which revealed the presence of hydrodynamic pressure in the fluid film. Both Petrov and Tower proposed their concepts through experimentation. The theoretical explanation was achieved by Osborne Reynolds, which was almost simultaneously with the experimental work of Petrov and Tower. Reynolds derived the basic lubrication equation that bears his name. The Reynolds equation has become the essential tool of hydrodynamic lubrication, and the mid-1880s is considered as the birthday of the lubrication science (Pinkus, 1987).

Albert Kingsbury discovered that it was not necessary for the fluid film in fluid bearings to be oils or liquids; it could also be gases. With a cylinder piston in vertical position Kingsbury one day twirled the piston and found that the slightest effort made it spin. After that, Kingsbury constructed a special bearing and published his findings in 1897. Thus, hydrodynamic lubrication was extended to compressible fluids (Pinkus, 1987).

Since the Reynolds equation is a non-homogenous partial differential equation with variable coefficients, it is difficult to solve analytically. Sommerfeld overcame the difficulty in 1904 by introducing a substitution now known as "Sommerfeld substitution" (Hamrock, 1994). Although the Sommerfeld's solution of Reynolds equation has an assumption of infinitely long shaft, the result can actually be applied to cases where the ratio of shaft length over shaft diameter is greater than 2.

Rayleigh derived a set of solutions for sliders of various film shapes. In 1918, Rayleigh calculated the load capacity of bearing and obtained the optimum values for the step ratios. Using calculus of variations, he showed that a stepped slider is the best configuration compared to those with a linear taper, a crowned or exponential film shape (Fuller, 1984).

In 1913, Harrison derived the differential equation for compressible fluid film. Instead of using continuity equation, he used the perfect gas equation under isothermal conditions to obtain the compressible Reynolds equation. The equation set a theoretical foundation for the hydrodynamic action of gas lubricants. Moreover, in gas-lubricated bearings, there was no cavitation and the simple periodic boundary conditions applied because the pressure could not fall below zero.

The problems of bearing dynamics and stability was addressed in 1925. It was Stodola who first realized that a bearing was not a rigid support but represented rather a set of springs and dashpots. Their characteristics have a telling effect on rotor critical and dynamic behavior. Since then, bearing stiffness and damping coefficients have become basic parameters in bearing analysis. At the General Electric Research

Laboratory, Burt Newkirk found the phenomenon of bearing-induced instability, which was first called as oil whip, and later generalized to half-frequency whirl.

During 1932 - 1937, Swift formulated fully the Reynolds equation applied to dynamic loading and extended to problems of hydrodynamic stability. Swift solved the question of the trailing boundary conditions on diverging films by showing that $p = dp / d\theta = 0$ is a requirement of both continuity and the minimum potential energy principle.

The idea of an infinitely short as opposed to an infinitely long bearing first occurred to Michell who suggested a simplified form of Reynolds equation for the short bearings in 1929. However, it was not until 1952 that Ocvirk provided a detailed and full solution to the problem of short bearings (Pinkus, 1987).

The first numerical solution of finite Reynolds equation using proper boundary conditions was made by Pinkus in 1956. He obtained the solutions not only for circular but also for elliptical and three-lobe bearings for the ratios from L/D = 1.5 to L/D = 0.25, as well as for finite sector thrust bearings of various arcs and ($R2/R1$) ratios. Within a very short period, a whole spectrum of comprehensive solutions for full and partial journal bearings began to appear for both liquid and gas bearings. Some of major contributors are Raimondi and Boyd (1958), Hays (1958), Raimondi (1961), Gross (1962), and Castelli and Pirvics (1967).

Based on some correction factors to the edge effect, Muijderman (1964) derived a set of half-analysis formulae to calculate the pressure distribution and load capacity of spiral groove thrust bearing in detail. In 1963, Vohr and Pan derived a differential equation for the smoothed overall pressure distribution of a spiral-grooved, self-acting bearing of arbitrary geometry based on the "narrow groove theory" (NGT) by assuming that the number of grooves approaches to infinity. The narrow groove theory was presented in detail by Malanoski and Pan (1965), Smalley (1972), Bootsma (1973), Constantinescu *et al*. (1985) and Kawabata *et al*. (1991).

Vohr and Chow (1965) presented an analysis for the herringbone-grooved gas-lubricated, cylindrical journal bearings. The pressure distribution was obtained by numerical integration, and the solutions were based on a perturbation of eccentricity ratio and only valid for small eccentricities. Using the equations of Vohr and Chow, Hamrock and Fleming (1971) showed a procedure to determine optimal parameters of self-acting herringbone journal bearings for maximum radial load capacity and maximum stability (Fleming and Hamrock, 1974), respectively. The analysis is, however, valid for the cases of small eccentricities only. The limitations for the above methods are that accurate results cannot be obtained for high eccentricities or small number of grooves.

With the progress in computer technology and numerical methods, the Reynolds equation was directly discretized either by finite difference method (FDM) or finite element method (FEM). The alternating direction implicit (ADI) method was modified and applied to the Reynolds equation for thin gas films (Bonneau and Absi, 1994). A code was developed to predict both steady state and dynamic performance for an aerodynamic journal bearing and the results were compared with those of Raimondi (1961). Using FEM, the performance characteristics of hydrodynamic and aerodynamic journal bearings were also investigated by Kinouchi and Tanaka (1990), Bonneau and Absi (1994), respectively. Ono *et al*. (1998) investigated the characteristics of several different types of journal bearings and thrust bearings (Zhu and One, 1999) using FDM algorithm. Zang and Hatch (1995) published an algorithm to calculate the pressure distribution of journal bearing and thrust bearing together.

For high speed rotating journal bearings, it is possible that cavitations occur in bearing divergent area. Jang and Chang (2000) investigated the performance of HGJB by considering the effect of cavitation, and the finite volume method (FVM) was used in their investigation. To overcome the difficulties of film thickness discontinue and the groove apex singularity in HGJB, Wan *et al*. (2002), and Lee *et al*. (2003) proposed a scheme of grid transformation and studied the cavitation foot-prints in symmetrical and non-symmetrical grooved herringbone grooved journal bearings.

One of the important areas in lubrication is hydrodynamic seal. The early interest in the hydrodynamic seal goes back to Nau (1964, 1968). Vohr and Chow (1969) published a theoretical analysis of spiral grooved screw seal for turbulent operation. Sneck and Mcgovern dealt with the spiral-groove face for inward pumping in 1973 (Pinkus, 1987). The sealing effect by viscous pumping of a herringbone journal bearing was numerically investigated by Kawabata *et al*. (1991). Winoto *et al*. (2001a & b) experimentally studied the effect of visco-sealing generated by the visco-pumping effect of herringbone grooves as well as the effect of geometric parameters on sealing performance and a set of optimum parameters were identified based on the experimental results.

1.3 Objectives and Scope

The application of fluid bearing in spindle motors for hard disk drives or other data storage devices is relatively new. The spindle motors used in storage devices usually operate at conditions of high-speed, light-load and high-precision. It is different from the conventional applications of fluid bearings in low-speed and heavy-loaded conditions. Therefore, it is necessary to investigate the performance of fluid bearings at such high-speed, light-loaded and high-precision applications to have a better understanding of fluid bearings in such situations.

Most of previous mentioned works just analyzed single type fluid bearing and did not compare the performance of different fluid bearings. Therefore, the present work intends to systematically investigate and compare the performance of different types of fluid bearings. The hydrodynamic bearing will be first investigated since, among fluid bearings, it is the most widely used in the spindle motors for data storage devices. However, with the rapid increase in spindle rotational speed, the hydrodynamic bearing will encounter two major problems: 1) lubricant deterioration caused by high shear rate, which will result in the performance degradation of the spindle motors, and 2) higher power consumption of spindle motors that use hydrodynamic bearings. In this situation, aerodynamic bearings are better alternatives than the hydrodynamic bearings. Hence, aerodynamic bearings are then investigated after the investigation of hydrodynamic bearings. To exploit the advantages of hydrodynamic and aerodynamic bearings and minimize their drawbacks, a hydro-aerodynamic bearing system is introduced and studied. To break the limitation of unidirectional rotation of the current fluid bearings and extend their application areas, a bi-directional rotating fluid bearing system is introduced and its characteristics are compared with those of the unidirectional rotating fluid bearings.

A further objective is to develop a fluid bearing spindle motor that can enhance the system performance of hard disk drives. For this purpose, the spindle motor should provide sufficient radial and axial stiffness so that the spindle can operate in any orientation of the spindle axis. The spindle should also possess an extremely low level of non-repeatable run out and hence enhance the recording density of the disk drives. In addition, the acoustic noise, wear rate and vibration of the spindle motor should also be reduced compared to those of the conventional ball bearing systems. The design issues of developing fluid bearing spindle motor prototypes will be addressed and the prototypes will be fabricated and tested. The experimental results of the prototypes will be presented and compared with the numerical predictions.

Finally, comparisons between ball bearing and fluid bearing spindle motors are carried out. First, the response of ball bearing and fluid bearing spindle motors to the unbalanced magnetic force due to asymmetric design of electric motor are studied. Then, the vibration characteristics of disks mounted on ball bearing and fluid bearing spindle motors are experimentally investigated and compared.

1.4 Outline of Thesis

The thesis consists of nine chapters and an appendix. Chapter 1 introduces the background and the objectives of the project. A brief historical review on the development of hard disk drives and the development of fluid bearings is also presented.

Chapter 2 briefly presents the principle of fluid bearings and the derivation of the Reynolds equation by means of the control volume method and the mass conservation. The numerical algorithm for solving the Reynolds equation is also addressed. The numerical code used in this thesis is validated by comparing the results obtained by our code with some published results. The concept of robust design and Taguchi method are also introduced in Chapter 2.

Four different types of fluid bearing systems are considered in Chapter 3 to Chapter 6. Chapter 3 first compares dynamic characteristics and motion stability of five types of journal bearings. Then, a parametric study for herringbone grooved journal bearing is carried out. The characteristics of two types of thrust bearings are also investigated and presented in Chapter 3. Using Taguchi robust design method, the effect of machining tolerance is also investigated.

Chapter 4 considers aerodynamic bearings. The advantages and disadvantages of air bearings are compared with those of hydrodynamic oil bearings. The performance and the optimum parameters of aerodynamic bearings are also numerically investigated.

A hybrid configuration of hydrodynamic journal bearing and aerodynamic thrust bearing together with its advantages are introduced and presented in Chapter 5.

A bi-directional rotating bearing system is introduced and analyzed by means of numerical simulation in Chapter 6. Its dynamic characteristics and parameters that affect the performance of the bi-directional rotating bearing system are discussed and compared with those of the one-directional rotating bearing system.

Chapter 7 presents the test results of the prototypes of hydrodynamic and hybrid fluid bearing spindle motors. The steps and major concerns in designing a hydrodynamic bearing spindle motor are also addressed.

The comparison between ball bearing and fluid bearing spindle motors are presented in Chapter 8. The effect of unbalanced magnetic force on the ball bearing and fluid bearing spindle motors is first investigated. Then, experimental comparison of vibration characteristics for disks mounted on ball and fluid bearing spindle motors are presented.

The conclusions and recommendations for further work are presented in Chapter 9.

The design steps of electric motor for spindles are shown in Appendix A.

Chapter 2

FLUID BEARINGS

2.1 Classification of Fluid Bearings

Fluid film bearing can be created by sliding motion, by squeeze motion or by external pressurization. According to the mechanism of pressure generation, it can be classified as static pressurized fluid bearing or self-acting fluid bearing. In a static pressurized fluid bearing, the pressure distribution is set up by an external device such as oil pump or air compressor. However, in a self-acting fluid bearing, the pressure distribution is generated by relative motion of its parts. Since the limitation of space, the spindle motors used in data storage devices cannot be an external pressurized fluid bearing, only self-acting fluid bearing spindle motors can be used in these devices. Hence, in the following sections, the focus will be on the self-acting fluid bearings, that is, hydrodynamic and aerodynamic bearings. Due to the obvious discrepancies on the compressibility and the viscosity between the liquid and gaseous lubricants, the performance of “hydrodynamic” and “aerodynamic” bearings is different, especially at high-speed situations.

2.2 Reynolds Equation

The equation that describes hydrodynamic or aerodynamic lubrication can be derived either from the Navier-Stokes equation or from the first principle of viscous flow and mass conservation. Here, the equation is derived from the first principle and mass conservation since it is simpler.

In the control volume shown in Fig. 2.1(a), the mass of lubricant in the control volume at any instant is $\rho h \Delta x \Delta z$. The rate of change within the control volume arises from the change in the difference between the rate of mass flowing into the control volume and the rate leaving the control volume, which is $(\partial \rho q_x^{'} / \partial x)\Delta x \Delta z$ in the x direction and $(\partial \rho q_z^{'} / \partial z)\Delta x \Delta z$ in the z direction. The principle of mass conservation demands that the rate at which mass is accumulating in the control volume must be equal to the difference between the rates at which mass enters and leaves. Therefore,

$$\frac{\partial \rho q_x^{'}}{\partial x} + \frac{\partial \rho q_z^{'}}{\partial z} = -\frac{\partial}{\partial t}(\rho h) . \tag{2.1}$$

From the results of viscous flow, we have

$$q_x^{'} = -\frac{h^3}{12\mu}\frac{\partial p}{\partial x} + \frac{u_a + u_b}{2} h , \tag{2.2}$$

and

$$q_z^{'} = -\frac{h^3}{12\mu}\frac{\partial p}{\partial z} + \frac{w_a + w_b}{2} h . \tag{2.3}$$

Since,

$$\frac{\partial}{\partial t}(\rho h) = \rho \frac{\partial h}{\partial t} + h \frac{\partial \rho}{\partial t} \tag{2.4}$$

and

$$\frac{\partial}{\partial t}(\rho h) = \rho (v_a - v_b - u_a \frac{\partial h}{\partial x} - w_a \frac{\partial h}{\partial z}) + h \frac{\partial \rho}{\partial t} , \tag{2.5}$$

substituting Eqs (2.2) - (2.5) into Eq. (2.1) produces

$$\begin{aligned} &\frac{\partial}{\partial x}(-\frac{\rho h^3}{12\mu}\frac{\partial p}{\partial x}) + \frac{\partial}{\partial z}(-\frac{\rho h^3}{12\mu}\frac{\partial p}{\partial z}) + \frac{\partial}{\partial x}\left[\frac{\rho h(u_a + u_b)}{2}\right] \\ &+ \frac{\partial}{\partial z}\left[\frac{\rho h(w_a + w_b)}{2}\right] + \rho(v_a - v_b) - \rho u_a \frac{\partial h}{\partial x} - \rho w_a \frac{\partial h}{\partial z} + h \frac{\partial \rho}{\partial t} = 0. \end{aligned} \tag{2.6}$$

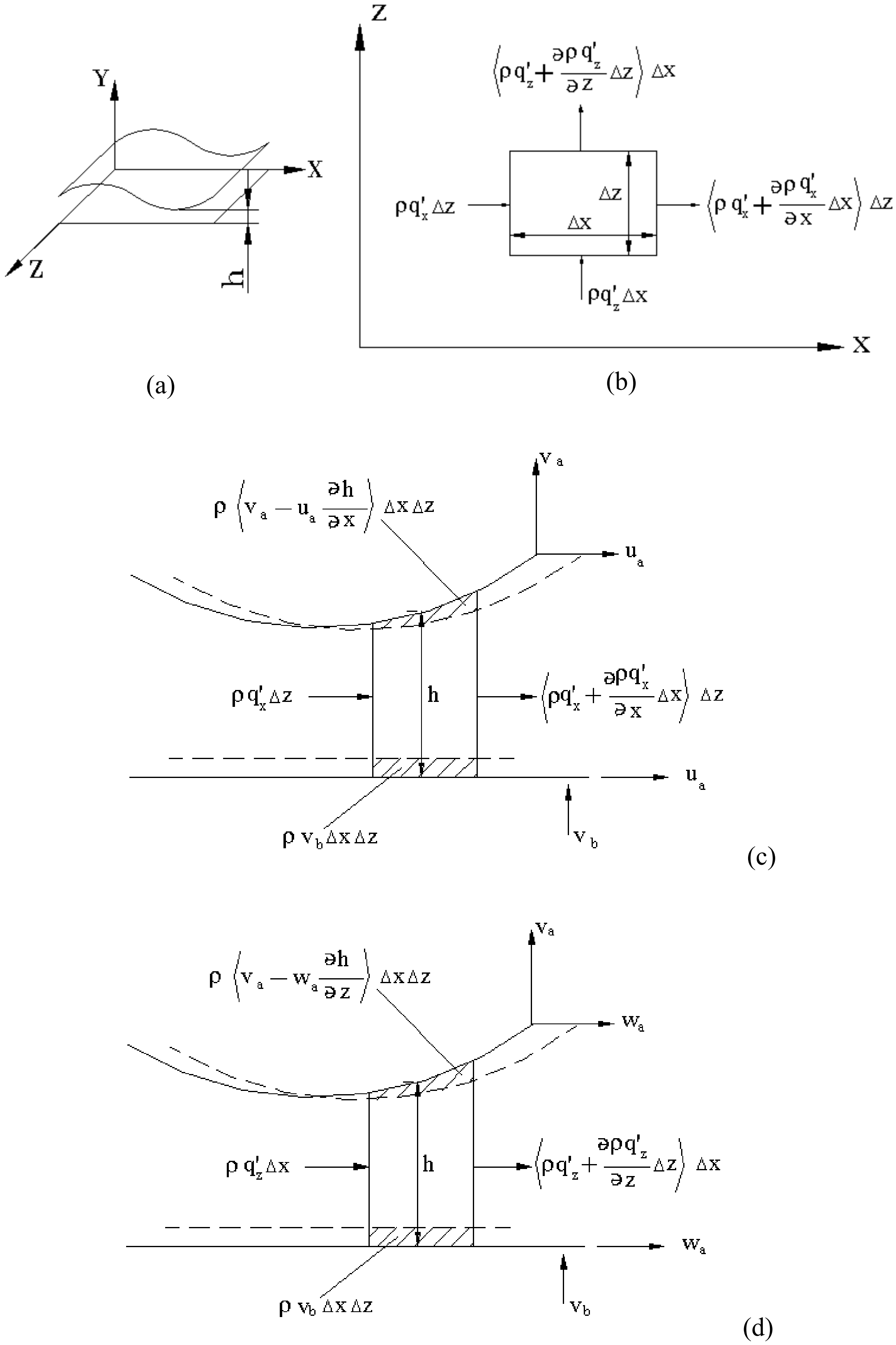

Fig. 2.1 Schematic of control volume of mass flow,
(a) coordinate system, (b) x, z plan, (c) x, y plan, (d) y, z plan.

Equation (2.6) is the general form of Reynolds equation which was first derived by Osborne Reynolds in 1886 (Constantinescu *et al.*, 1985; Hamrock, 1994).

If there is only tangential motion, Eq. (2.6) can be reduced to:

$$\frac{\partial}{\partial x}\left(\frac{\rho h^3}{\mu}\frac{\partial p}{\partial x}\right)+\frac{\partial}{\partial z}\left(\frac{\rho h^3}{\mu}\frac{\partial p}{\partial z}\right)=12\tilde{u}\frac{\partial(\rho h)}{\partial x}+12\tilde{w}\frac{\partial(\rho h)}{\partial z}, \tag{2.7a1}$$

where $\tilde{u}=\frac{(u_a+u_b)}{2}$ and $\tilde{w}=\frac{(w_a+w_b)}{2}$.

In cylindrical polar coordinates, Eq. (2.7a1) is expressed as:

$$\frac{\partial}{\partial r}\left(\frac{r\rho h^3}{\mu}\frac{\partial p}{\partial r}\right)+\frac{1}{r}\frac{\partial}{\partial \theta}\left(\frac{\rho h^3}{\mu}\frac{\partial p}{\partial \theta}\right)=12\left[\tilde{v}_r\frac{\partial}{\partial r}(\rho r h)+\tilde{v}_\theta\frac{\partial}{\partial \theta}(\rho h)\right]. \tag{2.7a2}$$

For incompressible lubricant, Eq. (2.7a1) can be written as:

$$\frac{\partial}{\partial \theta}\left(h^3\frac{\partial p}{\partial \theta}\right)+R^2\frac{\partial}{\partial z}\left(h^3\frac{\partial p}{\partial z}\right)=6\mu R^2\omega\frac{\partial h}{\partial \theta}. \tag{2.7a3}$$

Equations (2.7a1) – (2.7a3) are the frequently used forms of Reynolds equation in fluid film lubrication. Solving Eq. (2.7) using the appropriate boundary conditions will result in the pressure distribution in bearings.

For journal bearings, there are several boundary conditions for Eqs. (2.7a1) – (2.7a3). The first is the “Sommerfeld” boundary condition:

$p=0$ at $z = 0$ and l ; (2.7b1)

$p(\theta) = p(2\pi+\theta)$ in circumferential direction. (2.7b2)

Using Sommerfeld boundary condition, the pressure in the divergent film is negative, that is, lower than the ambient pressure. The pressure distribution for a journal bearing appears a skew symmetrical distribution. For $0 \le \theta < \pi$, the pressure is positive, and for $\pi \le \theta < 2\pi$, the pressure is negative. Such pressure distribution is rarely encountered in real bearing because oil lubricant usually contain some percentage dissolved air. This air will start to come out whenever the pressure lower than the saturation pressure, hence, maitain the pressure in divergence space close to the ambient pressure. Hence, using Sommerfeld boundary condition, there is a discrepancy between the predicted and the real bearing characteristics.

To overcome this problem, the "Half Sommerfeld" boundary condition is proposed. The half Sommerfeld boundary condition simply ignores the negative pressure and sets it as zero in analysis. This approach leads to more realistic predictions of some bearing characteristics. However, it results in a violation of the continuity of mass flow at the outlet of the pressure curve.

Therefore, the third boundary condition, the "Reynolds boundary condition" is proposed as:

$p = 0$ at $z = 0$ and l ; (2.7c1)

$p = dp/d\theta = 0$ at $\theta = \theta^*$, in circumferential direction. (2.7c2)

The "Reynolds boundary condition" meets the mass continue condition. The obtained bearing characteristics are also closer to the real situation. Hence, the Reynolds boundary condition is frequently used in practice.

For thrust bearings, the Reynolds equation and boundary condition becomes:

$$\frac{\partial}{\partial r}(rh^3 \frac{\partial p}{\partial r}) + \frac{1}{r}\frac{\partial}{\partial \theta}(h^3 \frac{\partial p}{\partial \theta}) = 6\mu\omega r \frac{\partial h}{\partial \theta}. \quad (2.8a)$$

$p = 0$ at $r = r_i$ and $r = r_e$; (2.8b1)

$p(\theta) = p(2\pi+\theta)$ in circumferential direction. (2.8b2)

Once the pressure distribution in fluid bearing is obtained by solving Eq. (2.7), the load-capacity of the bearing is calculated by integrating the pressure over the whole bearing surfaces. The components of the load are given by:

$$\begin{Bmatrix} w_x \\ w_y \end{Bmatrix} = \begin{Bmatrix} \int_z \int_{\theta'} (p)\cos\theta' r d\theta dz \\ -\int_z \int_{\theta'} (p)\sin\theta' r d\theta dz \end{Bmatrix}. \tag{2.9}$$

2.3 Dynamic Coefficients of Fluid Bearings

The dynamic coefficients of a journal bearing such as stiffness and damping coefficients are obtained from the dynamic response of the journal bearing to a small perturbation. Figure 2.2 shows a journal bearing at a quasi-steady-state. Assuming the journal bearing is subjected to a small external force (small perturbation), the effect of

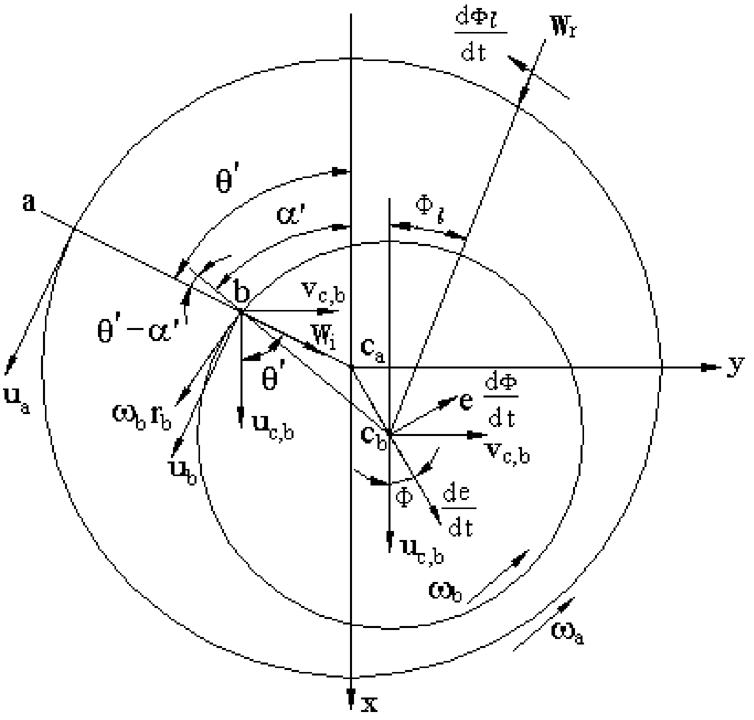

Fig. 2.2 Velocity components and film geometry in a journal bearing subjected to a dynamic load.

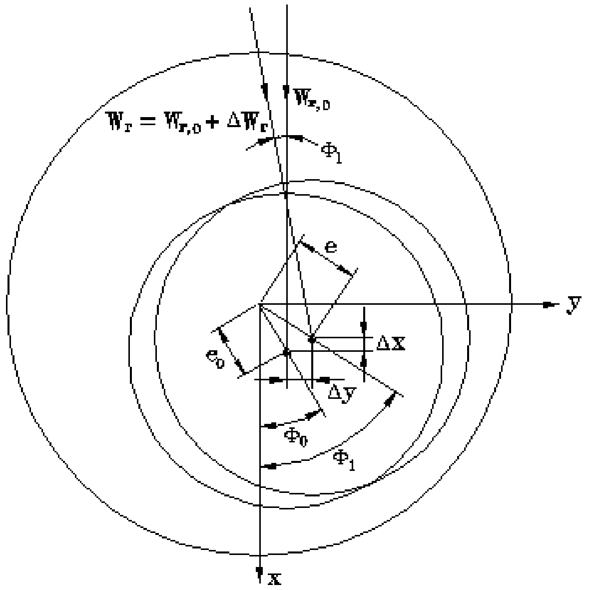

Fig. 2.3 Effect of changing load on bearing's shaft position and relevant parameters.

changing load on the bearing’s shaft position is shown in Fig. 2.3. The relevant parameters associated with these changes are also shown in Fig. 2.3, where subscript *0* refers to the quasi-steady-state position and Δx and Δy are the displacements of the shaft away from this position. The resultant reaction load present in Fig. 2.3 has components w_x and w_y. Performing a first order Taylor expansion of these components gives (Lund and Thomson, 1978; Hamrock, 1994):

$$w_x = (w_x)_0 + (\frac{\partial w_x}{\partial x})_0 \Delta x + (\frac{\partial w_x}{\partial y})_0 \Delta y + (\frac{\partial w_x}{\partial \dot{x}})_0 \Delta \dot{x} + (\frac{\partial w_x}{\partial \dot{y}})_0 \Delta \dot{y} \qquad (2.10a)$$

and

$$w_y = (w_y)_0 + (\frac{\partial w_y}{\partial x})_0 \Delta x + (\frac{\partial w_y}{\partial y})_0 \Delta y + (\frac{\partial w_y}{\partial \dot{x}})_0 \Delta \dot{x} + (\frac{\partial w_y}{\partial \dot{y}})_0 \Delta \dot{y}\,, \qquad (2.10b)$$

where the dots indicate time derivatives. Due to the direction chosen for the coordinate, $(w_y)_0 = 0$.

Let

$$K_{xx} = (\frac{\partial w_x}{\partial x})_0 \quad K_{xy} = (\frac{\partial w_x}{\partial y})_0 \quad K_{yx} = (\frac{\partial w_y}{\partial x})_0 \quad K_{yy} = (\frac{\partial w_y}{\partial y})_0$$

$$D_{xx} = (\frac{\partial w_x}{\partial \dot{x}})_0 \quad D_{xy} = (\frac{\partial w_x}{\partial \dot{y}})_0 \quad D_{yx} = (\frac{\partial w_y}{\partial \dot{x}})_0 \quad D_{yy} = (\frac{\partial w_y}{\partial \dot{y}})_0$$

then, Eqs. (2.10a) and (2.10b) can be expressed as

$$\begin{Bmatrix} w_x \\ w_y \end{Bmatrix} = \begin{Bmatrix} (w_x)_0 \\ 0 \end{Bmatrix} + \begin{pmatrix} K_{xx} & K_{xy} \\ K_{yx} & K_{yy} \end{pmatrix} \begin{Bmatrix} \Delta x \\ \Delta y \end{Bmatrix} + \begin{pmatrix} D_{xx} & D_{xy} \\ D_{yx} & D_{yy} \end{pmatrix} \begin{Bmatrix} \Delta \dot{x} \\ \Delta \dot{y} \end{Bmatrix}. \tag{2.11}$$

Consider a similar first-order expansion of the pressure profile:

$$p = (p)_0 + (\frac{\partial p}{\partial x})_0 \Delta x + (\frac{\partial p}{\partial y})_0 \Delta y + (\frac{\partial p}{\partial \dot{x}})_0 \Delta \dot{x} + (\frac{\partial p}{\partial \dot{y}})_0 \Delta \dot{y}. \tag{2.12}$$

To simplify the notation, let

$$p_0 = (p)_0 \quad p_x = (\frac{\partial p}{\partial x})_0 \quad p_y = (\frac{\partial p}{\partial y})_0 \quad p_{\dot{x}} = (\frac{\partial p}{\partial \dot{x}})_0 \quad p_{\dot{y}} = (\frac{\partial p}{\partial \dot{y}})_0$$

The bearing reaction components are found by integrating the force components over the bearing area, that is,

$$\begin{Bmatrix} w_x \\ w_y \end{Bmatrix} = \int_z \int_{\theta'} (p_0 + p_x \Delta x + p_y \Delta y + p_{\dot{x}} \Delta \dot{x} + p_{\dot{y}} \Delta \dot{y}) \begin{Bmatrix} \cos\theta' \\ \sin\theta' \end{Bmatrix} r d\theta dz. \tag{2.13}$$

The perturbation terms $\Delta x, \Delta y, \Delta \dot{x}, \text{and } \Delta \dot{y}$ are independent of the integration variables, and thus from Eqs. (2.11) and (2.13), we have

$$\begin{Bmatrix} (w_x)_0 \\ 0 \end{Bmatrix} = \begin{Bmatrix} \int_z \int_{\theta'} (p_0) \cos\theta' r d\theta dz \\ \int_z \int_{\theta'} (p_0) \sin\theta' r d\theta dz \end{Bmatrix}, \tag{2.14}$$

$$\begin{pmatrix} K_{xx} & K_{xy} \\ K_{yx} & K_{yy} \end{pmatrix} = \begin{Bmatrix} \int_z \int_{\theta'} p_x \cos\theta' r d\theta dz & \int_z \int_{\theta'} p_y \cos\theta' r d\theta dz \\ \int_z \int_{\theta'} p_x \sin\theta' r d\theta dz & \int_z \int_{\theta'} p_y \sin\theta' r d\theta dz \end{Bmatrix}, \tag{2.15}$$

$$\begin{pmatrix} D_{xx} & D_{xy} \\ D_{yx} & D_{yy} \end{pmatrix} = \begin{Bmatrix} \int_z \int_{\theta'} p_{\dot{x}} \cos\theta' r d\theta dz & \int_z \int_{\theta'} p_{\dot{y}} \cos\theta' r d\theta dz \\ \int_z \int_{\theta'} p_{\dot{x}} \sin\theta' r d\theta dz & \int_z \int_{\theta'} p_{\dot{y}} \sin\theta' r d\theta dz \end{Bmatrix}. \tag{2.16}$$

Equations (2.15) and (2.16) show that once p_x, p_y, $p_{\dot{x}}$ and $p_{\dot{y}}$ are determined, the dynamic coefficients K_{ij} and D_{ij} are also known. The p_x, p_y, $p_{\dot{x}}$ and $p_{\dot{y}}$ can be obtained by solving following equations:

$$\left[\frac{1}{R^2} \frac{\partial}{\partial \theta'} \left(\frac{h_0^3}{12\mu} \frac{\partial}{\partial \theta'} \right) + h_0^3 \frac{\partial}{\partial z} \left(\frac{1}{12\mu} \frac{\partial}{\partial z} \right) \right] \begin{Bmatrix} p_0 \\ p_x \\ p_y \\ p_{\dot{x}} \\ p_{\dot{y}} \end{Bmatrix}$$

$$= \begin{Bmatrix} \frac{\omega}{2} \frac{\partial h_0}{\partial \theta'} \\ -\frac{\omega}{2} [\sin\theta' + \frac{3\cos\theta'}{h_0} \frac{\partial h_0}{\partial \theta'} - \frac{h_0^3}{4\mu R^2} \frac{\partial p_0}{\partial \theta'} \frac{\partial}{\partial \theta'} (\frac{\cos\theta'}{h_0})] \\ \frac{\omega}{2} [\cos\theta' - \frac{3\sin\theta'}{h_0} \frac{\partial h_0}{\partial \theta'} - \frac{h_0^3}{4\mu R^2} \frac{\partial p_0}{\partial \theta'} \frac{\partial}{\partial \theta'} (\frac{\sin\theta'}{h_0})] \\ \cos\theta' \\ \sin\theta' \end{Bmatrix} \tag{2.17}.$$

Therefore, the steady-state pressure obtained can be used to obtain the perturbation pressure. Once the perturbation pressures are known, the dynamic coefficients given in Eqs. (2.15) and (2.16) can then be evaluated.

Besides the load capacity, stiffness and damping coefficients, the power consumption is also an important performance indicator of fluid bearing systems. The power loss of fluid bearing is caused by the viscous friction of lubricant. The power loss of fluid bearing P can be expressed as:

$$P_{0,h} = uf_{0,h} = u\int_0^{2\pi}\int_0^{L}\mu\left(\frac{\partial u}{\partial y}\right)_{0,h} Rd\theta dz\,, \tag{2.18}$$

where, u is the speed of the lubricant, f the friction force on the two surfaces, R, the radius of the shaft, the subscript *0* represents the surface on the shaft surface ($y = 0$) and the subscript h represents the inner surface of the sleeve ($y = h$).

2.4 Numerical Solution

2.4.1 Numerical method

Since Eq. (2.7a3) is a partial derivative equation, only in few cases, the analytical solution of Eq. (2.7a3) is possible. For example, if the journal bearing is infinitely long or very short, then either the second term (for infinitely long case) or the first term (for very short case) of the left side of Eq. (2.7a3) can be neglected, and therefore, the analytical solutions are possible. Otherwise, the solutions of Eq. (2.7a3) and Eqs. (2.17) are usually obtained numerically.

The performance of fluid bearings have been analyzed using different algorithms and schemes. Raimondi and Boyd (1958, 1961) analyzed the performance of plain journal bearing using a numerical method and obtained the results for incompressible fluid and gaseous bearings. Kang *et al.* (1996) investigated the herringbone grooved journal bearing (HGJB) using a finite difference method (FDM). Bonneau and Absi (1994) introduced an analysis of HGJB using a finite element method (FEM). Zirkelback and Andres (1998) carried out a parameter study of the

HGJB using FEM. Wu *et al*. (2002) studied the cavitation flow in HGJB with the operator-splitting method (OSM).

In the present work, a FDM was selected because of its reliability and simplicity in discretizing equation and developing a numerical code. To numerically solve Eq. (2.7a3), it was first non-dimensionalized by defining the following non-dimensional parameters:

$$\overline{P} = p / p_a; \quad \overline{H} = h / C_0; \quad \overline{X} = \theta \quad \overline{Z} = z / L;$$

$$\Lambda = 6\mu\omega(R / C)^2 / p_a; \quad B_r = L/D .$$

Where, p_a is the ambient pressure, C, bearing clearance at eccentricity ratio $\varepsilon = 0$, L, bearing width, Λ, bearing number, and B_r, bearing ratio. $\overline{P}$, $\overline{H}$, $\overline{X}$ and $\overline{Z}$ are non-dimensional pressure, film height, circumferential and axial direction coordinates, respectively. Substituting the above dimensionless parameters into Eq. (2.7a3) and removing the upper bar for simplicity; Eq. (2.7a3) can be re-written as:

$$\frac{\partial}{\partial X}(H^3 \frac{\partial P}{\partial X}) + c_z \frac{\partial}{\partial Z}(H^3 \frac{\partial P}{\partial Z}) = \Lambda \frac{\partial H}{\partial X} \tag{2.19}$$

where $c_z = R^2 / L^2 = D^2/(4*L^2) = 1/(2B_r)^2$.

Using the FDM, the first and second derivatives of an unknown function can be expressed as:

$$\left(\frac{\partial P}{\partial \sigma}\right)_{i,j} = \frac{P_{i+1,i} - P_{i-1,j}}{2\Delta\sigma}, \tag{2.20}$$

$$\left(\frac{\partial^2 P}{\partial \sigma^2}\right)_{i,j} = \frac{P_{i+1,i} - 2P_{i,j} + P_{i-1,j}}{\Delta\sigma^2}, \tag{2.21}$$

where the σ represents X or Z. Substitute Eq. (2.20) and (2.21) into Eq.(2.19), the Eq. (2.19) is converted into a linear system equations:

$$a_1 P_{i,j-1} + a_2 P_{i-1,j} + a_3 P_{i,j} + a_4 P_{i+1,j} + a_5 P_{i,j+1} = b_{i,j}$$

$$i = 1, \ldots\ldots, N_X;\ j = 1, \ldots\ldots, N_Z. \qquad (2.22)$$

where

$$a_1 = c_z \Delta X^2 H^3_{i,j-1} \qquad a_2 = \Delta Z^2 H^3_{i-1,j} \qquad a_3 = -2(\Delta Z^2 + c_z \Delta X^2) H^3_{i,j}$$

$$a_4 = \Delta Z^2 H^3_{i+1,j} \qquad a_5 = c_z \Delta X^2 H^3_{i,j+1} \qquad b_{i,j} = 0.5 \Delta X \Delta Z^2 (H_{i+1,j} - H_{i-1,j})$$

and N_X, N_Z are the number of the total grid points in X and Z directions respectively.

Let:

$$x[(j-1)*N_x + i] = P_{i,j}; \qquad A[(j-1)*N_x + i, (j-2)*N_x + i] = a_1$$

$$A[(j-1)*N_x + i, (j-1)*N_x + i - 1] = a_2; \quad A[(j-1)*N_x + i, (j-1)*N_x + i] = a_3$$

$$A[(j-1)*N_x + i, (j-1)*N_x + i + 1] = a_4; \quad A[(j-1)*N_x + i, j*N_x + i] = a_5$$

$$B[(j-1)*N_x + i] = b_{i,j}$$

Substituting the above expressions into Eq. (2.22), it can be re-written in matrix form as:

$$[\boldsymbol{A}]\{\boldsymbol{x}\} = \{\boldsymbol{B}\} \qquad (2.23)$$

Solving Eq. (2.23), the pressure distribution can be obtained. With further manipulations, other performance indicators, such as load capacity, power consumption, stiffness and damping coefficients of fluid bearings, etc. can be obtained.

A commercial available software package called “AMRD” (by RBTS Inc.) was also used for the analysis of fluid bearings in this work. It also employs a FEM algorithm to solve the Reynolds equation (2.17). If cavitations are not considered in the analysis, the Reynolds boundary condition is used in AMRD for journal bearings. It can also solve the cavitation problems in journal bearings if the effect of cavitation is to be considered.

Since AMRD is designed to analyse performance of different fluid bearings not just for herringbone grooved bearings only, hence, instead of taking the body-match scheme, it employs an algorithm to distribute the mesh points with variable grid step length, so that the ridge or the groove regions can be exactly captured as shown in Fig. 2.4. The information for each grid node, such as the step length along *x* and *z* directions between the nodes, a ridge point or a grooved point, value of groove depth, etc. is provided and assigned to each node in the input file. If change of groove angle or groove width is needed in analysis, then, new input files have to be revised to accommodate the changes of groove parameters. Therefore, using AMRD, the preparation of input files is a tedious and time-consuming task (RBTS, 1998).

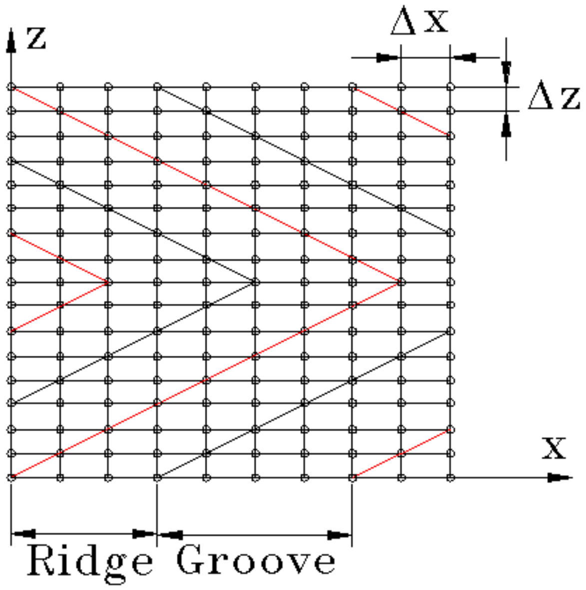

Fig. 2.4 Schematic of mesh node distribution in AMRD.

2.4.2 Code validation

To validate the numerical code, the results obtained by this code are first compared with some published results. Three comparisons are presented here, for a plain journal bearing, a herringbone grooved journal bearing and a herringbone grooved thrust bearing.

Case 1: Plain Journal Bearing

The results for a plain journal bearing obtained by the present code are compared with those of Constantinescu et *al.* (1985). The parameters used for this comparison are:

Diameter of the journal bearing D = 5 mm,

Length of the journal bearing L = 10 mm (L/D = 2) and L = 5 mm (L/D = 1),

Radial clearance R_c = 5.0 μm,

Dynamic viscosity $\mu = 19.5 \text{x} 10^{-3}$ Pa.s at 20 °C,

Rotational speed N_S = 7,200 rpm,

Eccentricity ratio ε = 0.0 - 0.9.

The load capacity and the eccentricity angle obtained by the present code are listed and compared with the results of Constantinescu *et al.* (1985) in Table 2.1 for L/D = 1 and L/D = 2. The results for L/D = 1 are also presented in Figs. 2.5 and 2.6. Good agreement between the results is obvious. The maximum discrepancy between the two set results for both load capacity and attitude angle is less than 5% as shown in Table 2.1.

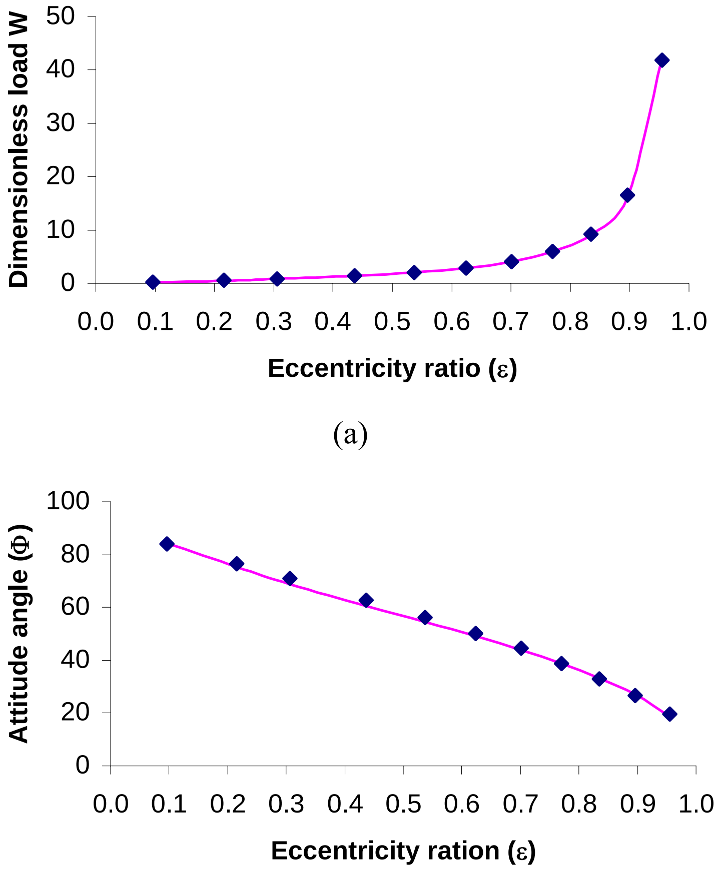

(a)

(b)

Fig. 2.5 Variation of load capacity (a) and attitude angle (b) versus eccentricity ratio for plain journal bearing with L/D = 1.
Legend: ♦ Constantinescu *et al.* (1985), — present result.

Table 2.1 Comparison of load capacity and attitude angle of plain journal bearings with Constantinescu *et al.* (1985), referred as C's

	Dimensionless load capacity				Attitude angle °			
L/D = 1								
ε	C's	present	Δ	%	C's	present	Δ	%
0.0960	84.03	84.29	-0.26	-0.31	0.24	0.23	0.01	2.25
0.2160	76.61	75.35	1.26	1.64	0.56	0.55	0.01	1.67
0.3060	70.96	68.85	2.11	2.97	0.85	0.84	0.01	1.40
0.4360	62.69	60.59	2.10	3.35	1.40	1.40	0.00	0.21
0.5370	56.07	54.56	1.51	2.69	2.05	2.05	0.00	0.01
0.6240	50.11	49.12	0.99	1.98	2.91	2.89	0.01	0.42
0.7010	44.53	43.89	0.64	1.44	4.12	4.11	0.01	0.24
0.7700	38.85	38.73	0.12	0.31	5.99	5.94	0.05	0.88
0.8350	33.03	33.28	-0.25	-0.76	9.23	9.14	0.09	0.92
0.8960	26.70	27.06	-0.36	-1.35	16.58	16.44	0.14	0.83
0.9550	19.50	19.61	-0.11	-0.56	41.88	42.22	-0.34	-0.81

(continued)

L/D = 2

0.1120	0.71	0.68	0.02	3.02	0.71	84.48	0.41	0.48
0.2490	1.61	1.59	0.02	1.22	1.61	75.53	2.90	3.70
0.3470	2.34	2.33	0.00	0.11	2.34	70.98	2.29	3.13
0.4880	3.60	3.56	0.04	1.12	3.60	63.17	2.65	4.03
0.5900	4.86	4.76	0.10	2.14	4.86	58.65	0.77	1.30
0.6720	6.34	6.26	0.08	1.32	6.34	51.93	1.12	2.10
0.7410	8.23	8.15	0.07	0.90	8.23	45.31	2.26	4.75
0.8030	11.01	10.99	0.02	0.21	11.01	40.38	1.31	3.14
0.8580	15.45	15.34	0.11	0.70	15.45	35.13	0.17	0.48
0.9100	25.26	24.89	0.38	1.49	25.26	28.69	-0.23	-0.81
0.9610	55.84	56.46	-0.62	-1.10	55.84	19.95	0.57	2.78

Case 2: Herringbone Grooved Journal Bearing

Then, the results for herringbone grooved journal bearing obtained by our code are compared with the results of Zirkelback and Andres (1998) for the following parameters:

Diameter of the journal bearing D = 40 mm,

Length of the journal bearing L = 40 mm (that is, L/D = 1),

Radial clearance R_c = 33.0 μm,

Dynamic viscosity $\mu = 9.74\text{x}10^{-4}$ Pa.s

Herringbone groove pattern:

Groove number N_g = 20,

Groove angle α = 20.8°,

Groove depth G_d = 33.0 μm,

Groove width a_g = 0.5,

Groove region ratio γ_g = 1.0,

Rotational speed N_s = 80 rpm,

Eccentricity ratio ε = 0.0 to 0.8.

The present results as shown in Fig. 2.6 show a good agreement with those obtained by Zirkelback and Andres (1998). The maximum discrepancy of the load capacity between the two sets of results is less than 4.7%.

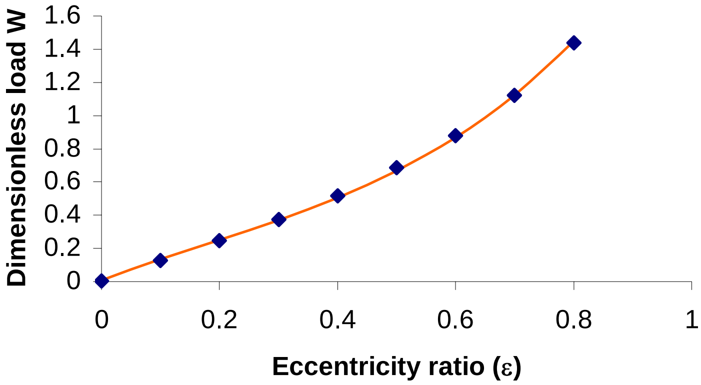

Fig. 2.6 Variation of load capacity versus eccentricity ratio for a herringbone grooved journal bearing, with L/D = 1.
Legend: ♦ Zirkelback and Andres(1998), — present result.

Case 3: Herringbone Grooved Thrust Bearing

The third case is for a herringbone thrust bearing with the geometric parameters as given in the following:

Inner radius of the thrust plate $r_i = 2.80$ mm,

Outer radius of the thrust plate $r_o = 4.205$ mm,

Dynamic viscosity $\mu = 8.33\text{x}10^{-3}$ Pa.s,

Herringbone groove pattern:

Groove number $N_g = 12$, Groove angle $\alpha = 19.7°$,

Groove depth $G_d = 2.33A_c$, Groove width $a_g = 0.60$,

Rotational speed $N_s = 10{,}000$ rpm,

Axial clearance $A_c = 9.0$ µm.

Using the above parameters, the load capacity, power consumption, stiffness and damping coefficients are obtained and listed in Table 2.2 together with the results of Zhu and Ono (1999). The power consumption is the same but the load capacity, stiffness and damping coefficient is about 5% lower than the Zhu and Ono's values. Therefore, the code used here is validated and reliable, and will be used in following chapters for bearing performance analysis.

Table 2.2 Comparison of thrust bearing results

	Zhu and Ono (1999)	Present result	Δ(%)
Load capacity W (N)	1.26	1.21	-4.1
Power consumption (W)	0.287	0.287	0
Stiffness K_{zz} (N/m)	$3.35\text{x}10^6$	$3.25\text{x}10^5$	-3.1
Damping coefficient D_{zz} (Ns/m)	$1.92\text{x}10^2$	$1.87\text{x}10^2$	-5.3

2.5 Robust Design of Fluid Bearings

The performance of fluid bearing is affected by many parameters. To determine what parameters have more influence on the performance of fluid bearings, Eq. (2.19) is re-written as given below:

$$\frac{\partial}{\partial X}(H^3\frac{\partial P}{\partial X})+c_z\frac{\partial}{\partial Z}(H^3\frac{\partial P}{\partial Z})=\Lambda\frac{\partial H}{\partial \theta} \tag{2.19}$$

where H is the lubricant film height which can be expressed as

$$H=h/C=(1+\varepsilon\cos\theta), \tag{2.24}$$

in which C is the radial clearance when the eccentricity of bearing is zero and ε is the ratio of eccentricity. From Eqs. (2.19) and (2.24), it can be seen that the pressure distribution in a journal bearing is affected by bearing radius *R*, bearing length *L*, radial clearance *C*, lubricant viscosity μ and bearing rotating speed ω. To increase the load capacity and motion stability of the bearing system, some grooves are engraved on the surface of the shaft or on the inner surface of the shaft sleeve of the journal bearing. For thrust bearing, the grooves are etched either on the thrust plate or its mating bearing surfaces. The numbers and patterns of these grooves also affect the performance of the fluid bearings. The groove pattern parameters of the journal/thrust bearing are N_g, the number of grooves; α, the groove angle; G_d, the groove depth; a_g, the groove width; and γ, the ratio of grooved area over the whole surface area of the bearing in axial direction of the journal bearing. These parameters are implicitly involved in the Reynolds equation (Eq. (2.19)) through the film height *H*. Therefore, the performance of such fluid bearing can be expressed in a general form as given by

$$\Phi = \Phi(R, L, C, \mu, \omega, N_g, \alpha, G_d, a_g, \gamma_g)\,. \tag{2.25}$$

where Φ can represent either the bearing load capacity *W*, power loss *P*, stiffness K_{ij} or damping coefficients D_{ij}. To investigate the effect of these parameters on the performance of bearing with traditional method, each parameter has to be changed one by one, which is a time consuming and arduous task even for numerical experiments. Hence, an efficient method to design the numerical experiments is needed. The method should be able to obtain an optimum result with a greatly reduced number of experiments, and at the same time, make the final products robust to the changes of working environment. It is found that the Taguchi method meets the above-mentioned requirement and is suitable for the purpose.

2.5.1 Concept of robust design

The concept of robust design will first be introduced briefly in this section since it is closely related to the Taguchi method.

The concept of robust design is stemmed from the recognition that quality cannot be achieved economically through inspection. Designing in quality is cheaper than trying to inspect and re-engineer it after a product hits the production floor or worse, after it reaches the customer. Thus, new philosophy, technology and advanced statistical tools must be employed to design high quality products at low cost (Gunter, 1987).

The robust design method provides a systematic and efficient approach to find the near optimum combination of design parameters, so that the product is functional, exhibits a high level of performance, and is robust to noise factors (Bendell *et al.*, 1989, Taguchi, 1993). Noise factors are those parameters that are uncontrollable or are too expensive to control. Robust design has been used very successfully in designing reliable, high quality products at low cost in areas such as automobiles and consumer electronics (Cullen and Hollingum, 1987).

The eight steps required to conduct a robust design cycle are (Phadke, 1989):

1. Identify the main function,
2. Identify the noise factors and testing conditions,
3. Identify the quality characteristics to be observed and the objective function to be optimized,
4. Identify the control factors and their alternative levels,
5. Design the matrix experiment and define the data analysis procedure,
6. Conduct the matrix experiment,

7. Analyze the data and determine near optimum levels for the control factors,
8. Predict the performance at these levels.

The first five steps are used to plan the experiment, and the sixth step is used to conduct the experiment. In the seventh and eighth steps, the experimental results are analyzed and verified.

2.5.2 Taguchi method

Significant cost savings and improvements in quality can be realized by optimizing product designs. The three major steps in designing a quality product are: system design, parameter design, and tolerance design (Bendell *et al*., 1989).

System design is the process of applying scientific and engineering knowledge to produce a basic functional prototype design. The prototype model defines the configuration and attributes of the product undergoing analysis or development. The initial design may be functional, but it may be far from optimum in terms of quality and cost.

Parameter design is conducted to identify the settings of design parameters that optimize the performance characteristic and reduce the sensitivity of engineering designs to the sources of variation (noise). Parameter design requires some form of experimentation to evaluate the effect of noise factors on the performance characteristic of the product defined by a given set of values for the design parameters. This experimentation aims to select the optimum levels for the controllable design parameters such that the system is functional, exhibits a high level of performance under a wide range of conditions, and is robust to noise factors.

Experimenting with the design variables one at a time or by trial and error until a first feasible design is found, is a common approach to design optimization (Bendell *et al*., 1989). However, this approach can lead to either a very long and expensive time span for completing the design or a premature termination of the design process due to budget and schedule pressures. The result in most cases is a product design which may be far from optimal. As an example, if the designer is studying 13 design parameters at 3 levels, varying one factor at a time would require studying 1,594,323 experimental configurations ($=3^{13}$). This is a "full factorial" approach where all possible combinations of parameter values are tried. Obviously, the time and cost involved in conducting such a detailed study during advanced design is prohibitive.

In contrast, Taguchi's robust design method provides the designer with a systematic and efficient approach for conducting experimentation to determine the near optimum settings of design parameters for performance and cost. The robust design method uses orthogonal arrays (OA) to study the parameter space, usually containing a large number of decision variables, with a small number of experiments. Based on design of experiments theory, Taguchi's orthogonal arrays provide a method for selecting an intelligent subset of the parameter space.

A typical tabulation is shown in Table 2.3 (Bagchi, 1993). In this array, the columns are mutually orthogonal. That is, for any pair of columns, all combinations of factor levels occur, and they occur an equal number of times. Here there are four factors A, B, C, and D, each at three levels. This is called an "L9" design, the 9 indicating the nine rows, configurations or prototypes to be tested, with test characteristics defined by the row of the table.

Table 2.3 L9 (3^4) Orthogonal Array

	A	B	C	D
1	1	1	1	1
2	1	2	2	2
3	1	3	3	3
4	2	1	2	3
5	2	2	3	1
6	2	3	1	2
7	3	1	3	2
8	3	2	1	3
9	3	3	2	1

Table 2.4 Common orthogonal arrays with number of equivalent full factorial experiments

Orthogonal Array	Factors and Levels	No. of Experiments
L4	3 Factors at 2 levels	8
L8	7 Factors at 2 levels	128
L9	4 Factors at 3 levels	81
L16	15 Factors at 2 levels	32,768
L27	13 Factors at 3 levels	1,594,323
L64	21 Factors at 4 levels	4.4×10^{12}

The number of columns of an OA represents the maximum number of factors that can be studied using that array. Note that this design reduces 81 ($=3^4$) configurations to 9. Some of the commonly used orthogonal arrays are shown in Table 2.4 (Bendell *et al.*, 1989). As Table 2.4 shows, there are greater savings in testing for the larger arrays.

Using an L_9 OA means that 9 experiments are carried out in search of the 81 control factor combinations which gives the near optimal mean, and also the near minimum variation away from this mean. To achieve this, robust design method uses a statistical measure of performance called signal-to-noise (*S/N*) ratio borrowed from electrical control theory. The *S/N* ratio developed by Taguchi is a performance measure to choose control levels that best cope with noise (Bendell *et al*., 1989). The *S/N* ratio takes both the mean and the variability into account. In its simplest form, the *S/N* ratio is the ratio of the mean (signal) to the standard deviation (noise). The *S/N* equation depends on the criterion for the quality characteristic to be optimized. While there are many different possible *S/N* ratios, three of them are considered standard and are generally applicable in the situations (Bagchi, 1993):

- Biggest-is-best quality characteristic (strength, yield),
- Smallest-is-best quality characteristic (contamination),
- Nominal-is-best quality characteristic (dimension).

Whatever the type of quality or cost characteristic, the transformations are such that the *S/N* ratio is always interpreted in the same way, the larger the *S/N* ratio the better. Using the orthogonal arrays, the robust design approach improves the efficiency of generating the information necessary to design systems which are robust to variations in manufacturing processes and operating conditions. As a result, development time can be shortened and research and development costs can be reduced considerably. Furthermore, a near optimum choice of parameters may result in wider tolerances so that low cost components and production processes can be used.

The third step, tolerance design, is a process of determining tolerances around the nominal settings identified in the parameter design process. Tolerance design is required if robust design cannot produce the required performance without costly special components or high process accuracy (Bendell *et al*., 1989). It involves tightening of tolerances on parameters where their variability could have a large negative effect on the final system. Typically tightening tolerances leads to higher cost.

Optimizing a product or process design means determining the best system architecture, optimum settings of control factors, and tolerances. Using Taguchi's robust design helps find a near optimum setting of the control factors to make the product insensitive to noise factors. It will be used to find the effect of individual parameter on performance of fluid bearings and the sensitivity of machine tolerance.

Chapter 3

HYDRODYNAMIC BEARINGS

Hydrodynamic bearings are most widely used fluid bearings. The advantages of hydrodynamic bearings are lower non-repeatable run out and lower acoustic noise compared with those of ball bearings, and higher load capacity, higher stiffness and higher damping coefficients compared with those of aerodynamic bearings. The components of hydrodynamic bearings are also relatively easier to be fabricated compared with those of air bearings. Therefore, the performance of the hydrodynamic bearings will be investigated first in this chapter.

3.1 Comparison of Different Journal Bearings

There are several types of journal bearing, such as plain journal bearing (PJB), stepped journal bearing (STJB), tapered journal bearing (TPJB), multi-lobe (three or four lobes) journal bearing (MLJB) and herringbone grooved journal bearing (HGJB), etc. To select a suitable journal bearing for data storage devices, the performance of the above-mentioned five types of journal bearing will be investigated and compared. Then, the journal bearing that is suitable for data storage devices will be identified.

Figure 3.1 shows the schematic of STJB, TPJB, MLJB and HGJB. The sleeves of STJB, TPJB and MLJB have three identical partial bearings, which are separated by deep axial grooves. The deep axial grooves separate the entire bearing into three independent partial bearings so that negative pressure will not be generated in the entire bearing. Parameters that determine the groove geometries are groove depth over nominal clearance, h_1/ h_0 and groove width over ridge width, b_1/ b_0 for STJB, TPJB and MLJB. For HGJB, the groove pattern parameters should also include the groove angle α and grove number N_g in addition to $h_1/\ h_0$ and $b_1/\ b_0$. The parameters used in the following investigations are given in Table 3.1.

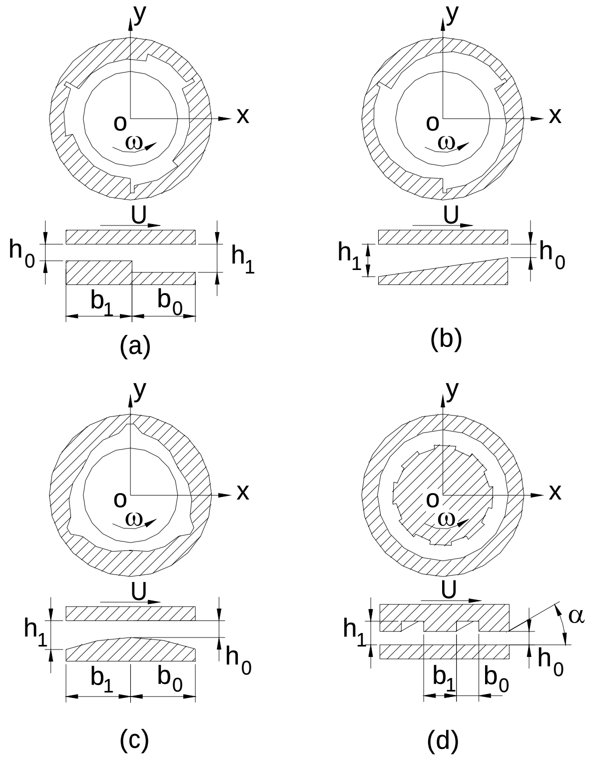

Fig. 3.1 Schematic of four journal bearings: (a) Step (STJB), (b) Tapered (TPJB), (c) Three lobe (MLJB), and (d) Herringbone grooved (HGJB).

Table 3.1 Geometrical parameters of journal bearings

Common conditions					
Diameter D = 4mm;	Length L = 4 mm				
Radial clearance R_c = 5 μm;	Dynamic viscosity μ = 20.0x10^{-3} Pa.s at 20 °C				
Rotational speed N_S = 7200 rpm;	Eccentricity ratio ε = 0.0 – 0.9				
Non-common conditions	PJB	STJB	TPJB	MLJB	HGJB
Groove depth G_d	–	3.0	3.0	3.0	3.0
Groove width a_g	–	0.5	–	–	0.5
Groove number N_g	–	3	3	3	10
Groove angle α	–	–	–	–	24.0°
Axial grooved region ratio γ_g	–	1.0	1.0	1.0	1.0

The system equation (2.17) is solved and the Reynolds boundary condition (2.7c) is used to obtain the pressure distribution as well as other characteristics of the journal bearings. The cavitation is not considered in the analysis because the investigation is focused on the performance of journal bearings at small eccentricity ratios. According to the recently published results, cavitation does not occur or its effect can be ignored when the eccentricity ratio ε is less than 0.4 (Jang and Chang, 2000; Lee *et al.* 2003; Wan *et al.*, 2002, Wu *et al.*, 2002).

Figures 3.2 to 3.7 show the non-dimensional dynamic characteristics of the five journal bearings, such as load capacity $\overline{W}$, power consumption $\overline{P}$, stiffness $\overline{K}$, damping coefficients $\overline{D}$ and the onset speed $\overline{S_{crit}}$ for motion stability of the journal bearings. The non-dimensional parameters are defined as:

$$\overline{W} = \frac{W}{W_0} = \frac{WR_c^2}{\mu\omega LR^3}, \quad \overline{M} = \frac{M}{M_0} = \frac{MR_c}{\pi\mu\omega LR^3}, \qquad \overline{P} = \frac{P}{P_0} = \frac{p}{M_0\omega},$$

$$\overline{K} = \frac{K}{K_0} = \frac{WR_c^3}{\mu\omega LR^3}, \quad \overline{D} = \frac{D}{D_0} = \frac{WR_c^3}{\mu LR^3}, \qquad \overline{S_{crit}} = \frac{R_c\omega^2 M_c}{W}. \tag{3.1}$$

where μ is dynamic viscosity of lubricant; ω, angular speed of spindle; L, bearing length; R, radius of shaft, R_c, radial clearance of journal bearing; M, frictional torque and M_c, critical mass of fluid journal bearings.

Figure 3.2(a) shows that, at eccentricity ratio $\varepsilon = 0$, TPJB has the highest load capacity among the five journal bearings, followed by HGJB, STJB MLJB, and the load capacity of PJB is zero. However, the load capacity of PJB increases rapidly with the increasing of ε, after $\varepsilon > 0.02$, the load capacity of PJB is higher than that of other journal bearings. For $0.05 < \varepsilon \le 0.3$, the load capacity of PJB is the highest among the five journal bearings, followed by HGJB, then MLJB (3 lobe journal bearing) and STJB, the TPJB has the lowest load capacity as shown in Fig. 3.2(a). For $0.6 < \varepsilon \le 0.9$, the sequence of load capacity changes as PJB, STJB, MLJB, HGJB and TPJB as shown in Fig. 3.2(b). Figure 3.3 shows the power consumption of five journal bearings, for all eccentricity ratios (0 < ε ≤ 0.3), PJB has the highest power consumption among five journal bearings, followed by HGJB, STJB, MLJB and TPJB. The stiffness of K_{xx} and K_{yy} of the journal bearings are shown in Fig. 3.4(a) and (b).

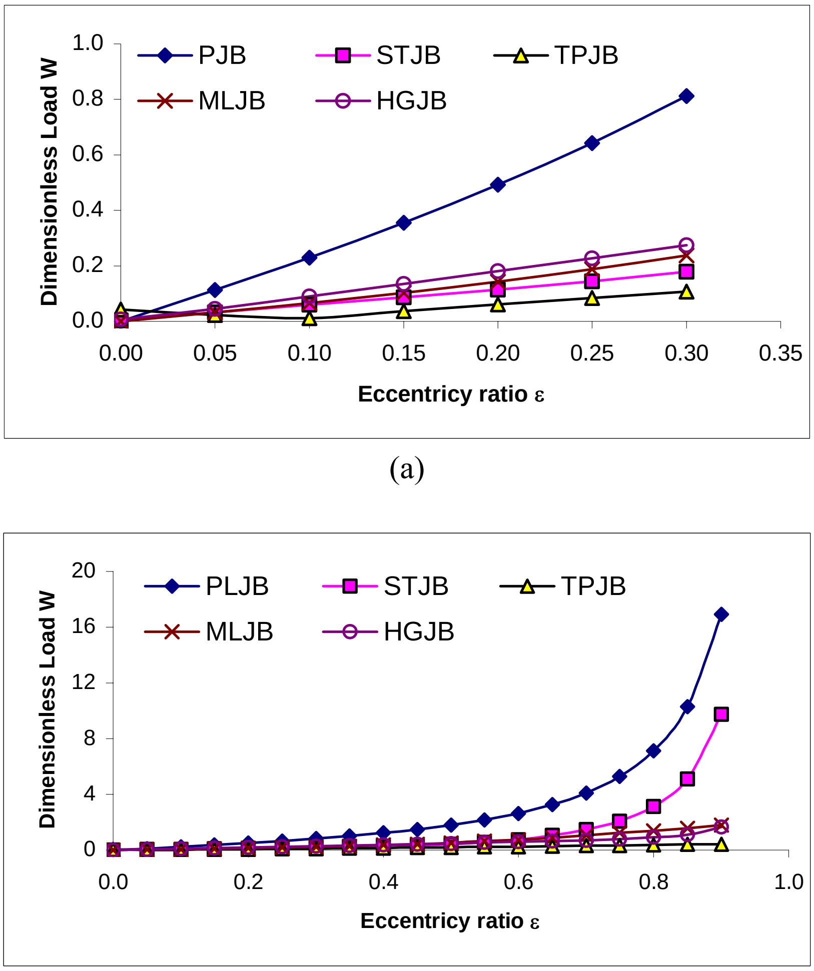

(a)

(b)

Fig. 3.2 Non-dimensional load capacity versus eccentricity ratio of five journal bearings.

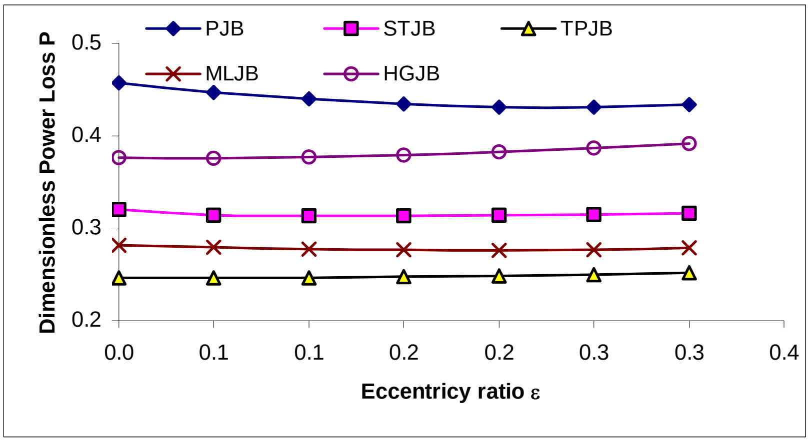

Fig. 3.3 Non-dimensional power consumption versus eccentricity ratio of five journal bearings.

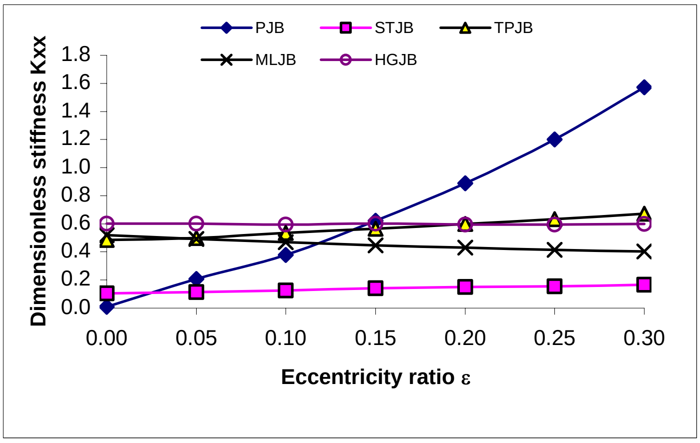

(a)

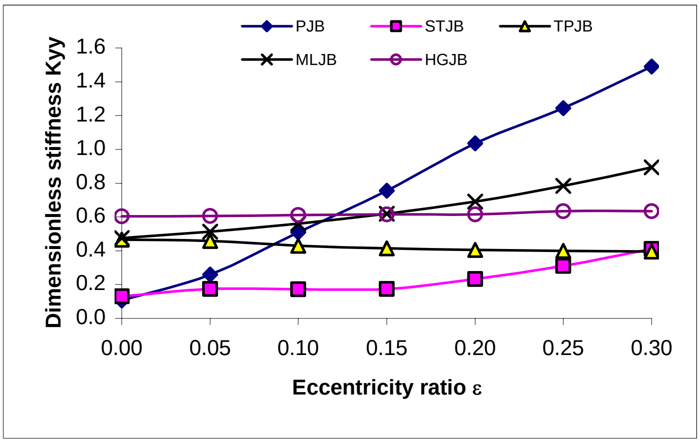

(b)

Fig. 3.4 Non-dimensional stiffness K_{xx} (a) and K_{yy} (b) versus eccentricity ratio of five journal bearings.

For $\varepsilon < 0.1$, HGJB has the highest K_{xx} and K_{yy} among the five journal bearings; then with the rapid increase, PJB has the highest stiffness for $\varepsilon > 0.15$; the stiffness of STJB, TPJB and MLJB are either in between the HGJB and PJB or lower than that of HGJB. It is also observed that the stiffness of HGJB keeps a almost constant value for $0 < \varepsilon \leq 0.3$ as shown in Fig. 3.4(a) and (b). Figure 3.5 (a) and (b) shows that PJB has the highest damping coefficients D_{xx} and D_{yy}, followed by HGJB, STJB and MLJB, and TPJB has the lowest D_{xx} and D_{yy}.

The motion stability of the journal bearings is compared in Fig. 3.6. The abscissa of Fig. 3.6 is eccentricity ratio and the vertical axis is the non-dimensional critical speed defined as $CM_c\omega^2/W$. For each journal bearing, the region below its own curve is the stable region and the region above the curve is the unstable region. It is observed that for $\varepsilon \leq 0.3$, TPJB has the highest onset speed, followed by MLJB, HGJB, STJB and PJB. At $\varepsilon = 0$, the PJB has zero load capacity and is unstable. It should be pointed out that MLJB has a very excellent performance for motion stability, after $\varepsilon > 0.3$, MLJB has the highest onset speed among the five journal bearings and it soon becomes unconditional stable for MLJB at $\varepsilon > 0.35$ (not shown). Figure 3.7 shows the ratio of radial stiffness K_{rr} over the power consumption P. For $\varepsilon < 0.1$, TPJB, MLJB and HGJB have a close ratio, PJB and STJB have an obviously lower ratio; then, for $0.1 < \varepsilon < 0.25$, MLJB has the highest ratio of K_{rr}/P, followed by TPJB, HGJB, PJB and STJB; for $\varepsilon > 0.25$, the PJB has the highest ratio of K_{rr}/P due to its rapid increase of stiffness.

Based on the above observations, following conclusions can be drawn: a) Among the five journal bearings, PJB has the highest load capacity and stiffness for most of eccentricity ratios (after $\varepsilon > 0.05$) but almost the lowest motion stability for

$0 < \varepsilon \leq 0.3$ and unstable at $\varepsilon = 0$. b) TPJB has the highest motion stability but the lowest load capacity and its damping coefficients are also obviously lower than those of the other journal bearings for $0 \leq \varepsilon \leq 0.3$. c) HGJB has the highest stiffness for $\varepsilon < 0.1$, the second high load capacity for $0 < \varepsilon \leq 0.3$, and the almost flat values of K_{xx}, K_{yy}, D_{xx} and D_{yy} for the whole range of $0 \leq \varepsilon \leq 0.3$. d) The load capacity of MLJB is very close to that of HGJB. The stiffness of MLJB is also close to HGJB for $0 \leq \varepsilon \leq 0.15$, then the K_{xx} of MLJB is lower but K_{yy} is higher than that of HGJB for $0.15 \leq \varepsilon \leq 0.3$. In view of load capacity and stiffness, the performance of MLJB is similar to those of HGJB. Due to its power consumption obviously lower than that of HGJB results in its K_{rr}/P ratio being higher than that of HGJB. However, the damping coefficients of MLJB are lower than those of HGJB for whole range of $0 \leq \varepsilon \leq 0.3$. e) The load capacity of STJB is a slightly lower than that of HGJB and MLJB and its power consumption is in between of them for $0 \leq \varepsilon \leq 0.3$. However, due to its relatively lower stiffness and damping coefficients, the motion stability of STJB is the lowest among five journal bearings for $0.05 < \varepsilon \leq 0.3$.

For spindle motors used in data storage devices, especially used in hard disk drives, they are required to operate in the conditions of high-speed, light-load and high precision. Because of the high-speed and light-load, the spindle motors in data storage devices usually operate in low eccentricity ratio range. Therefore, in evaluating the performance of the journal bearings, the performance in the lower eccentricity range ($\varepsilon \leq 0.3$) is more important. In view of the requirement of precision rotation, the motion stability of the spindle motors should be ensured. Therefore, based on the stability consideration at low eccentricities, plain journal bearings are not suitable for use in data storage devices. The stepped journal bearings can also be ruled out for the same reason plus other factors of lower load capacity and stiffness. Among TPJB, MLJB and HGJB, the herringbone grooved journal bearings are the most preferred journal bearing that is suitable for the spindle motors of data storage devices because its relative higher load capacity, stiffness and damping coefficients as well as the almost flat values of stiffness and damping coefficients for $0 \leq \varepsilon \leq 0.3$. In addition to the consideration of load capacity, stiffness and motion stability, HGJB also possesses an unique feature among the five journal bearings, that is, the lubricant sealing capacity to prevent the lubricant from leakage, which is not available for the other four journal bearings. Therefore, HGJB is the most suitable journal bearing to be used in the fluid bearing spindle motors for data storage devices.

The data of Figs. 3.2 to 3.7 are also given in Table 3.2 for quantitative comparison.

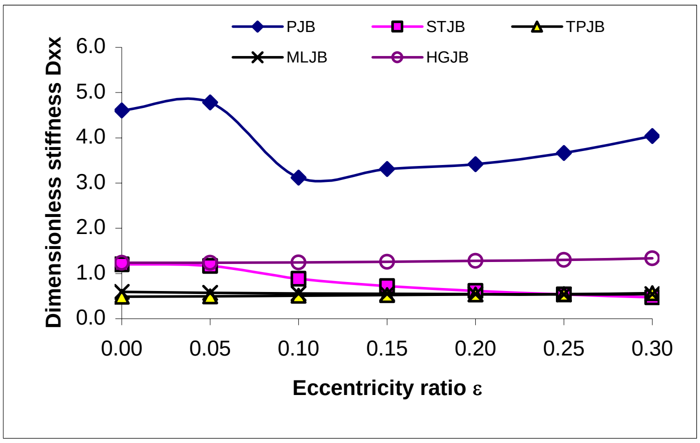

(a)

Fig. 3.5 (Continued)

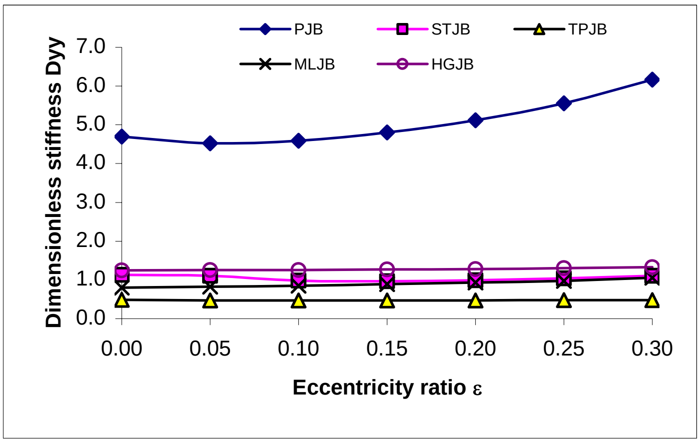

(b)

Fig. 3.5 Non-dimensional damping coefficients D_{xx} (a) and D_{yy} (b) versus eccentricity ratio of five journal bearings.

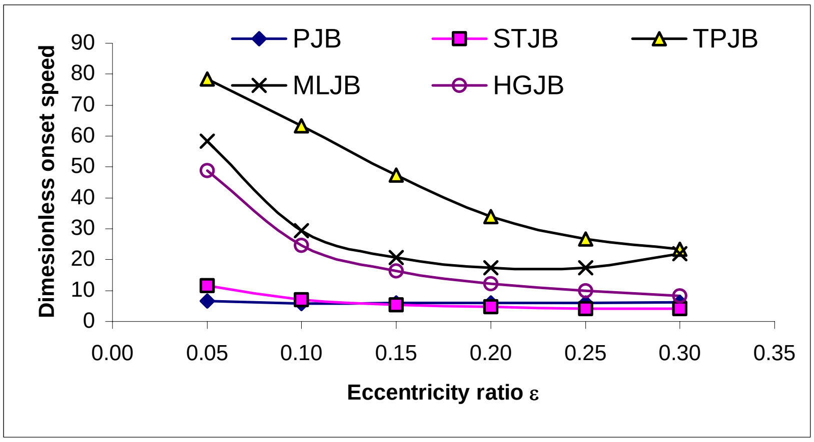

Fig. 3.6 Comparison of stability versus eccentricity ratio for five journal bearings.

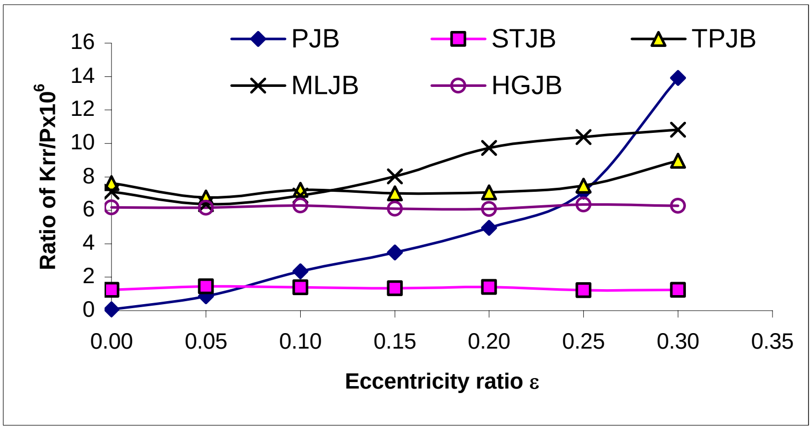

Fig. 3.7 Comparison of ratio of K_{rr}/P versus eccentricity ratio for five journal bearings.

Table 3.2 Performance comparison of five journal bearings

PJB

ε	φ°	W	P	K_{xx}	K_{xy}	K_{yx}	K_{yy}	D_{xx}	D_{xy}	D_{yx}	D_{yy}	Mc	K_{rr}/P
0.00	90.0	0.000	2.000	0.010	2.304	-2.246	0.207	4.609	-0.344	0.409	4.694	0.000	0.085
0.05	87.5	0.113	1.955	0.207	2.400	-2.265	0.109	4.785	-0.211	-0.318	4.525	6.600	0.870
0.10	84.0	0.230	1.923	0.379	1.560	-2.304	0.709	3.123	-0.335	0.378	4.589	5.857	8.347
0.15	80.3	0.356	1.901	0.622	1.641	-2.416	0.855	3.309	-0.568	0.090	4.801	5.947	7.475
0.20	76.5	0.492	1.886	0.888	1.658	-2.587	1.035	3.420	-0.819	-0.203	5.117	6.005	4.946
0.25	72.9	0.643	1.884	1.201	1.726	-2.830	1.245	3.668	-1.129	-0.562	5.558	6.079	7.109
0.30	69.3	0.812	1.896	1.573	1.813	-3.158	1.490	4.040	-1.528	-1.004	6.170	6.186	13.911

RSJB

ε	φ°	W	P	K_{xx}	K_{xy}	K_{yx}	K_{yy}	D_{xx}	D_{xy}	D_{yx}	D_{yy}	Mc	K_{rr}/P
0.00	90.0	0.004	1.401	0.104	0.611	-0.577	0.131	1.200	-0.020	0.070	1.129	100.502	1.250
0.05	87.3	0.032	1.375	0.063	0.589	-0.568	0.173	1.165	0.001	0.092	1.103	11.665	1.446
0.10	82.9	0.060	1.370	0.125	0.446	-0.504	0.143	0.884	-0.142	-0.058	0.980	6.973	1.391
0.15	79.0	0.086	1.371	0.142	0.363	-0.500	0.175	0.722	-0.183	-0.104	0.969	5.396	1.337
0.20	75.7	0.114	1.373	0.151	0.304	-0.514	0.233	0.613	-0.197	-0.120	0.993	4.665	1.513
0.25	72.8	0.144	1.377	0.156	0.260	-0.542	0.310	0.537	-0.201	-0.125	1.041	4.228	1.015
0.30	69.9	0.179	1.382	0.166	0.219	-0.582	0.411	0.472	-0.204	-0.131	1.109	4.093	0.951

TPJB

ε	φ°	W	P	K_{xx}	K_{xy}	K_{yx}	K_{yy}	D_{xx}	D_{xy}	D_{yx}	D_{yy}	Mc	K_{rr}/P
0.00	90.0	0.043	1.076	0.486	0.272	-0.229	0.467	0.485	-0.052	0.028	0.483	39.841	7.628
0.05	90.0	0.023	1.077	0.498	0.298	-0.206	0.458	0.498	-0.048	0.032	0.474	78.363	6.769
0.10	90.0	0.012	1.079	0.535	0.300	-0.212	0.430	0.512	-0.061	0.019	0.471	155.339	7.222
0.15	10.9	0.037	1.082	0.565	0.299	-0.218	0.415	0.521	-0.070	0.011	0.471	51.455	7.023
0.20	15.1	0.061	1.087	0.599	0.300	-0.223	0.404	0.535	-0.081	0.000	0.473	33.975	7.077
0.25	17.3	0.085	1.094	0.634	0.302	-0.230	0.399	0.548	-0.092	-0.009	0.476	26.753	6.467
0.30	18.5	0.108	1.101	0.672	0.303	-0.239	0.396	0.564	-0.101	-0.019	0.482	23.407	8.969

Table 3.2 Performance comparison of five journal bearings (continued)

MLJB

ε	ϕ°	W	P	K_{xx}	K_{xy}	K_{yx}	K_{yy}	D_{xx}	D_{xy}	D_{yx}	D_{yy}	Mc	K_{rr}/P
0.00	90.0	0.000	1.233	0.519	0.282	-0.411	0.475	0.592	-0.132	0.069	0.800		7.110
0.05	28.7	0.032	1.223	0.492	0.265	-0.431	0.513	0.576	-0.128	0.073	0.826	58.332	6.359
0.10	28.3	0.066	1.215	0.469	0.246	-0.454	0.561	0.558	-0.122	0.076	0.853	29.452	6.883
0.15	28.0	0.103	1.210	0.447	0.232	-0.482	0.619	0.555	-0.122	0.075	0.891	20.631	8.027
0.20	27.7	0.143	1.209	0.431	0.212	-0.514	0.692	0.547	-0.118	0.076	0.935	17.349	9.740
0.25	27.3	0.188	1.210	0.416	0.187	-0.553	0.783	0.537	-0.112	0.081	0.976	17.401	11.986
0.30	26.6	0.238	1.221	0.404	0.168	-0.607	0.894	0.548	-0.112	0.081	1.053	21.872	10.317

HGJB

ε	ϕ°	W	P	K_{xx}	K_{xy}	K_{yx}	K_{yy}	D_{xx}	D_{xy}	D_{yx}	D_{yy}	Mc	K_{rr}/P
0.00	90.0	0.007	1.645	0.602	0.650	-0.655	0.604	1.237	0.004	0.006	1.246	317.496	6.178
0.05	38.4	0.045	1.644	0.602	0.649	-0.656	0.606	1.237	0.003	0.007	1.254	48.846	6.159
0.10	42.9	0.090	1.649	0.596	0.648	-0.660	0.612	1.245	-0.002	0.000	1.257	24.518	6.288
0.15	44.4	0.135	1.658	0.601	0.654	-0.671	0.615	1.259	-0.007	-0.006	1.268	16.350	6.090
0.20	45.2	0.181	1.672	0.594	0.659	-0.680	0.615	1.278	-0.015	-0.013	1.282	12.211	6.072
0.25	45.8	0.227	1.690	0.594	0.663	-0.688	0.634	1.302	-0.031	-0.027	1.302	10.019	6.346
0.30	46.3	0.274	1.713	0.590	0.678	-0.709	0.634	1.336	-0.047	-0.040	1.329	8.209	6.267

3.2 Parametric Study of Herringbone Groove Journal Bearing

The characteristics of HGJB will be further investigated. Based on the parametric study, a set of optimal parameters that result in a better performance of HGJB will also be identified.

Figure 3.8 shows the schematic and the parameters of a HGJB. The performance of the HGJB is affected by the grooves engraved either on the shaft surface or on the inner surface of the sleeve. The groove parameters include the groove depth G_d, groove angle α, groove number N_g, groove width a_g, and the ratio of axial grooved length over the whole bearing length γ_g. Their effect on the performance of the HGJB will be investigated one by one in following.

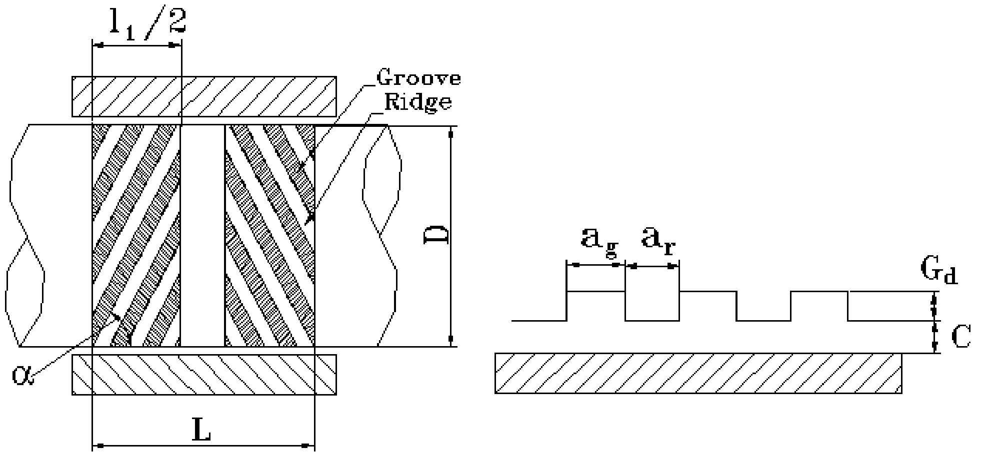

Fig. 3.8 Schematic of herringbone grooved journal bearing.

The basic dimensions of the groove parameters used in the parametric study are given as following:

$D = 4$mm, $L = 4$mm, $R_c = 5\mu$m $\mu = 20\text{x}10^{-3}$Pa.s, $N_s = 7{,}200$ rpm,

$N_g = 10$, $\alpha = 28^\circ$, $a_g = 0.5$, $G_d = 2.0$, $\gamma_g = 1.0$.

Groove depth (G_d)

Figure 3.9 shows the effect of groove depth on the performance of HGJB. When eccentricity $\varepsilon = 0.1$ and 0.2, Fig. 3.9(a) shows clearly that the load capacity decreases with the increase of groove depth; that is, the shallower groove depth, the higher load capacity. The same trend is also observed for other eccentricity ratios (not shown). For $\varepsilon = 0.1$, the load capacity when $G_d = 1.0$ is about 2 times of that when $G_d = 4.0$. This effect is more obvious when the eccentricity ratio is increased, for example, the differences are almost 3.5 times at $\varepsilon = 0.2$ and 4.6 times at $\varepsilon = 0.5$ (not shown) respectively. Therefore, in view of load capacity, to get higher load capacity, the groove depth should be reduced. However, on the other hand, checking the motion stability of the journal bearing at different groove depth, it is found that the deeper groove depth has better motion stability. This phenomenon is more obvious with decreasing eccentricity ratio, as shown in Fig. 3.9(b). With increasing groove depth, the increase of dimensionless critical speed at $\varepsilon = 0.1$ is faster than that at $\varepsilon = 0.2$ and 0.3. Obviously, the load capacity and the motion stability impose a contradicting demand on groove depth. To compromise the contradicting demands and make a reasonable choice for groove depth, another criteria, the ratio of radial stiffness K_{rr} over bearing power consumption P, is checked and compared because for most fluid bearings, an important requirement is to obtain as higher as possible stiffness with as lower as possible power consumption. It is found that for $\varepsilon \leq 0.2$, the peak value of K_{rr}/P is achieved at $G_d = 1.5$. However, for $\varepsilon = 0.3$ (and $\varepsilon > 0.3$, not shown), the highest value of K_{rr}/P is obtained at $G_d = 1.0$ as shown in Fig. 3.9(c). Since high-speed spindles usually work at low eccentricity range, therefore, the optimal condition of groove depth takes value of $G_d = 1.5$ after considering the factor of better ratio of K_{rr}/P.

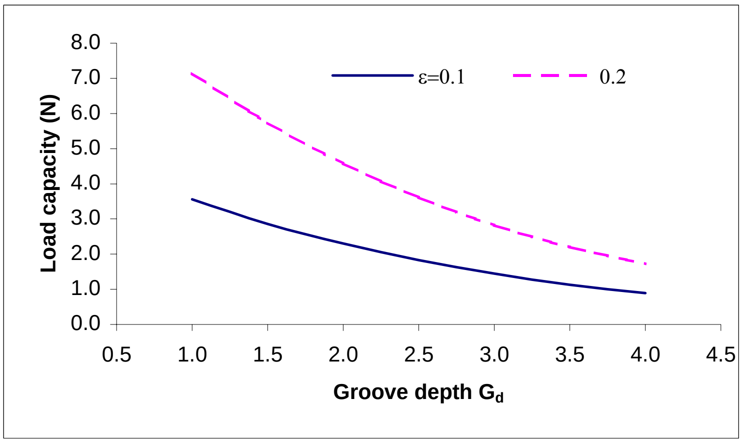

(a)

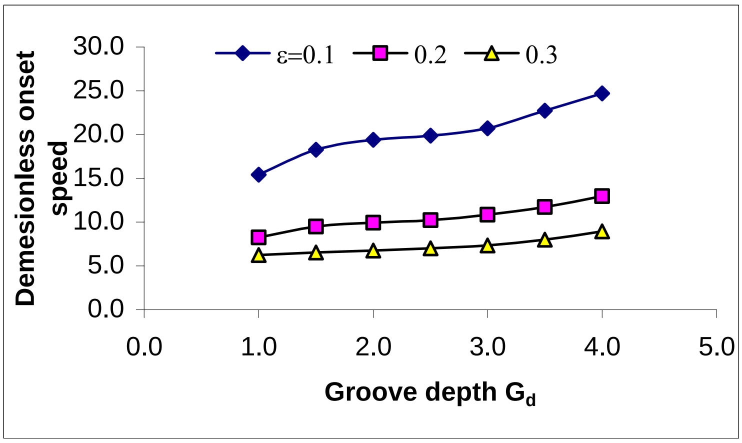

(b)

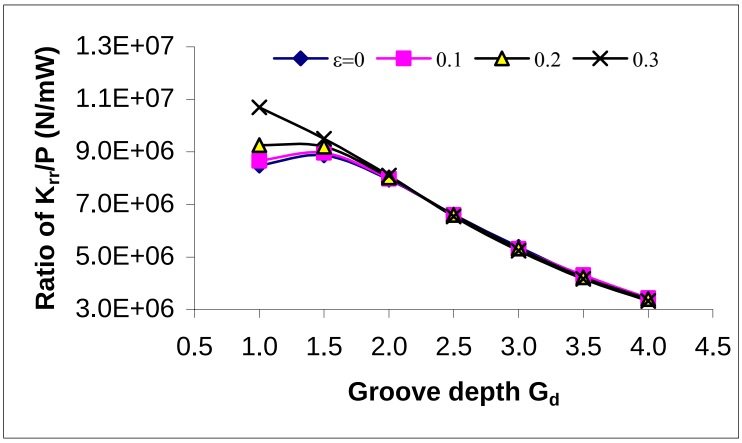

(c)

Fig. 3.9 Effect of groove depth on load capacity (a), dimensionless critical speed (b) and stiffness over power loss (c) of HGJB.

Groove number (N_g)

The effect of groove number N_g is shown in Fig. 3.10. The load capacity first increases with increasing groove number, the maximum load capacity is registered at $N_g = 10$, then, the load capacity decreases with further increase of the groove number. The load capacity for $N_g = 10$ is about 5% higher than that for $N_g = 4$ and 6% higher than that for $N_g = 16$.

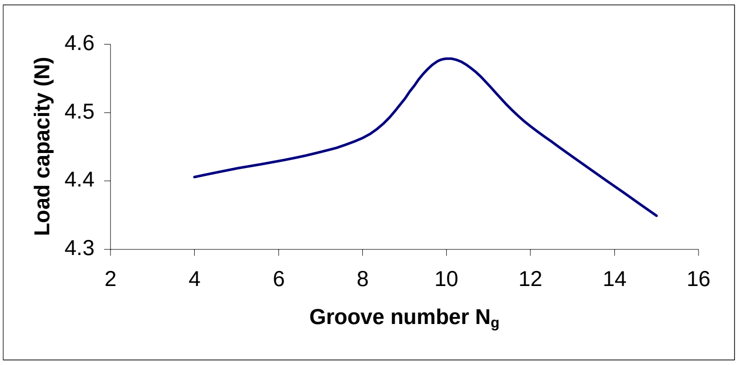

Fig. 3.10 Effect of groove number on load capacity of HGJB, $\varepsilon = 0.2$.

Groove angle (α)

Figure 3.11 shows that the load capacity increases with the increasing of groove angle α from 20° to 28°, then it decreases with the further increase of groove angle. Within the range of 25° to 36°, the change of the load capacity is relatively small, out of this range, the change is more obvious. The highest load capacity is

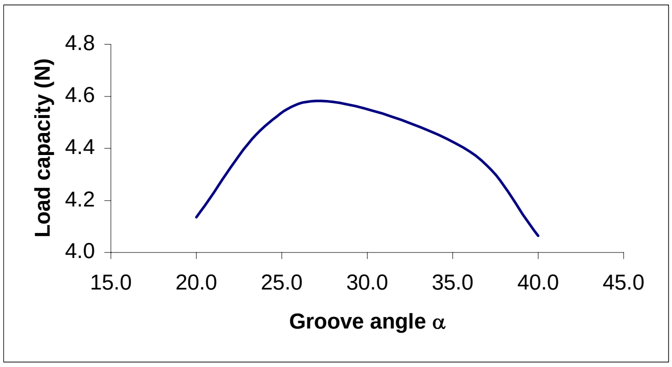

Fig. 3.11 Effect of groove angle on load capacity of HGJB, $\varepsilon = 0.2$.

obtained at α of around 28º, which is close to the conclusions of Hamrock and Fleming (1971) for which $\alpha = 28.6^\circ$, and Constantinescu *et al*. (1985) for which $\alpha = 28.5^\circ$.

Groove width (a_g)

The effect of groove width a_g is shown in Fig. 3.12, in which the load capacity almost linearly decreases with increasing groove width.

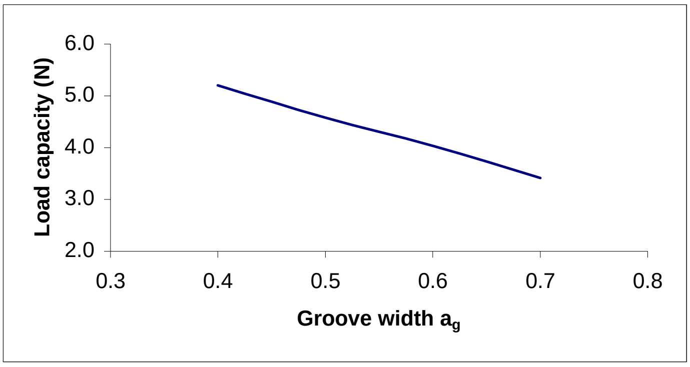

Fig. 3.12 Effect of groove width on load capacity of HGJB, $\varepsilon = 0.2$.

Axial groove ratio (γ)

Figure 3.13(a) shows the effect of axial groove ratio γ, the axial grooved length over the whole journal bearing length, similar to the effect of groove width a_g, the load capacity decreases with increasing γ. For $\gamma \leq 0.6$, the load capacity for groove angle $\alpha = 24°$ and 28° is almost the same, however, the discrepancy becomes larger with further increase of γ. The ratio of stiffness over power loss K_{rr}/P reaches a peak value at $\gamma = 0.8$ for $\alpha = 28°$ but it is $\gamma = 0.75$ for $\alpha = 24°$ as shown in Fig. 3.13(b). Figure 3.13(c) shows that the motion stability has peak value at $\gamma = 0.75$ for both $\alpha = 28°$ and $\alpha = 24°$. It is also noted that HGJB has a higher ratio of K_{rr}/P and better stability for $\alpha = 28°$ than that for $\alpha = 24°$. Hence, $\gamma = 0.75$ is taken as the optimal value. The same value was also used by Constantinescu *et al*. (1985).

Based on the above parametric studies and the criteria to obtain the highest ratio of K_{rr}/P, the optimum parameters of HGJB are determined as:

Table 3.3 Optimum parameters of herringbone grooved journal bearing

L/D	D (mm)	L (mm)	N_g	α	a_g	γ	G_d
½	4.0	2.0	10	14°	0.4	0.75	1.5
1	4.0	4.0	10	28°	0.4	0.75	1.5
2	4.0	8.0	10	32°	0.4	0.75	1.5

Using the optimal parameters given in Table 3.3, the non-dimensional dynamic characteristics of herringbone-grooved journal are obtained and tabulated in Table 3.4.

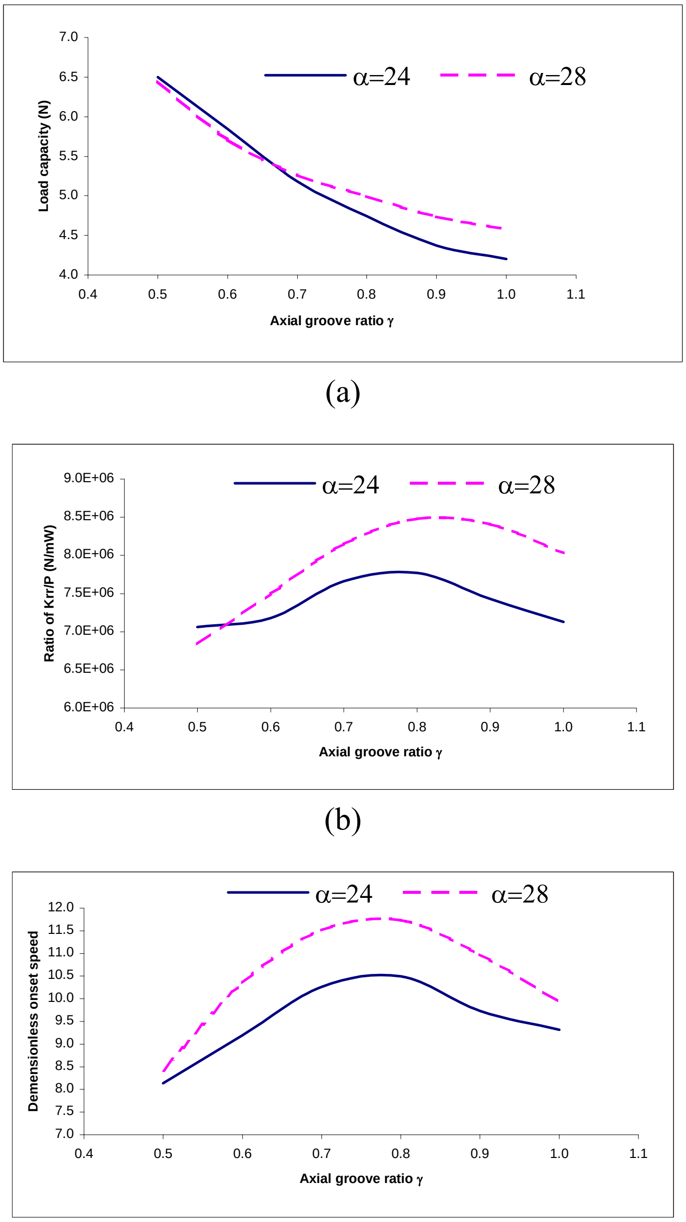

(a)

(b)

(c)

Fig. 3.13 Effect of axial groove ratio on load capacity (a), K_{rr}/P (b) and stability (c) of HGJB, $\varepsilon = 0.2$.

Table 3.4 Dynamic characteristics of herringbone grooved journal bearing (HGJB)

L/D=0.5												
	φ°	$\overline{W}$	$\overline{P}$	$\overline{K}_{xx}$	$\overline{K}_{xy}$	$\overline{K}_{yx}$	$\overline{K}_{yy}$	$\overline{D}_{xx}$	$\overline{D}_{xy}$	$\overline{D}_{yx}$	$\overline{D}_{yy}$	$\overline{M}$
0.0	90.00	0.0064	1.6903	0.5074	0.5846	-0.5801	0.5032	1.1325	0.0050	0.0084	1.1282	299.00
0.1	44.49	0.0798	1.6920	0.5168	0.5813	-0.5985	0.5222	1.1511	-0.0069	-0.0037	1.1450	24.60
0.2	46.03	0.1626	1.7148	0.5549	0.5841	-0.6507	0.5790	1.2114	-0.0439	-0.0399	1.1961	13.20
0.3	45.54	0.2553	1.7515	0.6367	0.5640	-0.7206	0.6755	1.2774	-0.1472	-0.1311	1.2518	9.81
0.4	43.24	0.3596	1.7717	0.7739	0.4664	-0.7876	0.8180	1.1941	-0.3323	-0.3325	1.2873	8.10
0.5	40.24	0.4884	1.8224	0.9182	0.4390	-0.9691	1.1232	1.2645	-0.4833	-0.5007	1.5615	7.71
0.6	37.32	0.6611	1.9204	1.0978	0.4074	-1.2460	1.5937	1.3076	-0.6631	-0.6864	2.0261	7.60
0.7	34.58	0.8987	2.0989	1.3283	0.4227	-1.6245	2.2660	1.3798	-0.9195	-0.9333	2.7705	7.04
0.8	32.40	1.2280	2.4383	1.6084	0.6610	-2.1306	3.1538	1.6775	-1.4515	-1.4309	4.1524	5.18
0.9	30.02	1.8093	3.2336	2.4826	-0.3056	-4.4833	8.7710	1.8803	-2.1238	-2.1737	7.3186	stable
L/D=1												
0.0	90.00	0.0093	1.7515	0.9251	1.5443	-1.5523	0.9222	2.9644	0.0022	0.0152	2.9844	366.97
0.1	56.58	0.1863	1.7546	0.9324	1.5431	-1.5766	0.9381	3.0041	-0.0187	-0.0003	3.0012	18.52
0.2	57.55	0.3732	1.7817	0.9713	1.5520	-1.6385	0.9858	3.1233	-0.0856	-0.0577	3.0506	9.75
0.3	57.26	0.5684	1.8206	1.0924	1.5222	-1.6730	1.0463	3.2309	-0.3113	-0.2193	3.0086	6.93
0.4	54.95	0.7554	1.8325	1.3810	1.2604	-1.5453	1.0722	2.8967	-0.7699	-0.7243	2.6996	5.85
0.5	51.65	0.9560	1.8788	1.5898	1.1694	-1.7182	1.3321	2.9017	-1.0497	-1.0457	3.0273	5.49
0.6	48.49	1.1959	1.9851	1.8230	1.0599	-2.0338	1.7619	2.9041	-1.3672	-1.3667	3.6193	5.24
0.7	45.29	1.5057	2.1754	2.1466	0.9028	-2.5781	2.5394	3.0484	-1.8039	-1.7927	4.6181	5.54
0.8	41.14	1.9632	2.4926	2.8549	0.2351	-4.0026	4.4101	3.0533	-2.7416	-2.6265	6.9920	7.81
0.9	34.46	2.9565	3.2603	6.6326	-2.8440	-12.3018	16.3927	4.9557	-6.5118	-6.4616	16.7027	stable
L/D=2												
0.0	90.00	0.0148	1.7692	0.7863	3.4285	-3.4429	0.8172	6.4832	0.0179	0.0196	6.5088	193.00
0.1	74.62	0.3503	1.7760	0.8093	3.4247	-3.4462	0.8295	6.5443	-0.0288	0.0154	6.4753	8.29
0.2	74.96	0.6977	1.7933	1.1777	3.2095	-3.0241	0.7573	6.2676	-0.6512	-0.3468	5.6668	4.63
0.3	71.76	0.9630	1.7811	1.5383	2.8703	-2.3185	0.7905	5.7822	-1.1715	-0.9713	4.3669	4.30
0.4	68.30	1.2137	1.8075	1.8207	2.6049	-2.3777	1.0001	5.5289	-1.4416	-1.3845	4.5064	4.35
0.5	64.61	1.4940	1.8841	2.2313	2.1017	-2.7009	1.4684	4.8336	-1.7468	-1.5185	4.9795	4.39
0.6	59.42	1.8549	2.0293	2.8216	1.7000	-3.2716	2.1547	4.6097	-2.3130	-1.8157	5.9620	4.73
0.7	54.44	2.3137	2.2616	3.6772	1.4540	-4.2969	3.1890	5.0891	-3.2296	-2.6251	7.5948	5.20
0.8	48.81	2.9974	2.6531	5.3262	0.4976	-6.7593	6.0298	5.9357	-4.7163	-4.1617	10.9250	8.52
0.9	38.79	4.7383	3.5236	12.2775	-6.9446	-21.279	27.0324	9.0234	-10.9610	-10.5400	26.5413	stable

3.3 Characteristics of Thrust Bearings

In this section, the performance of two types of thrust bearings, the herringbone grooved and the spiral grooved thrust bearings will be investigated and compared because these two types are most commonly used in fluid bearing systems. Figure 3.14 shows the schematic and the nomenclature used for herringbone and spiral grooved thrust bearings.

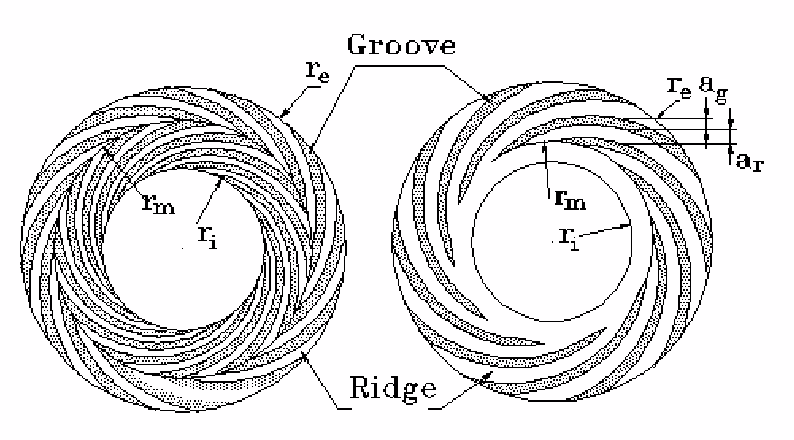

Fig. 3.14 Schematic of herringbone and spiral grooved thrust bearings.

3.3.1 Herringbone grooved thrust bearing

The performance of the herringbone grooved thrust bearing (HGTB) will be investigated first. The trial parameters of HGTB are given below:

Inner radius of the thrust plate r_i = 2.0 mm,

Outer radius of the thrust plate r_e = 4.0 mm,

Dynamic viscosity $\mu = 20.0\text{x}10^{-3}$ Pa.s at 20 °C.

Rotational speed N_S = 7,200 rpm;

Groove pattern: Herringbone groove;

Groove number N_g = 10;

Groove angle α = 10.9°;

Groove depth G_d = 1.0 -7.0;

Groove width a_g = 0.5;

Axial clearance A_c = 5.0 μm.

The effect of groove depth will be studied first. The variations of load capacity, stiffness and power consumption of the HGTB with groove depth are respectively shown in Fig. 3.15(a), (b) and (c). It is observed that the groove depth has great effect on the load capacity of HGTB and the highest load capacity is obtained at G_d = 4.0. At G_d = 4.0 (W = 17.6 N), the load capacity is almost 2.7 times of that when G_d = 1.0 (W = 6.47 N) as shown in Fig. 3.15(a). However, the highest stiffness is obtained at G_d = 3.0 as shown in Fig. 3.15(b). Figure 3.15(c) shows the power loss versus groove depth. At G_d = 1.0, the power loss of the HGTB is 0.648 W and is obviously higher than that at other groove depth ratios, then it is rapidly decreased to a saddle value of 0.604 W at G_d = 2.0. At G_d = 3.0, the power consumption is slightly higher than that at G_d = 2.0, then the power loss gradually increases with increasing groove depth and achieves the peak value of 0.618 W at G_d = 5.0. After G_d = 5.0, it decreases with the further increase of groove depth. The highest ratio of K_{zz}/P is obtained at G_d = 3.0 as shown in Fig. 15(d).

Figures 3.16(a) and (b) show the load capacity versus the ratio of r_i/r_e for fixed inner radius r_i or fixed outer radius r_e. In both cases, the load capacity and power loss decrease with the increasing ratio of r_i/r_e due to the reduction of the thrust bearing surface. For the fixed inner radius situation, if the inner radius is fixed to r_i = 2.0 mm, the outer radius of the thrust bearing takes value of r_e = 5.0 mm (r_i/r_e = 0.4), 4.0 mm (r_i/r_e = 0.5), 3.33 mm (r_i/r_e = 0.6) and 2.86 mm (r_i/r_e = 0.7), respectively. The load capacity decreases rapidly with the increase of the ratio r_i/r_e because the outer radius is

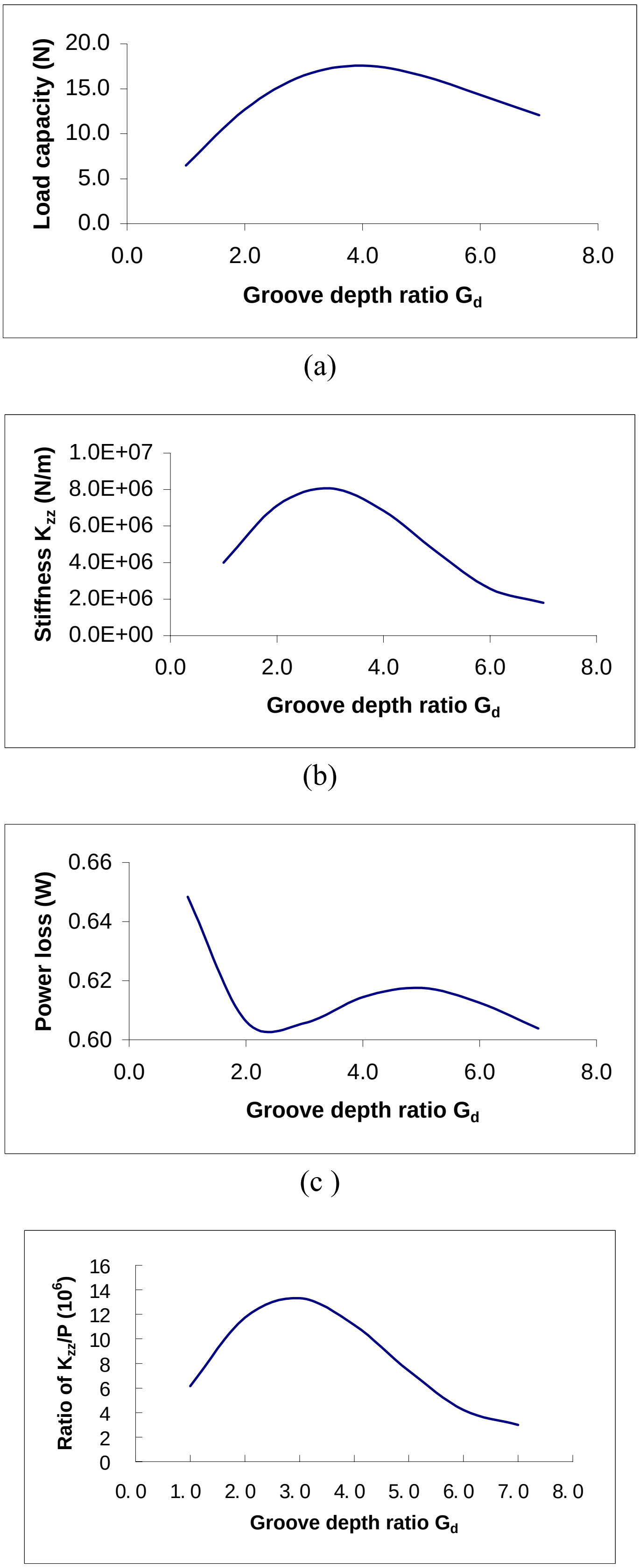

(a)

(b)

(c)

(d)

Fig. 3.15 Load capacity (a), stiffness (b), power loss (c) and K_{zz}/P (d) versus groove depth for herringbone grooved thrust bearing (HGJB).

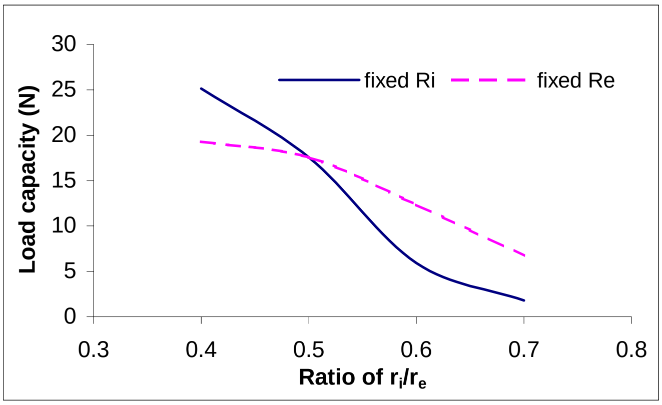

(a)

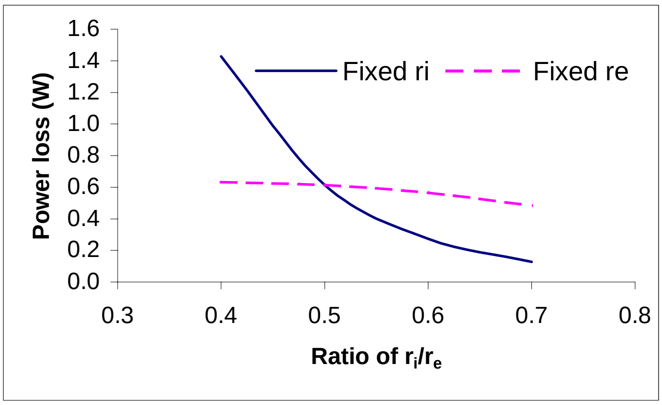

(b)

Fig. 3.16 Load capacity (a) and power loss (b) versus ratio of r_i/r_e for herringbone grooved thrust bearing.

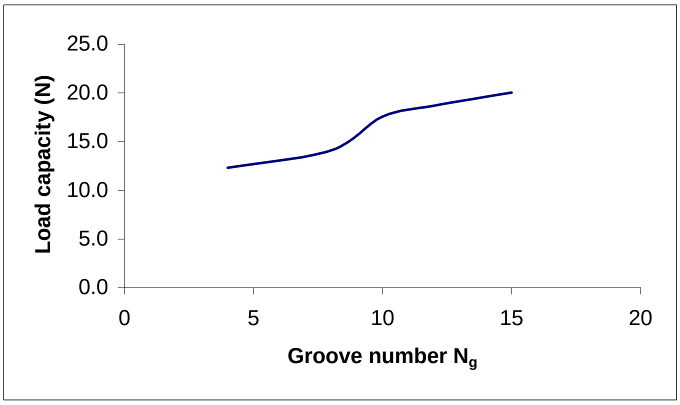

Fig. 3.17 Load capacity versus groove number for herringbone grooved thrust bearing.

reduced. The load capacity is 25.2 N at r_i/r_e = 0.4 and 1.8 N at r_i/r_e = 0.7, and the difference is almost 14 times between them as shown in Fig. 3.16(a). The power loss is also reduced rapidly with the increasing ratio r_i/r_e for the fixed inner radius case but not so obvious for the fixed outer radius case as shown in Fig. 3.16(b). The load capacity of the HGTB bearing increases with the increasing of groove number and has a higher value at $N_g = 15$ among the values of $N_g = 4$, 8, 10, 12 and 15 as shown in Fig. 3.17. The load capacity peaks at $a_g = 0.5$ and $\alpha = 11.5^{\circ}$ as shown in Figs. 3.18 and 3.19 respectively. The optimal parameters based on the highest ratio of K_{zz}/P are tabulated in Table 3.5.

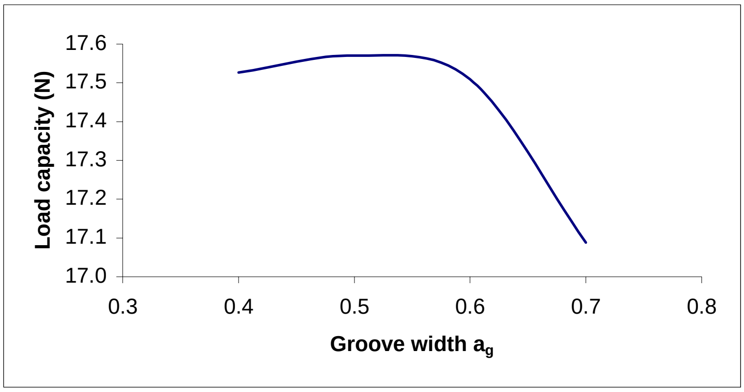

Fig. 3.18 Load capacity versus groove width for HGTB.

Fig. 3.19 Load capacity versus groove angle for HGTB.

Table 3.5 Optimal parameters of herringbone grooved thrust bearing

r_i/r_e	r_i(mm)	r_e(mm)	N_g	α	a_g	G_d
0.4	1.6	4	15	11.6°	0.5	3.0
0.5	2.0	4	15	11.5°	0.5	3.0
0.6	2.4	4	15	10.9°	0.5	3.0
0.7	2.8	4	15	8.5°	0.5	3.0

Based on the above optimal parameters, the non-dimensional load capacity, power consumption, stiffness and damping coefficients of herringbone grooved thrust bearing are obtained and tabulated in Table 3.6. The following definitions are used to obtain the non-dimensional values in Table 3.6:

$$\overline{W} = \frac{W}{W_0} = \frac{WA_c^2}{\mu\omega r_e^4}, \qquad \overline{M} = \frac{M}{M_0} = \frac{MA_c}{\pi\mu\omega r_e^4}, \qquad \overline{P} = \frac{p}{p_0} = \frac{p}{M_0\omega};$$

$$\overline{K} = \frac{K}{K_0} = \frac{WA_c^3}{\mu\omega r_e^4}, \qquad \overline{D} = \frac{D}{D_0} = \frac{WA_c^3}{\mu r_e^4}.$$

Table 3.6 Characteristics of herringbone grooved thrust bearing

$r_i/r_e = 0.5$	G_d	$\overline{W}_z$	$\overline{P}_z$	$\overline{K}_{zz}$	$\overline{D}_{zz}$
	1.0	0.0416	0.3518	0.1305	0.2563
	2.0	0.0874	0.3304	0.2568	0.2126
	3.0	0.1198	0.3337	0.3073	0.1770
	3.5	0.1276	0.3381	0.2876	0.1577
	4.0	0.1295	0.3414	0.2370	0.1353
	5.0	0.1185	0.3430	0.1448	0.0962
	6.0	0.0997	0.3386	0.0861	0.0659
	7.0	0.0823	0.3326	0.0534	0.0454
$r_i/r_e = 0.4$					
	1.0	0.0463	0.3704	0.1457	0.3784
	2.0	0.0725	0.3534	0.2176	0.3174
	3.0	0.0952	0.3468	0.2723	0.2734
	3.5	0.1263	0.3485	0.3018	0.2053
	4.0	0.1315	0.3518	0.2814	0.1760
	5.0	0.1308	0.3534	0.2429	0.1467
$r_i/r_e = 0.6$					
	1.0	0.0274	0.3277	0.0881	0.1462
	2.0	0.0596	0.3058	0.1801	0.1230
	3.0	0.0855	0.3074	0.2335	0.1052
	3.5	0.0926	0.3107	0.2260	0.0952
	4.0	0.0959	0.3146	0.1979	0.0837
	5.0	0.0907	0.3178	0.1244	0.0615
$r_i/r_e = 0.7$					
	1.0	0.0162	0.2834	0.0521	0.0698
	2.0	0.0356	0.2609	0.1075	0.0610
	3.0	0.0519	0.2588	0.1438	0.0537
	3.5	0.0576	0.2609	0.1431	0.0496
	4.0	0.0609	0.2642	0.1273	0.0449
	5.0	0.0608	0.2681	0.1033	0.0342

3.3.2 Spiral grooved thrust bearing

The spiral grooved thrust bearing investigated here is the pump-in configuration as shown in Fig. 3.14, that is, the lubricant is pumped from the outer edge to the inner edge of the thrust bearing by viscous pumping effect. The effect of changing geometrical parameters on the performance of the thrust bearing are shown in Figs. 3.20 – 3.25. The load capacity has the peak value at $G_d = 4.0$, but it is just a slightly higher than that of $G_d = 3.0$ as shown in Fig. 3.20(a). However, Figs. 3.20(b)

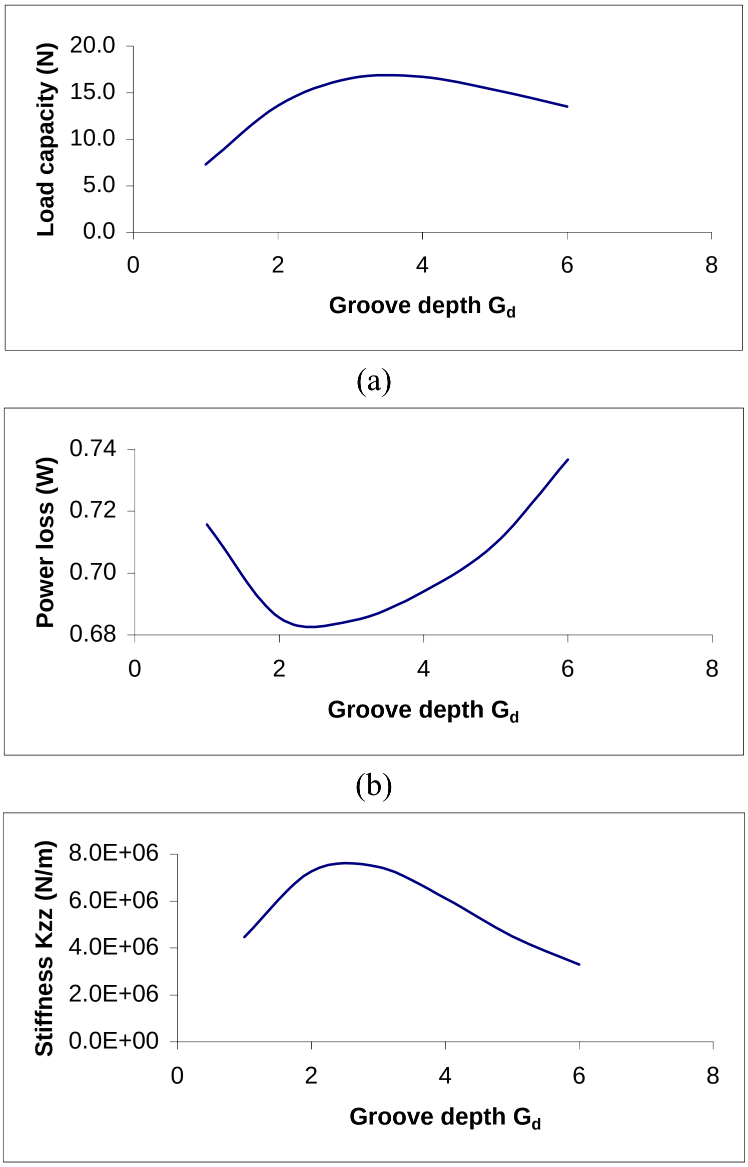

(a)

(b)

(c)

Fig. 3.20 (Continued)

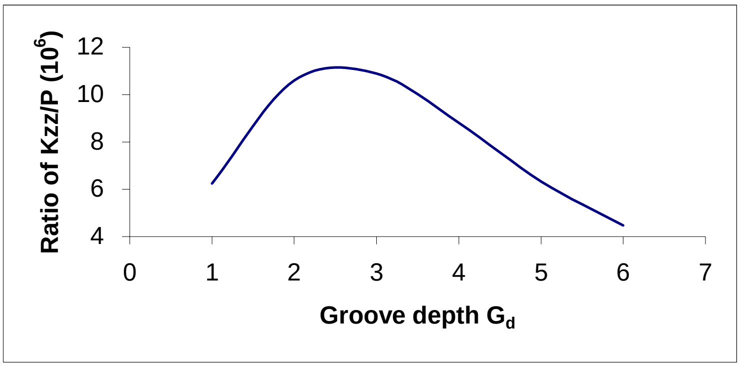

(d)

Fig. 3.20 Effect of groove depth on load capacity (a), power consumption (b), stiffness (c) and ratio of K_{zz}/P (d) for spiral grooved thrust bearing.

and (c) show that the lowest power consumption and the highest axial stiffness are obtained at $G_d = 3.0$. The ratio of W/P is 24.14 for $G_d = 3.0$ and 24.07 for $G_d = 4.0$, both values are close. But the ratio of K_{zz}/P is 1.09×10^7 for $G_d = 3.0$ and 0.88×10^7 for $G_d = 4.0$ respectively. Therefore, in terms of higher ratio of stiffness over power, $G_d = 3.0$ is an optimal value for groove depth.

Both the load capacity and the power consumption of the spiral grooved thrust bearing increase with increasing groove number as shown in Figs 3.21 (a) and (b). However, the increase of load capacity with the increase of groove number is more obvious than that of power consumption. Hence, the peak value of load capacity and the ratio of stiffness over power consumption are obtained at $N_g = 15$. The optimal values of groove width and groove angle are $a_g = 0.385$ and $\alpha = 12^\circ$ as shown in Figs. 3.22 and 3.23, respectively. With a fixed value of the outer radius of thrust bearing, Fig. 3.24(a) shows the effect of ratio of the inner radius over the outer radius of the thrust bearing. It appears an almost linear relationship between the load capacity and the ratio of r_i/r_e, and the load capacity decreases with the increasing value of r_i/r_e. Figure 3.24(b) shows the relationship between the load and the groove ratio R_m. Here, R_m is the radius of a middle circle between r_e and r_i that distinguishes the groove region from the ridge region and is defined as $R_m = (r_e - r_m)/(r_e - r_i)$. If $r_i/r_e = 0.5$, the load capacity reaches the peak value at $R_m = 0.75$.

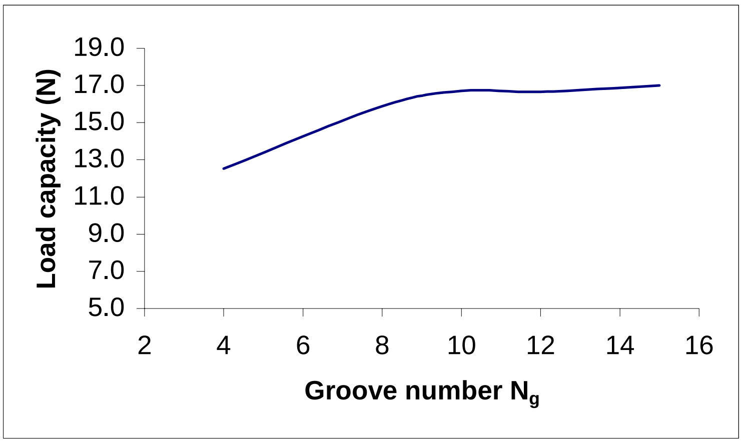

(a)

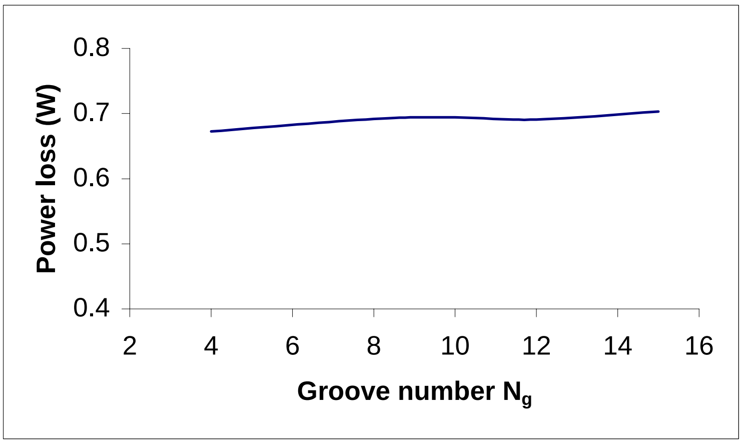

(b)

Fig. 3.21 Effect of groove number on load capacity (a) and power consumption (b) for spiral grooved thrust bearing.

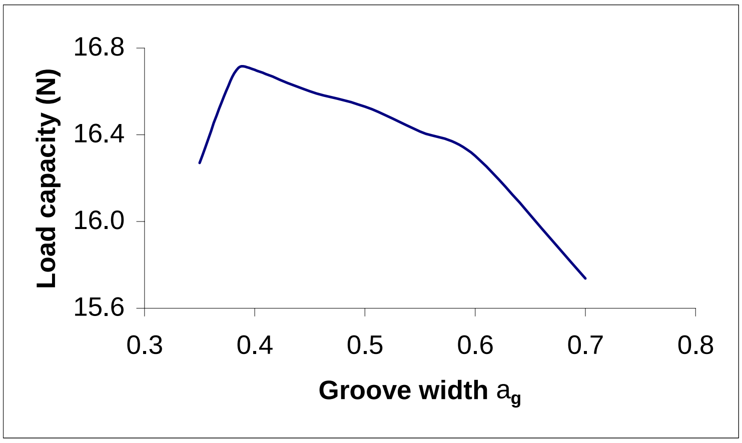

Fig. 3.22 Effect of groove width on load capacity for spiral grooved thrust bearing.

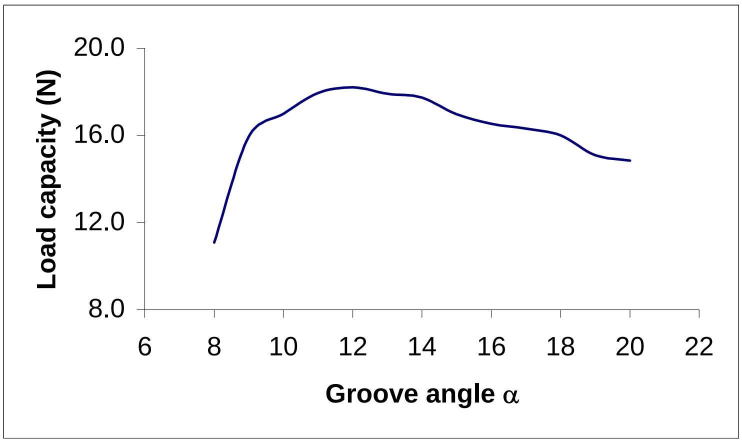

Fig. 3.23 Effect of groove angle on load capacity for spiral grooved thrust bearing.

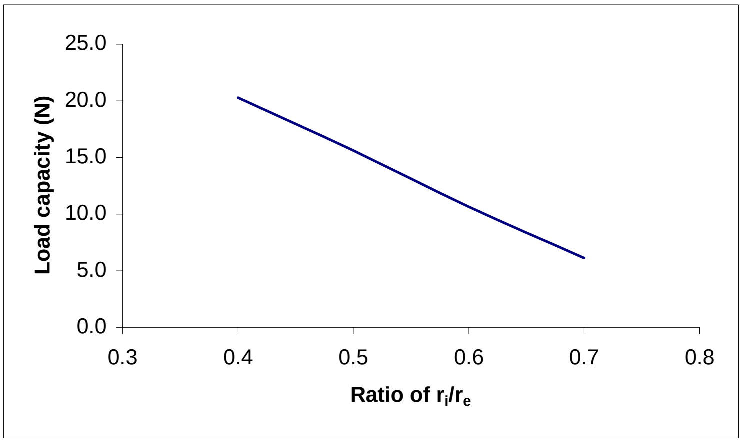

(a)

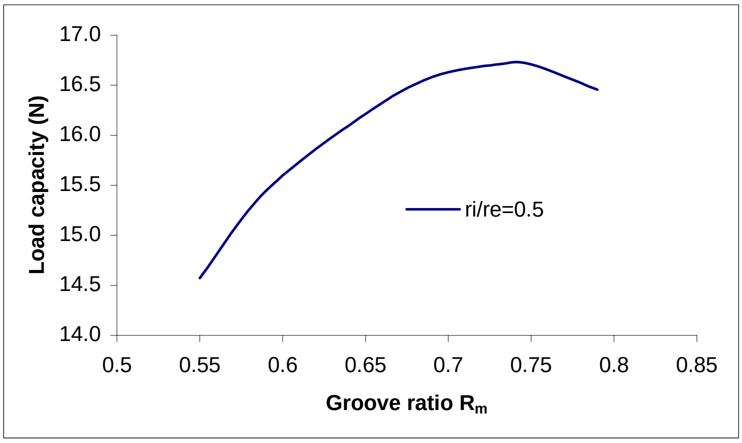

(b)

Fig. 3.24 Load capacity versus ratio of r_i/r_e (a) and ratio of R_m at $r_i/r_e = 0.5$ (b) for spiral grooved thrust bearing.

Summarizing the above results, the optimal parameters based on the highest ratio of K_{zz}/P are given in table 3.7. The non-dimensional load capacity, power consumption, stiffness and damping coefficients are tabulated in Table 3.8.

Table 3.7 Optimal geometrical parameters of spiral grooved thrust bearing

r_i/r_e	r_i(mm)	r_e(mm)	N_g	α	a_g	G_d	Y_m
0.4	1.6	4	15	12.2°	0.385	2.8	0.75
0.5	2.0	4	15	12.0°	0.385	2.8	0.75
0.6	2.4	4	15	11.0°	0.385	2.8	0.75
0.7	2.8	4	15	9.9°	0.385	2.8	0.75

Table 3.8 Characteristics of spiral grooved thrust bearing

	G_d	$\overline{W}_z$	$\overline{P}_z$	$\overline{K}_{zz}$	$\overline{D}_{zz}$
$r_i/r_e = 0.4$	1.0	0.0502	0.3902	0.1600	0.5646
	2.0	0.1044	0.3666	0.3011	0.4730
	3.0	0.1389	0.3640	0.3444	0.3905
	4.0	0.1478	0.3706	0.2854	0.3024
	5.0	0.1379	0.3834	0.2071	0.2236
$r_i/r_e = 0.5$	1.0	0.0352	0.3815	0.1133	0.3698
	2.0	0.0759	0.3597	0.2232	0.3203
	3.0	0.1068	0.3578	0.2813	0.2762
	4.0	0.1205	0.3658	0.2506	0.2230
	5.0	0.1165	0.3793	0.1724	0.1693
$r_i/r_e = 0.6$	1.0	0.0229	0.3503	0.0738	0.2041
	2.0	0.0502	0.3286	0.1513	0.1814
	3.0	0.0732	0.3264	0.2025	0.1624
	4.0	0.0864	0.3340	0.2032	0.1366
	5.0	0.0866	0.3473	0.1500	0.1053
$r_i/r_e = 0.7$	1.0	0.0124	0.3085	0.0401	0.0937
	2.0	0.0278	0.2899	0.0859	0.0871
	3.0	0.0421	0.2871	0.1227	0.0813
	4.0	0.0518	0.2933	0.1301	0.0708
	5.0	0.0541	0.3049	0.0925	0.0565

3.4 Effect of Machining Tolerance*

Equation (2.25) shows that there are more than 10 parameters that affect the performance of a fluid bearing. However, the effect of each parameter on the performance of fluid bearing is different and the sensitivity of each parameter to parts machining tolerance is also different. Here, the effect of parts machining tolerance to the performance of fluid bearings is investigated by Taguchi method.

To avoid too many runs of numerical simulations, four parameters, R, L, C and μ were first selected as the control parameters as they impose more influence on the performance of the fluid bearings than the other parameters based on the previous results. For the four selected parameters, if each variable is given three levels of settings, there will be altogether $3^4 = 81$ design variations. Using the traditional design optimization approach, a total of 81 calculations are required to determine a set of optimum design parameters. However, using Taguchi's robust design method, the number of experiments can be greatly reduced because the Taguchi's orthogonal arrays provide a method for selecting an intelligent subset of the parameter space, therefore, significantly reducing the number of experimental configurations. According to the number of selected parameters and their levels, different standard orthogonal arrays are designed. Here, there are four factors and each has three levels of setting. Therefore, a standard L_9 orthogonal array is used (refer to Table 2.3). According to the configuration and setting of Table 2.3, the actual values of four design parameters at each setting are given in Table 3.9.

To consider the effect of part machining tolerance or temperature changes on the lubricant viscosity (which can be considered as noise to the main control factor),

---

* Part of this Section has been published in the proceedings of ITC 2000, Nagasaki, Japan, pp. 1645-1650, 2000.

the noise orthogonal arrays are needed. Assuming each design parameter has three noise levels, then, for each row in Table 3.9, there exits a corresponding L_9 noise orthogonal array. Table 3.10 presents the deviation range of each design parameter. The deviation of diameter and length is 10% around their nominal value, the deviation of clearance is 10% of 5μm, that is, 10% of the second level value of the clearance and the deviation of lubricant viscosity is 10% of its third level value.

Table 3.11 shows schematically the final combination of the control factor orthogonal array with the noise orthogonal array. In Table 3.11, four design parameters first take the nominal values according to the rows in the lower left array, then according to the column settings in the upper right array to adjust the nominal value of

Table 3.9 Actual values of parameters *D*, *L*, *C* and μ at three level

Experiment	Diameter D (mm)	Length L (mm)	Clearance C (μm)	Viscosity μ (Pa.S)
1	3	3	3	10^{-2}
2	3	4	5	$2x10^{-2}$
3	3	5	7	$3x10^{-2}$
4	4	3	5	$3x10^{-2}$
5	4	4	7	10^{-2}
6	4	5	3	$2x10^{-2}$
7	5	3	7	$2x10^{-2}$
8	5	4	3	$3x10^{-2}$
9	5	5	5	10^{-2}

Table 3.10 Three levels of noise of parameters *D*, *L*, *C* and μ

Factor	Noise Level 1	Noise Level 2	Noise level 3
D	D – 10%	D	D + 10%
L	L – 10%	L	L + 10%
C	C - 0.5 μm	C	C + 0.5 μm
μ	$\mu - 3x10^{-3}$	μ	$\mu + 3x10^{-3}$

four design parameters to the corresponding noise level. For example, in the numerical experiment (1,1), the four design parameters take the following values:

$D = 2.7$ mm; $L = 2.7$ mm; $C = 2.7$ μm and $\mu = 7\text{x}10^{-3}$ Pa.s.

The actual values for the rest of experiments can be obtained with the same method.

Table 3.11 Combination of control factor orthogonal array with noise orthogonal array

						1	2	3	4	5	6	7	8	9
					μ	1	2	3	3	1	2	2	3	1
					C	1	2	3	2	3	1	3	1	2
					L	1	2	3	1	2	3	1	2	3
					D	1	1	1	2	2	2	3	3	3
	D	L	C	μ										
1	1	1	1	1		(1,1)	(1,2)	(1,3)	(1,4)	(1,5)	(1,6)	(1,7)	(1,7)	(1,9)
2	1	2	2	2		(2,1)	(2,2)							
3	1	3	3	3		(3,1)		(3,3)						
4	2	1	2	3		(4,1)			(4,4)					
5	2	2	3	1		(5,1)				(5,5)				
6	2	3	1	2		(6,1)					(6,6)			
7	3	1	3	2		(7,1)						(7,7)		
8	3	2	1	3		(8,1)							(8,8)	
9	3	3	2	1		(9,1)								(9,9)

Table 3.11 shows that there are a total of 81 numerical experiments to be carried out. In all experiments, except the above four design factors are varied, all other parameters are fixed to the following values:

Rotational speed $N_s = 7200$ rpm;

Groove pattern: herringbone groove;

Number of grooves $N_g = 10$;

Groove angle $\alpha = 28°$;

Groove depth $G_d = 1.5$;

Groove width $a_g = 0.5$;

Groove region ratio $\gamma_g = 0.75$.

Using a finite difference method scheme, Eq. (2.25) is solved with the following boundary conditions:

$p = p_a$ at $z = 0$ and $z = L$, (3.2)

and the Reynolds boundary condition at circumferential direction:

$p = \mathrm{d}p/\mathrm{d}\theta = 0$ at $\theta = \theta^*$, in circumferential direction. (3.3)

Once the pressure distribution of the bearing is obtained, the bearing load capacity, power consumption, stiffness and other dynamic characteristics can be determined. Then, the effect and relative importance of the selected design parameters can be calculated.

To investigate the effect of groove pattern on bearing performance, a second round of experiments are carried out in which, four design factors, clearance, lubricant viscosity, groove depth and groove angle, were chosen as the control parameters. The four control factors (parameters) were still set at three levels and each control factor was given a three-level noise. The values of control factors and noise level are listed in Table 3.12 and Table 3.13, respectively. The same combination of orthogonal arrays for control factor and noise as shown in Table 3.11 is used to determine the values of these parameters in every experiment.

The other fixed parameters in the numerical experiments are the same as used in the first round experiments except that now the bearing diameter and length are fixed to the value of $D = 4$ mm and $L = 4$ mm.

Table 3.12 Actual values of three settings of parameters C, G_d, μ and α

Experiment	Clearance C (μm)	Clearance G_d (μm)	Viscosity μ (Pa.S)	Angle α (°)
1	3	0.8C	10^{-2}	15
2	3	1.2C	$2x10^{-2}$	25
3	3	1.5C	$3x10^{-2}$	35
4	5	0.8C	$2x10^{-2}$	35
5	5	1.2C	$3x10^{-2}$	15
6	5	1.5C	10^{-2}	25
7	7	0.8C	$3x10^{-2}$	25
8	7	1.2C	10^{-2}	35
9	7	1.5C	$2x10^{-2}$	15

Table 3.13 Three noise-levels of parameters C, G_d, μ and α

Factor	Noise Level 1	Noise Level 2	Noise level 3
C	C - 0.5 μm	C	C + 0.5 μm
G_d	G_d - 3μm	G_d	G_d + 3μm
μ	μ - $3x10^{-3}$	μ	μ + $3x10^{-3}$
α	α - 1°	α	α + 1°

After the first round of 81 numerical experiments is conducted and all the experimental data are obtained, the data are analyzed by the statistical method of "Analysis of Means" and "Analysis of Variance". The average value and the standard deviation of load capacity, power consumption and stiffness for each row in Table 3.10 were first determined. The results are tabulated in Table 3.14. The ratio of the average value over the standard deviation for each row in Table 3.11 is also listed in Table 3.14 under the columns $SN1$. The value of $SN1$ is determined by the following equation:

$$SN1 = 10\log_{10}(\bar{y}^2 / \sigma^2), \tag{3.4}$$

Then, to estimate the effects of the four design parameters and to determine the relative importance of each design parameter, the values in Table 3.14 were further treated to find the average values of each design parameter at different setting levels. For example, the effect of bearing length *L* on the load capacity at level two is given by

$$m_L(W)_{level2} = \frac{1}{3}(W(2) + W(5) + W(8)), \tag{3.5}$$

where *L* (the bearing length) is set to level two only in the experiments (2, j), (5, j) and (8, j). Here *j* is from 1 to 9. The average load capacity, power consumption and stiffness for all levels of all factors can be determined in a similar way and the results are presented in Table 3.15.

Table 3.14 Average value, standard deviation and "signal-noise" ratio of load capacity, power consumption and stiffness for first round experiments

	Load capacity W (N)			Power Loss P (W)			Stiffness K (10^6N/m)		
No	Mean	stdev	SN1	Mean	stdev	SN1	mean	Stdev	SN1
1	1.4180	0.5716	7.8907	0.1081	0.0442	7.7591	2.8651	1.8278	3.9046
2	1.6690	0.5086	10.3240	0.2649	0.2790	0.4492	1.4853	0.6924	6.6299
3	1.8827	0.4914	11.6670	0.2246	0.0633	11.0020	0.8391	0.3657	7.2140
4	2.5162	0.7735	10.2550	0.4395	0.1354	10.2270	3.6311	0.4635	7.8932
5	0.7818	0.2754	9.0620	0.1395	0.5410	8.2273	0.6423	0.3002	6.6057
6	13.0930	4.7973	8.7209	0.8270	0.2991	8.8333	20.1850	14.7790	2.7075
7	1.2140	0.3300	11.3130	0.3668	0.0855	12.6520	1.3430	0.4116	10.2730
8	20.0480	7.1257	8.9848	1.9409	0.6607	9.3602	48.0140	25.8530	5.3771
9	3.7559	1.4119	8.4980	0.4788	0.1927	7.9046	4.3878	2.2959	5.6259

The average values in Table 3.15 are called the main factor effects. A plot of the main factor effects is shown in Figs. 3.25(a)-(c). It reveals that the factor-level combination (*D*3, *L*2, *C*1, μ3) gives the maximum load capacity and stiffness while the factor-level combination (*D*1, *L*1, *C*3, μ1) contributes to the minimum power consumption. Figs. 3.25(a) and 3.25(c) show that among these four design factors, the radial clearance has the maximum effect on the load capacity and stiffness.

Table 3.15 Average load capacity, power consumption and stiffness at three levels for first batch of four design factors

W	Mean	Diameter D	Length L	Clearance C	Viscosity μ
	Level 1	1.6566	1.7161	11.5197	1.9852
	Level 2	5.4637	7.4996	2.647	5.3253
	Level 3	8.3393	6.2349	1.2929	8.1490
P	Mean	D	L	C	μ
	Level 1	0.1992	0.3048	0.9587	0.2421
	Level 2	0.4687	0.7818	0.3944	0.4862
	Level 3	0.9288	0.5101	0.2436	0.8683
K	Mean	D	L	C	μ
	Level 1	1.7298	2.6131	23.688	2.6317
	Level 2	8.1528	16.714	3.1681	7.6711
	Level 3	17.915	8.4706	0.9415	17.495

To reveal the sensitivity of bearing performance to the noise of individual factor, the ratios of signal to noise (that is, the bearing performance corresponding to noise for all factors) can be calculated either using Eq. (3.4) or using the following formulae:

$$SN2 = -10\log_{10}[\sum_i y_i^2 / n], \tag{3.6}$$

and

$$SN3 = -10\log_{10}[\sum_i (1/y_i^2)/n]. \tag{3.7}$$

where y_i represents the values of *W*, (or *P*, or *K*) obtained in each numerical experiment, and $\bar{y}$ is the mean of y_i and σ is the standard deviation of y_i.

Equations (3.4), (3.6) and (3.7) are used for different goals. If the nominal value for a characteristic Y is the best, then Eq. (3.4) should be used and maximize the S/N ratio $SN1$. If the diminished characteristic of response Y results in improved product/process performance, Eq. (3.6) should be used. If the larger the characteristic Y, the better it is, then Eq. (3.7) should be used. The design requirements for load capacity and stiffness are: the higher, the better; while for power consumption: the lower, the better. Therefore, for load capacity and stiffness, Eq. (3.7) is used and for power consumption, Eq. (3.6) is used. To find out the individual design factor sensitivity at different levels, the calculated ratio of signal to noise are summed up and averaged corresponding to the three levels for all design factors. The method is similar to Eq. (3.5) and the results are plotted in Fig. 3.26. It is observed that the load capacity W and stiffness K are more sensitive to the noise of radial clearance while the power consumption P is more sensitive to the noises of lubricant viscosity and bearing diameter. They are less sensitive to the noise of bearing length.

Note that, in Figs. 3.25(a) to (c), the load capacity and stiffness at bearing length level 2 are higher than that of level 3. This phenomenon seems to contradict the common sense at a first look. However, after checking all the settings in Table 3.11, it is found that in the 8th row of Table 3.11, where all parameters are set for maximum load capacity and stiffness except the bearing length L is set to level 2. The combined effect of these three parameters is much higher than that of the bearing length alone, which causes the results of load capacity and stiffness in the 8th row to be much higher than that of the other rows. Therefore, the phenomenon appears that the effect of bearing length on load capacity and stiffness in level 2 is higher than that of level 3. This result reveals that the radial clearance has the most important effect on load capacity and stiffness. From Figs. 3.26(a) and 3.26(b), it is observed that the

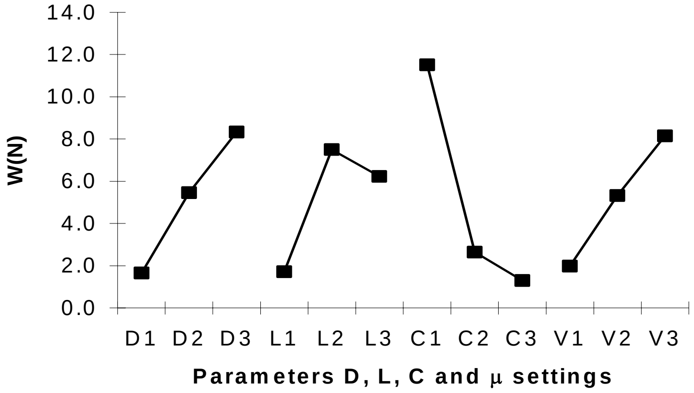

(a)

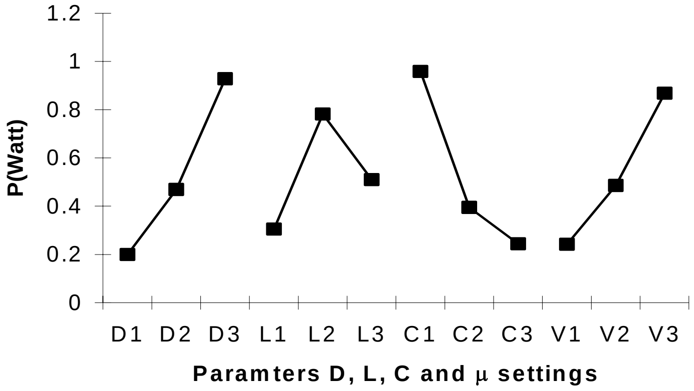

(b)

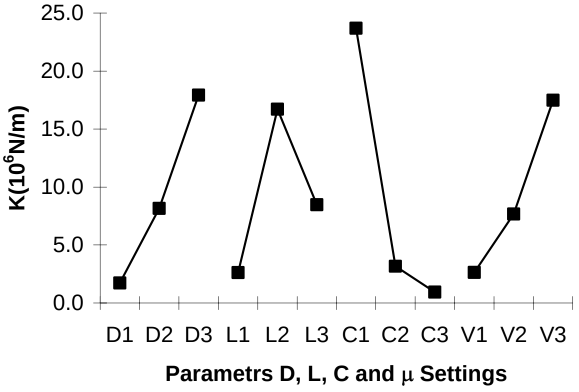

(c)

Fig. 3.25 Load capacity (a), power consumption (b) and radial stiffness (c) versus design factors of diameter (*D*), length (*L*), radial clearance (*C*) and viscosity of lubricant (μ) for fluid journal bearing.

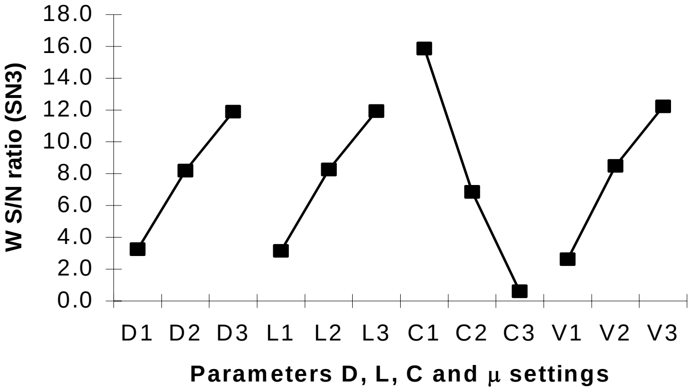

(a)

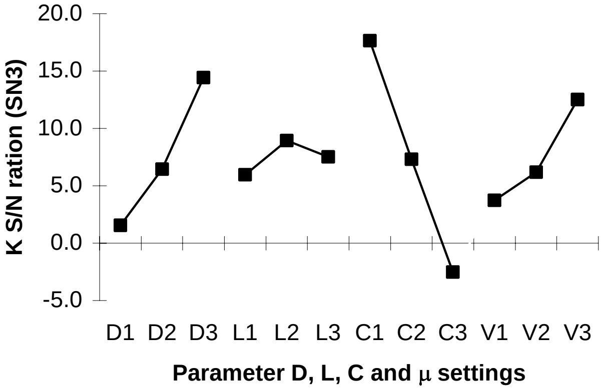

(b)

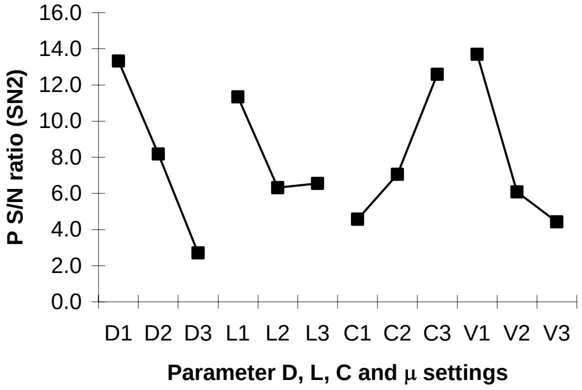

(c)

Fig. 3.26 SN3 ratio of load capacity (a), stiffness (b), and SN2 ratio of power consumption (c) at different levels of factors of *D*, *L*, *C* and μ.

bearing performance *W* and *K* are more affected by the noise of radial clearance. For power consumption, the noise of bearing diameter has more effect on it (see Fig. 3.26(c)). The noise of bearing length has the least influence on bearing dynamic characteristics among these four design parameters.

Using the same procedure and formulae, the effect of another four parameters (C, μ, G_d and α) are analyzed in second round numerical experiment. Tables 3.12 to 3.14 present the numerical data while Figs. 3.27 and 3.28 show the results graphically. The results indicate that the bearing performance is relatively less sensitive to the deviation of groove depth and groove angle. It can be observed from Figs. 3.27 and 3.28 that the radial clearance is the most importance factor on bearing performance and its noise is more critical than other factors. The bearing performance has less sensitivity to the deviation of groove depth. These results indicate that we should give a tight tolerance for radial clearance and a relatively loose tolerance for groove depth, groove angle and bearing length.

Table 3.16 Average value, standard deviation and ratio of load capacity, power consumption and stiffness for second batch of four design parameters

	Load capacity W (N)			Power Loss P (W)			Stiffness K (10^6N/m)		
No	Mean	Stdev	SN1	Mean	stdev	SN1	Mean	stdev	SN1
1	4.3018	1.4582	9.3967	0.3215	0.0944	10.644	4.0799	2.1483	5.5711
2	9.6679	2.4679	11.860	0.6460	0.1248	14.280	16.080	7.6526	6.4493
3	12.073	2.778	12.761	0.9897	0.1679	15.409	25.137	9.5494	8.4066
4	4.0564	0.777	14.354	0.3958	0.0615	16.172	3.5198	1.1196	9.9491
5	3.8667	0.6544	15.429	0.5592	0.0666	18.482	2.3764	0.6063	11.865
6	1.4908	0.4165	11.076	0.1899	0.0522	11.217	1.6693	0.6075	8.7798
7	3.0962	0.4256	17.237	0.4159	0.0436	19.590	1.6244	0.3745	12.745
8	0.8456	0.2280	11.385	0.1395	0.0374	11.434	0.6616	0.2070	10.093
9	1.0940	0.1849	15.442	0.2615	0.0374	16.892	0.4943	0.1196	12.325

Table 3.17 Average load capacity, power consumption and stiffness at three levels for second batch of four design factors

		Diameter	Length	Clearance	Viscosity
W	Mean	D	L	C	μ
	Level 1	8.681	3.818	2.213	3.088
	Level 2	3.138	4.793	4.939	4.752
	Level 3	1.679	4.886	6.345	5.658
P	Mean y	D	L	C	μ
	Level 1	0.6524	0.3777	0.2169	0.3807
	Level 2	0.3816	0.4482	0.4345	0.4173
	Level 3	0.2723	0.4804	0.6549	0.5084
K	Mean y	D	L	C	μ
	Level 1	15.10	3.075	2.137	2.317
	Level 2	2.523	6.373	6.698	6.458
	Level 3	0.9268	9.100	9.713	9.773

Both Tables 3.14 and 3.16 show that the setting in the 7th row gives out the maximum $SN1$ value if all the three dynamic characteristics W, P and K are considered together. This means that the setting ($D3$, $L1$, $C3$, $\mu 2$, $G_d 1$, $\alpha 3$) is the best setting for the purpose of on-target design, that is, the setting results in the least sensitivity of bearing performance to the variance of design parameters caused either by parts machining tolerance or by changes of environmental condition. Considering the practical requirement on load capacity and stiffness, a new setting of ($D3$, $L3$, $C3$, $\mu 2$, $G_d 1$, $\alpha 2$), that is, $D = 5$mm, $L = 5$mm, $C = 7\mu$m, $\mu = 3\text{x}10^{-2}$Pa.S, $G_d = 0.8C = 5.6\mu$m, $\alpha = 25°$ is selected as our design parameters. The noise level settings are the same as the settings in previous experiments. The confirmation experiments were carried out and the average values of W, P and K are as follow:

$W = 5.797$ N, $P = 1.008$ W, $K = 2.396 \text{ x } 10^6$ N/m.

The *S/N* ratios (*SN*1) are 10.778, 10.544 and 8.945 for *W*, *P* and *K*, respectively. Comparing these results with those in Table 3.14 and 3.15, the new setting gives us a set of reasonable load capacity, power consumption and stiffness with an almost best result for *SN*1 ratio. The higher *SN*1 ratio ensures that the bearing performance is more robust to resist external disturbances.

One of the goals in fluid bearing system design is to obtain as higher as possible load capacity and stiffness with as lower as possible power consumption. The graphical results of Figs. 3.25(a) and (c) indicate that the parameter setting (*D*3, *L*2, *C*1, μ3) gives the maximum load capacity and stiffness and those in Figs. 3.27(a) and (c) show that the setting (*C*1, G_d3, μ3, α3) gives the maximum load capacity and stiffness. For minimum power consumption, Figs. 3.25(b) and 3.27(b) show the best settings (*D*3, *L*2, *C*1, μ3) and (*C*1, G_d3, μ3, α3), respectively.

Then, we further look at the results for the maximum ratio of signal to noise. Fig. 3.26(a) and (b) show that the maximum ratio of signal to noise for load capacity and stiffness is obtained at the setting (*D*3, *L*3, *C*1, μ3). The maximum ratio of signal to noise for power consumption is the setting (*D*3, *L*2, *C*1, μ3) as shown in Fig. 3.26(c). For second batch parameters, the setting (*C*1, G_d1, μ3, α3) gives maximum *S/N* ratio for load capacity and stiffness while the (*C*1, G_d2, μ3, α3) gives maximum *S/N* ratio for power consumption.

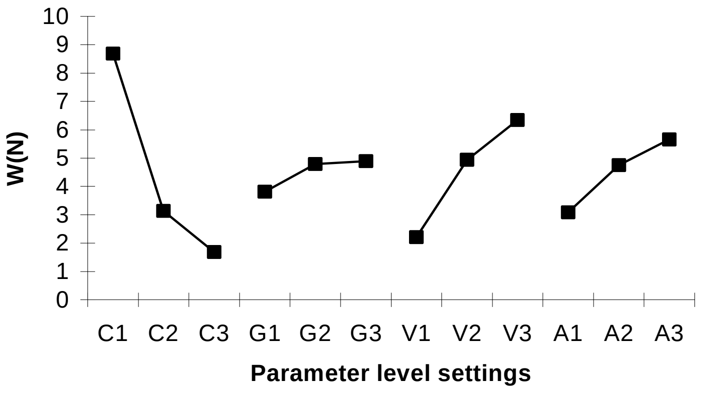

(a)

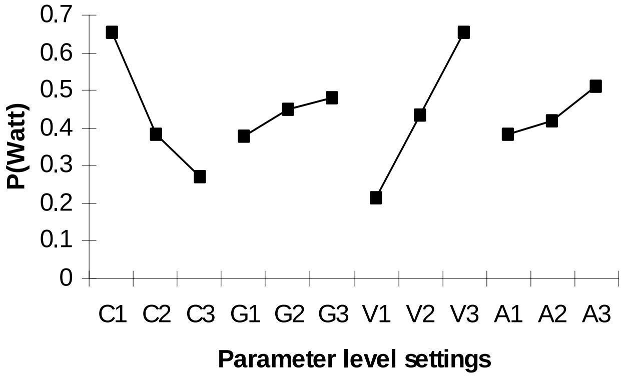

(b)

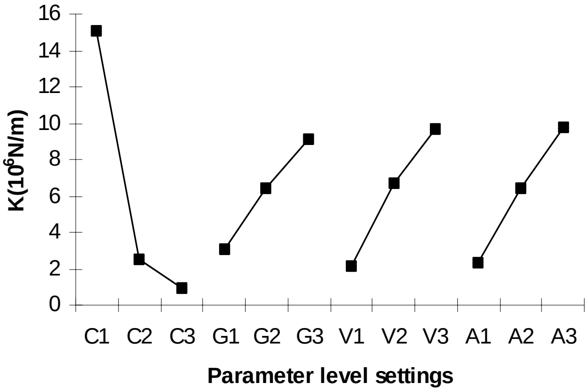

(c)

Fig. 3.27 Load capacity (a), power consumption (b) and radial stiffness (c) versus factors of radial clearance *C*, groove depth G_d, viscosity μ and groove angle (α) for fluid journal bearing.

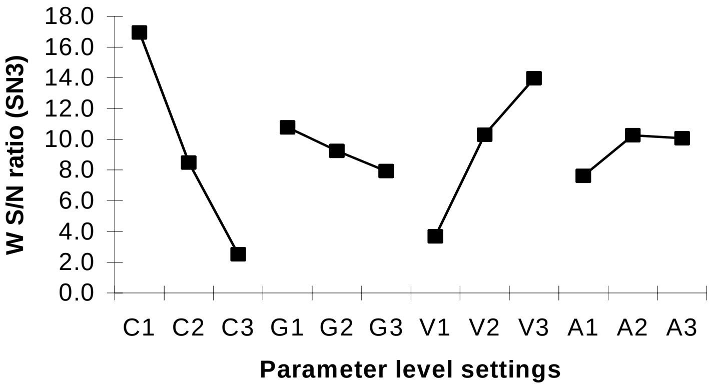

(a)

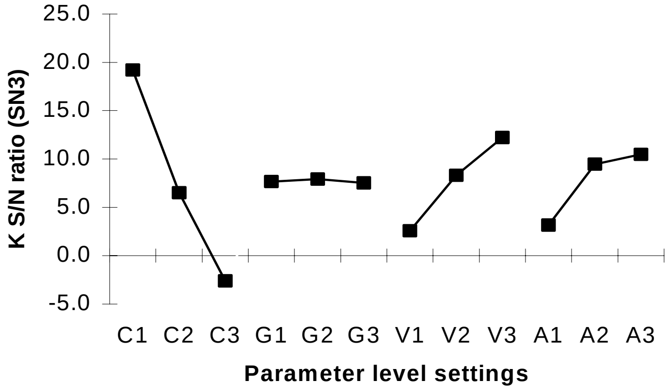

(b)

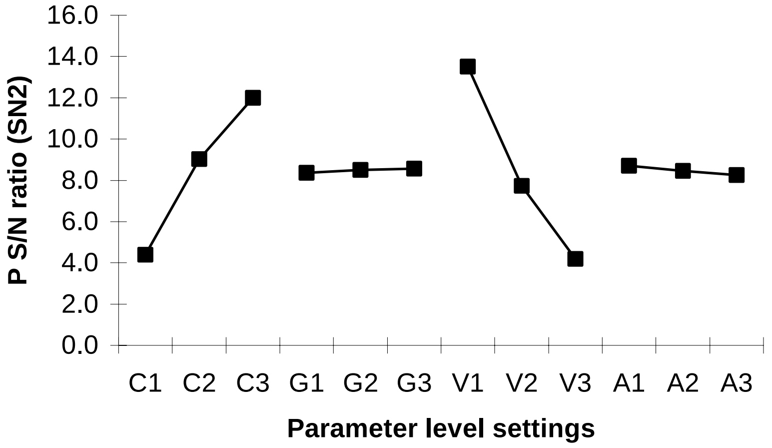

(c)

Fig. 3.28 SN3 ratio of load capacity (a) and radial stiffness (b), and SN2 ratio of power consumption (c) at different levels of factors of C , G_d, μ and α for fluid journal bearing.

Based on above observation, a new set of design parameters was selected. They are ($D3$, $L3$, $C1$, $\mu 3$, $G_d 2$, $\alpha 3$), that is, D = 5mm, L = 5mm, C = 3μm, μ = 30x10^{-3} Pa.S, G_d = 1.2C = 3.6μm, α = 35°. The confirmation experiment is carried out. The results are as following:

W = 33.84 N; K = 61.31x10^6 N/m; P = 2.376 W.

Comparing the above results with the results listed in Table 3.14, it can be seen that the maximum load capacity and stiffness are obtained by the new set of parameters. The power loss is also, of course, higher than that listed in Table 3.14. However, the gain can be compared with the loss to determine whether it is worthy or not. The ratios of power loss to load capacity and stiffness obtained by the new set of parameters are:

P/W = 0.0702 W/N, P/K = 0.0387 W/ (10^6 N/m).

For an overall average value of the first round experiments, the ratio of power loss to load capacity and stiffness are

P/W = 0.1033 W/N, P/K = 0.0574 W/ (10^6 N/m),

and for second round of experiments are:

P/W = 0.0968 W/N, P/K = 0.0704 W/ (10^6 N/m)

The ratios of power loss to load capacity and stiffness of the new setting are obviously reduced. Compared with results of the first and second round of experiments, the P/W ratio is reduced by 32.0% and 27.5% while the reduction of P/K ratio is 32.5% and 45.0%, respectively.

3.5 Discussion and Conclusions

The dynamic characteristics of hydrodynamic bearings are investigated in this chapter. Five types of journal bearings are investigated and compared. Based on the considerations of motion stability and lubricant sealing, the herringbone grooved journal bearing is selected and recommended as the journal bearing for spindle motors used in data storage devices.

A parametric study for the performance of HGJB is further carried out. The conclusions can be drawn from the parametric study are: a) Changing groove parameters such as reducing the groove width (a_g), groove depth (G_d) or axial groove ratio (γ_g), which leads HGJB close to PJB, the load capacity of HGJB can be increased, however, the motion stability is reduced at the same time. b) The ratio of K/P can be used as a criterion to determine a reasonable trade-off between load capacity and motion stability, and the optimal values of groove parameters. The optimal values identified for HGJB are tabulated in Table 3.3.

The groove depth ratio G_d has great influence on the load capacity of both herringbone and spiral thrust bearings. Both herringbone grooved thrust bearing and spiral grooved thrust bearings have similar load capacity and stiffness at their optimal conditions. Therefore, either groove pattern can be used in hydrodynamic thrust bearings for spindle motors used in data storage devices.

Among all the geometrical parameters, the radial clearance, shaft diameter and lubricant viscosity have relatively higher influence on the journal bearing performance. The radial clearance of the journal bearing is the most sensitive parameter that will be affected by the “noise”, that is, the deviations caused by machining tolerance of parts. The rest of the parameters are relatively less sensitive to the “noise” of machining tolerance of parts.

Chapter 4

AERODYNAMIC BEARINGS

4.1 Advantages and Disadvantages of Air Bearing

The spindle motors in data storage devices usually rotate at very high speed, which results in a high shear rate of the lubricant within fluid bearings. It is known that when shear rate is equal or greater than 10^6 1/s, the phenomenon of lubricant degrade occurs (Fuller, 1984). In general, for spindle motors used in hard disk drives, if the rotational speed of the spindle motors is greater than 20,000 rpm, the lubricant shear rate of the fluid bearings will be close or greater than 10^6 1/s. In this situation, the hydrodynamic bearing spindle motors have the risk of performance deterioration due to high shear rate of the lubricant. Hence, aerodynamic bearing spindle motors are the best alternatives.

Besides the high shear rate that causes performance deterioration, the viscosity of oil lubricants varies with the environment temperature change, which is another problem of hydrodynamic bearing spindle motors. Hard disk drives are required to work for a temperature range of 0 °C to 70 °C which results in a notable change of the lubricant viscosity. For example, the viscosity of a certain type of synthetic oil will change from 40×10^{-3} Pa.s to 7×10^{-3} Pa.s corresponding to the temperature change of 0°C to 70°C. Since many important parameters of fluid bearings, such as load capability, stiffness and friction torque, etc. are directly related to lubricant viscosity, the change of viscosity will affect the performance of spindle motors. On the other hand, the viscosity of air remains almost constant within a quite large temperature range (say, from 0°C to 100°C, its viscosity is from 17×10^{-6} to 22×10^{-6} Pa.s). Hence, the air bearing works at a quite stable condition regardless of changes in working temperature.

Furthermore, an important problem concerning the application of hydrodynamic bearing spindle motors in data storage devices is the lubricant leakage, which will cause disk contamination and the performance degradation of spindle motors. Hence, the sealing requirement is quite a challenging problem for the liquid lubricated bearings. Air bearings, however, have no such sealing problem and it is this feature that makes air bearings attractive.

The disadvantages of air bearing are its relatively lower load capacity and lower stiffness. This problem can be partially overcome by increasing the rotating speed of spindle because both load capacity and stiffness are increased when rotational speed is increased. This explains why the air bearings are always used for light-load, high-speed applications. Another disadvantage of air bearing is the surface wear at the

Table 4.1 Comparison between oil bearing and air bearing

Advantages	
Oil Bearing	Air bearing
Modest tolerances	Low power consumption
Boundary lubricated at start and stop	Using process fluid (air), no sealing requirement
High speed operation may be possible	Virtually no speed limits
	Virtually no temperature limits
	Simple geometry
Disadvantages	
Require sealing, seals may fail with shock	Demanding tolerance
Lubricant migration	Low load and stiffness
Cavitation instability	Surface wear at start and stop
Charring of lubricant	Stability consideration
Lubricant properties change with temperature	Compressibility

starting and stop of the spindle motors. With a coating of wear-resistant material on the bearing surfaces, this problem also can be solved. The advantages and disadvantages of hydrodynamic and aerodynamic bearings are compared and listed in Table 4.1.

4.2 Characteristics of Aerodynamic Journal Bearing

Aerodynamic bearings use air as lubricant. Since air (or gas) is compressible, the change of lubricant density must be counted. Using the gas state equation, The Reynolds equation (2.7a1) can be re-written as:

$$\frac{\partial}{\partial x}(ph^3\frac{\partial p}{\partial x})+\frac{\partial}{\partial z}(ph^3\frac{\partial p}{\partial z})=6R\mu\omega\frac{\partial(ph)}{\partial x}+12\mu\frac{\partial(ph)}{\partial t} \qquad (4.1).$$

The boundary conditions for Eq. (4.1) are:

$p = 0$ at $z = 0$ and l ; (4.2a)

$p(\theta) = p(2\pi+\theta)$ in circumferential direction. (4.2b)

From eq. (4.1), it is obviously that the characteristics of aerodynamic bearings are different from those of hydrodynamic bearings. Furthermore, due to the relative lower load capacity of aerodynamic bearing, the diameter of air journal bearing has to be increased to generate enough load capacity and stiffness required by the specifications of spindle motor. On the other hand, the height of the spindle motors used in hard disk drives is fixed for a specified format of hard disk drive and cannot be changed, which results in the lower ratio of *L/D* of air journal bearing and is usually less than 0.5 instead of *L/D* = 1 in hydrodynamic bearings. The lower ration of *L/D* also causes the characteristics of aerodynamic journal bearing to be different from the previously discussed hydrodynamic journal bearings. Therefore, the characteristics of aerodynamic journal bearings should be further investigated. An aerodynamic bearing system to be used in a spindle motor for 2.5-inch hard disk drive will be used as an example to discuss the characteristics of aerodynamic bearings.

For a spindle motor to be used in a 2.5-inch format hard disk drives with a nominal operation speed of 25,000 rpm, the allowable residual unbalance of the disk stack and spindle motor assembly is ≤ 0.3gram-mm. The motor must have the capability to resist the unbalance force in addition to the disks load. Therefore, the required load capacity and stiffness of the bearing system are:

$W_r \geq 2.5$ N, $W_z \geq 2.5$ N and $K_{rr} \geq 5.0 \text{x} 10^6$ N/m, $K_{zz} \geq 5.0 \text{x} 10^6$ N/m,

where, W_r and W_z are the radial and axial load capacity, K_{rr} and K_{zz} are the direct radial and axial stiffness[*].

According to the above requirements, the following design parameters were chosen for the first round simulation. It should be mentioned that the diameter and length of the journal bearing are limited by the dimensions of the spindle motor, which is specified by the format of hard disk drives. Here, the maximum values allowable by the space of the spindle motor for the journal bearing is taken. The major parameters used to predict the performance of the air journal bearing are summarized as following:

Diameter of the journal bearing $D = 15$ mm,

Length of the journal bearing $L = 3$ mm ($L/D = 0.2$),

Radial clearance $R_c = 2.0$ μm; Dynamic viscosity $\mu = 18.08 \text{x} 10^{-6}$ Pa.s at 20 °C.

Groove pattern: Herringbone groove; Groove number $N_g = 12$;

Groove angle $\alpha = 28.0°$; Groove depth $G_d = 1.2$;

Groove width $a_g = 0.5$; Groove region ratio $\gamma_g = 1.0$;

Rotational speed $N_s = 25{,}000$ rpm; Eccentricity ratio $\varepsilon = 0.0 - 0.5$.

---

[*] The radial and axial stiffness requirement is deduced from the ball bearing.

Using the above design parameters, the simulation results are presented in Table 4.2. The results show that if the radial clearance take the value of R_c = 2.0 μm, even the value at eccentricity ratio ε = 0.5 was taken; the radial stiffness K_{xx} was still 2.4x10^6 N/m only. Obviously, this radial stiffness was lower than the required stiffness of the spindle motor. Therefore, the radial clearance of the journal bearing had to be reduced to increase the stiffness of the journal bearing. Two more cases of R_c = 1.5 μm and R_c = 1.0 μm were considered. The results were also tabulated in Table 4.2. It is observed that for R_c = 1.5 μm, at ε = 0.4, the stiffness K_{xx} = 5.2x10^6 N/m and the load capacity W = 3.12 N. For R_c = 1.0 μm, the stiffness K_{xx} is greater than 1.0x10^7 N/m for all eccentricity ratios and W = 3.21 N at ε = 0.2. These results satisfy the requirements

Table 4.2 First round simulation results of aerodynamic journal bearing

ε	W (N)	P (W)	K_{xx} (N/m)	D_{xx} (N.s/m)
R_c = 2.0μm				
0	0.03	0.39	1.90x10^6	3.21x10^2
0.1	0.39	0.38	1.92x10^6	3.20x10^2
0.2	0.80	0.39	1.98x10^6	3.25x10^2
0.3	1.26	0.39	2.08x10^6	3.36x10^2
0.4	1.78	0.41	2.21x10^6	3.53x10^2
0.5	2.41	0.43	2.40x10^6	3.77x10^2
R_c = 1.5μm				
0	0.05	0.51	4.46x10^6	7.44x10^2
0.1	0.69	0.51	4.51x10^6	7.44x10^2
0.2	1.41	0.51	4.64x10^6	7.58x10^2
0.3	2.21	0.52	4.89x10^6	7.79x10^2
0.4	3.12	0.54	5.20x10^6	8.18x10^2
0.5	4.21	0.57	5.58x10^6	8.71x10^2
R_c = 1.0μm				
0	0.12	0.77	1.52x10^7	2.57x10^3
0.1	1.57	0.76	1.53x10^7	2.56x10^3
0.2	3.21	0.77	1.58x10^7	2.60x10^3
0.3	5.02	0.79	1.66x10^7	2.69x10^3
0.4	7.12	0.81	1.77x10^7	2.82x10^3
0.5	9.63	0.85	1.92x10^7	3.02x10^3

for both radial load capacity and stiffness. Hence, either R_c = 1.5 μm or R_c = 1.0 μm can be considered and selected.

Based on the above results, the second round simulations were carried out to investigate the effect of individual parameter.

a) Effect of groove angle

The effect of groove angle to the performance of the air journal bearing is first investigated. The parameters used in the simulations are:

R_c = 2, 1.5 and 1.0 μm;

α = 6°, 8°, 10°, 12°, 14°, 16°, 18°, 20°, 22°, 25°, 28°, 31° and 35°

and other parameters are kept unchanged. Figure 4.1(a) shows the variation of load capacity with groove angles α at radial clearance R_c = 1 μm and eccentricity ratio ε = 0.5. The load capacity initially increases with the increasing value of α. At α = 12°, it reaches a maximum value of 12.30 N and then gradually decreases with further increase of groove angle α. The variation of stiffness K_{xx} with the groove angle also has the similar trend as shown in Fig. 4.1(b). However, the power consumption of the journal bearing simply increases with increasing groove angle α as shown in Fig. 4.1(c). The same trend as shown in Figs. 4.1(a) – 4.1(c) was also observed for other values of eccentricity ratio ε ranging from 0.0 to 0.4 (not shown here).

b) Effect of groove depth

To investigate the effect of groove depth, the groove angle α was fixed at 12° and the groove depth ratio was varied. Let groove depth ratio G_d be:

G_d = 0.5, 1.0, 2.0, 3.0, 4.0, (x R_c while R_c = 2.0, 1.5 and 1.0 μm).

Figure 4.2(a) shows the result of journal bearing load capacity versus groove depth at R_c = 1 μm with the eccentricity ratio ε = 0.0, 0.1, 0.2. Obviously, the load capacity has the maximum value at G_d = 2.0. The same conclusion is also true for the radial stiffness K_{xx} as shown in Fig. 4.2(b). However, the power consumption decreases with the increasing groove depth as shown in Fig. 4.2(c).

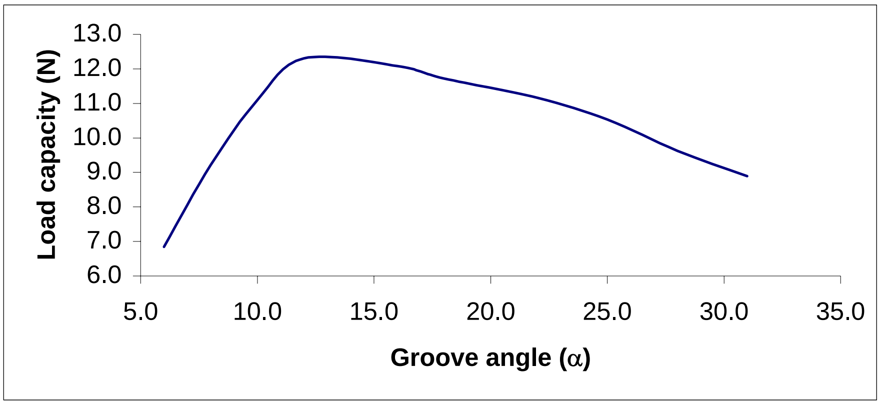

(a)

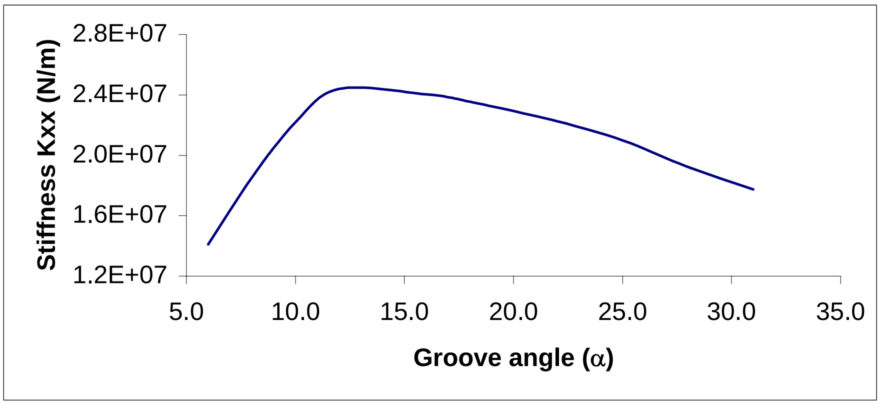

(b)

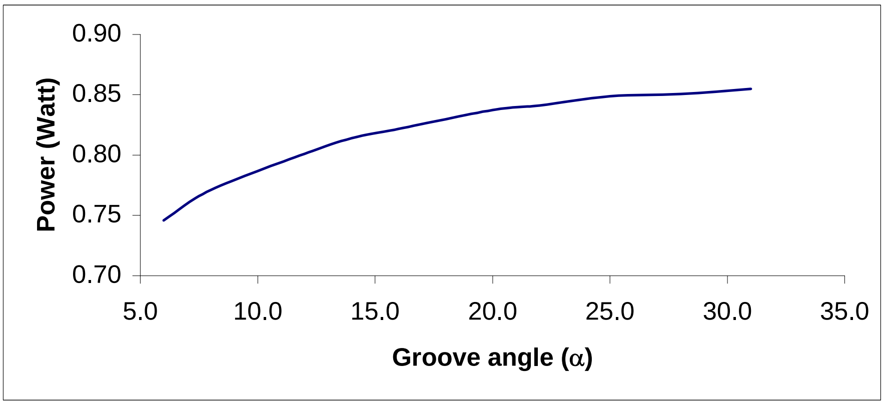

(c)

Fig. 4.1 Load capacity (a), stiffness K_{xx} (b) and power consumption of aerodynamic journal bearing versus groove angle (α) at $\varepsilon = 0.5$ and $R_c = 1$ μm.

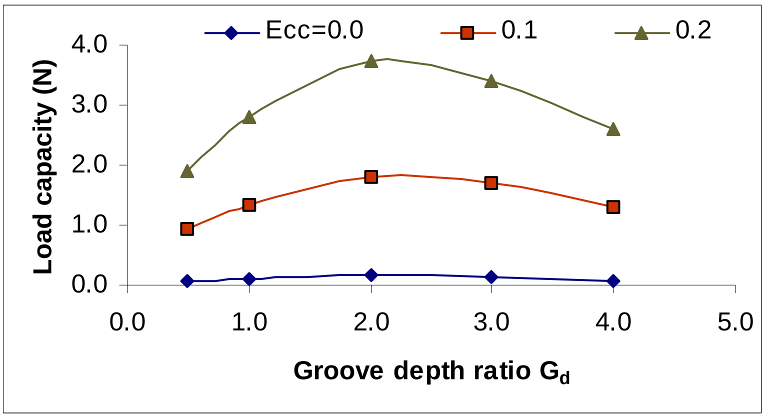

(a)

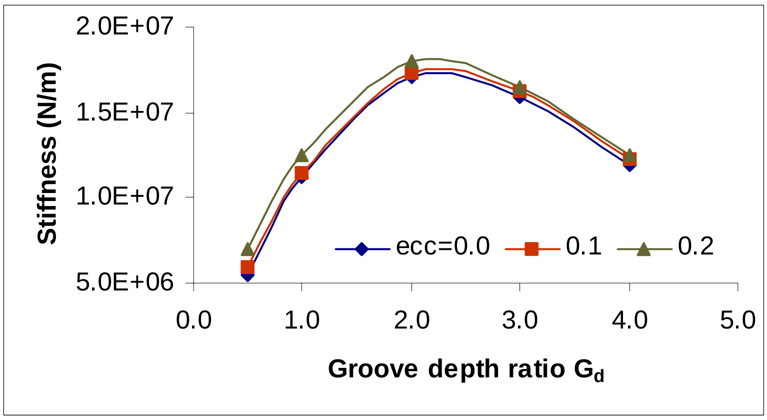

(b)

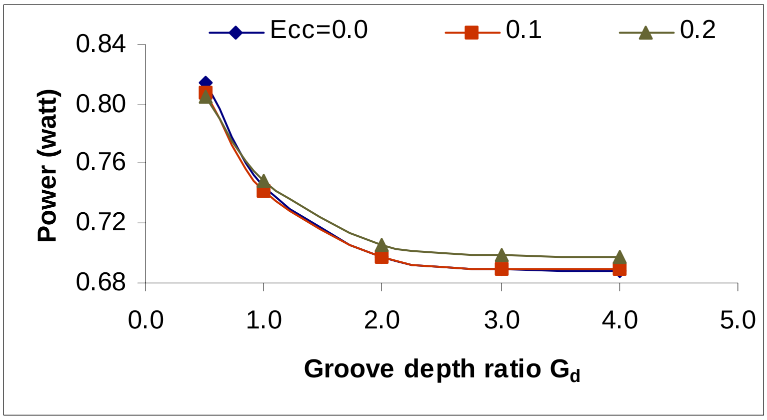

(c)

Fig. 4.2 Load capacity (a), stiffness K_{xx} (b) and power consumption (c) of aerodynamic journal bearing versus grove depth ratio (G_d) at Rc = 1 μm.

c) Effect of groove number and groove width

Following the above simulations, the effect of the groove number N_g and groove width a_g were investigated with the fixed value of groove angle $\alpha = 12°$ and

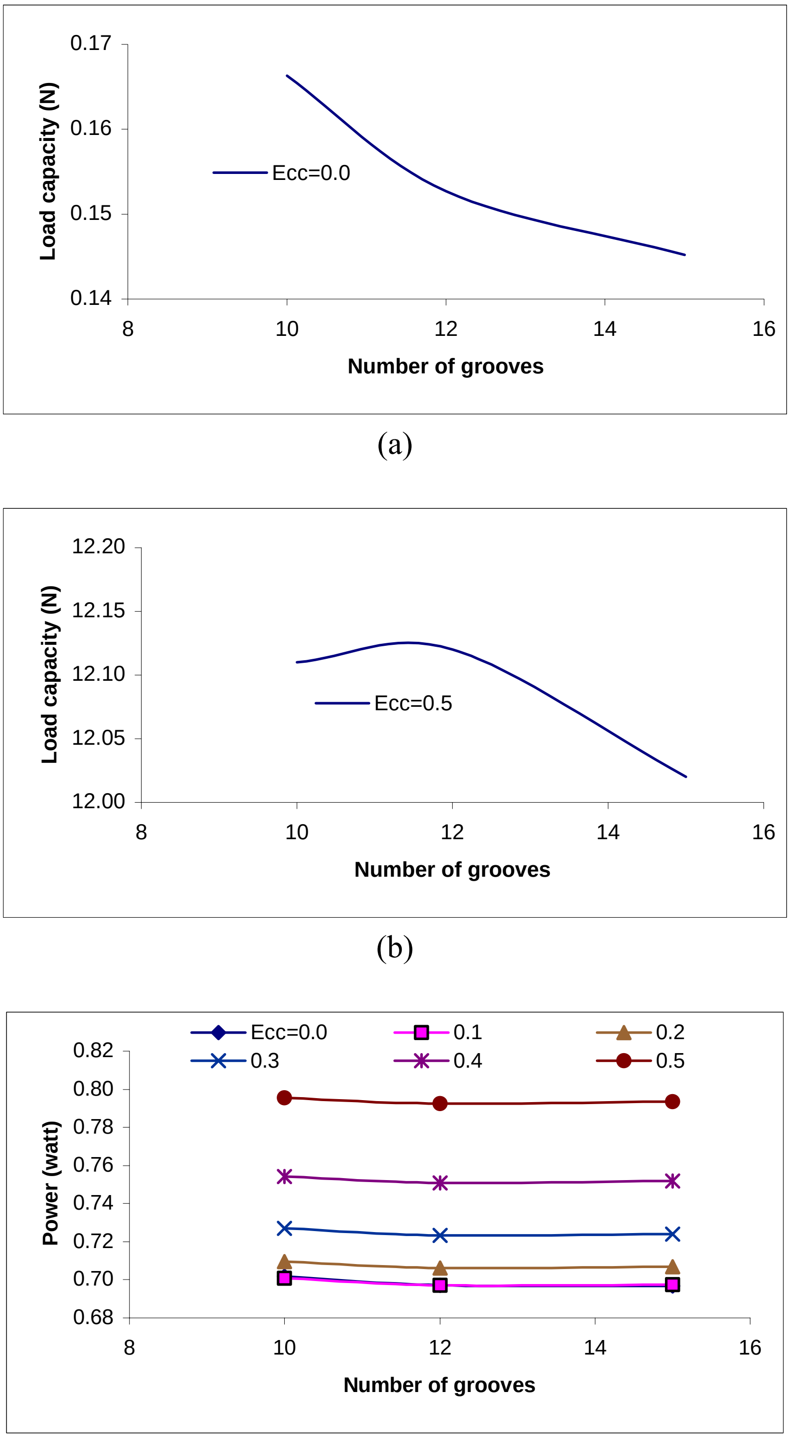

(a)

(b)

(c)

Fig. 4.3 Radial load capacity (a) $\varepsilon = 0.0$; and (b) $\varepsilon = 0.5$ and power consumption (c) ε=0-0.5 versus number of grooves (N_g) for aerodynamic journal bearing at $Rc = 1$ μm.

Groove depth G_d = 2.0. The groove numbers and groove width used in the simulations were:

N_g = 10, 12 and 15;

a_g = 0.4, 0.5, 0.6 and 0.7.

The results of changing the above parameters are presented in Figs. 4.3(a) - 4.4(c). Figure 4.3(a) shows the load capacity decreases with increasing of groove number N_g at ε = 0.0. The same trend is also observed at other eccentricity ratios of ε = 0.1, 0.2, 0.3 and 0.4 (not shown). However, at ε = 0.5, the load capacity has maximum value at N_g = 12 as shown in Fig. 4.3(b). Since the spindle motor will seldom operate at such high eccentricity ratio, therefore, N_g = 10 was taken as the optimum parameter for the next stage design. The power consumption of the aerodynamic journal bearing versus the groove number N_g for ε = 0 – 0.5 are shown in Fig. 4.3(c). Figures 4.4(a) – 4.4(c) show the effect of groove width. They were quite consistence, all performance indicators, such as load capacity, stiffness and power consumption, had a maximum value at a_g = 0.4 and all of them decreased with further increase of groove width.

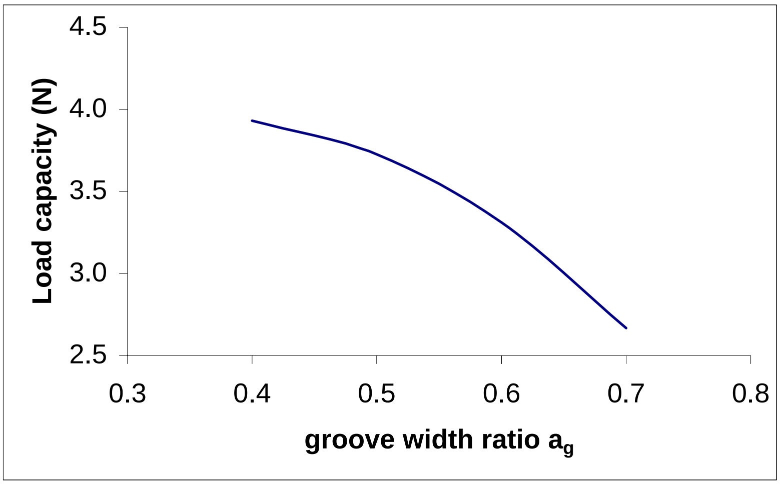

Fig. 4.4(a) (Continued)

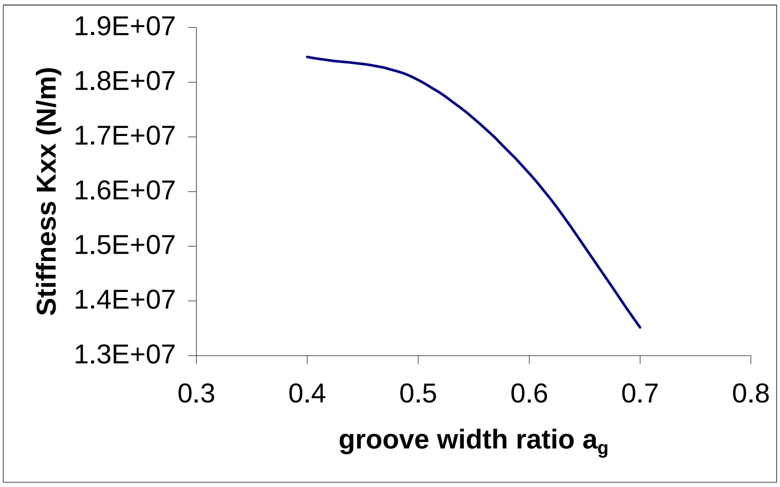

(b)

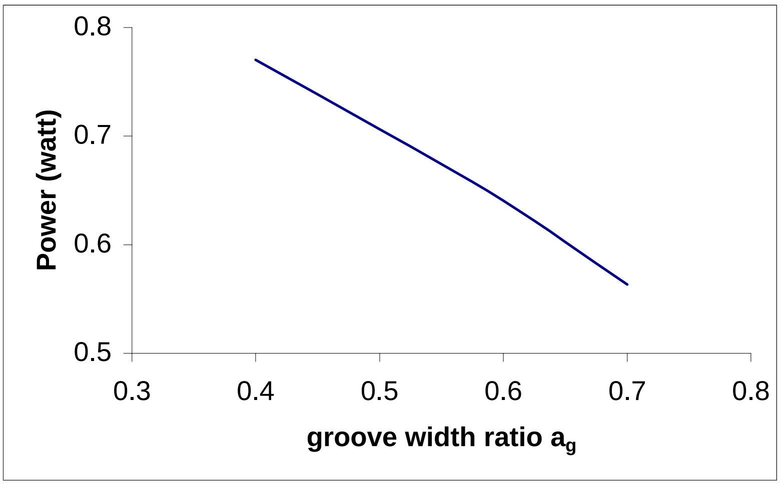

(c)

Fig. 4.4 Load capacity (a), radial stiffness K_{xx} (b) and power consumption (c) of aerodynamic journal bearing versus groove width ratio (a_g) at $\varepsilon = 0.2$ and $R_c = 1$ µm.

4.3 Characteristics of Aerodynamic Thrust Bearing

The following values are given as a starting point of simulation for the thrust bearing to be investigated:

Inner radius of the thrust plate = 3.0 mm,

Outer radius of the thrust plate = 7.5 mm,

Dynamic viscosity $\mu = 18.08 \times 10^{-6}$ Pa.s at 20 °C.

Groove pattern: Herringbone groove;

Groove number $N_g = 12$;

Groove angle $\alpha = 11.6°$;

Groove depth $G_d = 3.0C$;

Groove width $a_g = 0.455$;

Rotational speed $N_s = 25,000$ rpm;

Axial clearance $A_c = 1.0 - 5.0$ μm.

Using above parameters, the performance of air lubricated thrust bearing was investigated.

Figure 4.5 shows the variation of load capacity with the axial clearance. The load capacity is sharply increased when the axial clearance A_c is reduced from 2 μm to 1 μm. At $A_c = 1$ μm the load capacity is almost 5 times higher than that at $A_c = 2$ μm. To find the reason that causes this phenomenon, all parameters were fixed except the groove depth. The groove depth is then changed from 2 to 12 times of the axial clearance with the step increment of one. The results are plotted in Fig. 4.6. Checking the result shown in Fig. 4.6, it is found that the sharp increase of the load capacity is caused by the ratio of groove depth over the axial clearance. It is quite clear that when the ratio of groove depth over the axial clearance is close to 4, the load capacity reached the maximum value for each value of axial clearance as indicated in Fig. 4.6. In Fig. 4.5, the groove depth is fixed to 3 μm, that is, 3 times of the minimum axial clearance of 1 μm. This value is close to the optimum condition for $A_c = 1$μm. However, it is far away the optimum condition for $A_c = 2$ μm. This explains why there is a big difference of the load capacity between $A_c = 1$ μm and 2 μm and also identifies that the optimum value of G_d is around 4.0. This conclusion is close to the situation in the hydrodynamic thrust bearings.

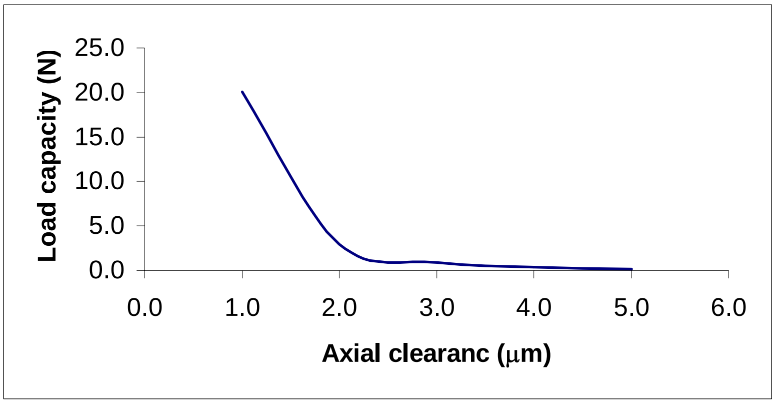

Fig. 4.5 Axial load capacity versus axial clearance for aerodynamic thrust bearing.

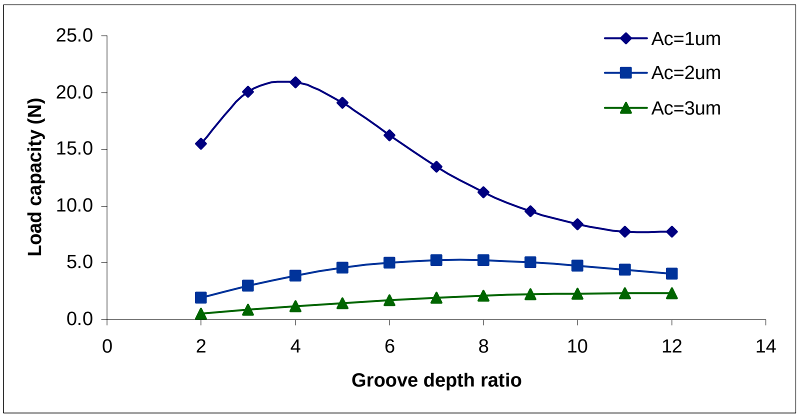

Fig. 4.6 Axial load capacity versus groove depth for aerodynamic thrust bearing.

Then the effect of other design parameters was further investigated. They were number of grooves, groove angle and groove width. The following values were taken in simulations:

$N_g = 10, 12, 15$;

$\alpha = 10.0°, 11.5°, 13.0°, 15.0°$;

$a_g = 0.4, 0.5, 0.6, 0.7$.

The effect of groove number on the axial load capacity is opposite to the situation in the journal bearing. Here, the load capacity increases with the increase of groove number. Among the three values of groove number, $N_g = 15$ registered the highest load capacity. The effect of increasing groove angle got diverse results. Refer to Fig. 4.8, it is observed that at axial clearance $A_c = 1$ μm, the highest load capacity is obtained at groove angle α = 13.0°. However, at A_c = 2 μm and 3 μm, the load capacity is increased with the increase of groove angle. The effect of the groove width on the axial load capacity is quite consistence and the load capacity reaches its peak value at a_g = 0.5 for all axial clearances as shown in Fig. 4.9.

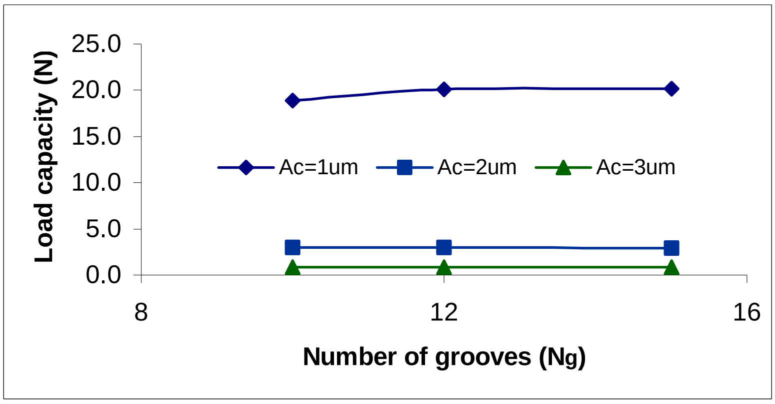

Fig. 4.7 Axial load capacity versus number of grooves for aerodynamic thrust bearing.

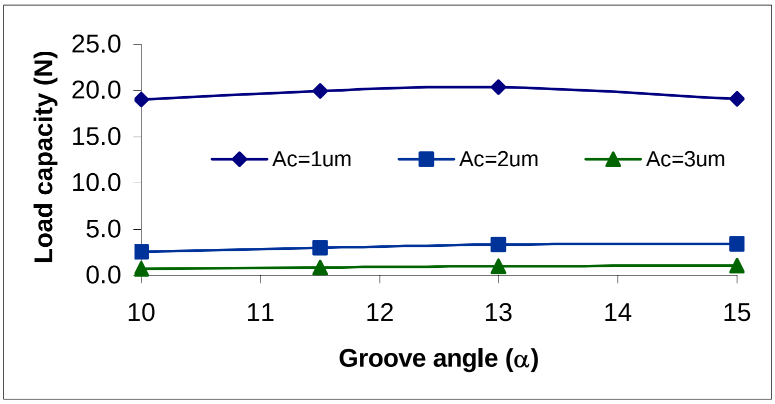

Fig. 4.8 Axial load capacity versus groove angle for aerodynamic thrust bearing.

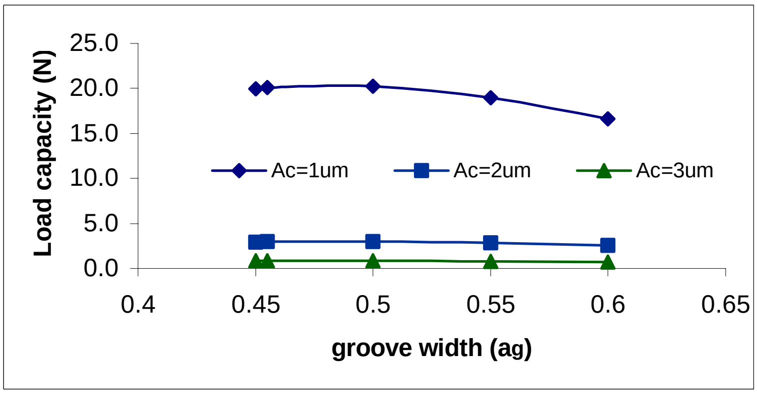

Fig. 4.9 Axial load capacity versus groove width for aerodynamic thrust bearing.

4.4 Optimum Parameters of Aerodynamic Bearing System

Based on above observations, a set of optimum parameters are selected for the air bearing system as given below:

Journal bearing:

Diameter of the journal bearing D = 15 mm;

Length of the journal bearing L = 3 mm; Radial clearance R_c = 1.0 μm;

Groove pattern: Herringbone groove; Groove number N_g = 10;

Groove angle α = 12.0°; Groove depth G_d = 2.0; Groove width a_g = 0.4;

Groove region ratio γ_g = 1.0; Eccentricity ratio ε = 0.0 - 0.5.

Thrust bearing:

Inner radius of the thrust plate R_i = 3.0 mm;

Outer radius of the thrust plate R_o = 7.5 mm, Axial clearance A_c = 1.0 μm.

Groove pattern: Herringbone groove; Groove number N_g = 15;

Groove angle α = 13.0°; Groove depth G_d = 3.5; Groove width a_g = 0.5;

With the above finalized design parameters, the performance of the air bearing system is simulated at the given rotational speed N_s = 25,000 rpm and the viscosity μ = 18.08x10^{-6} Pa.s at 20 °C.

The simulation results of the load capacity, power consumption, stiffness and damping coefficients of the journal bearing against the eccentricity ratio from ε = 0.0 to ε = 0.5, are presented in Figs. 4.10 - 4.13. Figures 4.14 - 4.17 show the load capacity, power consumption, stiffness and damping coefficients of the thrust bearing at groove depth ratio G_d = 3.5 and G_d = 4.0, respectively. Obviously, at the nominal axial clearance A_c = 1.5 μm, the axial load capacity, stiffness and damping coefficients at G_d = 3.5 were better than that at G_d = 4.0 while the power consumption had no substantial change. Therefore, the groove depth ratio $G_d = 3.5$ was chosen for the final design.

The dynamic characteristics of the air bearing system at the condition of $\varepsilon = 0.2$ can be summarized as follows:

$W_r = 3.985 \text{x} 2 = 7.97$ N, $W_z = 21.6$ N

$K_{xx} = 1.87\text{x}10^7\text{x}2 = 3.74\text{x}10^7$ N/m $K_{zz} = 4.22\text{x}10^7$ N/m

$P_{total} = (0.761+0.448)\text{x}2 \approx 2.5$ W.

Since there are two journal bearings distributed along the shaft, the stiffness and power consumption in radial direction should be doubled. The thrust bearing is a double size thrust bearing, so its power consumption is also doubled. The above results show a reasonable power consumption of the bearing system for such high-speed spindle motor. The bearing system also possesses sufficient load capacity and stiffness to carry the load and to resist external disturbances. The detailed values of the bearing system are tabulated in Tables 4.3 and 4.4.

To compare the power consumption of the aerodynamic with hydrodynamic bearing system, the power consumption of a hydrodynamic bearing system is calculated. The reference hydrodynamic bearing system has the dimensions of $D = 4$ mm and $L = 4$ mm for the journal bearing, $r_i = 1$ mm and $r_o = 2$ mm for the thrust bearing. At N_s =25,000 rpm, its load capacity, stiffness and power consumption are:

$W_r = 8.85$ N, $W_z = 27.2$ N

$K_{xx} = 3.01\text{x}10^6$ N/m $K_{zz} = 3.0\text{x}10^7$ N/m

$P_{total} = 2.93 + 1.17\text{x}2 = 5.28$ W.

Obviously, when the load capacity of the hydrodynamic bearing system is comparable to the aerodynamic bearing system, its stiffness is lower than that of the aerodynamic bearing system and its power consumption is almost 2.1 times of that of the aerodynamic bearing system.

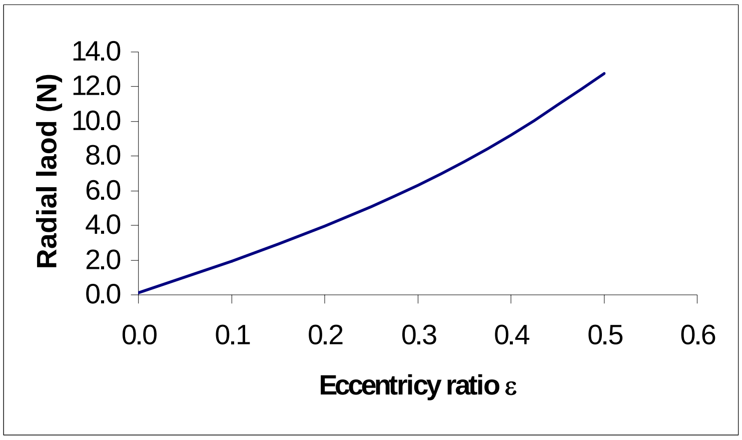

Fig. 4.10 Radial load capacity versus eccentricity ratio for optimum aerodynamic bearing system.

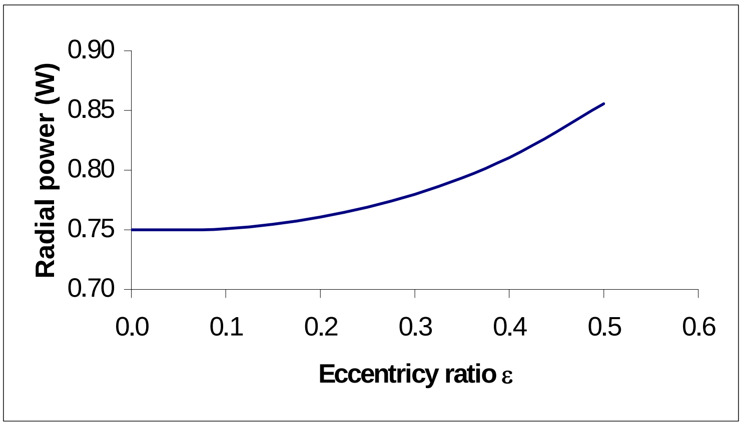

Fig. 4.11 Radial power consumption versus eccentricity ratio for optimum aerodynamic bearing system.

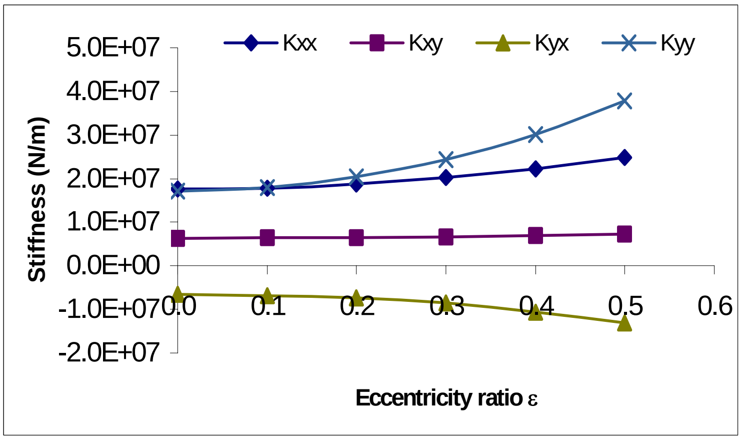

Fig. 4.12 Radial stiffness versus eccentricity ratio for optimum aerodynamic bearing system.

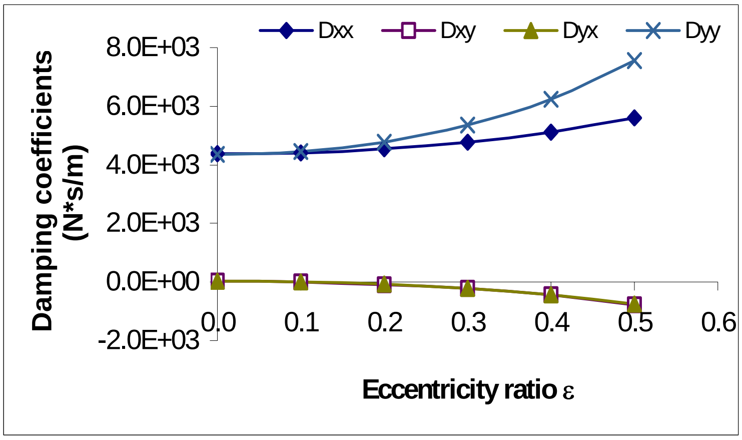

Fig. 4.13 Radial damping coefficients versus eccentricity ratio
for optimum aerodynamic bearing system.

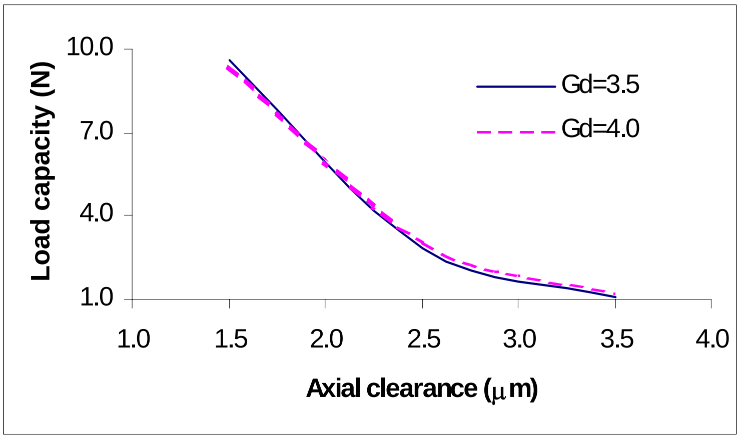

Fig. 4.14 Axial load capacity versus axial clearance
for optimum aerodynamic bearing system.

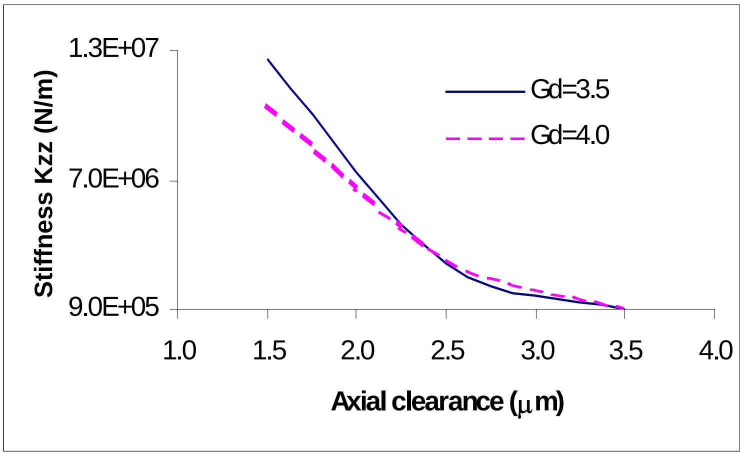

Fig. 4.15 Axial stiffness versus axial clearance
for optimum aerodynamic bearing system.

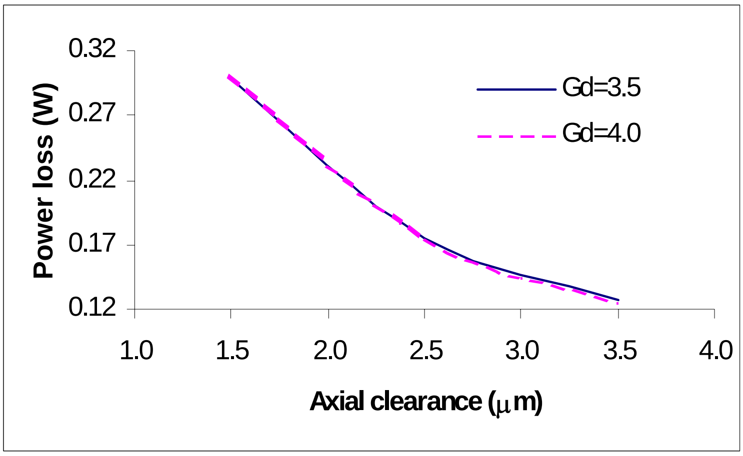

Fig. 4.16 Axial power consumption versus axial clearance for optimum aerodynamic bearing system.

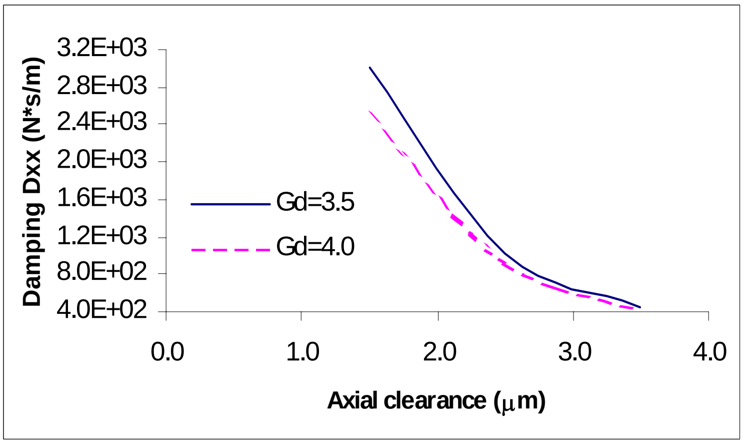

Fig. 4.17 Axial damping coefficients versus axial clearance for optimum aerodynamic bearing system.

4.5 Discussion and Conclusions

The advantages and disadvantages of aerodynamic bearings are addressed and discussed. The major advantages of aerodynamic bearings are power saving, seal free and no risk of performance degradation caused by lubricant deterioration. The main disadvantages of air bearing are relatively lower load capacity and difficulties in fabrication.

Due to the lower load capacity of aerodynamic bearing, the diameter of the air journal bearing usually is several times of that of oil lubricated journal bearings, which results in a small ratio of L/D. An aerodynamic bearing system with a configuration of short journal bearing (L/D = 0.2) for spindle motors used in hard disk drives is investigated. The optimum values of the air bearing system are proposed. The optimal value of the groove angle for air bearing is $\alpha = 12.0°$. This is smaller than that of the oil-lubricated journal bearing, for which is $\alpha = 28.0°$ as mentioned in Chapter 3.

The total power consumption of the air bearing system is around 2.5 W, which is almost 47% of that of the reference oil-lubricated bearing system that has the similar load capacity and the same rotating speed.

Table 4.3 Characteristics of aerodynamic journal bearing at optimum condition

ε	W (N)	K_{xx} (N/m)	K_{xy}(N/m)	K_{yx} (N/m)	K_{yy} (N/m)
0.0	0.144	$1.77\text{x}10^7$	$6.23\text{x}10^6$	$-6.51\text{x}10^6$	$1.72\text{x}10^7$
0.1	1.952	$1.78\text{x}10^7$	$6.45\text{x}10^6$	$-6.78\text{x}10^6$	$1.80\text{x}10^7$
0.2	3.985	$1.87\text{x}10^7$	$6.53\text{x}10^6$	$-7.40\text{x}10^6$	$2.05\text{x}10^7$
0.3	6.334	$2.03\text{x}10^7$	$6.65\text{x}10^6$	$-8.53\text{x}10^6$	$2.44\text{x}10^7$
0.4	9.193	$2.23\text{x}10^7$	$6.87\text{x}10^6$	$-1.06\text{x}10^7$	$3.01\text{x}10^7$
0.5	12.780	$2.48\text{x}10^7$	$7.34\text{x}10^6$	$-1.31\text{x}10^7$	$3.79\text{x}10^7$
ε	P (W)	D_{xx} (N*s/m)	D_{xy} (N*s/m)	D_{yx} (N*s/m)	D_{yy} (N*s/m)
0.0	0.7501	$4.37\text{x}10^3$	20.2	25.8	$4.36\text{x}10^3$
0.1	0.7508	$4.41\text{x}10^3$	-2.5	0.94	$4.46\text{x}10^3$
0.2	0.7606	$4.54\text{x}10^3$	-84.7	-78.6	$4.77\text{x}10^3$
0.3	0.7797	$4.77\text{x}10^3$	$-2.24\text{x}10^2$	$-2.20\text{x}10^2$	$5.35\text{x}10^3$
0.4	0.8103	$5.12\text{x}10^3$	$-4.42\text{x}10^2$	$-4.37\text{x}10^2$	$6.24\text{x}10^3$
0.5	0.8558	$5.61\text{x}10^3$	$-7.67\text{x}10^2$	$-7.56\text{x}10^2$	$7.56\text{x}10^3$

Table 4.4 Characteristics of aerodynamic thrust bearing at optimum condition

A_c	W (N)	P (W)	K_{zz} (N/m)	D_{zz} (N*s/m)
1.0	21.646	0.4484	$4.22\text{x}10^7$	$1.02\text{x}10^4$
1.5	9.621	0.2990	$1.25\text{x}10^7$	$3.01\text{x}10^3$
2.0	3.797	0.2192	$5.45\text{x}10^6$	$2.19\text{x}10^3$
2.5	2.814	0.1749	$3.04\text{x}10^6$	$1.02\text{x}10^3$
3.0	1.136	0.1505	$1.16\text{x}10^6$	$7.75\text{x}10^2$
3.5	1.077	0.1263	$9.05\ \text{x}10^5$	$4.40\text{x}10^2$

Chapter 5

HYBRID BEARING SYSTEMS*

5.1 Introductory Remarks

Air-lubricated bearing is attractive because the difficulty of lubricant sealing is circumvented. However, the spindle motors with fully air lubricated bearings have relatively lower load capacity compared to those with liquid lubricated bearings. Moreover the fully air lubricated bearings offer no path for discharging static electrical charges accumulated during hard disk drive operation. On the other hand, the spindle motors with fully oil lubricated bearings have higher bearing power losses. The sealing for both liquid lubricated journal and thrust bearings is relatively difficult to design and implement to achieve a "zero" leakage condition for ordinary liquid lubricants.

In the application to hard disk drives, the stiffness of journal bearing is more important and the required radial stiffness is normally higher than that of axial stiffness in many cases. Furthermore, as the rotational speed of hard disk drive spindles is continuously increased, the energy consumed by the spindles is also increased. Reducing the energy consumption of spindles is an important issue, especially for the spindles used in laptops and notebooks, where the power is supplied by backup battery.

To overcome the above-mentioned problems and find a solution, a hybrid hydrodynamic and aerodynamic bearing system is introduced in this chapter. In the hybrid fluid bearing system, air is used as lubricant for its conical thrust bearings while

---

*Part of this Chapter has been published in *IEEE Trans. on Magnetics*, v35, n2, pp. 2638-2640, 1999.

oil is used as lubricant for the journal bearings. The considerations of designing a hydro-aerodynamic hybrid fluid bearing system will be addressed and discussed in the following sections.

5.2 Hybrid Fluid Bearing System

Figure 5.1 shows the schematic of the prototype spindle unit for a 3.5 inch hard disk driver. The spindle motor consists of a brushless direct current (BLDC) motor, a hybrid fluid film bearing system, a hub and a base. The configuration of spindle motor is "motor-in-hub" design, that is, the motor and the bearings are all located in the space inside the hub. The motor consists of a stator and a ring magnet that is attached to hub together with a yoke. The bearing system consists of an oil lubricated journal bearing and an air lubricated thrust bearing. The sleeve of journal bearing is fixed to the base plate and the shaft of journal bearing is fixed to the hub. Therefore, the spindle motor is a "rotating shaft" design. Two herringbone groove journal bearings are machined at two separated locations on the shaft. The conical shaped thrust plate is fixed to the sleeve of journal bearing and its top and bottom surfaces are engraved with spiral

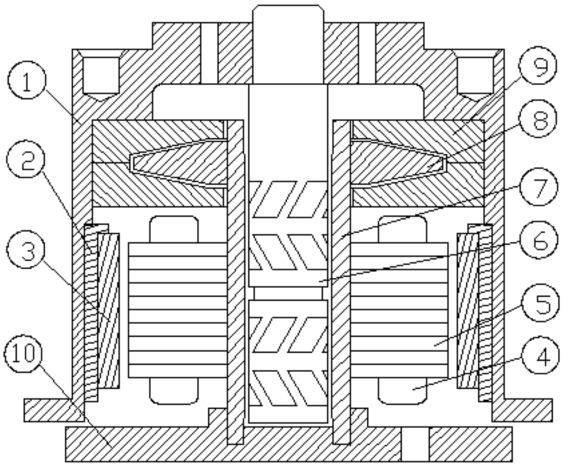

10	BASE	1	ALUM.
9	THRUST BEARING	2	Bronze
8	THRUST PLATE	1	STEEL
7	SLEEVE	1	Bronze
6	SHAFT	1	STEEL
5	Lamination Stator	1	STEEL
4	STATOR WINDING	1	Copper
3	MAGNET	1	STEEL
2	YOKE	1	STEEL
1	HUB	1	ALUM.
NO	PART NAME	REQD	MATL

Fig. 5.1 Schematic of hybrid design of fluid bearing system.

grooves. To prevent the thrust plate surface and its mating bearing surfaces from the wear damage at start and stop of the spindle motor, a narrow ring area on both upper and lower bearing surfaces is coated with anti-wearing material. Therefore, except for the coated area, the surfaces of thrust plate and thrust bearing are separated even when the spindle motor is at static state. The separation of thrust plate from its mating bearing also reduces dry friction at starting. The capillary sealing was designed to capture the lubricant within the gap of journal bearing when the spindle motor is at static state. The inward pumping effect of the herringbone grooves prevents the lubricant from leaking when the spindle motor is rotating. Furthermore, the surface areas at the top ends of the shaft and the sleeve are coated with an anti-migration material to prevent the lubricant from migration leakage due to the surface tension.

Table 5.1 Main parameters of spindle motor and features of bearing system

Parameters of Spindle Motor		
Disk drive format	3.5 inch	
Height of spindle motor	1 inch	
Operating speed	10,200 rpm	
Motor topology	3 phase BLDC 8 pole/ 9 slot	
Start current	≤ 2.0 A	
Supply voltage	12 V ±5%	
Torque Constant (Nm/A)	0.00654	
Features of Bearing System		
	Journal bearing	Thrust Bearing
Lubricant	Oil	Air
Mating materials	Steel/bronze	Steel/bronze
Groove	Herringbone	Spiral

5.3 Discussion and Conclusions

The non-dimensional formula of load and stiffness of fluid film journal bearing can be written as (Constantinescu *et al*., 1985):

$$\overline{W} = \frac{W}{\mu NDL}\left(\frac{c}{R}\right)^2, \tag{5.1}$$

$$\overline{K} = \frac{cK}{\mu NDL}\left(\frac{c}{R}\right)^2. \tag{5.2}$$

Hence, the load W and stiffness K can be respectively expressed as:

$$W = \overline{W}\mu NDL(R/c)^2, \tag{5.3}$$

$$K = \overline{K}\mu NDLR^2/c^3. \tag{5.4}$$

where μ is the lubricant viscosity, N rotational speed, D, L, R and c are diameter, length, radius and radial clearance of journal bearing, respectively. Equations (5.3) and (5.4) show that the load capacity and stiffness of journal bearing are functions of N, D, L, R, c and μ. Hence, if all parameters including the geometric dimensions of the grooves are kept unchanged except the lubricant viscosity, then W and K are directly proportional to lubricant viscosity μ. Refer to Eqs. (5.3) and (5.4), it is obvious that oil lubricated journal bearing will generate several hundred times higher load capacity and radial stiffness than that of air lubricated journal bearing due to the much higher viscosity. The load capacity and the radial stiffness of air lubricated bearing can be increased by reducing the radial clearance. However, Fig. 5.2 shows that only when the radial clearance of air lubricated journal bearing is reduced to 1/10 of that of oil lubricated journal bearing, will its stiffness be comparable to that of oil lubricated journal bearing. Furthermore, Fig. 5.3 shows that the load capacity of air lubricated bearing is still almost one order of magnitude lower than that of oil lubricated bearing at temperature 20 °C. In addition to lower load capacity, the narrower clearance results in a tighter tolerance requirement that inevitably increases the difficulty and the cost both in parts machining and assembling.

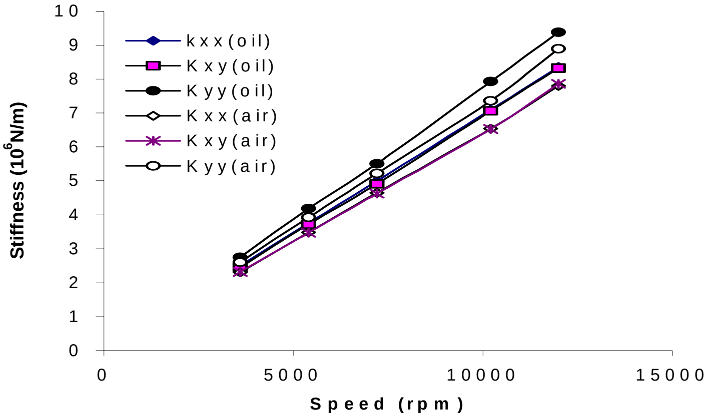

Fig. 5.2 Stiffness of journal bearing using oil as lubricant (R_c = 10 μm) and air as lubricant (R_c = 1 μm).

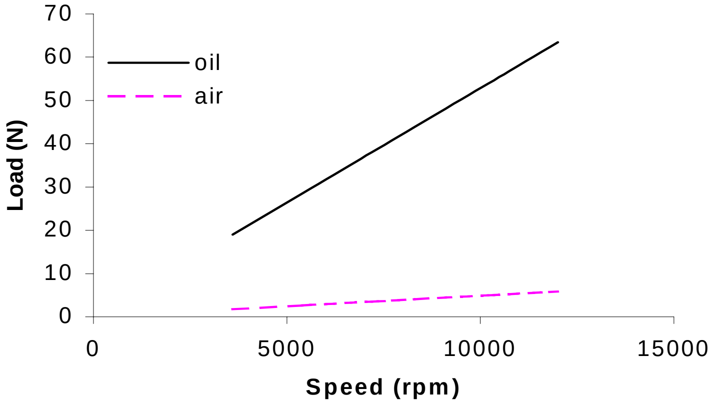

Fig. 5.3 Load capacity of journal bearing using oil (R_c = 10 μm) and air (R_c = 1 μm) as lubricant.

Alternatively, the load capacity and stiffness of journal bearing can be improved by increasing the shaft diameter. However, a small increment in the shaft diameter has little help to increase the load capacity and stiffness. If the shaft diameter is largely increased, the shaft will inevitably take some space reserved for the motor stator, which results in not enough space to accommodate the motor stator inside the hub. Therefore, increasing the load capability and stiffness of journal bearing by means of increasing the diameter of the shaft is not practically feasible.

Based on the above discussions and considerations, the oil lubricated journal bearing is preferably used in the hybrid bearing system. With herringbone grooves etched on the shaft or the sleeve, the journal bearing has enhanced load capacity, radial stiffness and motion stability. A typical gauge pressure distribution for the journal bearing at optimized groove parameters is shown in Fig. 5.4, the base is the reference pressure which is equal to the ambient pressure. The load capacity and stiffness of the journal bearing as the function of eccentricity ratio are shown in Figs. 5.5(a) and 5.5(b), respectively.

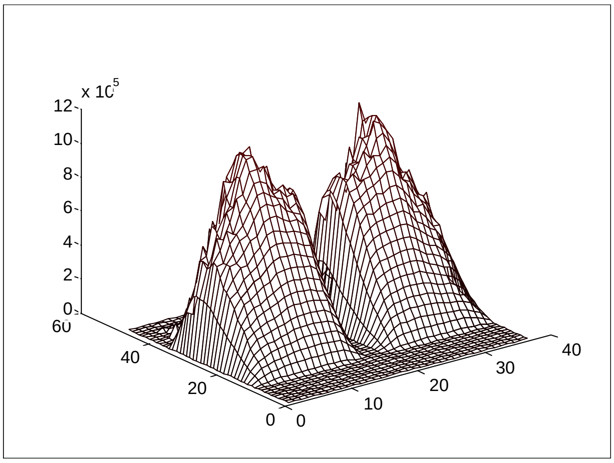

Fig. 5.4 A typical pressure distribution of oil lubricated journal bearing. (Unit: Pa)

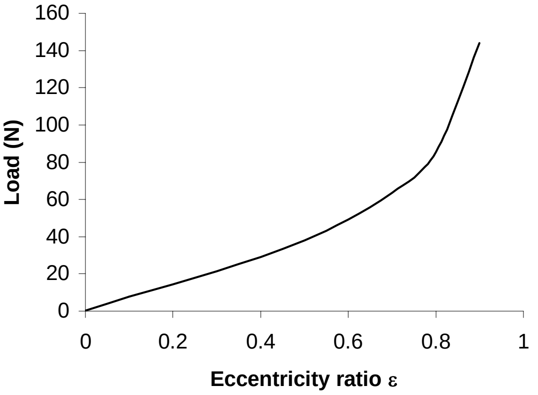

Fig. 5.5 (a) (continued)

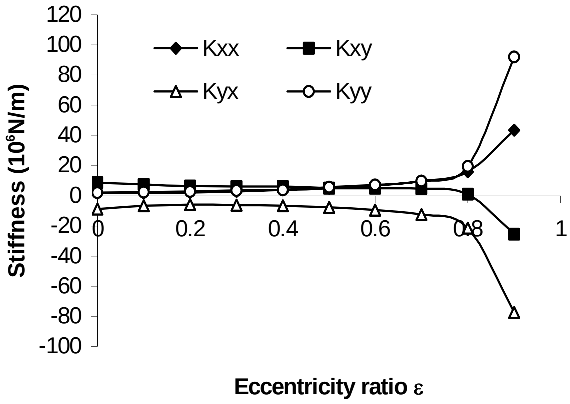

Fig. 5.5 Load capacity (a) and stiffness (b) versus eccentricity ratio for oil lubricated journal bearing in hybrid bearing system.

Air is selected as the lubricant for the thrust bearing of the hybrid bearing system. Unlike the journal bearing, increasing the diameter of the thrust bearing is practically feasible, and the reduction in the load capability and axial stiffness due to selecting air as the lubricant can be partly compensated by increasing its thrust plate diameter and partly by reducing the clearance between the thrust plate and its mating bearings. The increase of the thrust plate diameter lessens the reduction of clearance of the thrust bearing and, consequently, reduces the difficulty in the parts machining and the spindle motor assembly. At the comparable axial load capacity and axial stiffness conditions, the frictional loss of the thrust bearing using air as lubricant is much lower than that of a thrust bearing using oil as lubricant. As a result, the power loss of whole bearing system is reduced by about 20%. Figures 5.6(a) and (b) show the load capacity and axial stiffness of thrust bearings with oil and air as lubricant, respectively. In Fig. 5.6, the geometric parameters for the oil lubricated thrust bearing are: outer diameter of the thrust bearing *OD* = 9 mm, inner diameter *ID* = 4.5mm, axial clearance A_c = 12 μm, and lubricant viscosity μ = 19.5x10^{-3} Pa.s at 20 °C while the parameters for air lubricated thrust bearing are: *OD* = 18 mm, *ID* = 7 mm, A_c = 3 μm and μ = 18.08x10^{-6} Pa.s at 20°C. With these given parameters, the load capacity of the air thrust bearing is about 2.5 times lower than that of the oil thrust bearing as shown in Fig. 5.6(a). But the stiffness of the two thrust bearings are comparable. The stiffness of the air thrust bearing is only 5% lower than that of the oil thrust bearing as shown in Fig. 5.6(b). Figure 5.7 shows the energy consumption of different bearing systems. The upper curve in Fig. 5.7 represents the energy consumption of the pure oil lubricated bearing system while the lower curve represents the energy consumption of the hybrid bearing system.

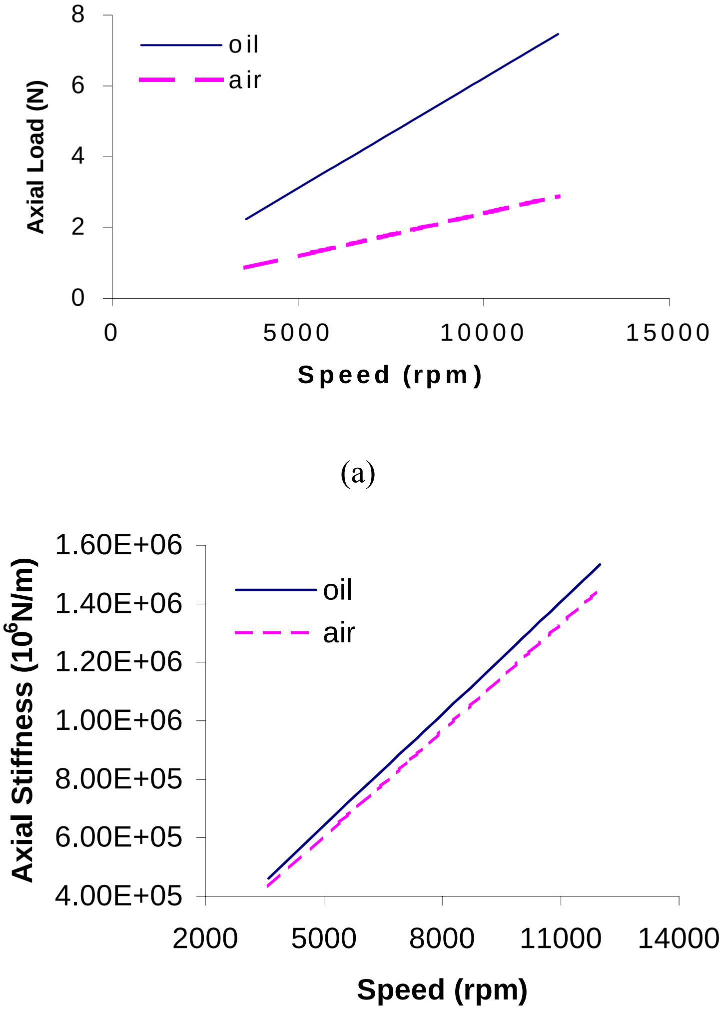

(a)

(b)

Fig. 5.6 Axial load capacity (a) and stiffness (b) of thrust bearing using oil and air as lubricant.

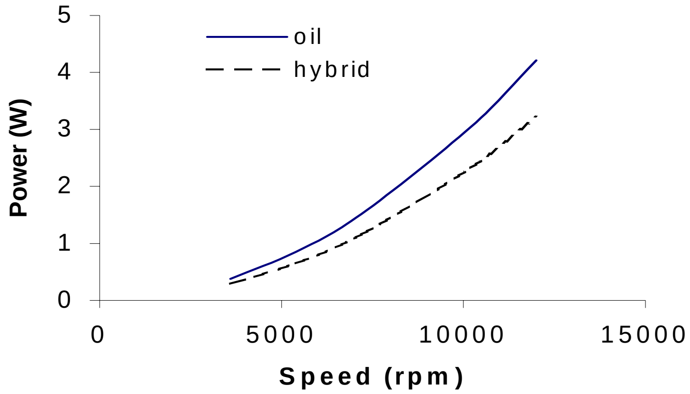

Fig. 5.7 Comparison of power consumption of different bearing systems.

Another unique feature in the hybrid bearing system design is that the thrust bearing is fixed to the sleeve instead of being fixed to the shaft and the thrust plate is in conical shape. This is based on the consideration of increasing the tilt stiffness of the spindle motor to prevent it from the wobble motion. Referring to Fig. 5.8, l is the distance between the centers of the forces generated by two journal bearings on the shaft, the tilt stiffness k_θ is directly related to the distance l by the following equation (Polch *et al.*, 1996):

$$k_\theta = kl/2, \tag{5.5}$$

where k is the journal bearing stiffness and θ is the angular tilt of the rotational axis between the upper and lower journal bearings. It is obvious from Eq. 5.5 that longer the l, the higher the tilt stiffness. When the thrust bearing is moved out of the shaft, the distance l is increased so that the tilt stiffness k_θ can also be increased. The design of conical thrust bearing also has its advantage. The horizontal component of thrust force has contribution to the tilt stiffness. Hence, the conical thrust bearing provides an additional moment to prevent the spindle wobble. Consequently, the spindle motor rotates at a more stable condition, which helps reduce RRO and NRRO of the spindle motor.

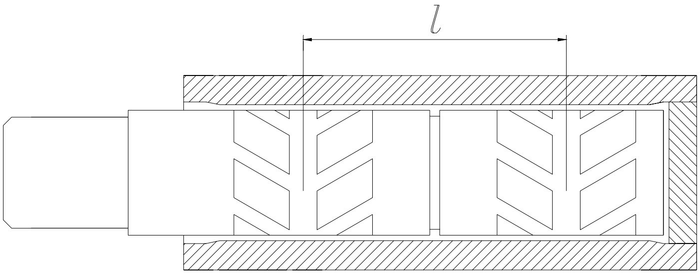

Fig. 5.8 Schematic of pressure center on journal bearing

The hybrid bearing design also provides a possible solution for discharging the static charges, which is a problem encountered in a fully air lubricated bearing system. It is well known; the magnetoresistive (MR) head is very sensitive to electrostatic charges accumulated in operation. In pure air bearing system, because of the poor conductivity of air, the hub and the base are electrically separated when spindle is in operation. The hybrid design may overcome this difficulty. With electrically conductive oil filled in the clearance of the journal bearing, the hub and the base of spindle motor are no longer electrically isolated, hence, an electrical path for discharging of electrostatic charges is provided in hybrid bearing system (see Fig. 5.1).

In the hybrid bearing system, the thrust bearing is air lubricated and only the journal bearing has sealing requirement. Since the thrust bearing is moved out of the sleeve of the journal bearing, the sealing length for capturing the oil lubricant within the journal bearing becomes longer, and therefore provides a more efficient sealing. So, the hybrid bearing design reduces the risk of lubricant leakage.

Chapter 6

BI-DIRECTIONAL ROTATING BEARING SYSTEM*

6.1 Introductory Remarks

To enhance the performance and increase the stability of the bearing systems, especially in light-load, high-speed applications, some grooves are engraved either on the moving surface or on the stationary surface of the bearings. Most fluid bearing systems for data devices consist of herringbone groove journal bearing(s) and herringbone or spiral groove thrust bearing(s). Almost all fluid bearing systems with grooves on the journal/thrust bearing surfaces are designed to rotate in a specified direction only. If the spindle motor is rotated in the opposite direction, the grooved fluid bearing system will have very small or even no load capacity, that is, it does not work if the rotational direction is reversed. This feature of fluid bearings somewhat limits their application. With the development of a bi-directional rotating fluid bearing spindle motor, such a limitation can be removed and many new applications will be possible (Kawabata *et al.*, 1989). In this chapter, a newly designed, bi-directional rotating fluid-bearing system is introduced, and its dynamic characteristics are numerically investigated and compared to those of one-directional rotating bearing system.

6.2 Characteristics of Bi-Directional Rotating Bearing System

The schematic diagram of a reversible rotating fluid bearing system assembly as well as the groove distribution of the reversible journal bearing and thrust bearing is

---

* Part of this chapter has been published in "Microsystem Technologies", v8, n4-5, pp. 271-277, 2002.

shown in Figs 6.1(a), (b) and (c), respectively. The shaft of the journal bearing is engraved with three regions of helix grooves. The surface of the shaft can be fully grooved or partially grooved as shown in Fig. 6.1(a), where L is the journal bearing length, D the diameter of the journal bearing, l_1 and l_2 are respectively the grooved and ridge area length along axial direction. If l_2 is equal to zero, it becomes fully grooved journal bearing. Otherwise, it is a partially grooved journal bearing. With such groove arrangement on the surface of journal bearing, there will always be one pair of groove regions that form the herringbone groove pattern to pump the lubricant into their center line to build up pressure and load capacity in the journal bearing regardless whether the spindle motor rotating clockwise or counterclockwise. Figure 6.1(b) shows the schematic diagram of the thrust bearing, which is engraved with several herringbone grooves that are bounded by two flat regions in the inner and outer edges of the thrust plate. It is expected that when the spindle rotates counterclockwise (view from top) the thrust bearing works as regular herringbone grooved thrust bearing. Since the lubricant is pumped from the inner and outer edges of the thrust plate to the center of the grooves, the highest pressure will be built up in the middle of thrust bearing which forms the pump-in working condition. When the spindle motor rotates clockwise, the lubricant is pumped out from the center of the grooves to the inner and outer edges of the thrust plate. The two flat regions at the edges of the plate provide a pressure dam for the lubricant and the highest pressure will be built up at the two circles that connect the groove region and ridge region. The assembly of journal bearing and thrust bearing is shown in Fig. 6.1(c).

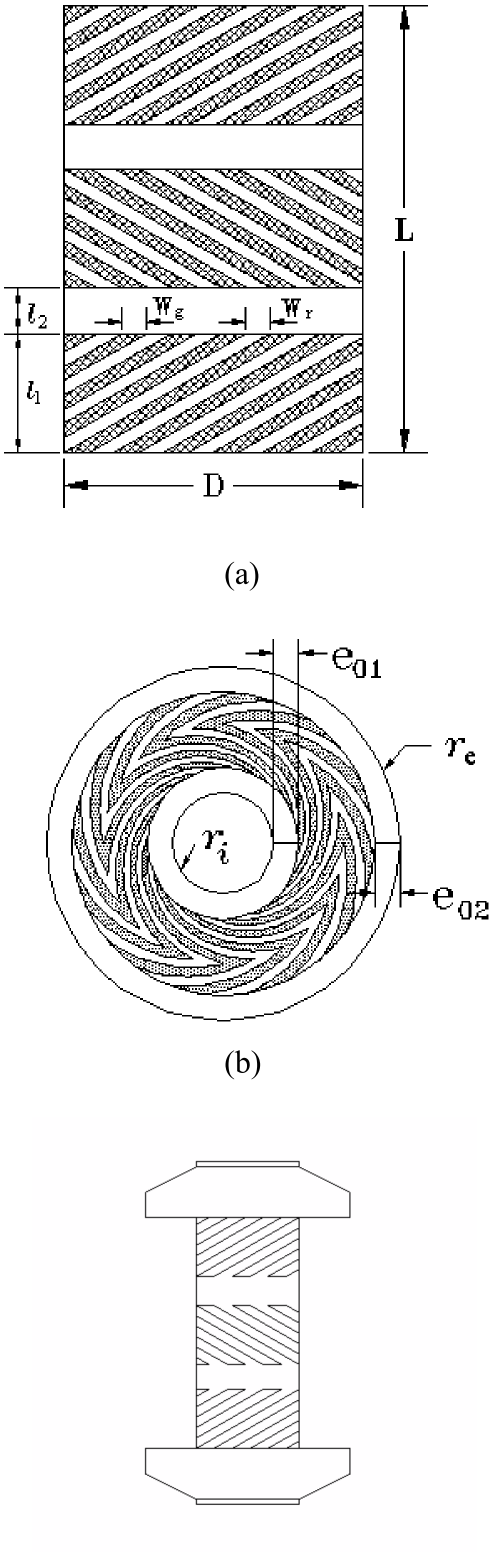

(a)

(b)

(c)

Fig. 6.1 Schematic of groove arrangement on journal bearing (a), thrust bearing (b) and assembly (c) of journal bearing and thrust bearing.

The journal bearing and the thrust bearing are assembled and matched in a specific way. That is, when the spindle motor rotates counterclockwise, the two groove arrays at the upper portion of the shaft form the pump-in herringbone grooves and a pressure peak will be built up in the ridge area between these two grooved regions. The grooves in the bottom region will, however, pump the lubricant to the lower edge of the shaft. To make use of this pump-out function, the thrust bearing at the lower end of the shaft is also designed for a pump-out condition, that is, the lubricant in the lower end of the thrust bearing is pumped-out to the inner edge and outer edge of the thrust plate. Therefore, another high-pressure region is setup in the inner edge of the lower thrust bearing. The working condition of the upper thrust bearing is, however, opposite to the lower thrust bearing, that is, it is working in a pump-in condition. The high pressure is built up at the middle area of the thrust bearing. If the spindle motor reverses its rotational direction, the pressure distribution in the bearings system is also changed concurrently.

The performance characteristics of fluid bearing, such as load capacity, stiffness and power consumption, are affected by many factors, such as bearing dimensions, groove patterns, lubricants, etc. (Zhang *et al*., 2001a, 2001b). To obtain a better understanding on such bi-directional rotating fluid bearing system, the effect of various design parameters on the dynamic characteristics of the bearing system is investigated numerically. The performance of the bearing system to be investigated takes the following parameters:

Nominal rotating speed N = 7,200 rpm;
Viscosity of lubricant $\mu = 30\text{x}10^{-3}$ Pa.S at 20°C;
Journal Bearing:
Length of journal bearing L = 9.0 mm;
Diameter of shaft D = 6.0 mm;

Nominal radial clearance $R_c = 5$ μm.
Thrust Bearing:
Inner radius of thrust plate $R_i = 3.0$ mm;
Outer radius of thrust plate $R_e = 6.0$ mm;

Using the above values, the effects of number of grooves N_g, groove angle α, groove width a_g and groove depth G_d, as well as the viscosity of the lubricant μ on the performance of the bearing system are investigated.

The results are presented in Figs. 6.2 - 6.7 for the journal bearing. Figure 6.2(a) and (b) show the effect of number of grooves on the load capacity of the journal bearing, for which curves 1 and 2 are respectively for fully grooved journal bearing rotating in counterclockwise and clockwise direction, while curves 3 and 4 are respectively for partially grooved journal bearing rotating in counterclockwise and clockwise direction. The same legend is also used for the other figures that show the results of the journal bearing. For zero eccentricity ratio ($\varepsilon = 0.0$), the effect of groove number is not clear as shown in Fig. 6.2(a), since different curves show different trends. But as clearly indicated in Fig. 6.2(b), the load capacity of the journal bearing decreases with increasing grooves at $\varepsilon = 0.4$. The same results are also observed at $\varepsilon =$ 0.1, 0.2 and 0.3 (not presented here). Figures 6.3(a) and (b) show the change of stiffness with the number of grooves, the same trend is observed as that of the load capacity. The variation of power consumption with the number of grooves is shown in Fig. 6.4(a) and (b). The power consumption is decreased with the increasing of groove number but the change of power consumption with the change of number of grooves is not very significant. Figures 6.2 – 6.4 also show that the partially grooved journal bearing has higher load capacity and higher radial stiffness than those of fully grooved journal bearing. Consequently, the power consumption of a partially grooved journal bearing is also higher than that of fully grooved journal bearing. Figures 6.5 – 6.7

show the effect of changing groove angle, groove width and the viscosity on the load capacity of the journal bearing. The load capacity reaches an optimum value at groove angle α ≈ 35° and the groove width ratio a_g = 0.6 as shown in Figs. 6.5 and 6.6 respectively. Figure 6.7 shows the linear effect of lubricant viscosity on the load capacity. The load capacity increases with increasing lubricant viscosity, as expected.

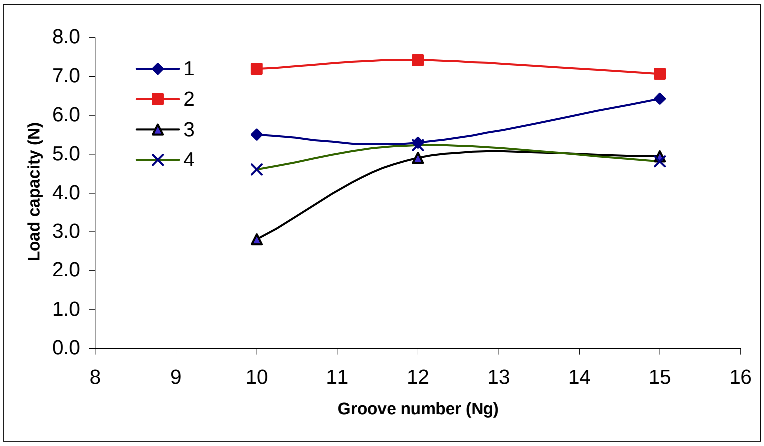

(a)

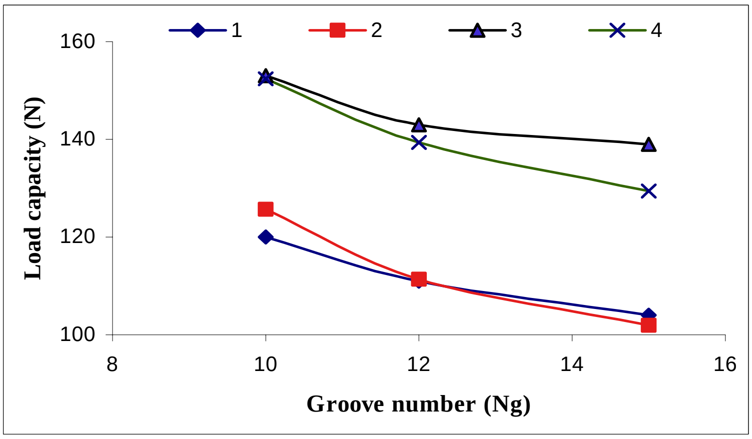

(b)

Fig. 6.2 Load capacity versus number of grooves at ε = 0.0 (a) and ε = 0.4 (b) for bi-directional rotating journal bearing.

Legend for Figs. 6.2 - 6.7:
1: Fully grooved journal bearing, rotating in CCW direction,
2: Fully grooved journal bearing, rotating in CW direction,
3: Partially grooved journal bearing, rotating in CCW direction,
4: Partially grooved journal bearing, rotating in CW direction.

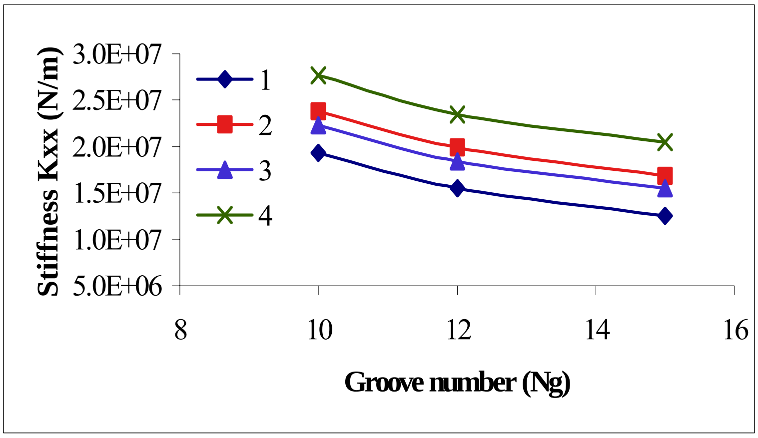

(a)

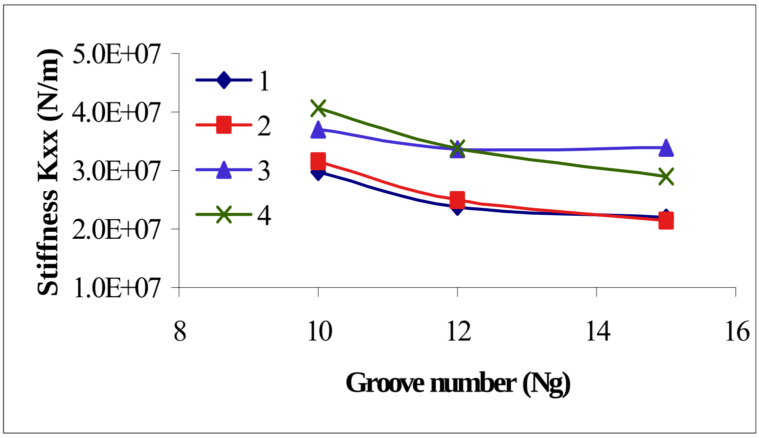

(b)

Fig. 6.3 Radial stiffness versus number of grooves at ε = 0.0 (a) and ε = 0.4 (b) for bi-directional rotating journal bearing.

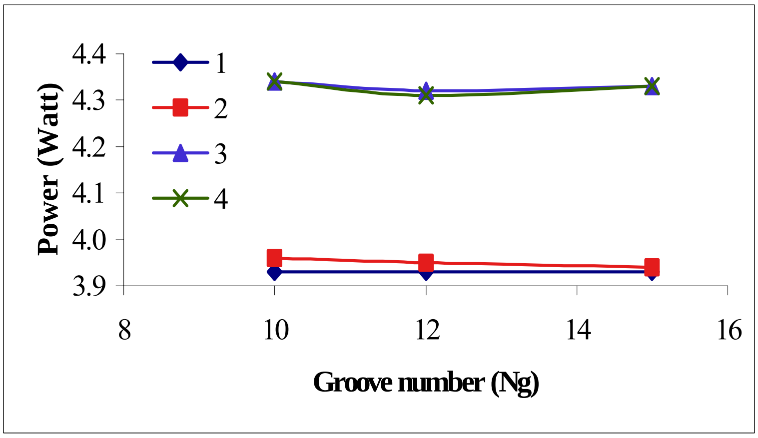

(a)

Fig. 6.4(a) Power consumption versus number of grooves at ε = 0.0 for bi-directional rotating journal bearing.

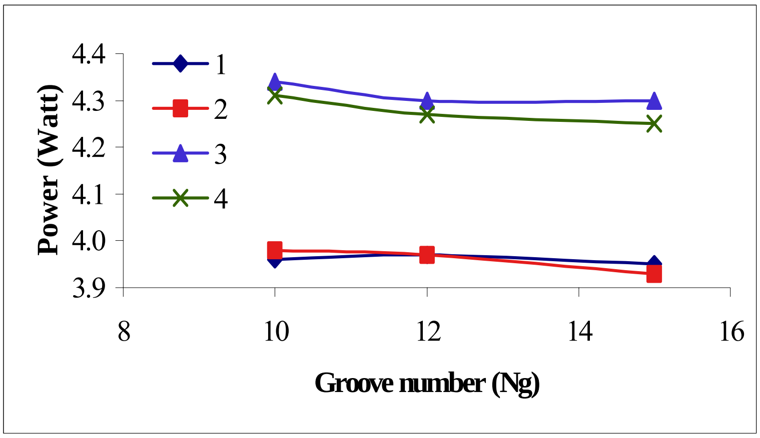

(b)

Fig. 6.4(b) Power consumption versus number of grooves at ε = 0.4 for bi-directional rotating journal bearing.

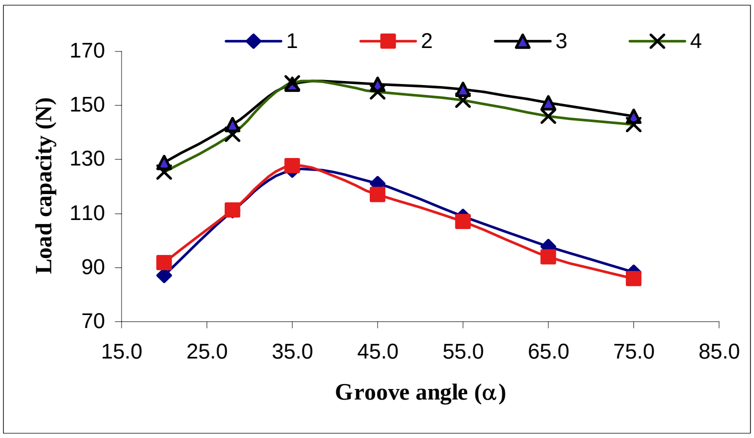

Fig. 6.5 Load capacity versus groove angle at ε = 0.4 for bi-directional rotating journal bearing.

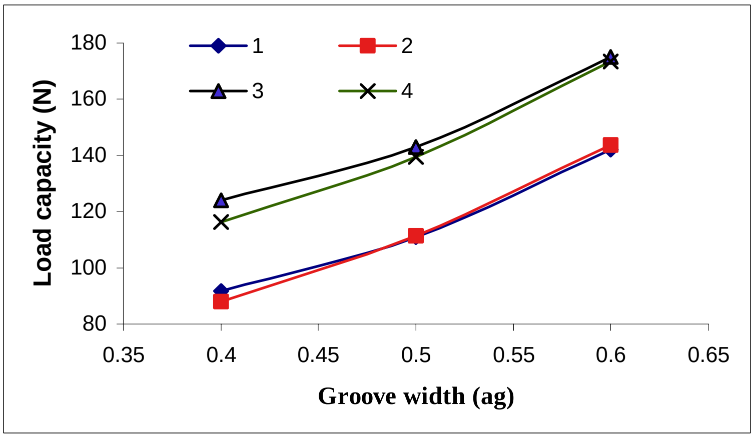

Fig. 6.6 Load capacity versus groove width at ε = 0.4 for bi-directional rotating journal bearing.

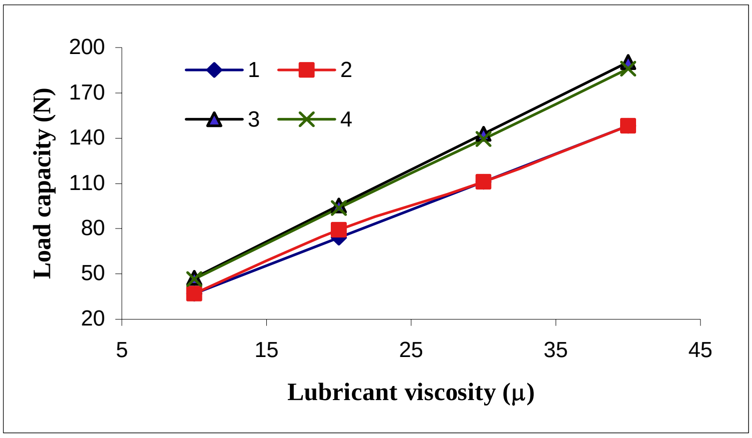

Fig. 6.7 Load capacity versus lubricant viscosity at ε = 0.4 for bi-directional rotating journal bearing.

A bi-directional rotating thrust bearing can be designed by engraving grooves on the surface of the thrust plate as shown in Fig. 6.1(b) such that regardless the rotational direction of the spindle motor, the same load capacity is achieved. It was found that the width of two flat regions located at the inner and outer edges of the thrust plate determines the performance of the thrust bearing when the spindle motor rotates in counterclockwise or clockwise direction. Figures 6.8, 6.9(a) and (b) show the gauge pressure distributions on a thrust plate. Figure 6.8 shows that when there is no flat region at the edges of the thrust plate, the pressure can only be built-up in one rotational direction (in this case, counterclockwise direction). If the rotational direction is reversed, the pressure built-up in thrust bearing will be negligible (not shown). However, with the help of two flat edges, it is possible to build-up the pressure when the motor is rotating in either direction. As shown in Fig. 6.9(a), the pressure profile is similar to that in Fig. 6.8, but it shrinks to the center region confined by the two strips when the motor rotates in the counterclockwise direction and only one pressure peak appears. However, when the motor spins in the clockwise direction, two pressure peaks appear at two circles that connect the groove region and the flat regions.

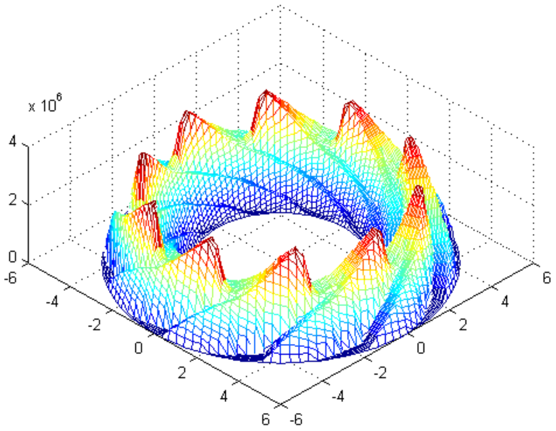

Fig. 6.8 Three-dimensional gauge pressure distribution of a uni-directional rotating thrust bearing (rotating in CCW direction, Unit: Pa).

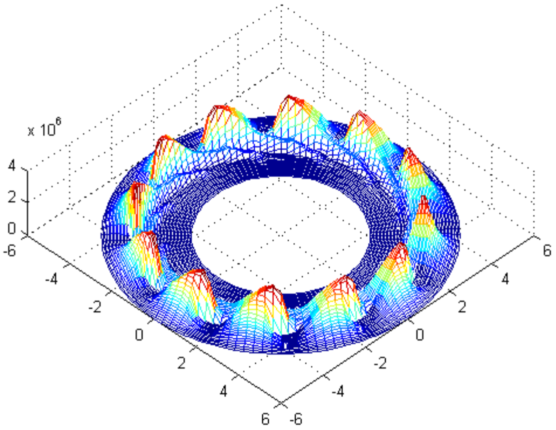

(a)

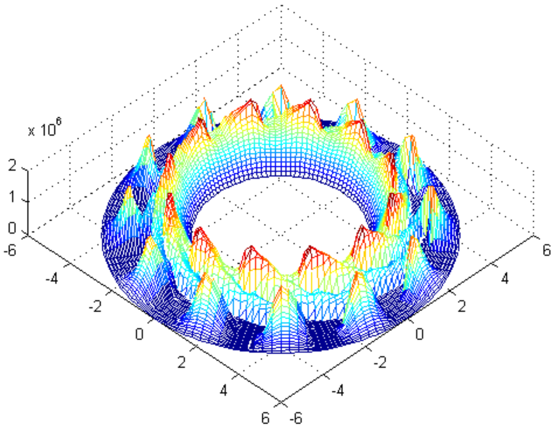

(b)

Fig. 6.9 Three-dimensional gauge pressure distribution of a bi-directional rotating thrust bearing rotating in CCW (a) and CW direction (b). (Unit: Pa)

The peak pressure value of the clockwise rotating thrust bearing is almost half of that of counterclockwise rotating one, as shown in Figs. 6.9(a) and (b), respectively. The load capacity versus the edge width of thrust bearing is plotted and compared in Fig. 6.10 for the counterclockwise and clockwise rotations. It is observed that with increasing edge width, the load capacity for counterclockwise rotation (pump-in) decreases very fast and it is relatively slow for the load capacity increases in clockwise rotation (pump-out). When the edge width reaches the level of almost 30% of the bearing surface, the load capacities of the counterclockwise and clockwise rotations are almost the same. The values of edge width and load capacity are listed in the Table 6.1.

The effect of changing parameters that control the groove pattern was also investigated as presented in Figs. 6.11 – 6.15. The groove depth, which has a relatively larger effect on the load capacity of the thrust bearing, is first investigated. Figure 6.11 shows the curves of the load capacity versus the groove depth G_d with the values from 3 to 20 μm at different axial clearances. It was found that for all values of the axial

Table 6.1 Load capacity of bi-directional rotating thrust bearing versus edge width

e_{01} mm	e_{02} mm	CCW W (N)	CW W (N)
0.0	0.0	339	7.0
0.1	0.1	288	38
0.2	0.2	249	46
0.3	0.3	233	52
0.4	0.4	188	59
0.5	0.5	157	64
0.6	0.6	137	67
0.7	0.7	106	73
0.8	0.8	89	73
0.9	0.9	80	72
0.9	0.95	74	72

clearances, the load capacity reaches a maximum value when $G_d = 3.0A_c$. For example, if the axial clearance takes a value of $A_c = 3.0$ μm, the maximum load is obtained at $G_d = 9.0$ μm. Then, with $A_c = 3.0$ μm and $G_d = 3.0A_c = 9.0$ μm, the effect of groove number, groove angle and groove width are investigated. The load capacity of the thrust bearing also decreases with increasing number of grooves as shown in Fig. 6.12. This is different from the uni-directional rotating thrust bearing in which the load capacity is increased with the increasing of groove number. The load capacity exhibits a maximum value at groove angle α = 15° as shown in Fig. 6.13.

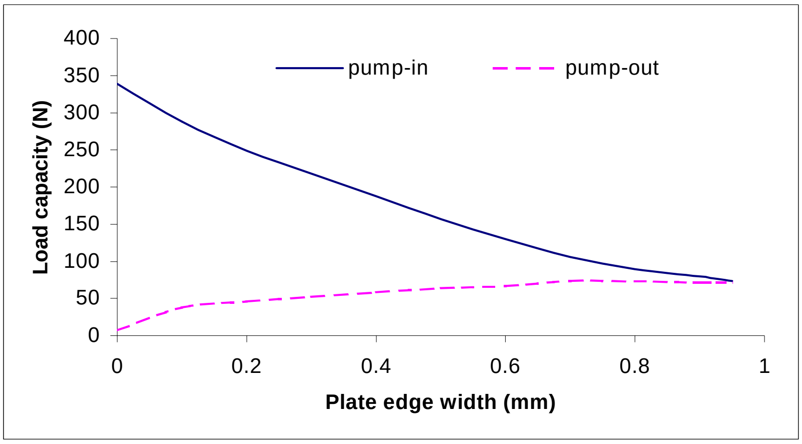

Fig. 6.10 Edge width effect on load capacity of bi-directional rotating thrust bearing.

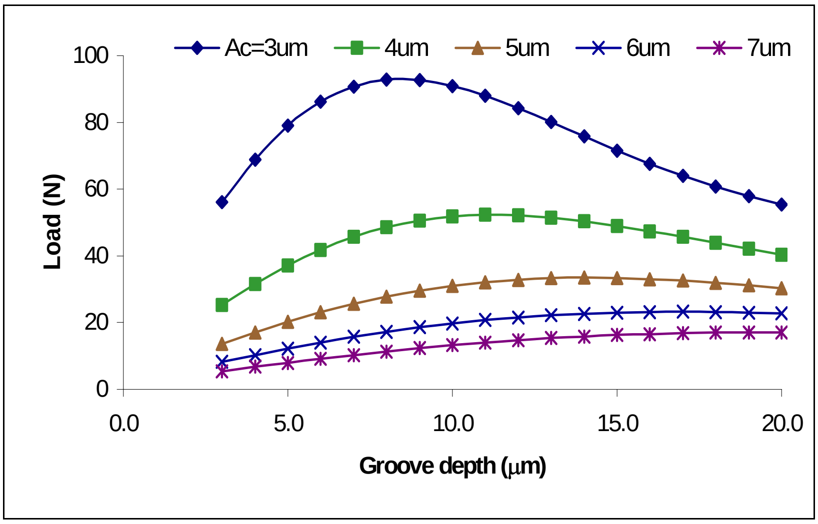

Fig. 6.11 Load capacity versus groove depth at different axial clearances for bi-directional rotating thrust bearing.

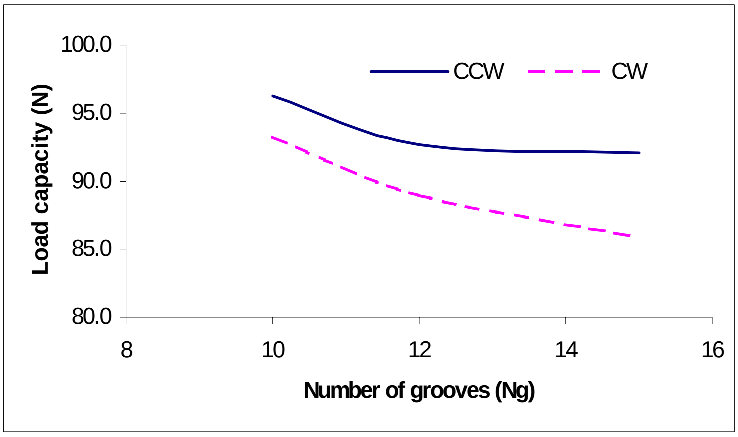

Fig. 6.12 Load capacity of bi-directional thrust bearing versus number of grooves at $A_c = 3.0$ μm.

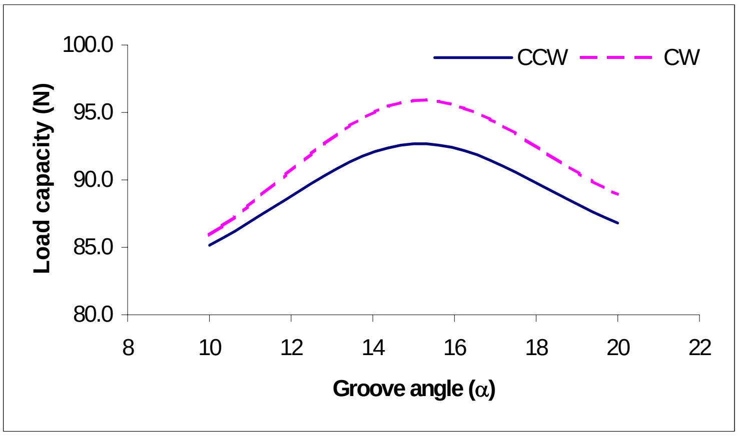

Fig. 6.13 Load capacity of of bi-directional thrust bearing versus groove angle at $A_c = 3.0$ μm.

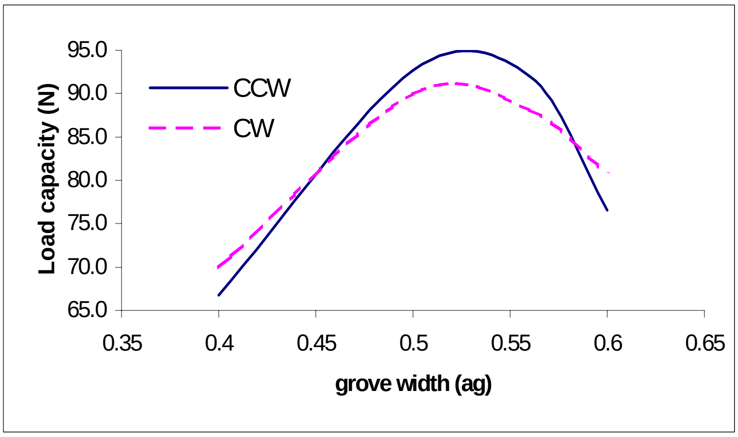

Fig. 6.14 Load capacity of bi-directional thrust bearing versus groove width.

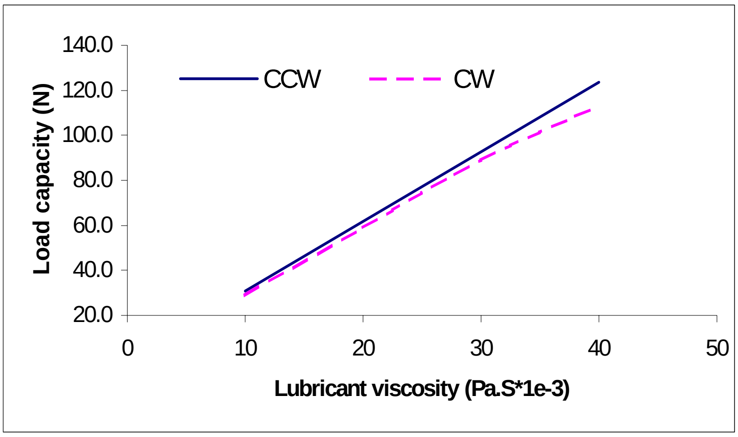

Fig. 6.15 Load capacity of of bi-directional thrust bearing versus lubricant viscosity at $A_c = 3.0$ μm.

The optimum value of groove width a_g is around 0.5 where the load capacity is higher than that in other cases (Fig. 6.14). The effect of lubricant viscosity on the axial load capacity is shown in Fig. 6.15.

The dynamic characteristics of bi-directional rotating bearing system is also compared with the one-directional rotating bearing system that takes the same geometrical parameters as those in the bi-directional bearing system. Figures 6.16 – 6.17 show the differences between these two configurations of bearing system. Referring to Fig. 6.16(a), for journal bearing with the ratio of $L/D = 1.5$, the load capacity of the bi-directional rotating bearing is almost 83.7% ($\varepsilon = 0.4$) of that of the one-directional rotating bearing as shown in Fig. 6.16 by the curve 1 (bi-directional) and curve 2 (one-directional $L = 9$ mm) respectively. Reducing the ratio of L/D to 1.0 for one directional rotating bearing, but keeping the ratio of $L/D = 1.5$ for the bi-directional rotating, that is, the length of the bi-directional rotating bearing is 50% longer than that of the one-directional rotating bearing, then, the load capacity of the bi-directional journal bearing is about 76.0% higher than that of the one-directional journal bearing, as shown in Fig. 6.16(a) by curves 1 and 3. Figure 6.16(b) compares the power consumption of these two types of journal bearing. In Fig. 6.16(b), curve 1 shows the power consumption of the bi-directional rotating journal bearing (CCW direction) while curve 2 (*L/D* = 1.5) and 3 (*L/D* = 1.0) represent the power consumption of the one-directional journal bearing at different *L/D* ratio. The power consumption of the bi-directional journal bearing is 102% (for *L/D* = 1.5) and 150% (for *L/D* = 1.0) of that of the one-directional journal bearing.

The case for the thrust bearing is slightly different from that of the journal bearing. By increasing the diameter of the thrust bearing, the load capacity of the reversible thrust, can of course, reach the same level as the one-directional bearing but the power consumption is also greatly increased. For a similar load capacity, the power consumption of bi-directional thrust bearing is almost 3.9 times of that of the one-directional bearing if we just depend on increasing the diameter of the reversible rotating thrust bearing. Obviously, the increment of the power consumption is too high by increasing the diameter of the thrust bearing, therefore, this approach is not recommended. Another method to increase the load capacity of the thrust bearing is to reduce its axial clearance. Figure 6.17(a) shows the load capacity of both bi-directional and one-directional thrust bearing rotating in counterclockwise direction but at different axial clearances. Curve 1 in Fig. 6.17(a) shows the variation of load capacity versus the groove depth for bi-directional thrust bearing at axial clearance 3 μm and curve 2 shows the same variation for one-directional thrust bearing at axial clearance 5 μm. It is observed that for the same diameter, the load capacity of the bi-directional rotating thrust bearing at axial clearance 3 μm is about 76% of that of the one-directional rotating thrust bearing at axial clearance of 5 μm when both thrust bearings reach their optimum condition. The power consumption of the two type thrust bearings is plotted in Fig. 6.17(b), for a comparable load capacity, the power consumption of the bi-directional thrust bearing is almost 2.0 times of that of the one-directional thrust bearing. The axial stiffness of the bi-directional thrust bearing is, however, 1.3 times higher than that of the one-directional thrust bearing. In most high-speed application, the axial load is very small and load capacity is usually not a problem. The stiffness instead of the load capacity is the major concern in the design of fluid bearing system. Therefore, the design having relatively lower load capacity but higher stiffness is acceptable. Adding the power consumption of the journal bearing and of the thrust bearing together, the total power consumption of the bi-directional rotating fluid bearing system is 52% higher than that of the one-directional rotating fluid bearing system. The design parameters and the dynamic characteristics of both bearing systems are listed in Table 6.2.

6.3 Discussion and Conclusions

A bi-directional rotating fluid bearing system has been introduced. Its dynamic characteristics have been investigated numerically and compared with those of one-directional rotating fluid bearing system. From the comparison, it can be concluded that: it is possible to design bi-directional rotating fluid bearing systems that have a comparable load capacity and stiffness as those of one-directional rotating fluid bearing systems. The power consumption of such bi-directional rotating fluid bearing system is almost 50% higher than that of the one-directional rotating fluid bearing system if both bearing systems take the same dimensions. However, the bi-directional rotating fluid bearing system provides us the freedom to rotate the spindle motor in both clockwise and counterclockwise directions, and hence, may widen the application range of such fluid bearing system.

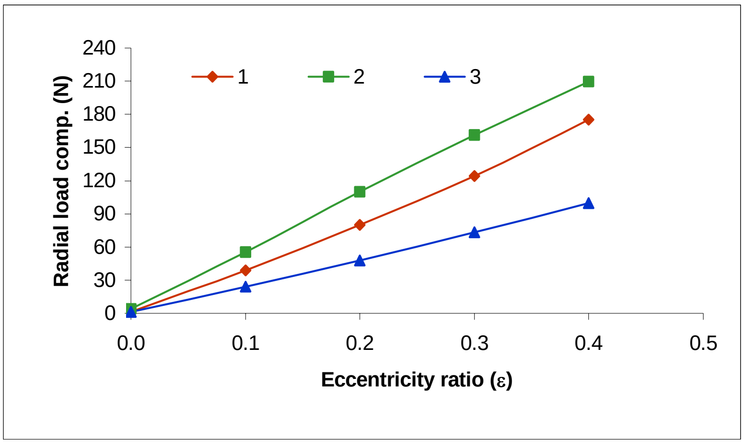

(a)

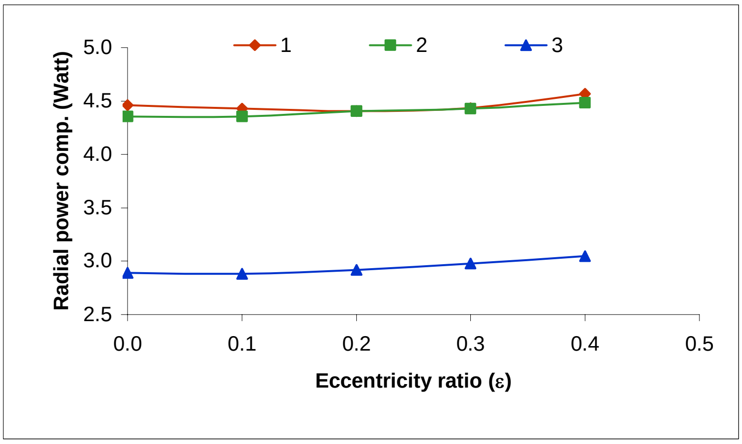

(b)

Fig. 6.16 Comparison of load capacity (a) and power consumption (b) between uni-directional and bi-directional rotating journal bearings in CCW direction rotation.
Legend: 1) Bi-directional *L/D* = 1.5,
2) Uni-directional *L/D* =1.5,
3) Uni-directional *L/D* = 1.0.

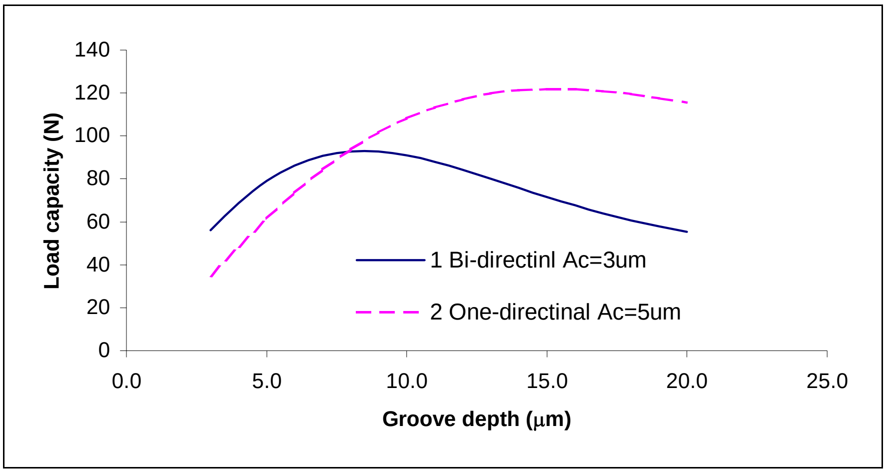

(a)

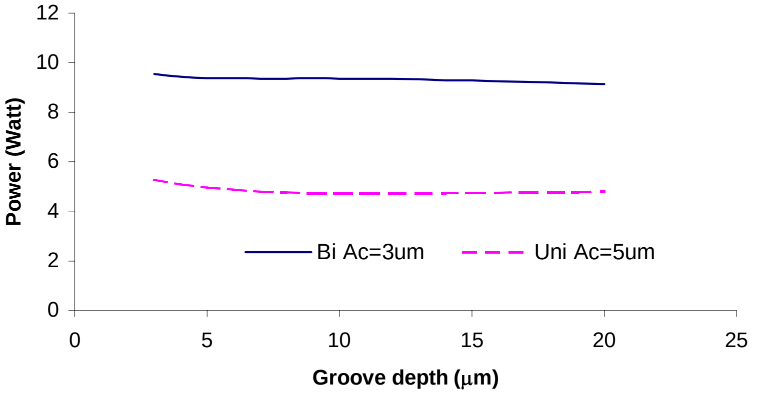

(b)

Fig. 6.17 Comparison of load capacity (a) and power consumption (b) between uni-directional rotating and bi-directional rotating thrust bearings in CCW direction rotation.

Table 6.2 Load, stiffness and power comparison of two types of bearing systems

	Journal bearing		
	Load capacity		
ε	Bi_CCW	Uni_L/D=1.5	ratio
0.0	1.431	4.23	0.338
0.1	38.70	5.53x10	0.700
0.2	79.92	1.10x10^{2}	0.726
0.3	124.20	1.61x10^{2}	0.770
0.4	175.40	2.10x10^{2}	0.837
	Bi_CCW	Uni_ L/D=1.0	
0.0	1.431	1.40	1.022
0.1	38.70	2.40x10	1.613
0.2	79.92	4.80x10	1.665
0.3	124.20	7.32x10	1.697
0.4	175.40	9.96x10	1.761
	Power consumption		
ε	Bi_CCW	Uni_L/D=1.5	ratio
0.0	4.567	4.36	1.048
0.1	4.453	4.36	1.022
0.2	4.407	4.41	1.000
0.3	4.432	4.43	1.000
0.4	4.565	4.48	1.018
	Bi_CCW	Uni_L/D=1.0	
0.0	4.567	2.89	1.580
0.1	4.453	2.88	1.546
0.2	4.407	2.92	1.509
0.3	4.432	2.98	1.487
0.4	4.565	3.05	1.497
	Stiffness (K_{xx})		
ε	Bi_CCW	Uni_L/D=1.5	ratio
0.0	3.04x10^{7}	4.03x10^{7}	0.755
0.1	2.54x10^{7}	4.15x10^{7}	0.612
0.2	3.23x10^{7}	4.63x10^{7}	0.697
0.3	4.27x10^{7}	6.20x10^{7}	0.689
0.4	5.90x10^{7}	7.33x10^{7}	0.805
	Bi_CCW	Uni_L/D=1.0	
0.0	3.04x10^{7}	2.62x10^{7}	1.161
0.1	2.54x10^{7}	2.70x10^{7}	0.941
0.2	3.23x10^{7}	2.90x10^{7}	1.113
0.3	4.27x10^{7}	3.31x10^{7}	1.291
0.4	5.90x10^{7}	3.90x10^{7}	1.512
	Thrust bearing		
	Bi_T (CCW)	Uni_T	ratio
W	92.77	121.93	0.761
P	9.35	4.75	1.968
K_{zz}	6.57x10^{7}	4.83x10^{7}	1.361

Chapter 7

DEVELOPMENT AND TEST OF FLUID BEARING SPINDLE MOTOR PROTOTYPES[*]

Two types of fluid bearing spindle motor prototypes are designed, fabricated and measured. This chapter will address some design issues and present the measurement results of the prototypes developed.

7.1 Prototype of Hydrodynamic Bearing Spindle

As mentioned previously, one of difficulties of developing hydrodynamic bearing spindle motor is the sealing of lubricant, especially for the applications where neither lubricant leakage nor adding lubricant into the bearing system is allowed. For example, if a spindle motor with hydrodynamic bearing is used in a hard disk drive, the lubricant leakage will cause the contamination of disk surfaces and results in failure of whole hard disk drive (Zhang and Koka, 1999). Furthermore, since it is impossible to add lubricant into the spindle motor, the lubricant leakage also causes the performance degradation of the spindle motor, consequently, a gradual degradation of the hard disk drive and finally total failure of the hard disk drive. In recent years, many fluid-bearing spindle motors have been developed. However, there are still some problems to be solved before a large-scale application of fluid bearing spindle in hard disk drives. Lubricant leakage is one of the major problems for the implementation of fluid bearing spindle motor in hard disk drives.

---

[*] Part of this chapter has been published in *IEEE Trans. on Magnetics*, v37, n2, pp. 805-809 and v37, n4, pp. 2647-2650, 2001.

In the following sections the design steps and considerations of developing a high-speed spindle motor that employs ferro-fluid as the bearing lubricant will be addressed and discussed. The bearing system to be developed possesses a compound seal system consisting of a magnetic seal and a viscous pumping seal in its leakage-free high-speed bearings. The intention is to take the advantages of hydrodynamic oil-film bearings with higher load capacity, higher stiffness and higher damping coefficients and at the same time, tackle the lubricant leakage problem by using the compound seal. The prototypes were fabricated and continuously run at 20,000 rpm for more than two months. The test results show that the prototypes did not suffer any lubricant leakage and had very low non-repeatable run out as well as lower acoustic noise. Hence, the developed ferro-fluid bearing spindle motor is a promising alternative to conventional ball bearing spindle motors.

7.1.1 Specifications

Different companies have different specifications for spindle motors used in hard disk drives and they are usually confidential. Therefore, the following specifications only provide a basic guideline for the design of spindle motors presented in the thesis. The major specifications of the spindle motor for a 2.5 inch format disk drive are:

Disk drive format:	2.5 inch
Height:	22 mm
Disks to be carried:	2 - 5 disks (max)
Operating speed	20,000 rpm
Motor topology:	3 phase (BLDC)
Supply voltage	12 V ±5%

Back emf (line)	7.6 V max.
Starting current	≤ 2.0 A
Starting Torque	$6.2\text{x}10^{-3}$N•m at $I_s = 1.7$ A
Run-up time	≤ 15 sec.
Non Repeatable Run- out	≤ 0.025 μm (1 μinch)
Acoustic noise	≤ 30 dB(A) (1 meter)
Operating temperature	0°C - 70°C max.
Projected MTBF	100,000 hrs
Unbalanced mass	3 gram-mm (max).

The spindle motors used in hard disk drives have two basic structural configurations for electrical motor, namely, motor-in-hub and motor-under-slung. The motor that has an in-hub structure is commonly used for the high capacity disk drives to carry about 4 to 10 disk platters. The motor that has under-slung structure usually carries fewer disks than that of the motor-in-hub. However, with the improvement of magnetic head and the actuator in hard disk drives, the gap between two adjacent disks is reduced. Hence, the spindle motors with the structure of motor-under-slung can also carry up to 5 disks.

7.1.2 Determination of shaft diameter of journal bearing

Journal bearing serves the function of guiding rotational motion and undertaking radial load of spindle motors no matter whether the spindle motor is set in vertical position or horizontal position. The journal bearing should also provide sufficient stiffness in the radial direction to resist any external disturbance and shock during operation. The performance of journal bearing will determine the level of radial non-repeatable run out of the spindle motor. Hence, the design of fluid bearing system usually starts from journal bearing.

To design a journal bearing system, first of all, the diameter of the shaft of the spindle motor should be determined. The minimum diameter of the shaft can be determined by the following expression (Beijing, 1988):

$$d \geq A\sqrt[3]{\frac{P}{N}} \text{ (mm)} \tag{7.1}$$

or, for hollow shaft

$$d \geq A\sqrt[3]{\frac{P}{N}}\sqrt[3]{\frac{1}{1-\gamma^4}} \text{ (mm), and } \gamma = \frac{d_0}{d} \tag{7.2}$$

where *P* is the power to be transmitted by the shaft (kw), *N*, revolution speed of the spindle motor (rpm), *A*, a coefficient of material properties, *D*, diameter of the shaft (mm) and d_0, diameter of the concentric hole (mm) along the shaft as shown in Fig. 7.1.

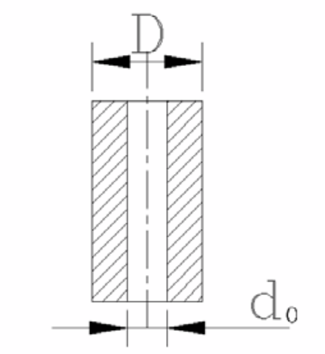

Fig. 7.1 Shaft diameter of journal bearing.

Assuming the power transmitted by the shaft is $P = 10(w) = 1 \times 10^{-2}(kw)$, the rotational speed of the spindle motor is N_s = 20,000 rpm, the shaft is solid and the value of *A* is 168. *A* is a constant that has different values for different materials. Here, for safety reason, *A* has been given the largest value among all materials.

Substituting the above values into Eq. (7.1), the diameter of the shaft should be

$$d \geq 168 \times \sqrt[3]{\frac{1\times 10^{-2}}{20000}} = 1.334(mm) \cong 1.4(\mathrm{mm}).$$

To drill a concentric hole along the shaft, let the diameter of the hole be half of the diameter of the shaft, then

$$\gamma = \frac{d_0}{d} = \frac{1}{2}, \quad \text{and} \quad \sqrt[3]{\frac{1}{1-\gamma^4}} = \sqrt[3]{\frac{1}{1-(1/2)^4}} = 1.0217.$$

Hence, the new diameter of the shaft should be $D \geq 1.022 \text{ x } 1.4 = 1.43$(mm). Taking $D \geq 4$ mm, the shaft will have enough strength to transfer the necessary power of driving spindle motor, even if there is a 2.0 mm diameter hole drilled along the axis of the shaft.

7.1.3 Determination of minimum clearance

The dynamic performance of a fluid journal bearing is closely related to the clearance of the bearing. Prior to calculation of the load capacity of journal bearing, the minimum clearance between the shaft and its mating sleeve should be determined. According to Constantinescu *et al.* (1985), the relative clearance Ψ can be approximately expressed as the function of relative translatory velocity *V*, that is: (Refer Fig. 7.2)

$$\Psi = 0.8 \times \mathrm{V}^{0.25} \times 10^{-3} \tag{7.3}$$

where Ψ is the relative clearance and *V* is the relative translatory velocity (in m/s).

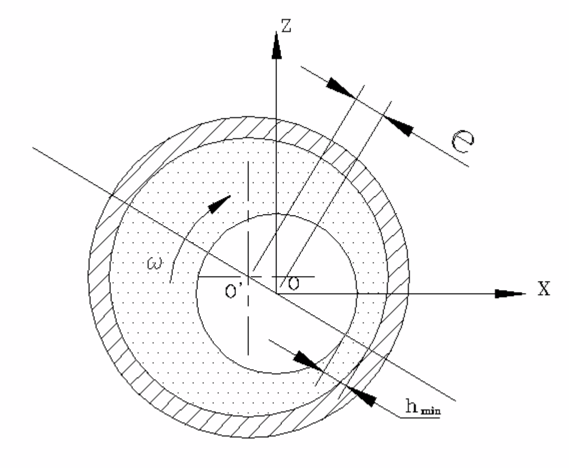

Fig. 7.2 Schematic of bearing clearance.

For a given speed N_s = 20,000 rpm, $\omega = 2\pi\ N_s /60 = 2 \text{ x } 3.14 \text{ x } 20000/60 =$ 2094 rad/sec. Let us choose the diameter of the shaft to be D_1 = 4 mm or D_2 = 5 mm. The corresponding values of the relative translatory velocities are:

$V_1 = r_1 {*}\omega = 2512$ mm/s = 2.512 m/s, $V_2 = r_2 {*}\omega = 3140$ mm/s = 3.140 m/s.

Consequently, the corresponding values of the relative clearances are:

$\Psi_1 = 0.8 \times 2.512^{0.25} \times 10^{-3} = 1.007 \times 10^{-3}$ $\Psi_2 = 0.8 \times 3.14^{0.25} \times 10^{-3} = 1.065 \times 10^{-3}$

$c_1 = \psi_1 r_1 = 1.007 \times 10^{-3} \times 2$ $c_2 = \psi_2 r_2 = 1.065 \times 10^{-3} \times 2.5$

$= 2.014 \times 10^{-3}$ mm ≅ 2.0 μm. $= 2.663 \times 10^{-3}$ mm ≅ 2.66 μm.

Here, c_1 and c_2 represent the minimum value of bearing clearance at $\varepsilon = 0$ between the shaft and the sleeve. The practical clearance should be greater than c_1 and c_2.

7.1.4 Selection of lubricant

In selecting a lubricant, its properties such as thermal stability, kinematic viscosity, flash point, oxidative stability and vapor pressure, etc. should be considered carefully (Khan and Rudd, 1998). It should have higher flash point, lower vapor pressure, excellent thermal and oxidative stability. Among the available lubricants, the phosphate esters, which is a synthetic lubricant, possesses the required properties as mentioned above (Bhushan, 1996). Therefore, a phosphate esters based ferrofluid was selected as the lubricant for the bearing system. Its dynamic viscosities μ are 30×10^{-3} Pa.s at 20 °C and 10×10^{-3} Pa.s at 60 °C.

Since the operating temperature range is from 0 to 70°C, the viscosity of lubricant at different temperatures can be estimated by using the viscosity-temperature equation (Stepina, 1992):

$$\mu = \rho(e^{A/T^m} - C) \tag{7.4}$$

where μ is the dynamic viscosity and ρ is density of lubricant, T is temperature in °C, A and m are constants determined by two known values of viscosity at known temperature. $C = 0.8$ is a constant.

7.1.5 Design of bearing system

According to the allowable unbalanced mass and the rotational speed specified in section 7.1, the radial load capacity of the journal bearing should be

$$W_R = ma_r = mu^2/r = mr\omega^2 = 3 \text{ x } 10^{-6} \text{ x } (20000 \text{ x } 2\pi/60)^2 = 13.2 \ (N) \tag{7.5}$$

In the axial direction, the load includes the weight of the rotational portion of the spindle motor plus its load consisting of five 2.5” disks, spacers, disk clamper and four to six small screws as well as the load of magnetic heads on the disk surfaces. Therefore, the total axial load is

$$W_A \approx 2.0 \ (N) \tag{7.6}$$

The radial and axial stiffness should be equal to or greater than $5\text{x}10^6$ (*N/m*) for the spindle motor to be designed (the stiffness value is deduced from ball bearings). The spindle motor should first meet the above load capacity and stiffness specifications, and at the same time, has as lower as possible power consumption.

A good spindle motor should also possess the characteristics of lower non-repeatable run out, lower acoustic noise, and higher shock-resistance capability. However, some of these requirements are contradicting, especially for a fluid bearing spindle motor. For example, higher stiffness of the bearing system results in lower non-repeatable run-out but causes higher power loss. Higher viscosity of lubricant enables higher load capacity and stiffness of bearing system but makes the performance of bearing system vulnerable to the changes of working temperature. Besides the considerations of bearing dynamic characteristics, the difficulty in machining of and the cost of bearing parts should also be considered carefully. Tighter tolerance specifications for parts machining necessitate high precision machining and, of course, ensure the required performance of the assembled spindle motor. But it inevitably causes higher cost for the final products. All of these contradictory requirements have to be carefully considered and balanced.

The performance of the fluid bearing is affected by many parameters. Using Taguchi method, the final optimal parameters in terms of the highest ratio of K_{rr}/P for the journal bearing were selected:

$D = L = 3.5$ mm; $C = 4$ μm; $\mu = 19.5\text{x}10^{-3}$ Pa*s at 20 °C, $G_d = 1.2$ and $\alpha = 28.4$ °

Figures 7.3(a) – (c) show the variation of stiffness, load capacity and power consumption with eccentricity ratios of the bearing system with the above design parameters at rotational speed of 20,000 rpm and environmental temperature of 20 °C. Figure 7.3 (a) showed that for all eccentricity ratios the radial stiffness of K_{xx} and

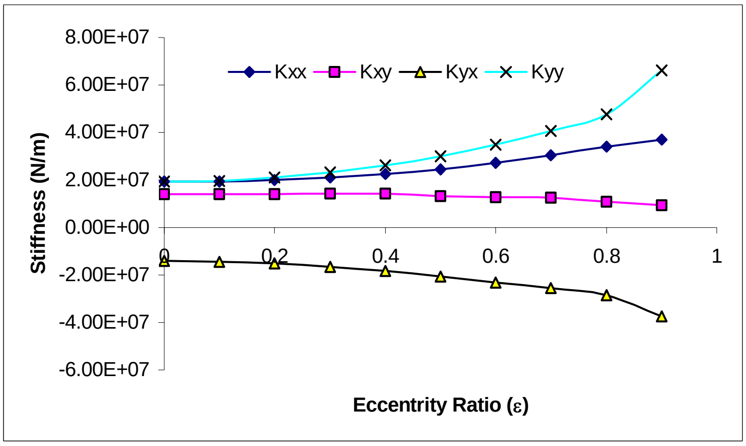

(a)

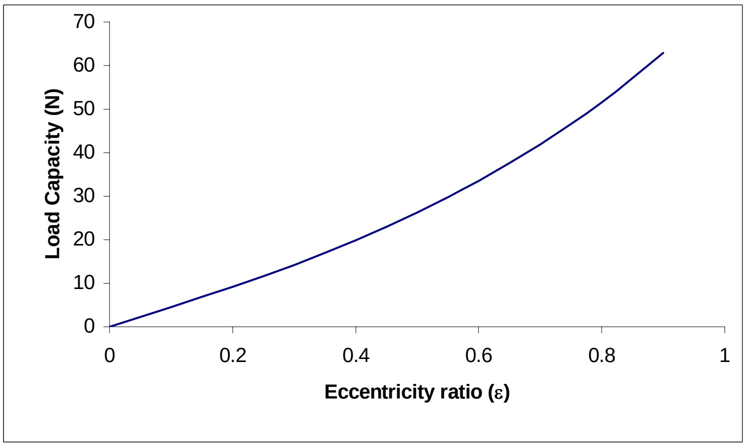

(b)

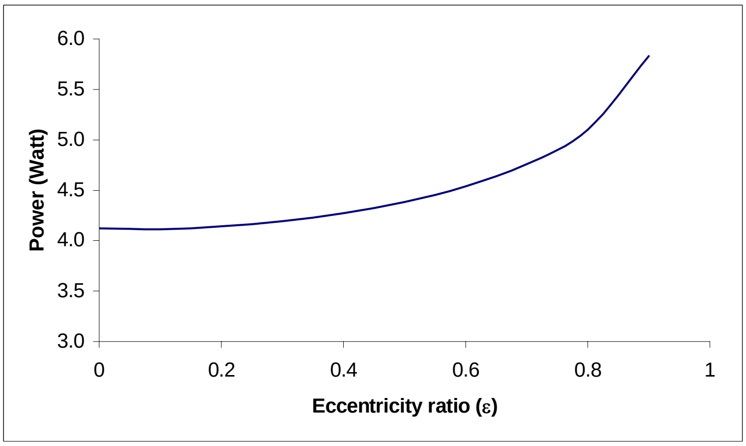

(c)

Fig. 7.3 Stiffness (a), load capacity (b) and total power loss (c) of ferro-fluid bearing system at different eccentricity ratios.

K_{yy} were equal to or greater than 2.0×10^7 (*N/m*). The load capacity was around 15 (*N*) at eccentricity ratio $\varepsilon = 0.3$ as shown in Fig. 7.3(b). From Figs. 7.3(a) and 7.3(c), it is also evident that for the range of eccentricity ratio ε from 0 to 0.3, the variations of the radial stiffness and total power consumption of the bearing system are quite small, and the curves are almost flat. That is, for a small range change in radial load, there will be no obvious change in the spindle motor performance. In addition, a low viscous ferro-fluid was selected as the lubricant of the bearing system to achieve a better bearing stability and robustness due to temperature changes.

7.1.6 Design of bearing sealing system

A reliable sealing system to prevent lubricant leakage from the bearing system is necessary to be incorporated in the design procedure of fluid bearing spindle motor for hard disk drives because of the strict requirement to prevent contamination in hard disk drives. To minimize lubricant leakage and achieve a "zero" leakage condition, a compound sealing system which consists of a magnetic seal and a viscous pumping seal was proposed and designed for the bearing system as shown in Fig. 7.4. The viscous pumping seal prevents lubricant from leakage when the motor is in operation while the magnetic seal keeps lubricant within the bearing when motor is at rest. A reservoir was also added to the sealing system to accommodate the extra volume of the lubricant due to temperature rise and keep it in the bearings.

When spindle motor is in operation, the viscous pumping effect will generate an inward force that pushes the lubricant into the middle region of journal bearing. From the results of numerical simulations, the sealing pressure of the viscous pumping seal can be as high as 1.0×10^7 Pa, which can effectively prevent the oil leakage from the spindle motor in operation.

Magnetic seal is an excellent non-contact seal especially for the seal between two relative moving surfaces (Berkovsky *et al*., 1993). Besides providing additional seal force when motor is rotational, the magnetic seal can also keep lubricant within the bearing system when motor is in static state or subjected to an external shock. As shown in Fig. 7.4, the magnetic seal consists of a shaft, two thrust plates, a ring shaped permanent magnet and a cylindrical back iron that is concentrically attached to the sleeve of the journal bearing and provides a magnetic path for the sealing magnetic circuit. Since the sealing capacity of the magnetic seal is directly linked with the magnetic field in the sealing area, therefore, we should start the design from the magnetic field analysis. According to the ferro-hydrodynamic analysis, the pressure in the ferrofluid of a static seal is (Zou and Lu, 1992)

$$p = \int_0^B M dB + C \tag{7.8}$$

where M is the magnetization of the ferrofluid, B is the flux density and C is a constant determined by the boundary condition.

The boundary condition differential caused by medium change on the ferrofluid is

$$\Delta p_b = -\frac{1}{2}\mu_0 M_t^2 \tag{7.9}$$

where μ_0 is the magnetic permeability at vacuum and M_t is the tangential component of the magnetization. From Eqs. (7.8) and (7.9), the seal pressure differential of a static seal is deduced as

$$\Delta p = p_2 - p_1 = \int_{B_1}^{B_2} M dB - \frac{1}{2}\mu_0 (M_{t2}^2 - M_{t1}^2) \tag{7.10}$$

When the magnetic intensity in the seal gap is rather intensive and the ferrofluid is magnetized in saturation condition. Therefore, $M = M_s$ in Eq. (7.10) (M_s is much lower than the magnetic intensity), then (7.8) and (7.10) can be expressed as

$$\begin{cases} p = M_s B + C \\ \Delta p = M_s (B_2 - B_1) \end{cases} \tag{7.11}$$

where M_s is the saturation magnetization.

Using commercial software ANSYS, the static magnetic field of the sealing system was analyzed. Figures 7.5 and 7.6 showed the flux distribution in the left seal and the right seal of the bearing. The flux density at the left end was obtained as $\Delta B_{left} = 0.75(T)$ and that at the right end $\Delta B_{right} = 0.85(T)$. Since $\Delta p = M\Delta B = M_s \Delta B$, where M_s = 60KA/m (provided by the supplier), the sealing pressure at the left end were Δp_{left} = 45 kPa and at the right end $\Delta p_{\mathrm{right}}$ = 51 kPa. This pressure difference is sufficient to keep the oil in the bearing system.

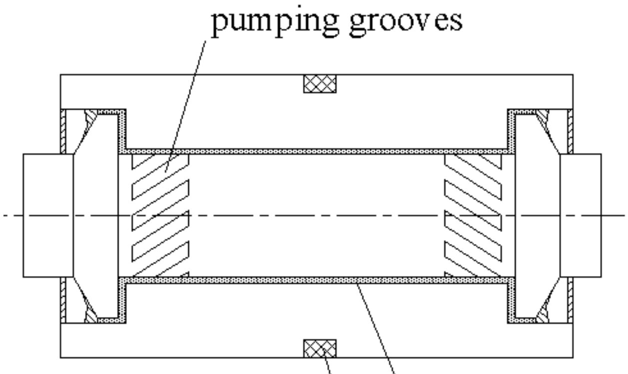

Fig. 7.4 Schematic of sealing system.

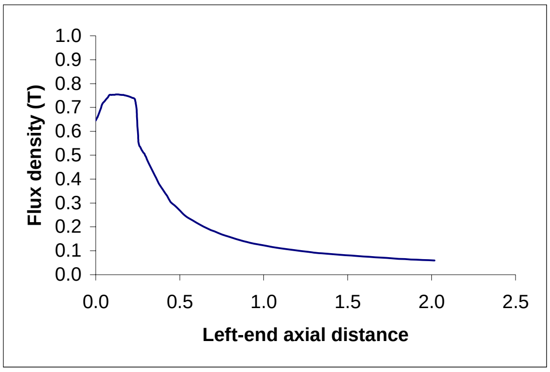

Fig. 7.5 Flux distribution in left magnetic seal.

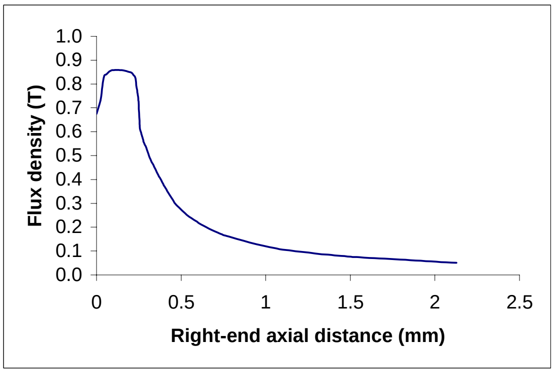

Fig. 7.6 Flux distribution in right magnetic seal.

Another concern for the magnetic seal is that it cannot prevent lubricant from leaking out due to thermal expansion of the lubricant. However, this problem can be overcome by providing a reservoir to accommodate the excess volume of lubricant caused by thermal expansion. This excess volume of the lubricant can be expressed as:

$$\Delta V = V_1 - V_0 = 3L^2\Delta L + 3L\Delta L^2 + \Delta L^3 \tag{7.12}$$

where V_0 is the original volume, V_1 the expanded volume of lubricant. Replace the ΔL with linear thermal expansion coefficient of the lubricant β and ΔT, and ignore the higher order terms, Eq. (7.12) becomes:

$$\Delta V = V_1 - V_0 = 3L^2\Delta L = 3L^3\beta\Delta T = 3V_0\beta\Delta T\ . \tag{7.13}$$

At 20°C, V_0 is around 11.0 mm^3 and $\beta = 10.6x10^{-4}$. Hence, for $\Delta T = 50°C$, $\Delta V \approx 1.8mm^3$. To accommodate such a volume of oil in our design, a reservoir with 2.5 mm^3 oil storage capacity was added to the sealing system. This reservoir can safely accommodate the lubricant expansion for a temperature rise ΔT of 70 °C.

7.1.7 Further considerations in spindle design

Except for the bearing system and its sealing system, some further considerations and important issues in spindle motor design are addressed and discussed in this section.

First is the spindle motor structure design issue. The dimensions of hard disk drives are specified by its form factor. Therefore, the total outer dimensions of the spindle motor to be designed are limited by the format of 2.5" hard disk drive. As mentioned previously, there are two configurations of spindle motor for hard disk drive. One is the motor-in-hub configuration and other one is the motor-under-slung configuration. Here, the motor-under-slung configuration is selected because it can provide more space to accommodate the electrical motor. However, even with the motor-under-slung configuration, the space is still very tight for the lamination of

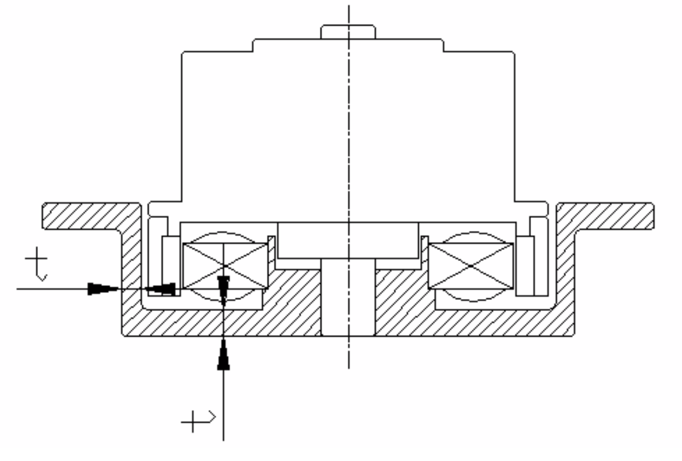

Fig. 7.7 Schematic of motor bracket.

electrical motor and the spindle base bracket. Referring to Fig. 7.7, it is obvious that if the outer dimension or the height of lamination stator is increased, the thickness of the bracket walls *t* has to be reduced, and vice versa. A thicker lamination stator will increase the working torque of the motor, but it will result in a thinner wall of the spindle bracket and will lower the resonance frequency of the spindle motor. Therefore, to improve the dynamic characteristics of the spindle motor, the working torque of the spindle motor has to be reduced to increase the wall thickness of the bracket. Table 7.1 presents the natural frequencies of the first mode of the bracket for different wall thickness. For 0.5mm wall thickness, the frequency of the first mode of the bracket is 4,476 Hz. The frequency of the first mode increases with increasing wall thickness, reaching 9,388 Hz for wall thickness of 1.26 mm. It is observed that for wall thickness thicker than 1.26 mm, the frequency increase with increasing bracket wall thickness is not significant. Hence, the wall thickness of 1.26 mm was chosen and it is a reasonable choice to trade-off the requirements from spindle motor dynamic consideration and the demands for a greater working torque.

Table 7.1 First mode frequency versus wall thickness of motor bracket

Bracket wall thickness (mm)	First mode frequency (Hz)
0.5	4475.9
0.8	6868.7
1.26	9388.7
1.76	10126.0
2.26	10228.0

Second is the shock resistant capability of the spindle motor. It must also be carefully considered in bearing design. Assuming the spindle is subjected to a 100g, 10 ms, half-sine shock, will the surfaces of bearing system hit each other and cause damage of the bearing system? This problem can be analyzed by using a simple model (Harris, 1996). Let the mass block represent the moving portion of the spindle motor and its load, the support represent the stationary portion of the spindle, and the spring-dashpot unit represent the effect of oil film between the bearing surfaces, the equations of motion were given by:

$$\begin{cases} m\ddot{z} + D\dot{z} + Kz = -m\ddot{u} \quad (0 \le \mathrm{t} \le \tau) \\ m\ddot{z} + D\dot{z} + Kz = 0 \quad (\mathrm{t} > \tau) \\ \mathrm{t} = 0,\ \mathrm{z} = 0, \dot{\mathrm{z}} = 0 \end{cases} \tag{7.14}$$

where m is the total mass of the moving portion of the spindle and its load, K and D are stiffness and damping coefficients and $\ddot{u}$ is the shock subjected by the spindle. Here, $m = 6.\mathrm{x}10^{-2}$ kg, $K = 1.451\mathrm{x}10^{7}$ N/m and $D = 1.439\mathrm{x}10^{5}$ N.s/m. Assuming the original distance between the moving portion and stationary portion of the spindle motor is 4 μm, the displacement of moving portion of the spindle along the motor axial direction (z) during the shock is shown in Fig. 7.8. It is observed that the maximum displacement along the z direction is 1.8 μm only. Hence, the risk of bearing system damage caused by shock is very low in the design.

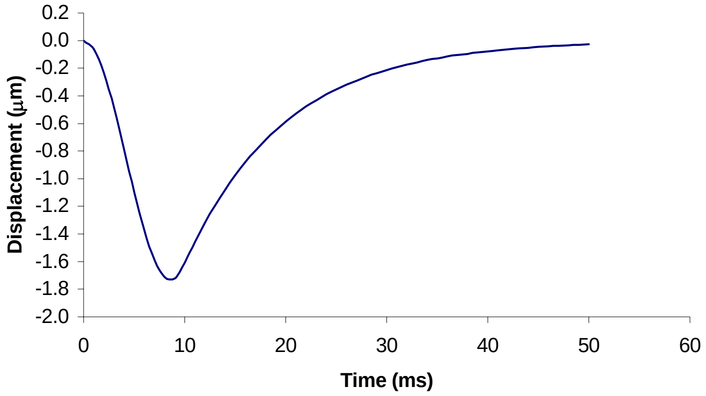

Fig. 7.8 Displacement of the moving portion of the spindle during shock.

Third is thermal and temperature effect on spindle motor performance. The working temperature of hard disk drives is supposed to be from 0 to 70 °C. Therefore, the temperature of hard disk drive as well as the spindle motor is higher than the room or ambient temperature when the disk drive is in operation. The increase of motor temperature results in the decrease of liquid lubricant viscosity, and consequently, the load capacity and stiffness of the bearing system is also lower than those when motor operates at room temperature. The change of bearing performance is linear to the change of lubricant viscosity as shown in Figs. 6.7 and 6.15. To reduce this effect, low viscosity lubricant is selected, such that the change of its viscosity is relatively small and hence the bearing performance will be less affected. The temperature rise also causes the material expansion. It results in some slightly change of spindle motor and its bearing system dimensions. To handle this thermal effect, two aspects are considered. First consideration is that through careful selection of parts materials, the effect of parts thermal expansion can be reduced. Two materials with similar thermal expansion coefficient (say, stainless steel to stainless steel) are chosen as the material of the shaft and its mating sleeve for journal bearing or thrust plate and its mating bearings for thrust bearing. Therefore, when motor temperature changes, both the shaft and the sleeve have similar dimension change so that the bearing performance will not be obviously affected by the thermal effect. Second consideration is to make use of thermal expansion effect to stable the bearing performance. As mentioned previously, temperature rising causes lower lubricant viscosity that results in lower load capacity and stiffness. However, the thermal expansion of bearing parts can be used to reduce the nominal bearing clearance, which can partially compensate the reduction of load capacity and stiffness due to temperature increase caused decrease of viscosity. Hence, the bearing performance will not be changed obviously by temperature change.

7.2 Test of Prototypes

7.2.1 Test results of hydrodynamic bearing spindle motor

The prototypes of previously mentioned ferro-fluid bearing spindle motor were fabricated and tested as shown in Fig. 7.9(a). Figure 7.9(b) shows the schematic of the experimental set-up. The run-out signals were collected by two capacitance probes in radial and vertical direction simultaneously, and then amplified by a two-channel amplifier (MTI, AS5000 SRT) that was connected to a computer. Other signals, such as rotating speed, working voltage and current are provided by the spindle-driver and also sent to the computer, in which all signals are digitalized and analyzed. Testes were carried out on the motor level, that is, without disks mounted on the spindle motor.

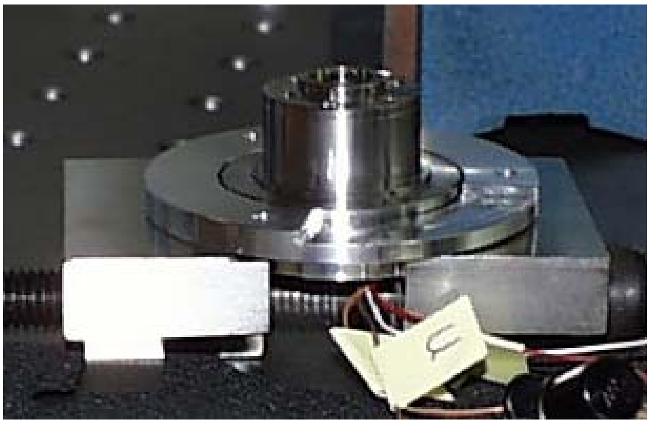

(a)

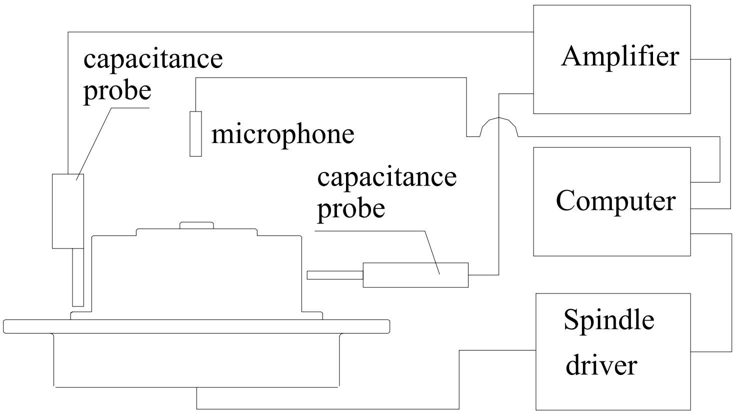

(b)

Fig. 7.9 Prototype of hydrodynamic bearing spindle motor under test (a) and schematic of experimental set-up (b).

Mechanical balancing for the prototyped motors was not carried out before testing. Figure 7.10(a) shows the measurement results of the radial and the axial repeatable run-out (RRO) of the prototypes at different speeds. It was found that the radial RRO simply increased with increasing of the rotational speed of the spindle motor from 4 μm at 5,000 rpm to 6.0 μm at 20,000 rpm, while the axial repeatable run-out showed a different result. At first, it decreased with increasing speed and had a saddle value of 1μm at 15,000 rpm, but after 15,000 rpm it is increased as the speed increased. This result can be explained. Since the spindle motor was not balanced, with increasing of the rotational speed, the radial unbalance force was also increased, resulting in greater vibration amplitude, therefore, the radial RRO increases with the increasing of the rotational speed. On the other hand, the effect of vibration caused by the unbalanced force was relatively smaller in axial direction. At first, the increase of the axial stiffness due to speed increase successfully suppressed the axial vibration amplitude. However, with further increase in motor speed, the increase of stiffness could not further suppress the amplitude of vibration. Consequently, the axial repeatable run-out became higher with the increase of the motor speed. The measurement accuracy of RRO is calculated; the maximum value of 3σ is 0.0559 μm for the radial RRO and 0.0643 μm for the axial RRO respectively at all rotational speeds. At 20,000 rpm, the radial and axial RRO were 6.01 μm and 2.24 μm, respectively. The radial non-repeatable run-out (NRRO) and axial NRRO at different speeds were shown in Fig. 7.10(b) and Fig. 7.10(c), respectively. The values of 3σ for radial and axial NRRO were 0.0195 μm and 0.0099 μm, respectively. It was observed that at 5,000 rpm, the radial NRRO registered the highest value of 0.0309 μm, which gradually reduced to 0.0168 μm at 10,000 rpm. With further increase in speed, the radial NRRO increased again. At 20,000 rpm, the radial NRRO was 0.0281 μm (1.1 μin). The axial NRRO also showed a similar trend except that its minimum value was at 15,000 rpm. At 20,000 rpm, the axial NRRO was 0.0356 μm (1.4 μin), slightly higher than that of

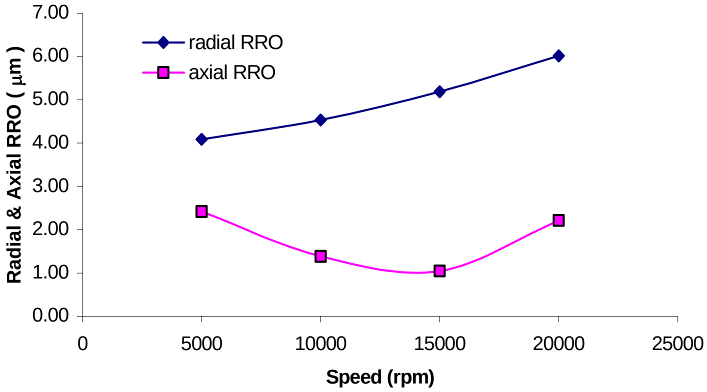

(a)

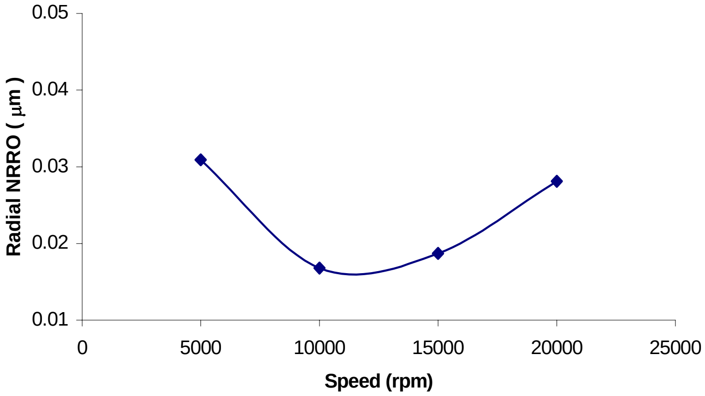

(b)

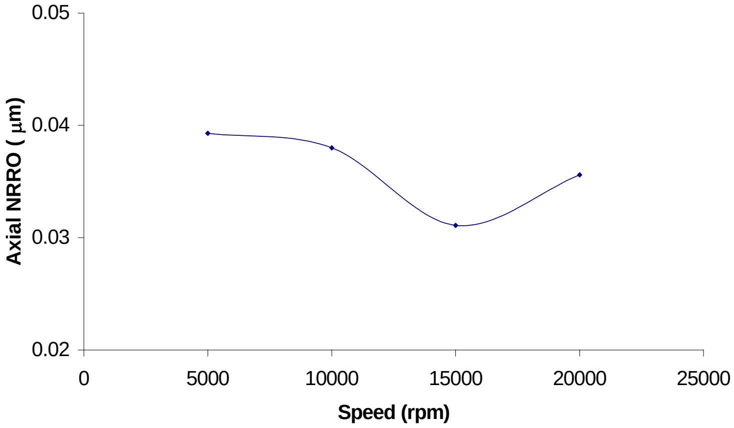

Fig. 7.10 Radial and axial repeatable run-out (a), radial non-repeatable run-out and axial non-repeatable run-out (c) versus speed of the hydrodynamic bearing spindle.

radial NRRO. The reason for the appearance of the minium point in both radial and axial NRRO measurements is to be identified. The starting time of the spindle motor at 20,000 rpm was around 3 seconds in unloaded condition (without disks mounted on the spindle motor). Figure 7.11 shows the working current versus the rotational speed. The working current at 20,000 rpm is around 0.6 A as shown in Fig. 7.12. The power consumption of the spindle motor at 20,000 rpm is about 7.2 W. The estimated windage loss, the iron loss and the copper loss together are around 1.6 W at 20,000 rpm. Subtracting the above power loss from the total power consumption of the spindle motor, the net power loss of the bearing system is about 5.6 W, which is almost 25% higher than that of the predicted power loss of 4.5 W. The difference between measured and predicted power loss comes from two aspects. One is the possible underestimation of core power loss and the second reason is that the lubricant filled into the gap of the fluid bearings is slightly higher than designed one which causes the power loss higher than predicted one. The measured back-EMF of the spindle motor is around 7.7 V that agreed very well with the predicted back-EMF calculated based on the design of the magnetic structure and the number of coil turns. After continuously running the spindle motor for more than two months, careful observation under a microscope did not reveal any oil traces on both end of the spindle motor. This means that the compound seal consisting of magnetic seal and viscous pumping seal succeeded to prevent lubricant leakage out of the spindle motor. Figure 7.13 shows the distribution of 1/3 octave spectrum and noise level of the prototype spindle motor at 20,000 rpm. The acoustic noise at 20,000 rpm is less than 34 dB(A), measured with a precision microphone which was located right above the spindle motor at a distance of 30 cm. The background noise level of the anechoic chamber is around 24 dB (A). It is almost 4 – 8 dB lower than that of most ball bearing spindle motors which have the acoustic noise level of around 38 – 42 dB(A) measured at the same condition but at much lower rotational speed of 7,200 rpm. It should be mentioned that to compare the acoustic noise level of the prototypes with ball bearing spindle motors at the same rotational speed, the acoustic noise of the prototypes were also measured at rotational speed of 7,200 rpm but the readings were very close to the background noise level. Therefore, the actual noise level of the prototypes at 7,200 rpm could not be identified but it was certain that the acoustic noise of the prototypes at 7,200 rpm was, at most, 24 –25 dB(A).

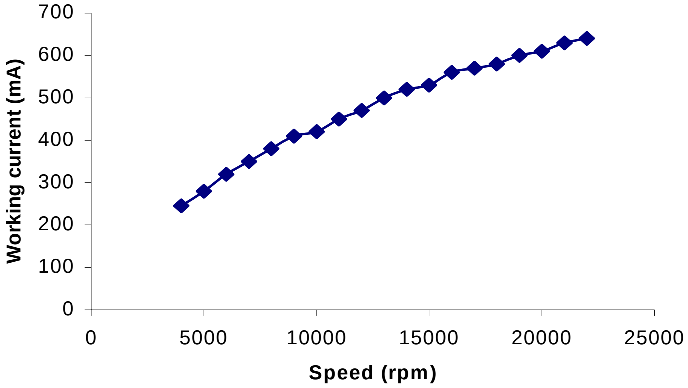

Fig. 7.11 Working current versus speed of ferro-fluid bearing spindle.

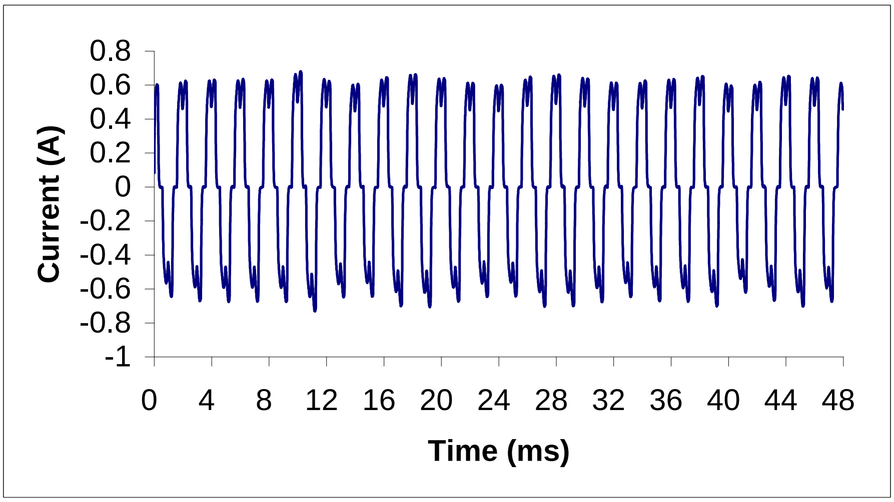

Fig. 7.12 Working current of ferro-fluid bearing spindle prototype at 20,000 rpm. (The total time shown is 48 ms).

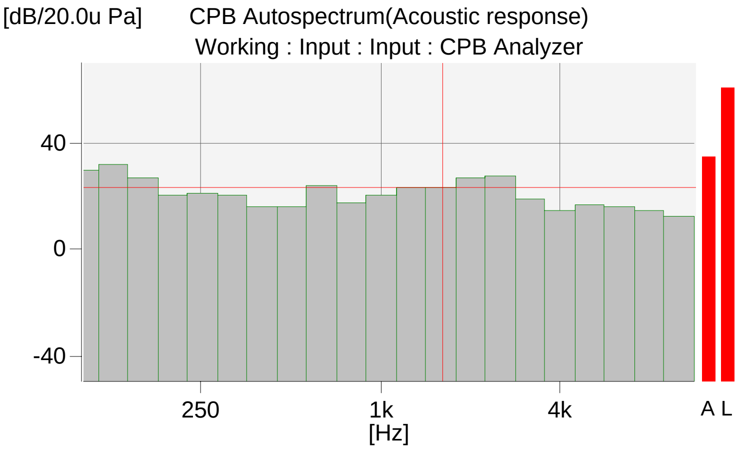

Fig. 7.13 Measured acoustic noise of ferro-fluid bearing spindle at 20,000 rpm
Acoustic Level: A: 33.9 dB(A)/20.0 μPa; L: 60.3 dB (A)/20.0 μPa.

7.2.2 Test results of hybrid bearing spindle motor

The prototypes of spindle motor using the hybrid fluid bearing system were also fabricated and tested. The test results are shown in the Figs. 7.14 to 7.19. Figure 7.14 indicates that both radial and axial RRO were within 2.6 μm at various rotational speeds from 4,000 to 10,200 rpm. The radial RRO decreased with increasing speed from 2.35 μm at 4000 rpm to 1.47 μm at 10,200 rpm. The axial RRO did not follow this trend. It oscillated as the increase of speed and took the minimum value of 1.998 μm at 7200 rpm. The axial and radial NRRO versus the rotational speed of spindle are shown in Fig. 7.15. It is observed that both axial and radial NRRO are less than 0.05 μm. Figure 7.16 shows the starting current of the hybrid fluid bearing (HFB) spindle motor when the operational speed was set at 10,200 rpm. The abscissa of Fig. 7.16 represents the time with a unit of 0.2s/div., while the vertical axis represents the current with a unit of 500 mA/div. From Fig. 7.16, it is observed that the starting current was around 910 mA and it took about 0.8 seconds for the spindle motor to reach the specified speed. Figure 7.17 presents the working current and voltage of both the fluid bearing spindle motor and the reference ball bearing spindle at steady state.

The dimensions of the reference ball bearing spindle motor was very close to the prototype of the hybrid fluid bearing spindle motor and it was to be used in a product of high-end disk drive. The working current of the hybrid fluid bearing spindle motor was higher than that of the ball bearing spindle while the working voltage of the ball bearing spindle was higher that that of hybrid fluid bearing spindle motor. The power consumption of the HFB spindle motor is higher than that of the ball bearing spindle motor as shown in Fig. 7.18. At nominal working speed of 10,200 rpm, the power loss of the hybrid fluid bearing spindle motor is only 26% higher than that of the reference ball bearing spindle motor. The power loss of pure oil lubricated bearing spindle motors is usually more than 50% higher than that of ball bearing spindle motors, the power loss of the hybrid bearing spindle motor is obviously reduced. Figure 7.19 compares the net power consumption of the hybrid fluid bearing system predicted by the numerical simulation with the measurement data. The copper loss and the iron loss of the motor were deducted from the measured total power consumption (refer to Fig. 7.18) of the spindle motor to obtain the net power consumption of the hybrid fluid bearing system. A good agreement between the predicted and the measured power consumption of the bearing system was observed.

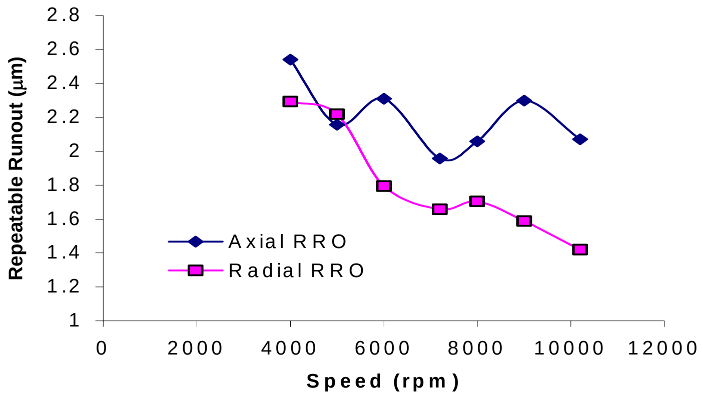

Fig. 7.14 Axial and radial repeatable run-out versus speed of hybrid bearing spindle.

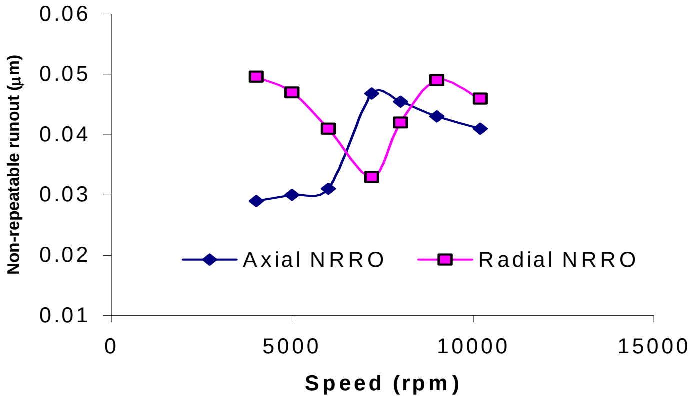

Fig. 7.15 Axial and radial non-repeatable run-out versus speed of hybrid bearing spindle.

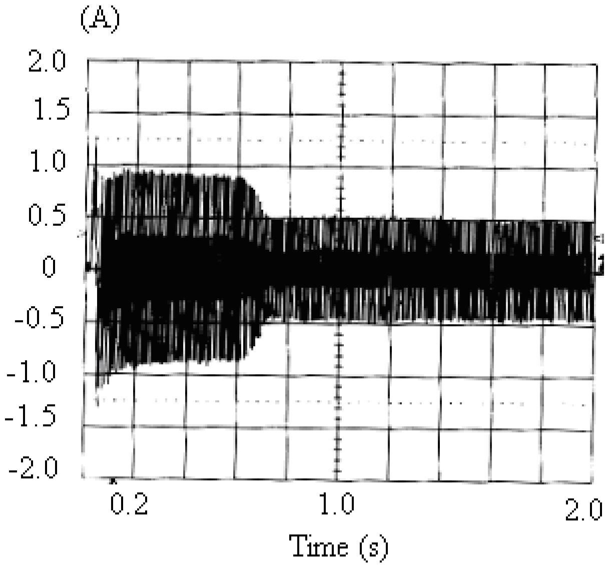

Fig. 7.16 Starting current of hybrid fluid bearing spindle motor at 10200 rpm.

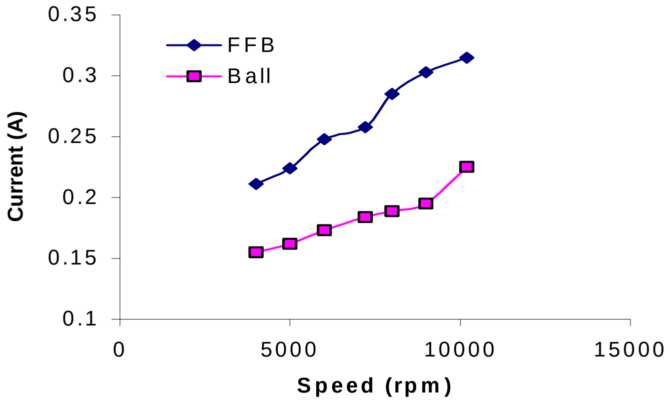

Fig. 7.17(a) (Continued)

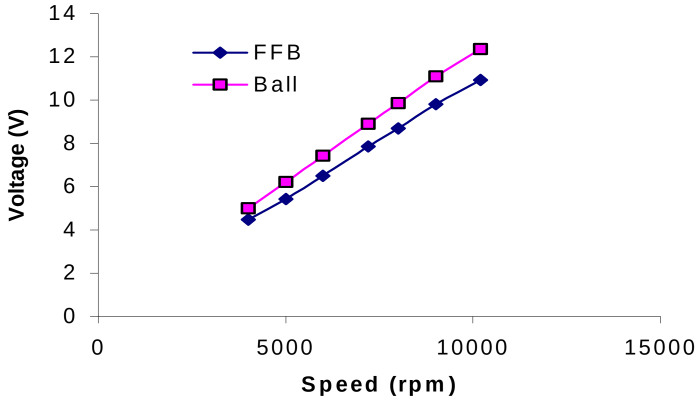

(b)

Fig. 7.17 Comparison of working current (a) and voltage (b) of hybrid bearing spindle with a ball bearing spindle.

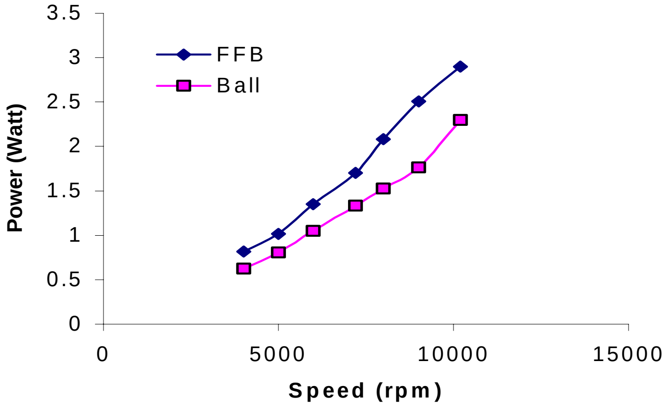

Fig. 7.18 Power consumption versus rotational speed of hybrid fluid bearing spindle (upper curve) and ball bearing spindle (lower curve).

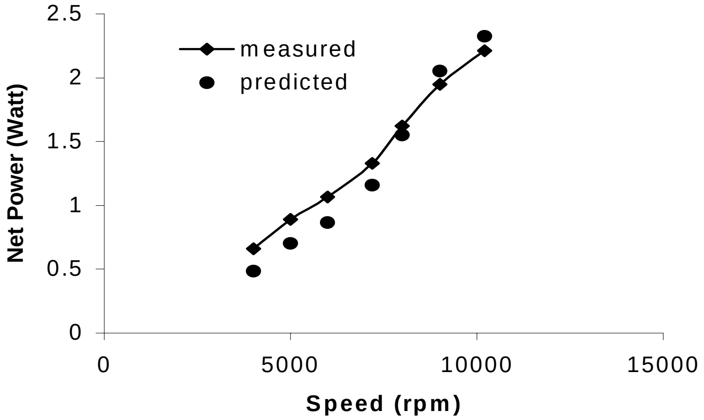

Fig. 7.19 Predicted power consumption and measured power consumption of hybrid fluid bearing system.

7.2.3 Discussion and conclusions

A high-speed ferro-fluid bearing spindle motor was introduced. Some design challenges and considerations of motor and bearing system were addressed and discussed. The test results show that at 20,000 rpm, the developed spindle motor has less than 0.03 μm (≈ 1 μinch) radial and axial NRRO and acoustic noise level of 34 dB(A). Hence the objectives of developing a high-speed, high performance fluid bearing spindle motor with lower non-repeatable run out, “zero” lubricant leakage and low level of acoustic noise have been fulfilled.

The proposed design of hybrid fluid bearing system has its advantages as well as disadvantages. The main advantages are high radial stiffness, lower power consumption, reduced difficulty in seal design and providing a possible solution for discharging electrostatic charges accumulated during operation. The test results on its prototypes show that the spindle motor using the hybrid fluid bearing system works well. The good agreement between predicted and measured power consumption shows that the objective of developing a power saving bearing system is achieved. So, it provides us a prospective configuration for the new generation spindles used in high-speed, high-performance hard disk drives.

However, the disadvantages of the hybrid bearing system design includes: 1) when spindle motor is subjected to a large external shock, the risk of the thrust bearing getting damaged is higher than that of a fully oil lubricated bearing system due to the lack of damping effect between the gaps of thrust plate and thrust bearings, and 2) the conical configuration of the thrust bearing may increase the difficulty in machining the parts resulting in higher cost.

Chapter 8

COMPARISON BETWEEN BALL BEARING AND FLUID BEARING SPINDLES

The performance of ball bearing and fluid bearing spindle motors is compared in this chapter. The effect of unbalance magnet force on the performance of ball bearing and fluid bearing spindle motors are first investigated, and the vibration characteristics of disks mounted on ball bearing and fluid bearing spindle motors are then analyzed and compared.

8.1 Effect of Unbalanced Magnetic Force on Spindle Motors*

An unbalanced electromagnetic force in a rotating motor can occur when there is an eccentricity between the stator and the rotor, which is the normal operation mode for the fluid film bearing system, or when the magnetic flux path is not symmetrical about the axis of the motor. Since its direction and magnitude are changing with the rotor position, such an unbalanced magnetic force can be a source of vibration and acoustic noise, in addition to the magnetic cogging effect. For fluid film bearing spindles, the unbalanced magnetic force affects the rotor dynamics and also the performance of the bearing system as the magnitude of the alternating force can be of a comparable order of the total load of the spindle.

It is known that in the spindle motors with the 8 poles / 9 slots configuration, an unbalanced magnetic force in the radial direction will be generated. The rotational speed of this unbalanced force can be as high as 9 times of the rotational speed of the journal of the spindle motor. Its amplitude is not negligible compared to the original

---

* Part of this Section has been published in the Proceedings of Intermag'97, CC-10, USA, 1997.

load of the spindle motor used in hard disk drive (Chen *et al*., 1996 & 1998; Liu *et al*., 1996). Hence, the effect of this unbalanced force on the dynamic performance of the spindle motors used in hard disk drive is not negligible.

The effect of this unbalanced force on the dynamic performance of the spindle motors is analyzed in this section. For comparison, both ball bearing and fluid bearing spindle motors are analyzed. It is found that for ball bearing spindle motors, this unbalanced force causes the spindle motor vibration with the frequency of the unbalanced force. For fluid film bearing spindle motors, the effect of the unbalanced force depends on the orientation of the spindle motors. When the spindle motor is in the normal vertical position, this unbalanced force can increase the stiffness of bearing, and hence, enhances the motion stability of the spindle motor. However, when the spindle motor is at horizontal position, this force causes a forced vibration of the spindle motor.

8.1.1 Effect on ball bearing spindle motor

Assuming that the motion of spindle motors can be simplified as a rigid rotor, the amplitude ($\hat{F}$) and the angular speed (ω_F) of the unbalanced magnetic force are constant, only the stiffness is considered and the damping coefficient of ball bearings is neglected. Under the above assumptions, the motion of the spindle rotor can be described by following equations:

$$M\ddot{x} + 2(K_{xx}x + K_{xy}y) = \hat{F}\cos(\omega_F t)\,, \tag{8.1}$$

$$M\ddot{y} + 2(K_{yx}x + K_{yy}y) = \hat{F}\sin(\omega_F t)\,. \tag{8.2}$$

In the above equations, M is the rotor mass; K_{xx}, K_{yy}, K_{xy} and K_{yx} are bearing stiffness; x, y are coordinates in the plane which is perpendicular to the axis of the spindle rotor.

From Eqs. (8.1) and (8.2), the locus of the rotor center can be described as:

$$x(t) = \hat{x}\cos(\omega_F t - \phi_1)\,, \tag{8.3}$$

$$y(t) = \hat{y}\cos(\omega_F t - \phi_2)\,. \tag{8.4}$$

where $\hat{x}$ and $\hat{y}$ are the vibration amplitudes in x and y directions, respectively, and they are functions of $\hat{F}$, ω_F, K_{xx}, K_{yy}, K_{xy} and K_{yx}.

Equations (8.3) and (8.4) show that under the action of exciting force, the unbalanced magnetic force, the center of the rotor undergoes harmonic motions in the x and y directions with the frequency of the exciting force.

The effect of this exciting force to the spindle motor with ball bearing system is shown in Table 8.1 and Fig. 8.1. It is observed that the vibration amplitude of the spindle motor rotor caused by the unbalanced magnetic force increases with the increasing of the motor rotational speed. For example, the vibration amplitude is around 0.1 μm at 3,600 rpm and it becomes 0.16 μm at 10,200 rpm. The motor vibration will cause the structure vibration of hard disk drives and emits a higher acoustic noise. Therefore, the effect of unbalanced magnetic force on the ball bearing spindle motors is harmful and should be avoided through the proper design of the electric motor.

8.1.2 Effect on fluid bearing spindle motor

The effect of unbalanced magnetic force on the spindle motors with fluid film bearing system depends on the orientation of the spindle motors. When spindle motor is in the normal vertical position, the static load in the radial direction is small for a well-balanced disk-motor stack. The unbalanced magnetic force acts as a load in the radial direction. Fixing coordinates to the rotor of the spindle motor, the pressure equation in the rotating coordinates is given by

$$\frac{\partial}{\partial\theta}\left(\frac{h^3}{\mu}\frac{\partial p}{\partial\theta}\right)+R^2\frac{\partial}{\partial z}\left(\frac{h^3}{\mu}\frac{\partial p}{\partial z}\right)=6R^2\left[2\dot{h}+(\omega-2\dot{\phi})\frac{\partial h}{\partial\theta}\right] \tag{8.5}$$

where p is the pressure, h the film thickness, μ dynamic viscosity, R the radius of journal, θ angular coordinate, z the coordinate along the direction of journal axis, $\dot{\phi}$ the angular speed of center-line, and $\dot{h}$ the derivative of h with respect to time.

Assuming that the amplitude and the angular speed of unbalanced magnetic force are constant, the centerline is rotating with the angular speed $\dot{\phi} = \omega_F$ and the eccentricity ratio remains constant. Consequently, $\dot{h} = 0$. Let $\overline{\omega} = \omega - 2\dot{\phi} = \omega - 2\omega_F$, since $\dot{\phi} = \omega_F$ is constant, hence, $\overline{\omega}$ is a constant also. Substituting into Eq. (8.5), it becomes

$$\frac{\partial}{\partial\theta}\left(\frac{h^3}{\mu}\frac{\partial p}{\partial\theta}\right)+R^2\frac{\partial}{\partial z}\left(\frac{h^3}{\mu}\frac{\partial p}{\partial z}\right)=6R^2\overline{\omega}\frac{\partial h}{\partial\theta}. \tag{8.6}$$

Equation (8.6) is exactly the same as the pressure equation for steady-state situation if ω is replaced by $\overline{\omega}$. However, $\overline{\omega}$ is now much greater than the original angular speed ω. This results in the load capacity and stiffness of journal bearing being greatly increased (because both the load capacity and stiffness are directly proportional to the angular speed ω). The increase of angular speed ω results in the increase of stiffness of fluid film bearings (Constantinescu *et al.*, 1985).

The critical frequency of motion instability of the rotor is related to the stiffness of the bearing. For the first order simplification, it can be expressed as

$$\omega_c = \sqrt{\frac{k}{M}}. \tag{8.7}$$

It is apparent that increasing stiffness enhances the motion stability of rotor and it also helps reduce the non-repeatable run out of the spindle motor. Figures 8.2 (a) and (b) show the stiffness and the critical frequency for a fluid film bearing spindle motor when it is subjected to, and not subjected to the action of an unbalanced force. It is clear from Fig. 8.2 that the stiffness and the critical frequency of motion instability are greatly increased due to the action of unbalanced magnetic force.

When the spindle motor is placed in horizontal position, the resultant force acting on the rotor consists of two components, the static load and the unbalanced magnetic force. The static load tries to keep the rotor of the spindle motor at an equilibrium position, while the unbalanced magnetic force pulls the rotor away from its equilibrium position. Since the unbalanced magnetic force is continuously rotating, it will cause the rotor vibration around its equilibrium position. Assuming that under the sole action of static load, the equilibrium position of rotor center is (x_0, y_0), at this position the stiffness and damping coefficient are known. The motion of the rotor of the spindle motor is governed by equations:

$$M\ddot{x} + K_{xx}x + K_{xy}y + D_{xx}\dot{x} + D_{xy}\dot{y} = \hat{F}\cos(\omega_F t), \tag{8.8}$$

$$M\ddot{y} + K_{yy}y + K_{yx}x + D_{yy}\dot{y} + D_{yx}\dot{x} = \hat{F}\sin(\omega_F t), \tag{8.9}$$

where, D_{xx}, D_{yy}, D_{xy} and D_{yx} are damping coefficients of fluid film bearing and M, $\hat{F}$, ω_F, K_{xx}, K_{yy}, K_{xy} and K_{yx} are the same meaning as those used in Eqs.(8.1) and (8.2). The locus of the rotor motion under the action of unbalanced magnetic force can be obtained by solving Eqs. (8.8) and (8.9). Fig. 8.3 shows the result of rotor motion for a set of given stiffness and damping coefficients, $K_{xx} = K_{yy} = 1\text{x}10^6$ (N/m); $K_{xy} = -K_{yx} = 1\text{x}10^6$ (N/m); $D_{xx} = D_{yy} = 1.5\text{x}10^3$ (N*s/m). The values of the parameters M, $\hat{F}$ and ω_F are given in the second row of Table 8.1. It is observed that the unbalanced magnetic force causes the rotor moving around its equilibrium position. The amplitude of the vibration is around 0.3 μm (or 12 μin). For such high amplitude vibration, its effect to the track position error is not negligible. Furthermore, due to this forced vibration, the stiffness and the damping coefficients of fluid film bearing are also oscillating around its equilibrium position values. Consequently, the motion stability of the spindle motor is reduced and the difficulty for servo control to compensate the vibration caused track misregistration is also increased. Overall, the unbalanced magnetic force is harmful when the fluid bearing spindle motors are horizontally positioned.

8.1.3 Discussion and conclusions

Based on the above analysis, it can be concluded that the unbalanced magnetic force has a significant effect on the dynamic performance of spindle motors. For ball bearing spindle motors, it causes vibration of the spindle motors, which results in the problem of higher acoustic noise. Therefore, the unbalanced magnetic force should be removed in design of ball bearing spindle motors. For fluid film bearing spindle motors, it helps increase the load capacity and stiffness of the fluid bearing spindle motors when the spindle is vertically positioned. However, when the fluid bearing spindle motor is horizontally positioned, the unbalanced magnetic force causes a forced vibration of the spindle motor, therefore, increases the risk of track misregistration. Hence, in the design procedure of the spindle motors, the effect of the unbalanced magnetic force should also be carefully considered and treated according to the different application situations.

Table 8.1 Motor parameters and its amplitude of vibration excited by unbalanced force

Pole /Slot	$\hat{F}$ (N)	M (kg)	N (rpm)	ω (rad/s)	ω_F (rad/s)	K (N/m)	A (μm)
8/9	0.353	0.2	3600	377.0	3392.9	2.0x10^7	0.1
8/9	0.353	0.2	10200	1068.1	9613.3	2.0x10^7	0.16

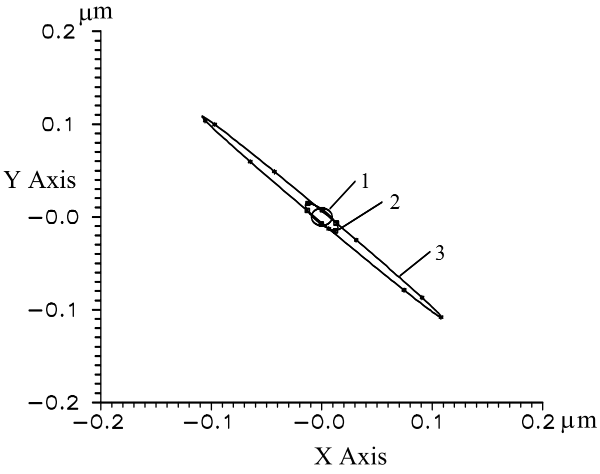

(a) at N = 3,600 rpm.

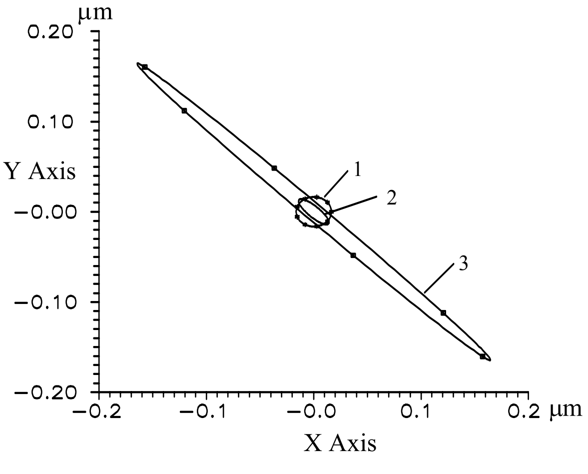

(b) at N = 10,200 rpm.

Fig. 8.1 Locus of journal under action of unbalanced magnetic force. Legend: 1) $K_{xx} = K_{yy} = 2x10^7$ (N/m), $K_{xy} = K_{yx} = 0$, 2) $K_{xx} = K_{yy} = 2x10^7$ (N/m), $K_{xy} = K_{yx} = 1x10^7$ (N/m), 3) $K_{xx} = K_{yy} = 2x10^7$ (N/m), $K_{xy} = K_{yx} = 2x10^7$ (N/m).

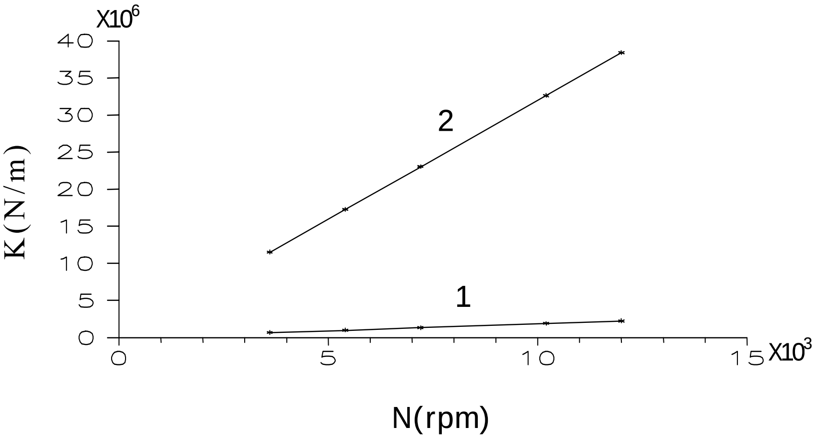

(a) Stiffness *K* versus rotational speed *N*.

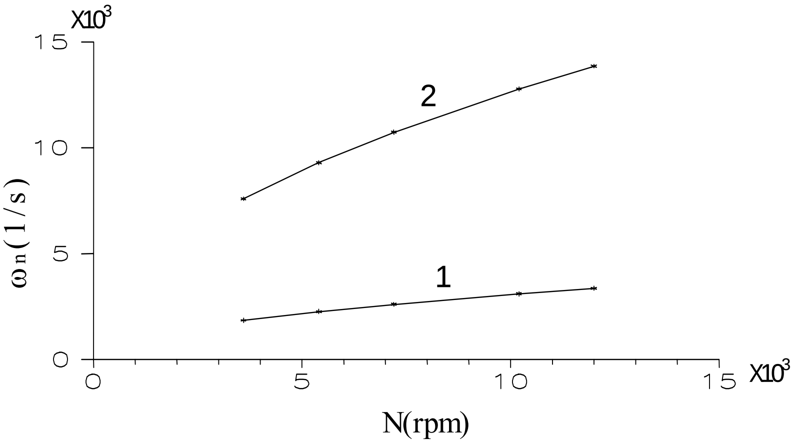

(b) Critical frequency ω_n versus rotational speed *N*.

Fig. 8.2 Variation of stiffness and critical frequency with rotational speed.
Legend: 1) no action of the unbalanced force,
2) under the action of the unbalanced force.

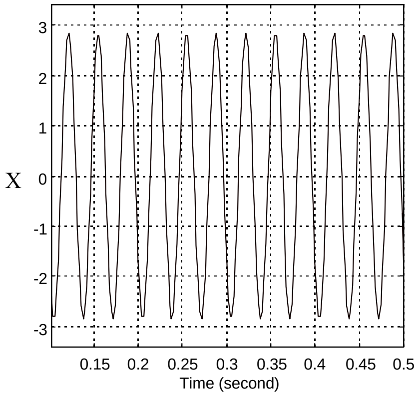

(a) x-direction motion
Fig. 8.3 (continued)

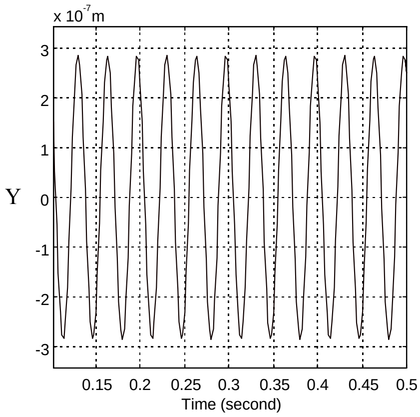

(b) y-direction motion

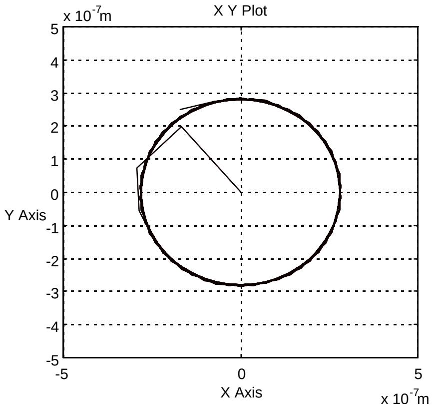

(c) Locus in x-y plan

Fig. 8.3 Vibration amplitude (a & b) and locus (c) of journal of fluid film bearing under unbalanced magnetic force.

8.2 Experimental Comparison of Disk Vibration Characteristics[*]

8.2.1 Introductory remarks

In response to the demand for higher data storage capacity in the computer industry, the areal density of hard disk drive has increased rapidly. The increase of areal density of hard disks depends on the linear density BPI (bits per inch) and the track density TPI (tracks per inch). The increase of BPI is due to improvement of

---

[*] Part of this Section has been published in *STLE Tribology Transactions*, v46, n3, pp 465-468, 2003.

recording media while the increase of TPI is the result of improvement of the components of hard disk drives. Recently, the track density has been increased to a very high level (around 60K TPI in production and even higher in laboratory). The higher the track density, the tighter the requirement on the non-repeatable run out of spindle motors. On the other hand, to reduce the access time, the rotating speed of spindle motors in hard disk drives has also increased. These requirements make the conventional ball bearing spindle motors unsuitable to be used in future hard disk drives. With the development of fluid bearing spindle motor, the trend is to gradually replace the ball bearing spindle motors with the fluid bearing spindle motors in hard disk drives. Therefore, an investigation of vibration characteristics of disks supported by a fluid bearing spindle is necessary.

It is known that air turbulence caused by a high speed rotating disk stack will induce vibration in the disks and actuator arm. The combined effects of high track density and the vibration of the disks and actuator is one of the major problems of track misregistration during data read and write processes. The vibration characteristics of disks mounted on ball bearing spindle motors were well investigated by many researchers, such as Wang (1994), McAllister (1996 & 1997), Shen and Ku (1997) and Srikrishna and Kasetty (2000). Ku and Jennings (1996) theoretically investigated the dynamic characteristics of disks that were supported by a fluid bearing spindle motor. In this paper, an experimental investigation on vibration characteristics of two different size disks of 3.5 inch diameter and 2.5 inch diameter, supported by fluid bearing spindle motors is presented and compared with those supported by ball bearing spindle motors.

8.2.2 Experimental set-up

The schematic of the experimental set-up is shown in Fig. 8.4. The disk base plate is placed on a vibration-free table to isolate external disturbances. The spindle motor is fixed to the base plate and the stack of disks (2 or 3 disks) is fixed to the motor. A proximity capacitance probe is placed vertically above the edge of the top disk with a nominal offset distance of 0.127mm. When the disk assembly is at static state, an impact hammer is used to excite the static mode of the disks. When the spindle motor is rotating, no external excitation is provided. The rotational speed of the spindle motor was controlled by an external spin-box that can accurately control the speed of the spindle motor and arbitrarily adjusted from 400 rpm to 40,000 rpm with a minimum increment of 100 rpm. The signals of the disk vibration were picked by a proximity capacitance probe in vertical direction. The output of the probe was connected to an HP 35670A analyzer that collected the signals in a specified times, which averaged the collected signals and converted them from time domain into frequency domain.

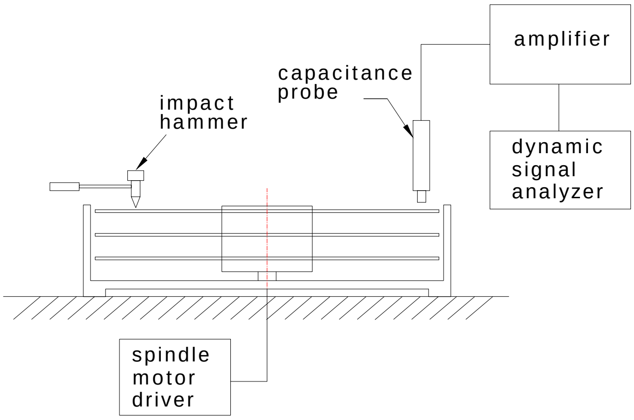

Fig. 8.4 Schematic of experimental set-up.

8.2.3 Discussion and conclusions

The vibration characteristics of 3.5 inch disks supported by conventional ball bearing spindle motor and fluid bearing spindle motor were obtained first. The static response of the disks mounted on a ball bearing spindle motor with external excitation is shown in Fig 8.5. The first static resonance is at about 376 Hz, which is the whole disk stack rocking on the bearings (Shen and Ku, 1995). The second, third and fourth peaks are disk modes, which are at 580, 684 and 1132 Hz respectively.

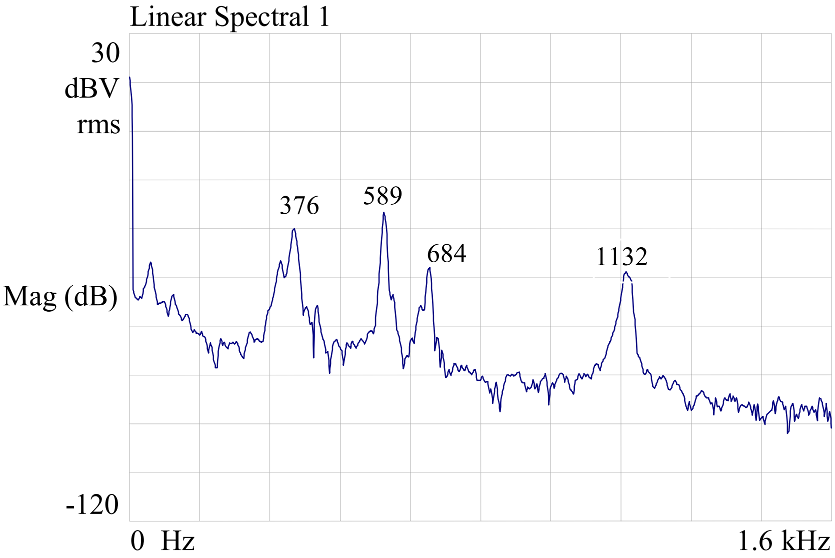

Fig. 8.5 Static response of 3.5 inch disk to an external excitation, supported by ball bearing spindle motor.

Figure 8.6 shows the waterfall plot of disk vibration for two 3.5 inch disks supported by a ball bearing spindle motor. The rotational speed of the spindle motor was changed from 3,000 rpm to 6,000 rpm with an increment of 200 rpm. For disks mounted on the ball bearing spindle motor, the peaks of 1st, 2nd, 3rd, 4th and 5th of harmonics are clearly visible in Fig. 8.6. Besides these harmonic peaks, there are other peaks that show the characteristics of the disk vibration. Different disk vibration modes can be shown by connecting these relevant peaks. As shown in Fig. 8.6, the lines 1B' and 1F' show the rocking mode and the lines 1B and 1F, 2B and 2F, and 3B and 3F show the (0,1), (0,2) and (0,3) modes of disk vibration. Extend these lines to zero rpm, the static modes of disk vibration are obtained. The lines 1B' and 1F' intersect the zero rpm line at about 380 Hz and the other disk modes intersect the zero rpm line at 594 Hz for (0,0) mode, 580 Hz for (0,1) mode, 680 Hz for (0,2) mode and 1125 Hz for (0,3) mode. They are quite close to the results for static response when the spindle motor is not rotating as shown in Fig 8.5. A vertical line at 594 Hz indicates the (0, 0) mode that does not split with the rotating of disks. The (0, 0) mode is a radial mode and there is no nodal diameter. Hence, it does not split because there is no amplitude modulation of the observed vibration in the stationary reference frame versus the rotating reference frame (Frees, 1995; McAllister, 1996 & 1997). The other static modes are split due to the rotation of the disks. The lines indicated by 1B' and 1F' show the backward and forward peaks of the rocking mode split by one time of the rotating speed. According to Shen and Ku (1995), this mode results from the gyro motion of the whole disk stack. The lines assigned by 1B and 1F, 2B and 2F, and 3B and 3F indicate the backward and forward peaks of disk modes of (0,1), (0,2) and (0,3) that are split by one, two and three times of the disk rotating speed. For example, at 6,000 rpm, the resonant frequencies are 500 Hz (1B) and 694 Hz (1F), 500 Hz (2B) and 904 Hz (2F), and 856 Hz (3B) and 1452 Hz (3F). They are slightly higher than their corresponding static modes due to the disk rotating. Besides the harmonics and resonance peaks, there also exist some peaks caused by the waviness of balls, inner and outer race of the ball bearing. The frequencies of these peaks caused by the waviness of ball bearing parts are all lower than the frequency of the 4th harmonics as shown in Fig. 8.6. It is also observed that there exists a series of backward going peaks above 1400 Hz at 6000 rpm. Such high frequency of vibration is beyond the range of our interest because the servo control usually cannot compensate such high frequency vibration.

Figure 8.7 shows the result of disk vibration characteristics of two 3.5 inch disks that are supported by a fluid bearing spindle motor. The rotating speed was from 3,000 rpm to 6,000 rpm with an increment of 100 rpm at each step because the peaks of disk vibration mounted on fluid bearing spindle was not so obvious as shown in Fig. 8.6. To show the disk vibration characteristics clearly, the measurement points had to be increased. For disks mounted on a fluid bearing spindle, the 1st - 6th and 8th harmonic peaks of disk vibration are clearly observable. Since the stiffness of a fluid bearing is linked to the rotating speed of the spindle motor, the stiffness of the fluid bearing is not defined when the spindle is at static state. Therefore, all static mode frequencies were interpolated by extending the lines that connect the peaks of disk modes when the spindle motor was rotating. In this way, the disk resonance frequencies at static state are 583 Hz for (0,0) mode, 580 Hz for (0,1) mode, 686 Hz for (0,2) mode and 1125 Hz for (0,3) mode. The peaks caused by the half-frequency whirl of fluid bearing did not appear clearly. Only at a few speeds, the half-frequency whirl peaks are observed and the amplitudes were small. It means that even if there is a half-frequency whirl, the effect of half- frequency whirl is not serious enough to affect the performance of hard disk drives.

Comparing Fig. 8.6 and Fig. 8.7, it is observed that: a) The most notable difference between these two figures is that no rocking mode is observed for disks supported by a fluid bearing. A reasonable explanation for the lack of a rocking mode is that since the rocking mode is the whole disk stack wobbling on the bearing, fluid bearings have better damping than that of ball bearings, the amplitude of the rocking mode is too small to be observed. b) No peaks caused by parts waviness at lower

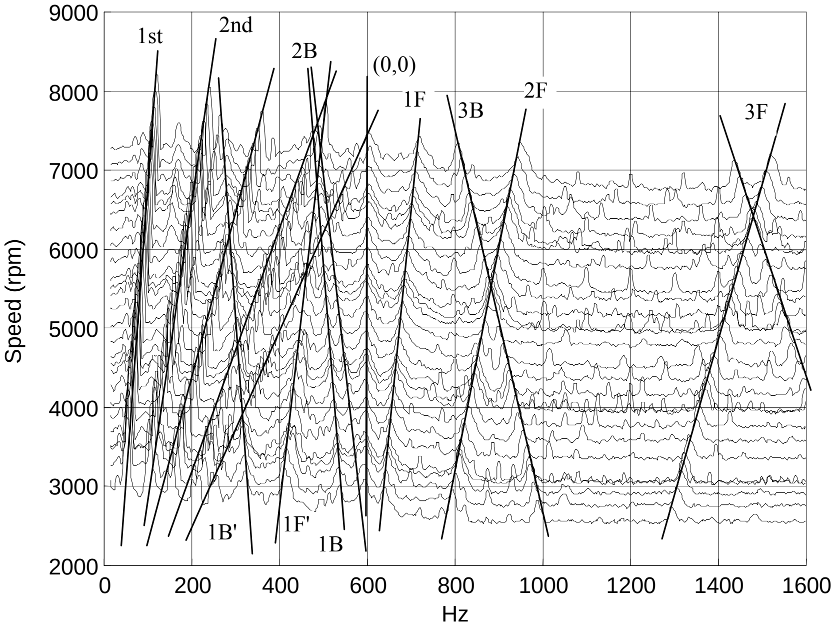

Fig. 8.6 Waterfall plot of 3.5" disk vibration supported by ball bearing spindle motor.

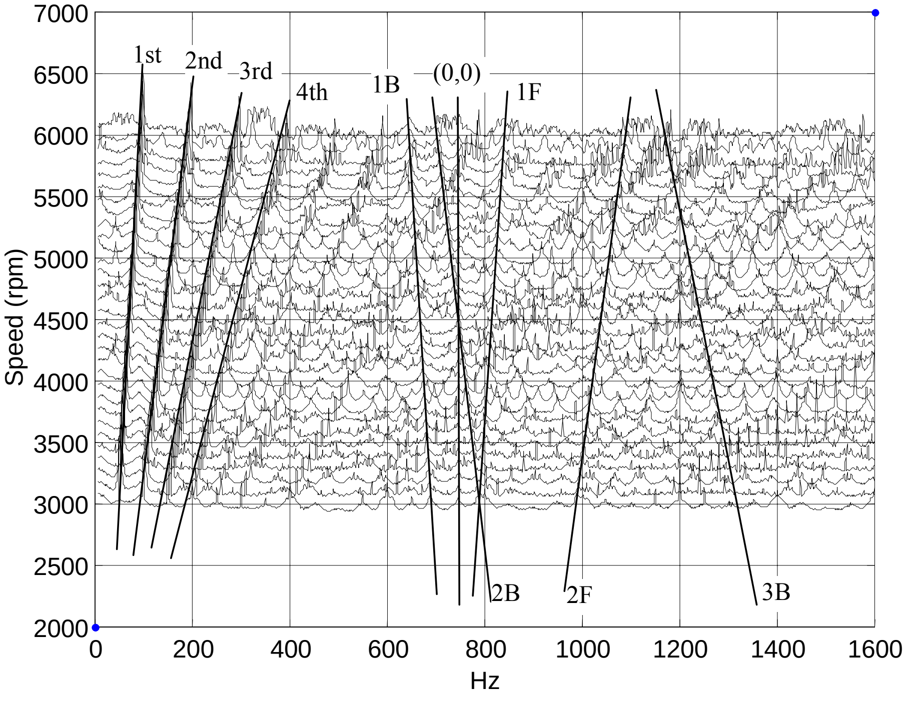

Fig. 8.7 Waterfall plot of 3.5" disk vibration supported by fluid bearing spindle motor.

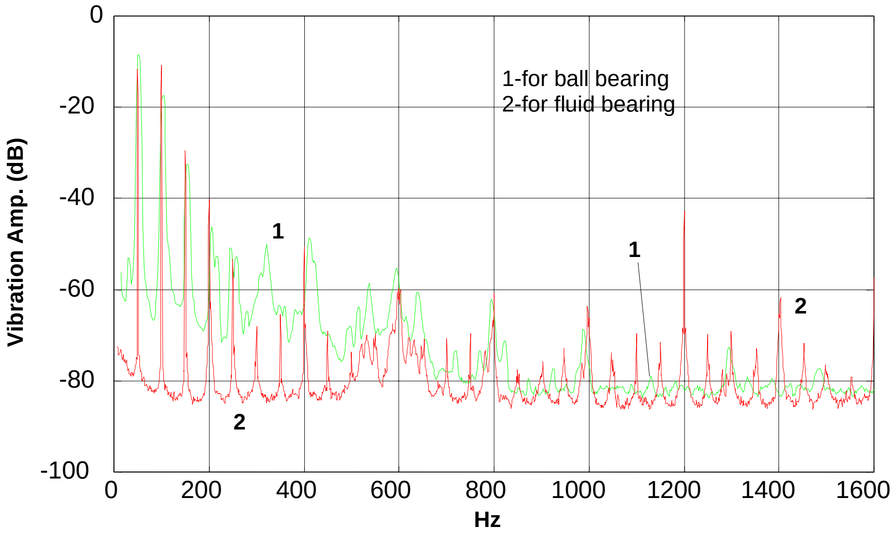

(a) 3,000 rpm

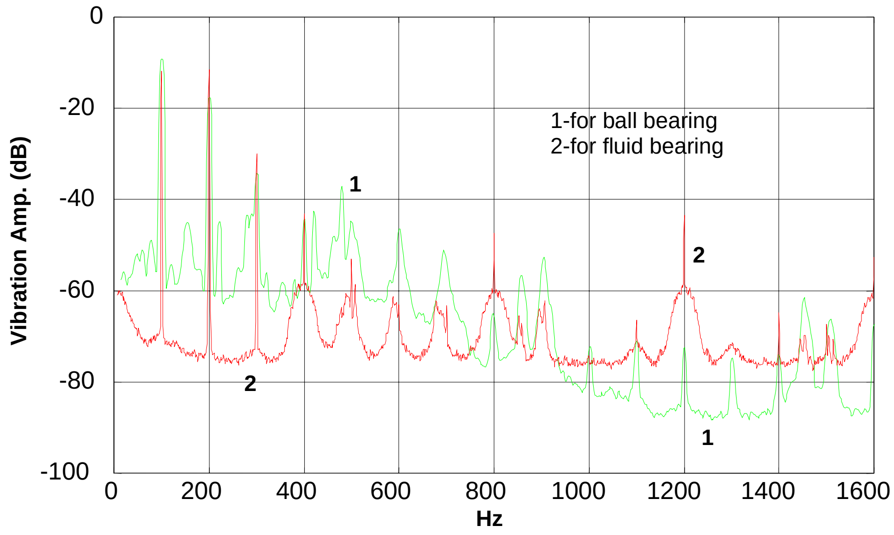

(b) 6,000 rpm

Fig. 8.8 Comparison of vibration amplitude of disks supported by ball and fluid bearing spindles at 3,000 rpm (a) and 6,000 rpm (b).

frequency range are observed for disks supported by a fluid bearing spindle. Only a few small amplitude peaks appear in between the harmonic peaks at low frequency range (below the frequency of 4th harmonics). c) The vibration amplitudes at the frequencies of the harmonics have almost the same height for both disks supported by ball bearing and fluid bearing spindles. At some frequencies, the disks mounted on fluid bearing spindle even have slightly higher amplitude than those mounted on ball bearing spindle. However, these vibration peaks are repeatable motion (that is, RRO peaks) and the off-track effect caused by them can be compensated by the servo control. The peaks that cannot be compensated by the servo control are NRRO peaks that are not coincided with the harmonics. Obviously, for the disks on a fluid bearing spindle, the vibration amplitude of NRRO peaks is lower than that on a ball bearing spindle in a lower frequency region (<800 Hz as shown in Fig. 8.8) for rotational speeds of 3,000 and 6,000 rpm. A direct relationship between the off-track and the disk axial displacement is given by Guo and Chen (2001) as:

$$Ot = 0.0032h, \tag{8.10}$$

where Ot is the head off-track caused by disk vibration and h is the magnitude of the disk flutter in the axial direction. Guo and Chen (2001) also pointed out that the first four modes of disk vibration are the most dominant ones that cause the head off-track. Therefore, reducing the vibration amplitude in lower frequency region will help reduce track misregistration.

Figures 8.9 and 8.10 show the waterfall plots of ball bearing and fluid bearing spindle motors, each loaded with three 2.5 inch disks. The speed range for ball bearing spindle motor is 3,000 to 6,000 rpm with a step increment of 200 rpm. The speed range for fluid bearing spindle motor is 4,000 to 10,000 rpm, with a step increment of 500 rpm for 4,000 - 8,000 rpm, and 1,000 rpm for 8,000 - 10,000 rpm. Comparing these two figures, similar conclusions can be drawn as for those in the 3.5 inch disks situation. As shown in Fig. 8.9, there are a lot of peaks caused by the flaws of ball bearings around the 1st to 5th harmonics. Four disk modes were observed. They are the rocking mode 1B' and 1F'; (0,0) mode at 1090 Hz, (0,1) mode 1B and 1F and (0,2) mode 2B and 2F, respectively. Figure 8.10 shows the results for disks mounted on a fluid bearing spindle. Only three modes can now be observed: (0,0) mode at 1146 Hz; (0,1) mode 1B and 1F, (0,2) mode 2B and 2F. Again, the rocking mode was not observed. Unlike the ball bearing result, there are no peaks around harmonic peaks for disks on fluid bearing spindle. Only a few very weak "half-frequency whirl" peaks are observed in Fig. 8.10.

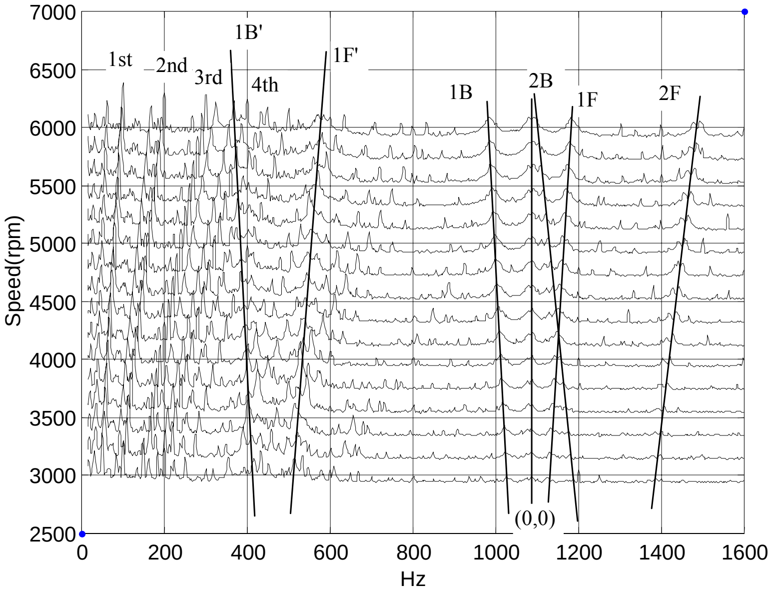

Fig. 8.9 Waterfall plot of 2.5" disk vibration supported by ball bearing spindle motor.

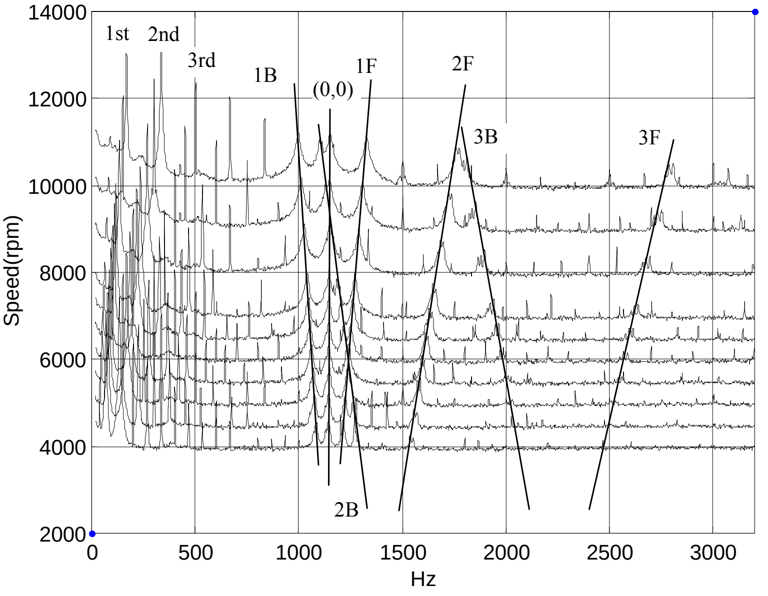

Fig. 8.10 Waterfall plot of 2.5" disk vibration supported by fluid bearing spindle.

The disk vibration characteristics of 3.5-inch and 2.5-inch disks supported by a ball bearing spindle motor or a fluid bearing spindle motor were measured and compared. The experimental results obtained lead to the following conclusions:

1. When the spindle motor was rotating, the static modes of disks are split into forward and backward traveling waves. The frequencies of the forward and backward traveling waves are approximately $\omega = \omega_n \pm n\Omega$, where n is the mode number and Ω is the rotational speed of the spindle motor.
2. The rocking mode was clearly observed for both 3.5 and 2.5 inch disks when they were mounted on the ball bearing spindle motors but there was no rocking mode observed for the disks mounted on fluid bearing spindles.
3. Except for the rocking mode, all other disk modes observed were the same for disks mounted on the fluid and ball bearing spindle motors. However, there was some discrepancy in terms of vibration amplitude. At lower frequency region (< 800 Hz), the amplitude of the disks mounted on the fluid bearing spindle motor is lower than that on the ball bearing motor. At higher frequencies (> 800 Hz), the amplitude of the disks on the fluid bearing spindle motor was higher than that on the ball bearing motor, especially, when the rotational speed was increased.
4. Since there is no direct surface contact in the fluid bearing, the small vibration peaks caused by the waviness on the ball bearing part surfaces were suppressed for the disks mounted on the fluid bearing motors. That is, the non-repeatable run out caused by the ball bearing inherent flaws is removed, resulting in less track center movement for the servo control to follow. This helps reduce the track misregistration.

Chapter 9

CONCLUSIONS AND RECOMMENDATIONS

9.1 Conclusions

Four different types of fluid bearings, namely, hydrodynamic, aerodynamic, hybrid and bi-directional rotating, have been systematically investigated and assessed for application in data storage devices. Since the results obtained are discussed and concluded in the corresponding chapters, hence, only the main conclusions and contributions are summarized in the following.

Among the different journal bearings considered, the herringbone grooved journal bearing is the most suitable for application in the spindle motors for data storage devices because of its better motion stability, higher load capacity and stiffness, and consistent performance in small eccentricity ratios and its unique feature of lubricant sealing capacity.

For thrust bearings, both the herringbone grooved and the spiral grooved (pump-in) thrust bearings can be used because they have similar dynamic characteristics and sealing capacity.

The optimal parameters based on the highest ratio of stiffness to power consumption for the herringbone groove journal bearing, the herringbone groove thrusts bearing and the spiral groove thrust bearing are proposed. The data can be used in such bearing designs.

Using Taguchi robust design approach, it was found that radial clearance is the most influential parameter on the performance of journal bearings, and also the most sensitive parameter to the machining tolerance that will affect the bearing performance.

Air bearings are attractive because of no sealing requirement, and therefore, no risk of lubricant leakage. It is also an ideal alternative of the hydrodynamic bearings for very high-speed applications and no risk of performance degradation caused by lubricant deterioration. Due to its lower load capacity, the diameter of aerodynamic journal bearing is usually several times of that of oil-lubricated journal bearing, which results in a lower ratio of L/D of aerodynamic journal bearing. Therefore, the optimal value of the groove angle α for air bearing is smaller (that is, $\alpha = 12.0°$) than that of the oil-lubricated journal bearing for which $\alpha = 28.0°$, as mentioned in Chapter 3. The total power consumption of the air bearing system is only 47% of that of the reference oil-lubricated bearing system that has the similar load capacity and rotates at the same rotational speed.

The concept of hybrid bearing system was proposed and its characteristics were analyzed. The prototypes of the spindle motors that use such a hybrid bearing system are fabricated and tested. The measured power consumption of the hybrid bearing spindle motor agrees well with the predicted value. The test results show that the hybrid bearing system has 20% power saving compared to a hydrodynamic bearing system. Hence, the proposed hybrid bearing system is really a power saving design and the objective to develop a spindle motor with an efficient fluid bearing system has been achieved.

A bi-directional rotating fluid bearing system is proposed, which can extend the application of such a fluid bearing system. The investigation shows that the power consumption of the bi-directional rotating fluid bearing system is about 50% higher than that of unidirectional rotating fluid bearing system if both the unidirectional and the bi-directional rotating bearing systems take the same dimensions and have comparable load capacity and stiffness.

A compound sealing system, which consists of viscous pumping seal and magnetic seal, was introduced and designed. The experimental results of its prototypes show that the compound seal work very well. It provides a solution for lubricant sealing problem, that is the most challenging in the design of a hydrodynamic bearing.

The ferro-fluid bearing spindle motor was fabricated and tested. It is a 20,000 rpm fluid bearing spindle motor for hard disk drives. The prototype test results of the ferro-fluid bearing spindle motor show that the prototypes have very low NRRO, which is less than 0.03 μm or only half or 1/3 of the NRRO value of the conventional ball bearing spindle motors. The acoustic noise of the prototypes is also low, which is almost 6 to 10 dB(A) lower than that of the ball bearing spindle motors. The compound seal worked very well, since even after more than two months of continuous operation, no lubricant leakage was observed. Hence, the objective of developing a high-speed, high performance spindle motor for data storage devices has been achieved.

The performance of ball bearing and fluid bearing spindle motors has been studied by first, comparing the effect of the unbalanced magnetic force on the performance of these two type spindle motors. It was found that the unbalanced magnetic force caused vibration and acoustic noise for ball bearing spindle motors and horizontally positioned fluid bearing spindle motors. In general, the asymmetric configurations of electric motor in spindles for data storage devices should be avoided to minimize the unbalanced magnetic force and its negative effect.

The disk vibration characteristics for disks mounted on ball bearing or fluid bearing spindle motors are different. The experimental results show that for the disks mounted on fluid bearing spindle motors, the rocking mode of disks is not observed, and the vibration modes caused by the waviness and flaws on the ball bearing surface are successfully suppressed. The vibration amplitude of the disks mounted on the fluid bearing spindles is also lower than that mounted on the ball bearing spindles at low frequency (of less than 800 Hz) region. Therefore, the risk of the track misregistration caused by disk vibration is much reduced.

9.2 Recommendations

For the application of fluid bearing spindle motors in the data storage devices, there are still some areas that are worthy of further investigation as described in the following.

Accurate measurement of stiffness and damping coefficients of fluid bearings is important in evaluating the performance of fluid bearings, but it is difficult to perform the measurement. This is because unlike the ball bearings, the stiffness and damping coefficients of fluid bearings are not defined at static state. The stiffness and the damping coefficients can only be measured when the fluid bearings are in operation and the values of stiffness and damping coefficients are also closely related to the operating speed. Hence, it is very difficult to use the conventional method to measure the stiffness and the damping coefficients of fluid bearings when the spindle motors are rotating at high-speed. To date, there is still no efficient way to measure the stiffness and the damping coefficients of fluid bearings. Therefore, it will be very useful to develop some efficient and reliable methods or devices to measure all the dynamic characteristics of fluid bearings.

The miniature and micro electron-mechanical system (MEMS) devices have attracted much attention recently. It is almost impossible to use the conventional ball bearings for such miniature and micro devices. Therefore, aerodynamic bearings seem to be the best choice for these applications. However, due to the physical dimensions of these micro devices, the behavior of air bearings in such micro size is different from the normal size air bearings, which is an interesting research topic.

Spindle motors are usually imbalanced after being assembled. The imbalance is due to uneven mass distribution caused by the parts imperfection and assembly misalignment. This causes the vibration of the spindle motor that results in performance degradation of the whole device to which the spindle motor is attached. To overcome this problem, spindle motors have to undergo a balancing procedure, which is costly and time consuming. Hence, to design a spindle motor using fluid bearing system that has the "self-balance" capability will be very challenging and useful. Here, the so called "self-balance" means automatic adjustment of the bearing eccentricity and attitude angle, so that the spindle is capable of to compensating the effect caused by unbalance mass without undergoing a balancing procedure after assembly.

With increasing rotational speed, the occurrence of cavitation is more likely in journal bearings, which is undesirable and will definitely affect their performance. The cavitation has not considered in this work, however, the study on cavitation generation, its effect to bearing performance and how to prevent it from occurring is an important and interesting topic.

The thermal effect is important issue and should be considered in future work. Since the lubricant viscosity changes with temperature, the bearing characteristics will also change with the temperature. Hence, it is important to remove the thermal energy generated by spindle motors from the system, so that the operational temperature of the recording system is maintained at an acceptable level, especially for future micro recording systems.

Appendix A ELECTRIC MOTOR DESIGN

The procedures of designing an electromagnetic motor will be described through two different configurations of spindle motors for hard disk drives, namely, a 3.5 inch format spindle with motor-in-hub and a 2.5 inch format spindle with motor-under-slung.

A.1 Electromagnetic Design of 8 Poles 9 Slots Motor

The spindle motors used in data storage devices usually rotate at high speed. For example, the speed of many commercially available disk drives (as well as the two prototypes discussed in the present work) is equal or higher than 10,000 rpm. High-speed motor means higher power dissipation because the windage loss increases at a rate of at least the square (or even higher) of the disk rotational speed, depending on disk spacing. Iron loss of the spindle motor running at such high speed will be much increased. The spindle motor should be designed within a limited space, still it should produce sufficient torque to drive all these loads without generating excess heat. In order to reduce acoustic noise, speed fluctuation and high frequency repeatable run out (RRO), the spindle motor should have low cogging torque and low unbalanced radial force. All of these requirements impose a big challenge for motor designers (Chen *et al.*, 1996, 1998).

Here, the design procedures of an electric motor are briefly introduced. Generally, the design of brushless direct current (BLDC) electric motor includes following steps:

1) Determination of magnet thickness h_m;
2) Determination of rotor back iron height, $h_{ry;}$

3) Determination of dimensions of stator laminations;
4) Determination of number of turns per phase based on back electromotive force (EMF) requirement;
5) Determination of starting torque;
6) Determination of wire gauge;
7) Determination of winding resistance;
8) Estimation of iron loss.

In the following sections, the design of an in-hub configuration, 8 pole/9 slot, permanent magnet and BLDC motor (as shown in Fig. 5.1) is used as an example to demonstrate the detailed design of the above-mentioned steps.

A.1.1 Determination of magnet thickness

In the spindle motor to be designed, a compression molded NdFeB (Neodymium-Iron-Boron) magnet will be used. The specifications of the magnet are listed in Table A.1. The minimum magnet height can be determined by assuming that the total FFM drop across the soft magnetic portion of the main flux path, that is, the rotor back iron, stator tooth tip, tooth body and stator yoke, is about half of that dropped across the air gap. This includes the effect of the saturation in these soft magnetic components, hence,

$$H_m h_m = 1.5 H_g g, \tag{A.1}$$

and

$$h_m = \frac{1.5 H_g g}{H_m} = \frac{1.5 B_g g}{\alpha_w \mu_0 H_m} = \frac{1.5 B_{gm} g}{\mu_0 H_m} \tag{A.2}$$

where, g is the air gap length, B_g and B_{gm} the average and peak flux density in the air gap, H_m the field intensity level in the magnet, μ_0 the magnetic permeability in air, and

α_w the wave form factor. Take $\alpha_w = 0.8$ and the air gap length g = 0.28 mm, which is based on the parts manufacturability consideration, and the average air gap flux density level to be designed is 0.4 T. From the demagnetization curve, it can be found that corresponding to the maximum flux density level of B_g / α_w in the air gap (assuming it is the same as that in the magnet), the field intensity H_m should be 150 × 10^3 KA/m. Hence:

$$h_m = \frac{1.5 \times 0.4 \times 0.28}{4\pi \times 10^{-7} \times 150 \times 10^3 \times 0.8} = 1.11 \text{ mm} \tag{A.3}$$

The axial length of the magnet is 8.8 mm, which is determined by the space available for the electrical motor in the particular design of fluid film bearing spindles. Taking the factor of manufacturing capability into account, a magnet height of 1.25 mm is finally chosen. The ring magnet has an axial length to thickness ratio of about 7:1. A magnet with even higher axial length to thickness ratio may be difficult to fabricate.

A.1.2 Determination of rotor back iron height

For a 3.5 inch format disk drive, the outer diameter of the spindle motor hub must be 25mm. Therefore, the outer diameter of the rotor back iron, d_{or} is 23.0 mm to allow 1.0 mm wall thickness for a aluminum hub. It is assumed that the flux density in the rotor back iron, B_{ry} is about 1.8 T. The rotor back iron height, h_{ry}, can then be determined by:

$$h_{ry} = \frac{\pi (d_{or} - 2h_m) B_g}{4pB_{ry} + 2\pi B_g} \tag{A.4}$$

where p is the number of pole pairs. For an 8 poles motor, p = 4, and hence:

$$h_{ry} = \frac{\pi \times 0.4(23.0 - 2 \times 1.25)}{16 \times 1.8 + 2 \times \pi \times 0.4} = 0.82 \text{ mm} \tag{A.5}$$

To avoid magnetic leakage caused by the saturation in the back iron yoke, a rotor back iron height of 0.9 mm was chosen based on the above estimation. Note that in the above calculation, the average value of the air gap flux density was used.

A.1.3 Determination of dimensions of stator laminations

In the present design, the stator core use 0.35mm thickness, M19 silicon steel sheet. The magnet overhang should be half of the thickness of the magnetic, therefore, total overhang length was 1.25 mm. Thus 20 pieces of laminations were used in the stator core stack, leading to an axial effective length l_s of 7.0 mm. The outer diameter of the stator core d_{os} was 18.04 mm. Other specifications of the M19 silicon steel are given in Table A.2.

Assuming that the flux density level in the tooth body, B_{tb} is 1.5 (T), the tooth body width b_{tb} can be determined by:

$$b_{tb} = \frac{\pi d_{os} B_g}{2pB_{tb}} = \frac{\pi \times 18.04 \times 0.4}{8 \times 1.6} = 1.8 \text{ mm} \tag{A.6}$$

A tooth body width of 1.9 mm was chosen for the 8 pole 9 slot BLDC motor. The internal diameter of the stator core d_{is} is 7.0 mm constrained by the space occupied by the journal fluid bearing. The stator yoke height, h_{sy} is 1.8 mm, which is determined primarily on the basis of mechanical strength consideration rather than the concern of saturation level in this component. Other dimensional parameters are summarized in Table A.3.

A.1.4 Determination of number of turns per phase

The back EMF of stator winding may be expressed by:

$$E_a = 2B_g l_s \frac{\pi n d_{os}}{60} N_p. \tag{A.7}$$

where N_p is the number of turns per phase, l_s the effective axial length of the stator laminations, and E_a the average value of the back EMF per phase (for Y-connected winding, $E_a = E_m/2$). Note that the total number of conductors per phase Z = 2 N_p and that for 3 phase BLDC motor the number of coils per phase $q = 3$. Thus the number of turns per phase can be determined as:

$$N_p = \frac{E_m}{4B_g l_s n \pi d_{os} / 60} = \frac{7.6}{4 \times 0.4 \times 7.0 \times 10^{-3} \times 10.39} \approx 66. \tag{A.8}$$

and the number of turns per coil N (the number of conductors per coil per slot) is:

$$N = N_p/q = 22. \tag{A.9}$$

A.1.5 Determination of starting torque

The starting torque developed in a BLDC motor with Y-connected windings may be expressed as:

$$T_s = 2N_p l_s d_{os} B_g I_{st}. \tag{A.10}$$

The current limit is 2.0 A. Therefore, the electromagnetic torque at start position is estimated as:

$$T_s = 2 \times 66 \times 7.0 \times 10^{-3} \times 18.04 \times 0.4 \times 2.0 = 13.3 \text{ mNm}. \tag{A.11}$$

It should be noted that N_p must be reduced proportionally to the increase of speed, since the limit on the peak value of the back EMF is more or less the same as for spindle motors with different operating speeds. Therefore, the starting torque developed in high-speed motor will be less than that in low speed motors if the current limiting remains unchanged.

A.1.6 Determination of wire gauge

Referring to Fig. A.1, the available slot space for the winding conductors can be calculated based on the following parameters as shown in the figure,

$$a' = 0.55, \qquad b' = 1.33, \qquad c' = 2.71, \qquad \text{and} \qquad c_2' = 0.40. \tag{A.12}$$

The coating thickness on the stator core surface is specified as 5 mil, i.e. 0.127 mm, in the design. Therefore, the actual dimensions for the winding space are:

$$a = 0.423,\ b = 1.203,\ c = 2.456, \text{ and } c_2 = 0.273, \tag{A.13}$$

and it can be calculated that the available space in the slot for one coil is:

$$S_s' = 2.161 \text{ mm}^2. \tag{A.14}$$

If assuming the packing factor, k_{pc} = 65%, the actual space occupied by conductor bundles should be:

$$S_s = 1.4 \text{ mm}^2. \tag{A.15}$$

The outer diameter (including insulation) of the conductor can be estimated by:

$$d_{co}' = \sqrt{\frac{4S_S}{\pi N}} = \sqrt{\frac{4 \times 1.4}{\pi \times 22}} = 0.2851 \text{ mm}. \tag{A.16}$$

Therefore, 0.285 mm enameled copper conductor (S.W.G. 33 copper wire) with grade 2 insulation will be used. The actual parameters for this wire gauge are as following:

d_{co} (diameter of conductor including insulation) = 0.285 mm. (A.17)

d_{ci} (diameter of bare copper wire) = 0.254 mm. (A.18)

S_c (net cross-sectional area of bare copper wire) = 0.05067 mm^2. (A.19)

A.1.7 Determination of winding resistance

The mean length of one turn of stator coil may be estimated by the following factors:

i. the axial length of lamination stack including the coating,	l_a = 7.954 mm;
ii. the tooth body width including the coating,	b_{tb} = 2.154 mm;
iii. the mean winding width	b_w = 1.0 mm;
Thus the mean length of one coil is	l_{mean} = 24.22 mm;
and the total length of the conductors per phase:	$L=N_p\, l_{mean}$ = 1598.3 mm.

The phase resistance at 24 °C can be calculated by:

$$R_a = \frac{\sigma_c L}{S_c} = \frac{1.73\times 10^{-8}\times 1598.3\times 10^{-3}}{0.05067\times 10^{-6}} = 0.56\ \Omega. \quad \text{(A.20)}$$

where σ_c is the resistivity of the conductors which is 1.73×10^{-8} at 24 °C. The line resistance for Y-connected windings is

$$R_m = 2R_a = 1.12\ \Omega. \quad \text{(A.21)}$$

A.1.8 Estimation of iron losses in stator

It is well known that the prediction of iron loss is a difficult task (MacLeaod and Williams, 1993). The local iron loss rate also depends on the shape of the locus which is formed when the local magnetic field vector rotates. The omission of the effect of rotational core loss may lead to errors in the prediction of iron loss. An estimation of iron losses in a designed spindle motor stator based on the information of magnetic field distribution will be presented here.

In the iron loss model, the effect of the excess loss is also included. This assumption will lead to an over estimation, which is, however, better than underestimation, when alternating field model is used.

The total iron loss, P_{il} may be expressed as

$$P_{il} = k_e B_m{}^2 f^2 + k_a B_m{}^{3/2} f^{3/2} + k_h B_m{}^{\chi} f \tag{A.22}$$

where k_e, k_a, and k_h are the loss coefficient for classical eddy current loss, excess(anomalous) loss, and hysterisis loss, respectively, f the frequency, and the value of χ is between 1.0 - 2.0.

In Eq. (A.22), the constants χ, k_e, k_a, and k_h should be obtained experimentally. For 0.35 mm M19 silicon steel, the data for these constants used in the iron loss analysis are as follows:

χ, = 1.58, k_e, = 4.74×10^{-5}, k_a, = 1.07×10^{-3}, and $k_h = 1.96 \times 10^{-2}$

The flux density distribution in the 8-pole 9-slot motor:

Pole pitch	$\tau = 7.08$ mm
Stator tooth arc	$a_c = 3.78$ mm
Flux density at tooth tip surface	Bc = 0.75 T
Flux density at tooth body	$B_{tb} = 1.50$ T

Flux density at tooth tip	$B_{tt} \approx 0.5\ (Bc + B_{tb}) = 1.12$ T
Flux density at stator yoke	$B_{sy} = 0.5\ B_{tb}(b_{tb}/h_{sy}) = 0.8$ T

Weights of stator core components are calculated as follows:

Weight of tooth tip	Wtt = 0.0019 Kg
Weight of tooth body	Wtb = 0.0025 Kg
Weight of stator yoke	Wst = 0.0027 Kg

Iron losses at various locations, for 10,000 rpm, f = 667 Hz,

Iron loss at tooth tip	$p_{tt} = 0.125$ W
Iron loss at tooth body	$p_{tb} = 0.265$ W
Iron loss at stator yoke	$p_{st} = 0.100$ W
The total iron loss	$P_{il} = 0.49$ W

The above data show that for high-speed spindle motors, an accurate prediction of the iron losses is necessary.

Table A.1 Data for plastic bonded NdFeB magnet

Grade	Br	Hc	Hci	$(BH)_{max}$	μ_r	α_T	H_s	ρ
	(KG)	(KOe)	(KOe)	(MGOe)	(H/m)	%/°C	(KOe)	g/ cm^3
NP-11L	690-730	5.5~5.9	9.0~10.5	10.0~11.0	1.20	-0.10	>=20	5.9~6.2

Note: H_s is the saturation magnetization force, and ρ the density, and α_T the temperature coefficient.

Table A.2 Data of M19 silicon steel for stator lamination stack

Grade	Demsity	Resistivity	Core losses (W)				Magnetic flux density (T)			
	$\rho(kg/m^3)$	$\sigma(\mu\Omega m)$	W_{10f50}	W_{15f50}	W_{10f60}	W_{15f60}	B_{H10}	B_{H15}	B_{50}	B_{H100}
M19	7650	0.55	1.03	2.40	1.30	2.98	1.50	1.58	1.68	1.79

Note: W_{10f50} indicates the core loss at 50 Hz and 1.0 T, B_{H15} indicates the magnetic flux density at a field intensity of 1500 KA/m.

Table A.3. Design data sheet of 8 poles 9 slots BLDC motor

DESCRPTION	SYMBOL	UNIT	VALUE
Global requirements & parameters			
Connection			Y
Supply voltage	V_C		12.0
Operating speed	N	rpm	11,000
No. of pole pairs	P		4
No. of slots	Z		9
Back emf (peak)	E_m		7.6
Starting torque	T_S	mNm	17.0
Commutation angle	α	°elec.	0
Dimensional and related parameters			
AXIAL			
length of stator core	l_{sy}	mm	7.7
steel packing factor	k_{Fe}		0.91
length. of rotor yoke	l_{ry}	mm	9.5
length. of magnet	l_{mg}	mm	8.8
RADIAL			
OD of motor	D	mm	24.60
OD of rotor yoke	D	mm	23.00
OD of magnet	D	mm	21.10
air gap height		mm	0.28
OD of stator	D	mm	18.04
tooth body height	Hlb	mm	2.71
tooth tip height	H	mm	1.10
Stator yoke height	H	mm	1.80
ID of motor	D	mm	7.00
TOOTH/SLOT			
tooth body width	Bb	1.90	
tooth pitch		6.30	
slot opening	b@	1.26	
tooth tip edge h,	h,	0.44	
tooth wedge angle	G	0	105
Winding			
No. Tunilphase	W	1	66
wdg width	B	mm	1.0
wire gaugellnsul.		I	S.W.0.33
Conductor dia(C)	Di	mm	0,254
Conductor dia.(T)	D	mm	0,285
conductor x-section area	Sc	mm	0.05067
No. turns /slot /coil		1	22
Packing factor	K		0.82
Performance Indices/parameters			
Starting Current		A	2.6
Running current		A	0.42
Resistance (phase)	R	Q	0.56
Resistance (motor)	R	cl	1.12
Losses			
Copper loss	Pc.	W	
iron loss	Pfe	W	
Windage loss	Pwd	W	
other mechanical loss	Pme	W	

Note: The above data is for 3.5" HDD, carrying 4-6 platters, 8 pole/9 slot spindle motor

A.2 Electromagnetic Design of 6 Poles 9 Slots Motor

The design of an under-slung 6 pole 9 slots motor will be discussed in this section. The motor to be designed is for a 2.5” hard disk drive spindle motor with the specified speed of the motor 20,000 rpm. As previously mentioned, there are two configurations for spindle motors, motor-in-hub and motor-under-slung configurations. For a fixed voltage supply and spindle speed, torque constant of the spindle motor is almost fixed and the same for these two configurations. Thicker conductor is needed to carry higher current to produce higher torque, without generating excess heat. Because of the space limitation, it is difficult for the design of motor-in-hub configuration to generate enough working torque. Therefore, the motor-under-slung configuration is adopted to meet the load requirement and get a better power management. To avoid high frequency repeatable run out (RRO) and position error single (PES) caused by unbalanced radial magnetic force arising from the interaction between unsymmetrical stator magnetic structure and magnet poles, the spindle motor should be devised from one of the balanced configurations, such as 4-pole/6-slot, 6-pole/9-slot, 8-pole/12-slot, and 12-pole/9-slot, etc. Spindle motor iron loss is primarily dependent on the square of the multiplication of the spindle motor speed (in revolutions per second) and the number of magnet pole pairs of the motor. Compared to copper loss, iron loss is dominant in high speed spindle motors. A spindle motor with fewer pole pairs has less iron loss. However, magnetic flux per pole will be higher for the motor with fewer pole pairs. Thicker back iron ring has to be used. As a result, the effective diameter D_{eff} of the motor will decrease and so will the motor torque that is proportional to the square of D_{eff}.

Based on above considerations, a brushless DC motor with a balanced configuration of 6 poles and 9 slots was adopted for the 20,000 rpm ferro-fluid bearing spindle motor. The balanced configuration of 6-pole/9-slot is associated with high cogging toque. To minimize the cogging torque, a special magnetization technique and the tooth shape optimization were used to reduce the cogging torque. Magnetization wires of the magnetization fixture were arranged such that about 70% of every magnet segment (the ring magnet has 6 segments) was magnetized. Reshaping the top surfaces of stator teeth with an optimal curvature that is performed according to Taguchi's robust design method (Chen *et al*, 2001). Figures A.2 and A.3 show the cogging torque and working torque of the motor after optimization. The motor current used in the modeling and simulation is 0.8 A. Before the optimization, the peak to peak value of the cogging torque of the motor is 5.80 milli-Nm, the average working torque was 3.96 milli-Nm. The torque ripple ratio, (Trmax-Trmin)/Trava, is around 140%, where Trmax, Trmin and Trava are respectively the maximum working torque, the minimum working torque, and the average working torque. Contribution of cogging torque to the torque ripple was dominant before optimization. After optimization, the peak to peak value of the cogging torque is reduced to 0.492 milli-Nm. The average working torque is 3.87 milli-Nm and the ratio of (Trmax-Trmin)/Trava is reduced to 14.2%. Contribution of cogging torque to the torque becomes minor compared to the commutation torque ripple.

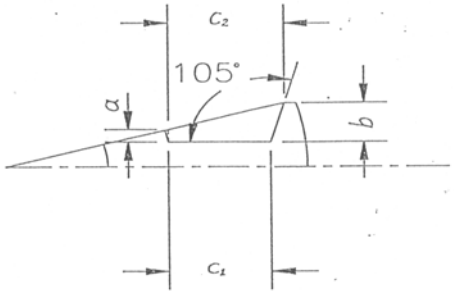

Fig. A.1. Slot dimensions for 8 poles 9 slots motor

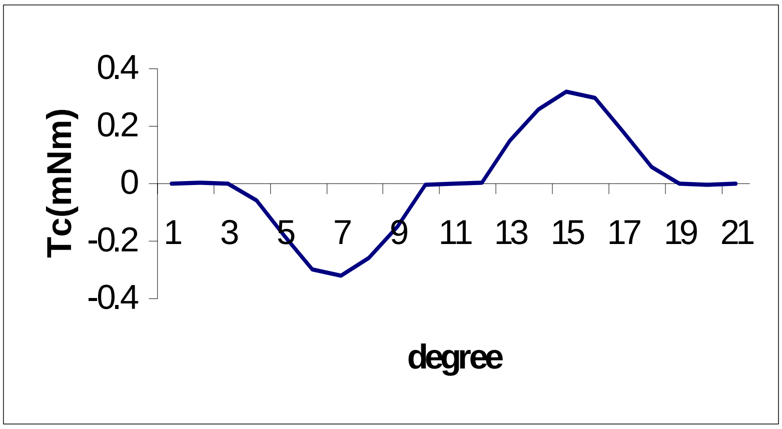

Fig. A.2 Motor cogging torque after optimisation (under-slung design).

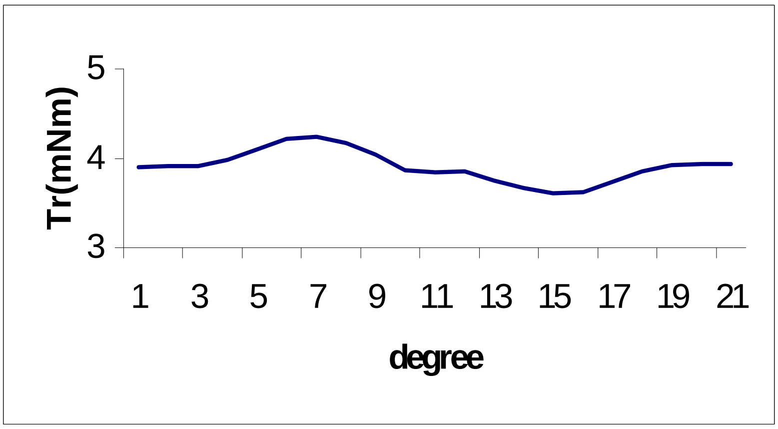

Fig. A.3 Motor running torque after optimization (under-slung design).

REFERENCES

Ashar, K. G., Magnetic Disk Drive Technology--Heads, Media, Channel, Interfaces and Integration, IEEE Press, 1997.

Bagchi, T. P., Taguchi Method Explained: practical Steps to Robust Design, Prentice-Hall of India, 1993.

Beijing, Handbook of Mechanical Design, (in Chinese), Metallurgy Press, Beijing, 1988

Bendell, A., Disney, J. and Pridmore, W. A., Taguchi Methods : Applications in World Industry, Springer-Verlag, 1989.

Berkovsky, B. M., Medvedev, V. F. and Krakov, M. S., Magnetic Fluids :Engineering Applications, Oxford University Press, 1993.

Bhushan, B., Tribology and Mechanics of Magnetic Storage Devices, New York, Springer-Verlag, 1996

Blount, W.C., "Fluid dynamic bearing spindle motor", IBM Storage Systems Group, IBM Corp., Feb. 2001.

Bonneau, D. and Absi, J., "Analysis of aerodynamic journal bearing with small number of herringbone grooves by finite element method", *ASME Trans., J of Tribology*, v116, pp. 698-704, 1994.

Bootsma, J., "The gas liquid interface and the load capacity of helical grooved journal bearings", *ASME Trans., J of Lubrication technology*, pp. 94-100, Jan., 1973.

Bouchard, G., Lau, L. and Talke, F. E., "An investigation of non-repeatable spindle motor", *IEEE Transactions on Magnetics*, v23, n5, pp. 3687-3689, 1987.

Brink, R. V., Czernik, D. E. and Horve, L. A., Handbook of Fluid Sealing, McGraw-Hill, 1993.

Brown, M. W., Seals and Sealing Handbook, Elsevier Advanced Technology, 1995.

Castelli, V. and Pirvics, J., " Equilibrium characteristics of axial groove gas lubricated bearings", *ASME J of Lubrication Technology*, v89, n2, pp. 177-196, 1967.

Chen, S. X., Jabbar, M. A., Zhang, Q. D. and Liu, Z. J., “New challenge: Electromagnetic design of BLDC motors for high speed fluid film bearing spindles used in hard disk drives”, *IEEE Transactions on Magnetics*. v32, n5, pp. 3854-3856, 1996.

Chen, S. X. and Low, T. S., “The Robust Design Approach for Reducing Torque in Permanent Magnet Motors”, *IEEE Transactions on Magnetics*, v34, n4, pp. 2135-2137, 1998.

Chen, S. X., Liu, Z. J., Low, T. S. and Zhang, Q. D., “Future High Speed Spindle and Components for Hard Disk Drives” *INSIGHT, IDEAMA Journal*, January/February, pp. 26-28, 1999.

Chen, S. X., Zhang, Q. D., Chong, H. C., Komatsu, T. and Kang, C. H., "Some design and prototyping issues on a 20k rpm HDD spindle motor with a Ferro-fluid bearing system", *IEEE Transactions on Magnetics*. v37, n2, pp. 805-809, 2001.

Constantinescu, V. N., Nica, A., Pascovici, M. D., Centureanu, G. and Nedelcu, S., Sliding Bearings, Allerton Press, New York, 1985

Cullen J. and Hollingum, J., Implementing Total Quality, Springer-Verlag, 1987.

Daniel, E. D., Mee, C. D. and Clark, M. H., Magnetic Recording -- The First 100 Years, IEEE press, 1999.

DISK/TREND News, "Hard disk drives", Source: 1999 DISK/TREND Report, 1999.

Donovan, J., “The HDD industry’s return to growth”, *Proceedings of Storage Leadership in Asia Pacific,* Diskcon Asia-Pacific 2003, IDEMA, March, 2003

Fleming, D. P. and Hamrock, B. J., "Optimization of self-action herringbone journal bearings for maximum stability", *Proceedings of 6th International gas bearing symposium*, University of Southampton, March 27-29, 1974.

Frees G. M., "Disk drive spindle dynamics – analysis and measurement", *Advances in Information Storage System,* v6, pp. 237-262, 1995.

Frey, E. and Zipperian, D., "Reduced fly height through reduction in static-attitude distribution", *Data Storage*, Oct. PP. 30-34, 2000.

Fuller, D. D., Theory and practice of lubrication for Engineers, Wiley, 1984

Grochowski, E. G., Hoyt, R. F. and Heath, J. S., "Magnetic hard disk drive form factor evolution", *IEEE Transactions on Magnetics*, v26, n6, pp. 1850-1854, 1993.

Grochowski, E. G. and Thompson, D. A., "Outlook for maintaining areal density growth in magnetic recording", *IEEE Transactions on Magnetics*, v32, n2, pp. 1850-1854, 1996.

Grochowski, E. G. and Hoyt, R. F., "Future trends in hard disk drives", *IEEE Transactions on Magnetics*, v32, n2, pp. 1850-1854, 1996.

Gross, W. A., Fluid film lubrication, Wiley, 1962. (Refer to his new book of Fluid film lubrication, Wiley, 1980).

Gunter, B, A, Perspective on the Taguchi Methods, Quality Progress, June, pp. 44-52, 1987.

Guo, L. and Chen, Y. J., "Disk flutter and its impact on HDD servo performance", *IEEE Trans. on Magnetics*, v37, n2, pp. 866-870, 2001.

Guo, W. and Bozorgi, J., "Dual-stage servo system with microactuated head gimbal assemblies", *J. of Information Storage and Processing Systems*, v2, n1, pp. 101-108, 2000.

Hamrock, B. J. and Fleming, D. P., “Optimization of Self-acting Herringbone Grooved Journal Bearings for Maximum Radial Load Capacity”, *5th Gas Bearing Symposium*, Paper 13, Southampton, 1971.

Hamrock, B. J., Fundamentals of fluid lubrication, McGraw-Hill, Inc., 1994.

Harker, J. M., "A quarter century of disk file innovation", *IBM J. of Res. and Devel.*, v25, p677, 1981.

Harris, C.M., (ed) Shock and vibration handbook, 4th ed. Mcgraw-Hill Inc., pp31-32, 1996

Hays, D.F., "Plane sliders of finite width", *Trans ASLE*, v1, n2, 1958.

Haystead, J, " No place like home for HDDs", *Data Storage*, Jan. p2, 2001.

IBM, “IBM introduces world's smallest hard drive”, http://www.storage.ibm.com/press/hdd/micro/980909.htm, 1998.

IBM, “100 years of magnetic recording milestones: 1898 to 1998”, http://www.storage.ibm.com/hardsoft/diskdrdl/technolo/100yea..., 2000.

IBM, “IBM introduces record-breaking 15,000 rpm, 36-GB hard disk drive”, http://www.storage.ibm.com/press/hdd/20010130.htm, 2001.

Jang, G.H. and Chang, D.I., “Analysis of a hydrodynamic herringbone grooved journal bearing considering cavitation”, *ASME Trans., J. of Tribology*, v122, pp. 103-109, 2000.

Kang, K., Rhim, Y. and Sung, K., “A study of the oil-lubricated herringbone-grooved journal bearing—Part1:Numerical analysis”, *ASME Trans., J. of Tribology*, v118, pp. 906-911, 1996.

Kawabata, N., Ozawa, Y., Kamaya, S. and Miyake Y., "Static characteristics of the regular and reversible rotation type herringbone grooved journal bearing", *ASME Trans., J. of Tribology,* v111, pp. 484-490, 1989.

Kawabata, N., Ashino, I., Sekizawa, M. and Yamazaki, S., "Spiral grooved bearing utilizing the pumping effect of a herringbone journal bearing", *JSMS International journal, serials III*, v34, n3, pp. 411-418, 1991.

Khan, R. and Rudd, G., “What's the best lube for fluid bearing”, *Data Storage*, Sept. 1998.

Khan, R. and Rudd, G., “Fluid bearings: A cleaner option for spindle motors”, *Data Storage,* Oct. 1999,

Kinouchi, K. and Tanaka, K., "Performance characteristics of heeringbone grooved journal bearings using a finite element method", *Proc. Japan Inter. Tribology Conference*, Nagoya, Japan, pp. 935-940, 1990.

Kozierok, C. M., “Hard disk drive”, PC Guide, http://www.storagereview.com/guide/guide_index.html, 1999.

Ku, C.-P. R. and Jennings, D. "Effect of disk and structure Flexibility on rocking mode frequencies of a hydrodynamic bearing spindle motor system", *Proceedings of 26th Annual Symposium of Incremental Motion Control Systems and Devices*, San Jose, June 11-14, pp. 113-122, 1996.

Ku, C-P, R., Parsoneault, S. and Leuthold, H., "Hydrodynamic motors trim disk drive run out", *Data Storage*, Jan. 1998.

Lee, T.S., Liu, Y.G. and Winoto, S.H., “Analysis of liquid-lubricated herringbone grooved journal bearing”, *Inter. J. of Numerical methods for Heat and Fluid Flow*, Paper No. HFF808, July, 2003

Liu, Z. J., Bi, C., Zhang, Q. D., Jabbar, M. A. and Low, T. S., “Electromagnetic design aspects for hard disk drive spindle motors with fluid film lubricated bearings”, *IEEE Transactions on Magnetics*. v32, n5: p3893-3895, 1996.

Lund, J.W. and Thomsen, K.K., “A calculation method and data for the dynamic coefficients of oil-lubricated journal bearing”, Topics in fluid film bearing and rotor bearing system design and optimization, edited by Rohde *et al*., ASME New York, pp. 1-28, 1978.

MacLeaod, D. J. and Williams, M. M., "Design of spindle motors for high performance disk drives", Proc. of 22nd Annual Symposium on Incremental Motion Control Systems and Devices’, pp. 1-9, ed. B. C. Kou, June 8, Champain, USA, 1993.

MacLeod, D. J., "Spindle motor design for small disk drives", *Data Storage*, pp. 49-53, Jan/Feb. 1995.

Malanoski, S. B. and Pan, C. H. T., "The static and dynamic characteristics of the spiral-grooved thrust bearing", *J of Basic engineering*, pp. 547-558, 1965.

Matsuoka, K., Obata, S., Kita, H. and Toujou, F., "Development of FDB spindle motors for HDD use", *IEEE Transactions on Magnetics*, v37, n2, pp. 783-788, 2001.

McAllister, J.S., "The effect of disk platter resonances on track misregistration in 3.5 inch disk drives", *IEEE Trans. on Magnetics*, v32, n3, pp. 1762-1766, 1996.

McAllister, J.S., "Characterization of disk vibrations on aluminum and alternate substrates", *IEEE Transactions on Magnetics*, v33, n1, pp. 968-973, 1997.

Muijderman, E. A., Spiral Groove Bearings, Philips Research Laboratories, Philips Research Report Supplements, 1964.

Nau, B. S., "Hydrodynamic of face seal films", paper F5, second international conference on fluid sealing, BHRA, Canfield, England, April, 1964.

Nau, B. S., "Centripetal flow in face seals", ASLE paper No. 68, AM 4B-3, 1968.

Noguchi, S., Tanaka, K. and Ono, K., "Theoretical analysis of a ball bearing used in HDD spindle motors for reduction of NRRO", *IEEE Transactions on Magnetics*, v35, n2, pp. 845-849, 1999.

Ono, K., Zhu, J. S. and Cui, C. Z., “A comparison study on the characteristics of five types of hydrodynamic oil bearings for hard disk spindles”, *Advanced in Information Storage System*, v9, pp33-46, 1998.

Phadke, S. M., Quality Engineering Using Robust Design, Prentice Hall, 1989.

Pinkus, O., "The Reynolds centennial: A brief history of the theory of hydrodynamic lubrication*", ASME Trans., J. of Tribology*, v109, pp. 2-20. 1987.

Polch, E. Z., Williams, C. D. and Cordova, J., "Hydrodynamic bearing having inverted surface tension seals", *U. S. Patent No. 5 533 811*, 1996.

Porter, T., "Fluid dynamic-bearing motors overcome cost/longevity challenges", *Data Storage*, Jan. 2001.

Quantum, “FDB in Quantum”, http://www.quantum.com/src/whitepapers/wp_fbplusas.htm, 2000a.

Quantum, “Hydrodynamic bearing technology in Quantum hard disk drives”, http://www.maxtor.com, July, 2000b.

Raimodi, A. A. and Boyd, J. "A solution for the finite journal bearing and its application to analysis and design-III", *Trans ASLE*, v1, n1, 1958.

Raimodi, A. A., "A numerical solution for gas-lubricated full journal bearing of finite length", *Trans. ASLE*, v4, pp. 131-155, 1961.

RBTS, User manual of advanced rotating machinery dynamics (ARMD), RBTS Inc. 1998.

Seagate, “Seagate salutes the 100th anniversary of magnetic recording”, http://www.seagate.com/newsinfo/newsroom/papers/, 2000.

Shen, I.Y. and Ku, C.-P. R., "A nonclassical vibration analysis of a multiple rotating disk and spindle assembly", *J. of Applied Mechanics*, v64, pp. 165-174, 1997.

Shen, I.Y. and Ku, C.P., "On the vibration of analysis of multiple rotating flexible disks", ISPS Vol.1, ASME 1995, pp. 259-270, 1995.

Schirle, N. and Lieu, D. K., "History and trends in the development of motorized spindles for hard disk drives", *Digest of the Asia-Pacific Magnetic Recording Conference*, p. WA-01-1, Singapore, Nov. 29 - Dec. 1, 1995.

Smalley, A. J., "The narrow groove theory of spiral grooved bearings: Development and application of a generalized formulation for numerical solution", *ASME Trans., J of Lubrication Technology*, pp. 86-92, Jan., 1972.

Speliotis, D., "Magnetic recording: the next 100 years", *Data Storage*, Jan. pp. 25-28, 1999

Srikrishna, P. and Kasetty, K., "Predicting track misregistration (tmr) from disk vibration of alternate substrate materials", *IEEE Transactions on Magnetics*, v36, n1, pp. 171-176, 2000.

Stepina, V., Lubricants and Special Fluids, Vaclav-Vesely, Amsterdam, 1992

Stevens, L. D., "The evolution of magnetic storage", *IBM J. of Res. and Devel.*, v25, p. 663, 1981

Swan, A. C., Harrison, J. C. and Talke, F. E., "Non-repeatable runout measurement and simulation of fluid lubricated spindles", *IEEE Transactions on Magnetics*, v32, n3, pp. 1727 -1732, 1996.

Szeri, A. Z., Fluid Film Lubrication: Theory and Design, Cambridge University Press, 1998.

Taguchi, G., Yokoyama, T. and Wu, Y., Taguchi Methods: Design of Experiments, Japanese Standards Association, 1993.

Vohr, J. H. and Pan, C. H. T, "On the spiral-grooved, self-acting, gas-bearing", MTI report No. 63TR52, 1963.

Vohr, J. H. and Chow, C. Y., "Characteristics of herringbone-grooved, gas-lubricated journal bearings", *J of Basic Engineering*, pp. 568-577, 1965.

Vohr, J. H. and Chow, C. Y., "Theoretical analysis of spiral-grooved screw seal for turbulent operation", *ASME Trans., J of Lubrication Technology*, pp. 675-686, Oct., 1969.

Wan, J.M., Lee, T.S., Shu, C. and Wu, J.K., "A numerical study of cavitation foot-prints in liquid-lubricated herringbone grooved journal bearing", *Inter. J. of Numerical methods for Heat and Fluid Flow*, v12, n5, pp. 518-540, 2002

Wang, J., "On the dynamics of rocking motion of the hard-disk drive spindle motors system", *Advances in Information Storage Systems*, v7, pp. 251-267, 1994.

Winoto, S. H., Zhang, Q. D., Tan, P. Y. Joyce, Hou, Z. Q. and Rondonuwu, C. C., "Herringbone grooves for pumping sealing of lubricant in vertical hydrodynamic journal bearing", *International Journal of Transport Phenomena*, v3, pp. 1-8, 2001a.

Winoto, S. H., Hou, Z. Q. and Zhang, Q. D., "Performance comparison of vertical herringbone grooved journal bearings", *Journal of Flow Visualization and Image processing*, v8, pp. 203-212, 2001b.

Wood, R.W., Miles, J., Olson, T., "Recording technologies for terabit per square inch systems", *IEEE Transactions on Magnetics*, v38, n4, pp. 1711-1718, 2002.

Wu, J.K., Li, A.F., Lee, T.S., and Shu, C., "Operator-splitting method for analysis of cavitation in liquid-lubricated herringbone grooved journal bearing", *J. of Hydrodynamics,* Serial B, v4, pp. 95-101, 2002.

Yoshida, S., Kohno, T., Saegusa, S., Terayama, T., Yoshida, T., Hirai, H., Hamada, Y. and Yamaguchi, T., "Non-symmetrical three-lobe bearing spindle technology: a drive technology to increase aerial density", *IEEE Transactions on Magnetics*, v32, n3, pp. 1721-1726, 1996.

Zang, Y. and Hatch, M. R., "Analysis of coupled journal bearing and thrust hydrodynamic bearing using finite volume method", *ASME Advances in Information and Storage and Processing System*, v1, pp. 71-79, 1995

Zhang L. H. and Koka, R., “Lost data: how a little dirt can do a lot damage”, *Data Storage*, Mar. 1999.

Zhang, Q.D., Chen, S.X. and Liu, Z.J., “The effect of unbalanced magnetic force on the dynamic performance of spindle motors”, *Proceedings of International Magnetics Conference (INTERMAG’97) CC-10*, (USA), 1997.

Zhang, Q.D., Chen, S.X. and Liu, Z.J., “Design of a hybrid fluid bearing system for HDD spindles”, *IEEE Transactions on Magnetics*, v35, n2, pp. 2638-2640, 1999.

Zhang, Q.D., Winoto, S.H., Chen, S.X. and Chong, H.C., “Design of fluid film bearing for spindle motor in hard disk drives”, *Proceedings of International Tribology Conference 2000*, Nagasaki, Japaen, pp. 1645-1650, 2000.

Zhang, Q. D., Chen, S. X., Winoto, S. H. and Ong, E. H., "Design of High-Speed Magnetic Fluid Bearing Spindle Motor", *IEEE Transactions on Magnetics*, v37, n4, pp. 2647-2650, 2001a.

Zhang, Q.D., Chen, S.X., Winoto, S.H. and Yang, J.P., “A bi-directional rotating fluid bearing system”, *Proceedings of ISPS*, MA6, 2001b.

Zhang, Q.D., Winoto, S.H. Guo G.X. and Yang, J.P., "Experimental comparison of disk vibration mounted on ball bearing and fluid bearing spindles", *STLE Tribology Transactions*, v46, n3, pp 465-468, 2003.

Zhu, J. S. and Ono, K., " A comparison study on the performance of four types of oil lubricated hydrodynamic thrust bearings for hard disk spindles", *ASME Trans., J of Tribology*, v121, pp. 114-120, 1999.

Zirkelback, N. and Andres L. S., “Finite element analysis of herringbone groove journal bearings: a parametric study”, *ASME Trans., J of Tribology*, v120, pp. 234-240, 1998.

Zou, J. B. and Lu, Y. P., "Numerical calculation for Ferrofluid seals", *IEEE Transactions on Magnetics*, v28, n6, pp.3367-3371, 1992.

PUBLICATIONS FROM THIS WORK

Journal Papers:

Zhang, Q.D., Winoto, S.H. Guo G.X. Yang, J.P., "Experimental comparison of disk vibration mounted on ball bearing and fluid bearing spindles", *STLE Tribology Transactions*, v46, n3, pp 465-468, 2003.

Zhang, Q.D., Chen, S.X., Winoto, S.H. and Yang, J.P., “A bi-directional rotating fluid bearing system”, *Microsystem Technologies,* v8, n4-5, pp 217-277, 2002.

Zhang, Q. D., Chen, S.X., Winoto, S. H. and Ong, E. H., "Design of High-Speed Magnetic Fluid Bearing Spindle Motor", *IEEE Transactions on Magnetics*, v37, n4, pp. 2647-2650, 2001.

Zhang, Q. D., Chen, S. X. and Liu, Z. J., “Design of a hybrid fluid bearing system for HDD spindles”, *IEEE Transactions on Magnetics*, v35, n2, pp. 2638-2640, 1999.

Chen, S. X., Zhang, Q. D., Chong, H. C., Komatsu, T. and Kang, C. H., "Some design and prototyping issues on a 20k rpm HDD spindle motor with a Ferro-fluid bearing system", *IEEE Transactions on Magnetics*. v37, n2, pp. 805-809, 2001.

Chen, S. X., Liu, Z. J., Low, T. S. and Zhang, Q. D., “Future High Speed Spindle and Components for Hard Disk Drives” *INSIGHT, IDEAMA Journal*, January/February, pp. 26-28, 1999.

Winoto, S. H., Zhang, Q. D., Tan, P. Y. Joyce, Hou, Z. Q. and Rondonuwu, C. C., "Herringbone grooves for pumping sealing of lubricant in vertical hydrodynamic journal bearing", *International Journal of Transport Phenomena*, v3, pp. 1-8, 2001a.

Winoto, S. H., Hou, Z. Q. and Zhang, Q. D., "Performance comparison of vertical herringbone grooved journal bearings", *Journal of Flow Visualization and Image processing*, v8, pp. 203-212, 2001b.

Winoto, S. H., Hou, Z. Q., ONG, S. K., Rondonuwu, C. C. and Zhang, Q. D., "Effects of Herringbone Groove Patterns on Performance of Vertical Hydrodynamic Journal Bearings", STLE *Tribology Transactions*, v45, n3, pp. 318-323, 2002.

Conference papers:

Zhang, Q.D., Winoto, S.H., Chen, S.X. and Chong, H.C., "Design of fluid film bearing for spindle motor in hard disk drives", *Proceedings of International Tribology Conference 2000*, (Nagasaki, Japan), pp. 1645-1650, 2001.

Zhang, Q.D., Chen, S.X. and Liu, Z.J., "The effect of unbalanced magnetic force on the dynamic performance of spindle motors", *Proceedings of International Magnetics Conference (INTERMAG'97) CC-10*, (USA), 1997.